

.....

THÈSE DE DOCTORAT

Soutenue à Aix-Marseille Université
le 29 mars 2022 par

Asmaa HADJ AHMED

Design of new electrochemical cells for studying enzymes by
Protein film electrochemistry

Discipline

Sciences Chimiques

École doctorale

ED 250 SCIENCES CHIMIQUES DE MARSEILLE

Laboratoire/Partenaires de recherche

Bioénergétique et Ingénierie des Protéines
(UMR 7281)

Institut Universitaire des Systemes Thermiques
Industriels (UMR 7343)

Composition du jury

.....

Dr. Sophie GRIVEAU Chimie ParisTech - PSL	Rapporteure
Pr. Gerard L.VIGNOLES Université de Bordeaux	Rapporteur
Dr. Elisabeth LOJOU Aix-Marseille Université	Examinatrice/ Présidente de Jury
Pr. Philippe MANDIN Université de Bretagne Sud	Examineur
Dr. Vincent FOURMOND Aix-Marseille Université	Directeur de thèse
Dr. Jean-Vincent DAURELLE Aix-Marseille Université	Co-Directeur de thèse

Declaration

I, undersigned, Asmaa HADJ AHMED, hereby declare that the work presented in this manuscript is my own work, carried out under the scientific direction of Vincent FOURMOND and Jean-Vincent DAURELLE, in accordance with the principles of honesty, integrity and responsibility inherent to the research mission. The research work and the writing of this manuscript have been carried out in compliance with both the french national charter for Research Integrity and the Aix-Marseille University charter on the fight against plagiarism.

This work has not been submitted previously either in this country or in other country in the same or in a similar version to any other examination body.



HADJ AHMED Asmaa

April 2022

Acknowledgements

First and foremost, I would like to express my gratitude to my supervisors Vincent Fourmond and Jean Vincent DAURELLE for giving me the chance to pursue this PhD thesis. I really appreciate their support, their patience and their guidance. I am also grateful to the knowledge they have shared with me, for the time and energy they have invested in my thesis and for their very useful critics. A big thank to Jérôme Vicente for his help and for his comments.

I would like also to thank the members of the jury for accepting to evaluate my work and also Chrystelle LÉBOUIN for being in my “comité de suivi de thèse”.

I extend my gratitude to Christophe LÉGER for having welcomed me into his team.

A special thanks to Anna Aldinio-Colbachini for performing the last experiments of shear stress and for the nice conversations.

I also would like to acknowledge Alain Grossi and Sady Noel for their technical help; Gaëlle Coustillier and Philippe Delaporte from LPPP (Marseille) for their preparation of graphite samples; Americo G. Duarte and Inês Cardoso Pereira from ITQB (Lisbon) for ccNir enzyme.

A special thanks to Aurore for always being there for me, for her cheers and for her advices. Thanks to stéphanie, Gulia, Andrea, Christina, Marta, Mélanie and Mannon.

I warmly thank all the people I met in the BIP: Laure, Isabelle, Aurélia, Marjorie, Agnes, Chloé, Arlette, Simon, Killian, Ievgen, Anne, Emilien, Nora, Sevde, Lydia...

I also thank Mariam Fadel, Nadjet, Samira, Firas, Sanjeev, Arnaud, Keshvad and Naima.

A very deep thanks to Malia for listening to me and also for her support.

Finally, I would like to thank my family: my parents and my husband who have been always their for me, supporting me during this challenging phase of my life. My brother and my sisters Fatima, Sara and especially Ihsene for the deep discussions.

Abstract

Protein Film Electrochemistry (PFE) is an electrochemical technique that consists in adsorbing a film of enzyme at the surface of a suitable electrode in a configuration where the electron transfer is direct. In this technique, the catalytic turnover rate is measured as an electrical current, which allows the investigation of various aspects of enzyme's kinetics as a function of different experimental parameters using electrochemical methods. Since the catalytic reaction, which takes place at the surface of the electrode, consumes the substrate, a rotating disk electrode (RDE) is usually used to induce a convective motion in the buffer to provide fast transport of the substrate from the bulk towards the electrode so as to compensate substrate consumption. However, in the case of CO dehydrogenases, which are enzymes that catalyze the reversible oxidation of CO to CO₂ at very high rates (up to $4 \times 10^4 \text{ s}^{-1}$), the consumption of the substrate (CO) at the electrode is so fast that the catalysis is mostly limited by mass transport and not by the catalyzed chemical reaction, even at high RDE rotation rates. This limitation hides important features and complicates the analysis of the catalytic response.

To overcome this limitation, we have chosen to design a new electrochemical cell with improved transport properties, with the condition that mass transport should be as homogeneous as possible, to prevent heterogeneity of substrate concentration on the electrode. Moreover, a particular attention was given to the force applied by the fluid on the surface (shear stress), since it is suspected to wash the enzyme away. In a previous study, the team used computational fluid dynamics (CFD) to design a new cell based on the so-called "wall-tube" configuration in which a jet of electrochemical buffer is pumped towards a static electrode; this cell was built and tested experimentally. Simulations and experiments showed that it can provide 3 times faster mass transport than the RDE. However, that still wasn't enough for our application for studying fast enzymes. Hence, the transport in the cell should be further improved. Thus, in this thesis, we explored, using CFD, the effect of the various parameters of the cell and proposed semi-empirical formulas to predict the mass transport coefficient and shear stress at the electrode. We used a 3D-printed cell to validate experimentally our predictions. Furthermore, we investigated the relationship shear stress/enzyme washing using nitrite reductase which is an enzyme that reduces nitrite to ammonia.

Additionally, the new cell was found to be useful to solve a different limitation of the RDE setup which is the difficulty to control the concentrations of substrates and inhibitors that the enzymes are exposed to. Since the volume above the electrode is very small in the new cell (less than 1 μL), the wall-tube geometry offers the possibility to change the contents by just changing what it is pumped in. By pumping and mixing buffers with different compositions (concentrations, pH, temperature..), imposing arbitrary changes in concentrations, pH, or/and temperature would be realizable. This possibility was tested experimentally in the built cell by mixing two solutions with different concentrations of ferricyanide and recording the reduction current which is proportional to ferricyanide concentration as a function of time. The obtained results showed that the response time for changing concentrations and the mixing quality are not sufficient. Therefore, to address these two issues, we designed and built new cells based on wall-tube geometry with integrated mixers that should allow faster concentration changes.

Table of contents

List of figures	xiii
List of tables	xvii
Nomenclature	xix
1 Introduction	1
1.1 General introduction	1
1.2 Equilibrium and Nernst equation	3
1.3 Dynamic electrochemistry	4
1.4 Electrochemical reaction regimes	6
1.5 Mass transport-controlled voltammetry	8
1.5.1 Diffusion controlled voltammetry	9
1.5.2 Hydrodynamic controlled voltammetry	13
1.6 Influence of electrode's kinetics	18
1.7 Protein film Electrochemistry	19
1.7.1 Which working electrode's material for PFE?	20
1.7.2 Example of application: Determining Michaelis-Menten constant of molybdoenzyme <i>R.sphaeroides</i> periplasmic nitrate reductase	21
1.7.3 Enzyme's film loss	22
1.8 Limitations of the classical setup of PFE	23
1.8.1 In spite of the RDE, mass transport limitations can still occur	23
1.8.2 Imposing arbitrary concentrations/ Example: Study of Dv-CODH inhibition by oxygen	27
1.9 New electrochemical cell to solve transport limitation	29
1.10 Thesis objectives	30
2 Mass transport in hydrodynamic electrochemical cells	33
2.1 Useful concepts in hydrodynamics and mass transport	33
2.1.1 Laminar and Turbulent flow	33
2.1.2 Dimensionless numbers	34
2.1.3 Navier-Stokes equations	35
2.2 Rotating disk electrodes	36

2.2.1	Theory of rotating disk electrode	37
2.2.2	Applications and limitations of rotating disk electrode	39
2.3	Tubular and channel electrodes	39
2.3.1	Theory of tubular and channel electrodes	40
2.3.2	Applications and limitations of tubular and channel electrodes	42
2.4	Impinging jet electrodes	43
2.4.1	Theory of flow in impinging jets	44
2.4.2	Micro-jet electrodes	47
2.4.3	Application and limitations of impinging jet electrode	48
2.5	New cell based on wall-tube configuration for enzyme kinetics studies	48
2.5.1	The experimental setup	49
3	Enhancing mass transport in the wall-tube electrode	51
3.1	Numerical and physical model	53
3.2	From 3D to 2D axis symmetric	53
3.3	Simulation's results and studied quantities	54
3.3.1	Local and average mass transport	54
3.3.2	Shear Stress	55
3.3.3	Pressure drop	55
3.4	Design of experiment	55
3.5	DoE data analysis	56
3.5.1	Determining the main effects of factors	56
3.5.2	Determining the interaction effects	56
3.6	Optimizing the mass transport of wall-tube electrodes for protein film electrochemistry	56
3.7	Supplementary information	65
3.8	Additional results from DoE	77
3.8.1	Shear stress	77
3.8.2	Pressure drop	77
3.9	Experimental setup	78
3.9.1	Optimization of the pumping system	79
3.10	Conclusion	79
4	Shear stress and film loss on the electrode	83
4.1	Mechanical stress does not cause film loss in protein film electrochemistry	83
5	Mixing in the new cell: a means to control concentrations	97
5.1	Characterize the mixing in the first prototype	97
5.1.1	Mixing using Y and T junctions	97
5.1.2	Possible origins of the delay	100
5.1.3	Possible sources of fluctuations	103

5.2	Literature review of laminar mixing processes	104
5.2.1	Laminar micromixers	105
5.2.2	Industrial static mixers	109
5.3	Design of electrochemical cells with integrated mixers	112
5.3.1	Cells with vortex mixer	114
5.3.2	Cells with mixing plates	116
5.3.3	Cell with mixing channel of a square duct	118
5.3.4	Geometries with porous medium	120
5.4	Printed cell	121
5.5	Conclusion	121
6	General conclusion and perspectives	123
	References	125
	Appendix A Material and methods	141
A.1	Electrochemical cell	141
A.2	Preparation of electrodes	141
A.3	Syringe pump	143
A.4	Preparation of solutions	143
A.5	List of materials	144
	Appendix B Data analysis	145
B.1	Analysis of the electrochemical experiments data	145
B.2	Analysis of CFD data	146

List of figures

1.1	Top: The overall structure of CO dehydrogenase. Bottom: zoom to the NiFe ₄ S ₄ active site	2
1.2	Plot of the applied potential vs time during cyclic voltammetry	5
1.3	Schematic representation of a three electrode cell	6
1.4	Schematic representation of the steps of an electrode reaction	7
1.5	Cyclic voltammetry for a redox species free to diffuse in solution, at a stationary electrode	9
1.6	The concentration profiles as a function of the distance from the electrode at several time values for ferricyanide reduction under diffusion conditions .	13
1.7	Vector representation of fluid velocities near a rotating disk.	14
1.8	Steady-state concentration profiles at the RDE	17
1.9	Schematic representation of the classical setup (RDE as a working electrode) used in Protein Film Electrochemistry	19
1.10	Raw and corrected chronoamperogramms (red and green lines) for <i>R.sphaeroides</i> nitrate reductase (NapAB) adsorbed at a rotating disk electrode	21
1.11	The plot of the catalytic current (plateau) as function of the concentration of the substrate.	22
1.12	Scheme of substrate's concentration profiles against the distance from the electrode for two different cases	23
1.13	The response in current of a film of Dv-CODH after a single injection of 83 μM CO	25
1.14	Different forms of signals responses of CO dehydrogenase from <i>Desulfovibriovulgaris</i> to a single CO injection in chronoamperometry experiments . . .	26
1.15	Electrochemical response of a single film of Dv-CODH exposed to CO and O ₂ injections	27
1.16	Schematic representation of the built wall-tube electrode cell	29
1.17	Comparison of the transport in the two different geometries: RDE and the built wall-tube electrode cell	30
1.18	schematic representation of substrate and inhibitor concentrations profiles that may be possible to achieve in the wall-tube electrode cell	31

1.19	Schematic representation of the possibility to control dissolved substrates and inhibitors concentrations in the wall-tube electrode cell	31
2.1	Schematic representation of the two flow regimes: laminar and turbulent within a pipe	34
2.2	Schematic representation of Rotating Disk Electrode	36
2.3	Cylindrical coordinates for the rotating disk	37
2.4	Geometry of tubular electrode (A) and channel electrode (B)	39
2.5	Establishment of Poiseuille flow and diffusion layer under laminar flow in a tube	40
2.6	The flow behaviour within an impinging jet electrode	43
2.7	The two limiting forms of the impinging jet electrode geometry	45
2.8	The design of the wall-tube cell	49
3.1	Schematic representation of the geometry of the cell, indicating the 6 parameters varied in the systematic approach	52
3.2	The single and the interaction effects of the parameters on the simulated slope of shear stress	77
3.3	The single and the interaction effects of the parameters on the simulated pressure drop	78
3.4	Schematic representation of the experimental setup used to record the limiting current at different flow rate in the wall-tube cell.	79
3.5	Comparison of the flow fluctuations induced by using the peristaltic pump and the syringe pump	80
5.1	Schematic of the experimental setup	98
5.2	Mixing with different type of fitting tubes	99
5.3	Inset from the the first step of current in fig 5.2.B.	100
5.4	A: velocity profile in a pipe at laminar glow regime. B: schematic representation of the development of the average concentration in the section above the electrode over time.	101
5.5	Orange plot: Average concentration profile at the section (in the dashed orange section shown in fig 5.4.B) over time. Blue plot: The experimental current from fig 5.3 over time.	102
5.6	Mixing in the Y fitting tube. A: Map of axial concentration field in a Y fitting tube after injecting two liquids with same physical properties and different concentration $C_1 = 0$ and $C_2 = 1$. B: Radial concentration field's map in the section of the outlet of the Y fitting tube.	103
5.7	Simulated flow field in one mixing module of multi-lamination micromixer	106
5.8	Schematic illustrations of modified Planar Asymmetric Split-and-Recombine (P-SAR) micromixer with dislocation sub-channels.	107

5.9	Schematic illustration of the passive split and recombine (P-SAR) micromixer with convergent–divergent walls	107
5.10	Schematic square-wave micromixer with cubic groove	108
5.11	Schematic illustration of H-shaped micromixer	109
5.12	Some of the available commercial mixers	110
5.13	Geometry of SMX mixing elements with eight crossbars	111
5.14	Carriere’s mixing system in a three basic elements configuration	111
5.15	The four-blade mixing element	112
5.16	Scheme of cell with integrated mixers including sections S_H and S_V	113
5.17	The main geometries of the cell with integrated vortex mixers.	114
5.18	a: The streamlines colored with species concentration in Design 01. b: Concentration map at the cross section S_H in Design 01 (5.17a)	115
5.19	The different variants of the configuration with integrated vortex mixer.	116
5.20	a: The main geometry of the cell with mixing plates. b: The streamlines colored with species concentration in Design 09.	117
5.21	The different variants of the configuration with integrated mixing plates.	118
5.22	a: The main geometry of the cell with mixing channel of a square duct. b: The streamlines colored with species concentration in Design 16.	119
5.23	The different variants of the configuration with mixing channel of a square duct.	119
5.24	The flow streamlines before (a) and after (b) adding the porous medium to the design 16 at the jet channel	120
5.25	Non-verticality of the flow at section S_V as a function of the radial distance from the electrode for design 16 (5.22a).	120
5.26	(A) top view, (B) lateral view and (C) of the printed cell of the design 16 (5.22a). The cell was filled with a solution of methylene blue to better visualize the flow path.	121
A.1	Photos of the wall-tube electrochemical cell	142
A.2	Photo of the syringe pumps used in the experiments.	143

List of tables

3.1	Values of the low and high levels of the parameters varied in the sensitivity studies. The definition of the parameters is in figure 3.1.	52
5.1	Comparison of the cells with integrated vortex.	116
5.2	Comparison of the cells with mixing plates.	118
5.3	Comparison of the cells with mixing channel of a square duct.	119
A.1	Composition of the mixed buffer used in the PFE experiments	143
A.2	List of all the materials used for work in this thesis.	144

Nomenclature

Roman Symbols

A_f	surface area of the meshing cell's face
C	concentration of electroactive species
C^*	concentration of the electroactive species at the bulk
C^0	concentration of the electroactive species at the electrode
C_{avg}	the average dimensionless concentration at the radial cross-section
C_{inj}	the injected concentration
C_{max}	the maximum dimensionless concentration at the radial cross-section
C_{min}	the minimum dimensionless concentration at the radial cross-section
D	diffusion coefficient of the species
d_{jet}	diameter of the jet's nozzle
E_f	main effect
F	number of levels
g	gravity
H	Heterogeneity of concentration
H_m	non homogeneity of mass transport coefficient
i	current
i_p	pics current
$I_{(P)}$	interaction effect
i_{lim}	limiting current
J	flux of electroactive species

J_c	the flux of substrate consumed by the catalytic reaction at the electrode surface
J_m	mass flux
k	number of parameters
k^0	standard rate constant
K_m	Michaelis-Menten constant
k_{cat}	catalytic rate
k_{cat}^{max}	the maximum catalytic rate
k_{eff}	the catalytic efficiency
L	length of a cylindrical pipe
L_c	characteristic dimension
m	mass transport coefficient
m_i	the cell's face value of mass transport coefficient
m_l	local mass transport coefficient
m_{avg}	average value of mass transport coefficient
m_{max}	the maximum value of the local mass transport coefficient
m_{min}	the minimum value of the local mass transport coefficient
P	pressure
P_{in}	the pressure at the inlet
P_{out}	the pressure at the outlet
q	charge of species
Q_v	volume flow rate
R	radius of a cylindrical pipe
r	radial cylindrical coordinate
r_{elec}	radius of the electrode
Re	Reynolds number
s	Laplace variable

S_H	radial cross-section
Sc	Schmidt number
t	time
u	radial velocity
V	average velocity
v	axial velocity
w	angular velocity
z	axial cylindrical coordinate
z_l	distance from the beginning of the electrode
A	surface area of the WE
E	equilibrium potential
E^0	standard potential of the redox couple
F	Faraday's constant
k_o	oxidation constant rate
k_r	reduction constant rate
C_{Ox}	the concentration of the oxidized species
n	number of electrons exchanged
$\frac{dN}{dt}$	number of moles of reactants consumed or products formed over time
R	gas constant
C_{Red}	the concentration of the reduced species
T	temperature

Greek Symbols

α	electron transfer coefficient
ΔP	pressure drop
δ	diffusion layer thickness
δ_0	thickness of stationary diffusion layer

Γ	the enzyme coverage concentration
μ	dynamic viscosity
∇	the vector differential operator
ν	kinematic viscosity
ω	rotation rate
ϕ	electrostatic potential
ρ	density
τ	the time constant of the exponential decrease in substrate concentration
τ_w	wall shear stress
θ	angular cylindrical coordinate
v	scan rate
$A\Gamma$	electroactive coverage

Acronyms / Abbreviations

CA	chronamperometry
CE	counter electrode
CFD	Computational Fluid Dynamics
CODH	carbon monoxide dehydrogenase
CV	cyclic voltammetry
DoE	Design of Experiment
IJE	impinging jet electrodes
Ox	oxidant
PFE	protein film electrochemistry
RDE	Rotating Disk Electrode
Red	reductant
RE	reference electrode
WE	working electrode

WJE wall-jet electrodes

WTE wall-tube electrodes

Chapter 1

Introduction

1.1 General introduction

The growing worldwide consumption of fossil fuels and the rise in the atmospheric CO₂ levels are the major energy-related issues that are confronting the world in the last decades [1]. Thus, strategies to reduce CO₂ emissions and to afford new energy supplies that are independent of fossil fuels are needed. Therefore, many efforts have been put to develop the production of bio fuels from algae and biomass [2, 3] and to use of wind and solar power [4, 5]. Furthermore, there is a significant interest to capture atmospheric CO₂ and use it to produce useful chemicals [6]. For instance, CO₂ can be used as a reagent with H₂ in the reverse water-gas shift reaction (1.1) which is an industrial process that produces a mixture of water and CO. The latter can be converted to high mass alkanes that can be used as fuels. However, this reaction needs high temperatures catalysis which makes it a very challenging process and not environmentally practical [7].



Most of the actual proposed solutions to reduce CO₂ are quite difficult to achieve as they require a lot of energy and efficient catalysts (CO₂ molecule dissociation energy is 750 kJ mol⁻¹) [8]. As it was stated in the 2008 Bell/ DOE report, “The major obstacle preventing efficient conversion of carbon dioxide into energy-bearing products is the lack of catalysts” [9], Thus, developing efficient and highly selective catalysts for CO₂ reduction is needed.

In this regard, seeking inspiration in nature might be a good option. The biological fixation of CO₂ is the source of carbon in living organisms and its mechanisms have evolved over billions of years [1]. There are at least six pathways for CO₂ fixation in which several enzymes are involved [11, 12] but only two enzymes are known to directly catalyze the reduction of CO₂: CO dehydrogenases (CODHs) which catalyze the reversible reduction of CO₂ into CO at their Nickel-Iron active site and Formate dehydrogenases (FDHs) which catalyze the reduction of CO₂ into formate at their Tungsten or Molybdenum active

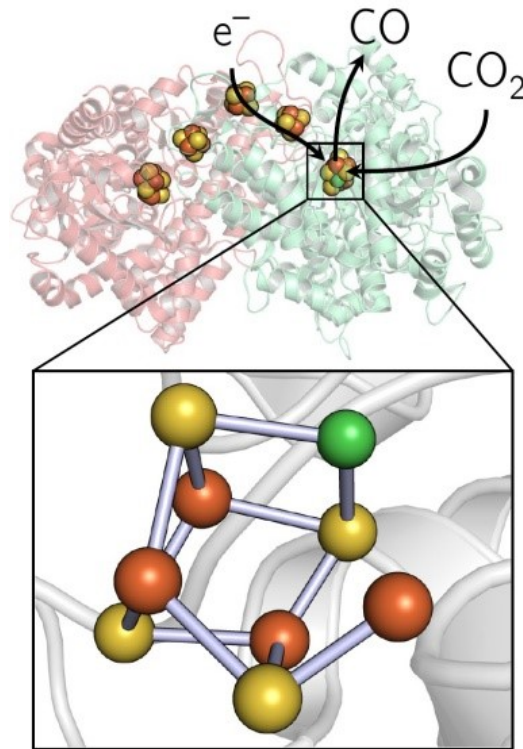


Fig. 1.1 Top: The overall structure of CO dehydrogenase. Bottom: zoom to the NiFe₄S₄ active site. Reprinted from ref 10.

site [10]. Both of these metalloenzymes are involved in Wood-Ljungdahl pathway which is one of the main CO₂ fixation pathways in anaerobic organisms [13–15].

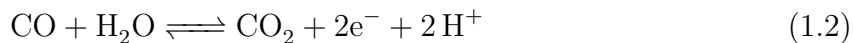
In the last decades, there were many studies about these enzymes as they display very high catalytic performances: they catalyze the reaction at high rates without requiring high driving force [16], they are very active [14] and unlike the synthesised catalysts, they are highly specific in terms of product: while a mixture of reduced carbon compounds (CO, formate, oxalate...) and even H₂ are being produced by synthesised catalysts, FDH and CODH give no by-products [10].

All these characteristics make them very attractive either to use them directly in biotechnological devices as bio-catalysts or to study them in order to understand how they function, which may allow to form a foundation for the development of bio-inspired catalysts for high-performance CO₂ reduction [1, 17].

Some studies showed that both CODHs and FDHs can have potential applications in the industrial CO₂ capture: they can be used in artificial photosynthesis coupled with photosensitizers to catalyze the photoreduction of CO₂ or in the reverse water-gas shift reaction coupled with hydrogenases or even incorporated into electrodes for catalyzing the reduction of CO₂ or the oxidation of CO or formate [10]. There are several reviews that highlight the mentioned points[10, 1]. However, in this thesis, I only focus on CODHs as a case example to justify the motivation behind this work.

Overall, there are two categories of CODHs:

- The MoCu-CODH, which are found in aerobic carboxydophilic bacteria [18]. Their active site contains molybdenum and copper; they only catalyze the oxidation of CO and not the reverse;
- the Ni-CODHs, which catalyze the reversible [16] reduction of CO₂ into CO (1.2) at a [NiFe₄S₄] active site [19].



Many Ni-CODHs from different organisms were characterised so far by various techniques [19]. It was found that they have an overall structure that resembles that of *Carboxydotherrmus hydrogenoformans* (Ch) CODH II which is illustrated in figure 1.1. They have homodimeric structure, they contain five metallic clusters: two B clusters ([4Fe4S]), two C clusters ([NiFe4S4]) and a D cluster (either [4Fe₄S] or [2Fe₂S]) which is located between the two monomers.

Distinct Ni-CODHs have been studied using protein film electrochemistry (PFE) [20–24]. It is an electrochemical technique that consists simply in connecting an enzyme to an electrode then applying a potential, which allows electrons exchange between the electrode and the active sites. This exchange can be measured as current signal that is proportional to the catalytic activity of the enzyme [25–27]. My team in Bioenergetic and protein engineering (BIP) laboratory (CNRS-Marseille) developed an expertise in this technique. It has used it to learn about various aspects of redox metalloenzymes such as conformational changes, inactivation and reactivation processes and this has contributed to the understanding of the chemistry of the enzymes active sites [28–30].

Since PFE is an electrochemical technique, and in order to understand how it works, I will first present some basic aspects of the electrochemical methods. Then, I will show some applications of PFE. Finally, I will underline some of the limitations that can be encountered using this technique for studying enzymes and the approaches that we adopted attempting to solve them. In fact, CODH will be the main case example as my PhD project arises from a tentative to solve issues that the team came across when trying to study CODHs by PFE.

1.2 Equilibrium and Nernst equation

We consider an electrode which is a conductive metal (working electrode “WE”) dipped into a solution that contains electroactive species Red and Ox (redox couple). These species may be interconverted by adding electrons to Ox (reduction) or by removing electrons from Red (oxidation). In this case, the electrode plays the role of a source or a sink of a these electrons. In practice, both reactions (reduction and oxidation) take place very shortly after the electrode is dipped into the solution and at the end, the following

equilibrium (1.3) is established on the electrode's surface [31]:



The potential measured at the electrode (E) is the equilibrium potential which is given by Nernst Equation (1.4) [32] as following:

$$E = E^0 - \frac{RT}{nF} \ln \frac{C_{Red}}{C_{Ox}} \quad (1.4)$$

where: E^0 is the standard potential of the redox couple, C_{Red} , C_{Ox} are respectively the concentrations of the reduced and the oxidized species at equilibrium at the surface of the electrode, F is Faraday's constant, R is the gas constant, n is the number of electrons exchanged and T is the temperature.

Nernst equation can be used to determine the direction in which a redox reaction will proceed spontaneously and also to deduce the redox potential of a redox couple at equilibrium.

However, one cannot measure an absolute electrode potential; only the difference between the potentials of two electrodes can be measured. Therefore, an electrode of a known potential (called reference electrode "RE") is used to measure this potential difference [33].

The standard hydrogen electrode H^+/H_2 (SHE) is the conventional reference element in electrochemical devices, it is composed of a platinum electrode immersed in an electrolyte where $\text{pH}=0$ under 1 bar of H_2 . However, in practice, this electrode is complicated to build and use. Thus, other reference electrodes can be used such as: standard calomel electrode ($E_{calomel} = 0.242 \text{ V}$ vs SHE), Ag/AgCl electrode, ($E_{Ag/AgCl} = 0.199 \text{ V}$ vs SHE) [34]. When using $E_{calomel}$ or $E_{Ag/AgCl}$, in the end, one should convert the potential back to SHE.

A good reference electrode must maintain a constant composition during the experiment, so that it can maintain a stable potential and the reaction that takes place at the RE should be fast and reversible obeying to Nernst equation [35].

1.3 Dynamic electrochemistry

Dynamic electrochemistry consists in applying a potential that is different from the equilibrium one to the WE. In this case, the system progresses towards a new equilibrium by exchanging electrons with the electrode. The number of electrons exchanged per unit time is measured as electrical current (i) [36, 32, 34]:

$$i = nFA \frac{dN}{dt} \quad (1.5)$$

where $\frac{dN}{dt}$ is the the number of moles of reactants consumed or products formed over time and A is the surface area of the WE.

In this thesis, two dynamic electrochemical methods were used in the experiments: cyclic voltammetry and chronamperometry.

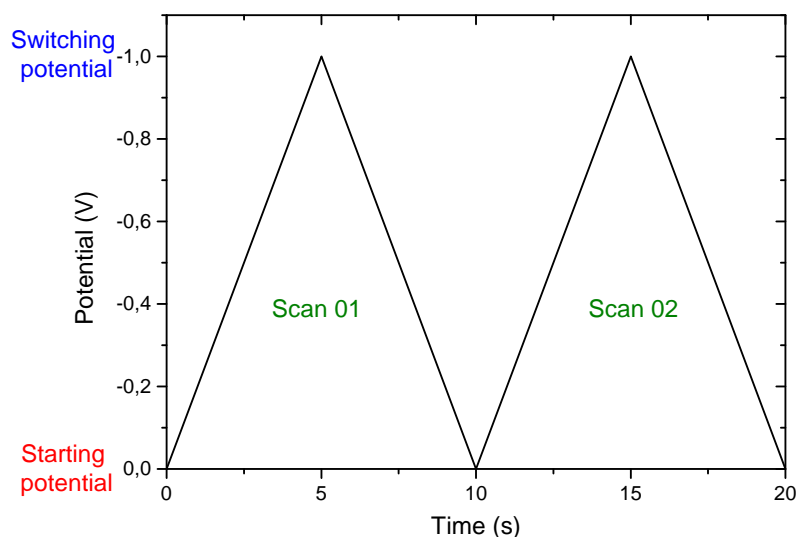


Fig. 1.2 Plot of the applied potential vs time during cyclic voltammetry. scan rate = the rate of voltage change over time ($\frac{dE}{dt}$).

Cyclic voltammetry (CV) is performed by applying a potential to the WE, that is swept linearly over time and recording the resulted current. The speed of the sweep is called scan rate (fig 1.2). In chronoamperometry (CA) experiments, the potential is held constant (or varied in steps) and the current is measured as function of time.

During these experiments, the electrical circuit has to be closed so that the electrons can come back to the solution. It can't be closed by the RE, because the potential of RE wouldn't be constant anymore if the current is flowing through it. In this case, it can't be used as RE to control the WE potential anymore. Therefore, a third electrode should be used to close the circuit; this electrode is called the counter electrode (CE).

In this thesis, two different cells configurations were employed and both of them composed of three electrodes 1.3.

- The working electrode (WE) is where the studied reaction occurs. It is essential to select a suitable working electrode depending on the experimental conditions.
- The reference electrode (RE) which permits the control of the potential of the working electrode. It is composed of a system of phases, which should maintain a constant composition, and therefore provides a stable potential by which the WE potential can be monitored [33].

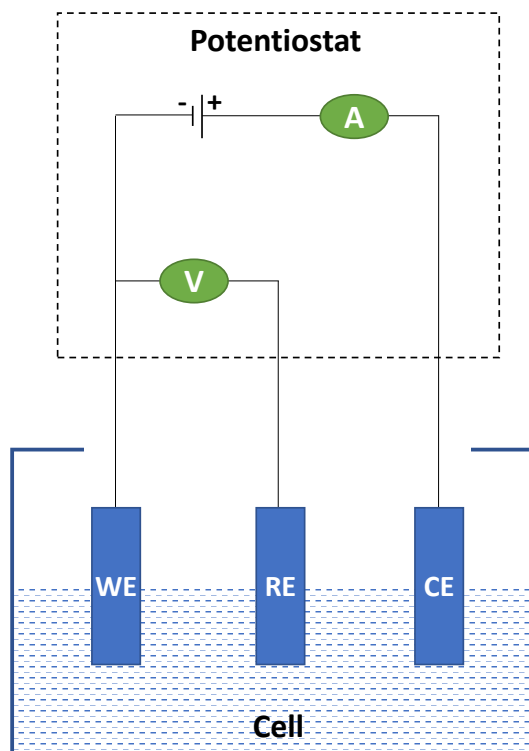


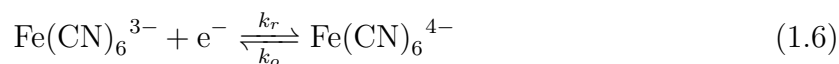
Fig. 1.3 Schematic representation of a three electrode cell, the potential is controlled between the working and the reference electrodes while the current is measured between the working and the counter electrodes.

- The counter electrode (CE) is used to close the electrical circuit so the current generated as a result to the applied potential at the WE passes between it and the CE.

The three electrode cell (fig 1.3) should be connected to a potentiostat which is an electronic apparatus that measures the potential between the WE and the RE and apply a voltage across the WE and the CE so that the potential difference between the WE and RE is the one requested by the operator. It also measures the current between the WE and the CE [37].

1.4 Electrochemical reaction regimes

We consider the simple reaction of the standard redox couple $\text{Fe}(\text{CN})_6^{3-}/\text{Fe}(\text{CN})_6^{4-}$ (ferricyanide/ferrocyanide) at the electrode. This couple is known as well behaved electrochemical reversible system in aqueous solution [38].



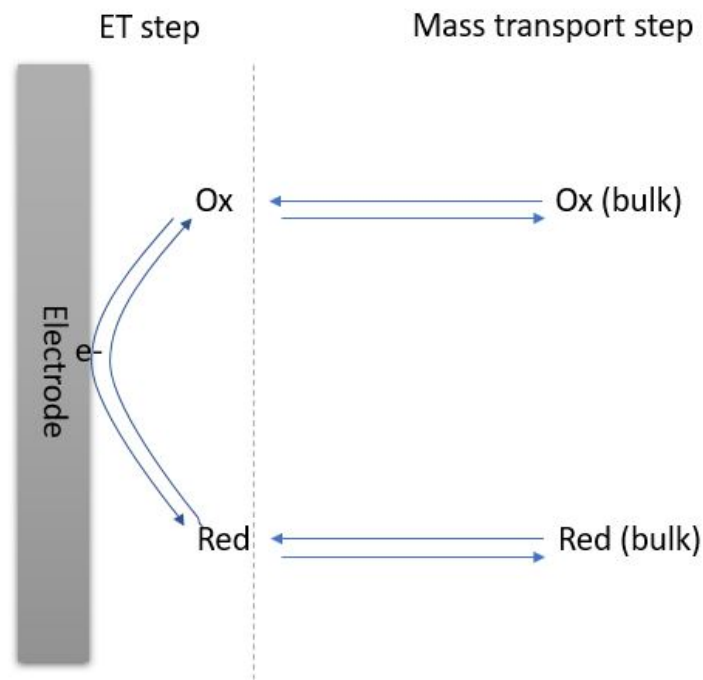


Fig. 1.4 Schematic representation of the steps of an electrode reaction.

with: k_r and k_o are respectively the reduction and oxidation constant rates; these rates depend on the electrode potential.

Reaction (1.6) is the result of two steps (fig 1.4) and the current measured at the electrode is governed by these steps:

- The mass transport step which requires the transport of the electroactive species from the bulk towards the electrode;
- The electron transfer step which occurs at the surface of the electrode where the electrons are exchanged between the electrode and the electroactive species.

In more complex electrode reactions, more steps can take place such as chemical reaction, adsorption/desorption steps.

The magnitude of the recorded current is often limited by the slowest step. In this sense, three cases can be distinguished:

Case 01 If the applied potential (driving force) at the electrode has small values, then the electron transfer is going to be slow and will become the limiting step; in this case, we can neglect the contribution of the transport. Then, the reaction is called electron transfer controlled and the measured current i can be expressed as:

$$i = nFAk_r C \quad (1.7)$$

Where A is the surface of the electrode and C is the concentration of the electroactive species.

Case 02 If the applied potential has high values, then the charge transfer is very fast, and the electroactive species that reach the electrode are fully converted (oxidised or reduced). In this case, the mass transport is the rate limiting step and the measured current is proportional to the flux J of species¹ towards the electrode and can be written as [39]:

$$i = nFAJ \quad (1.8)$$

in which the flux J can be expressed as:

$$J = m(C^* - C^0) \quad (1.9)$$

where C^* is the concentration of the electroactive species at the bulk (far from the electrode), C^0 is the concentration at the electrode which is 0 here since the electroactive species are assumed to be fully consumed and m is the mass transport coefficient.

Case 03 If the applied potential is between the two extremes mentioned above, then both regimes can exist and the recorded current depends on mass transport and the reaction rate which depends in its turn on the potential.

The last two cases will be discussed in the next sections.

1.5 Mass transport-controlled voltammetry

In this section, we consider reaction (1.6) when the mass transport is the rate limiting step. Mass transport of a charged species in a solution can be done in three different modes and it is governed by the Nernst-Planck equation [37, 40]:

$$\vec{J} = \underbrace{-D \vec{\nabla} C}_{\text{diffusion}} + \underbrace{C \vec{V}}_{\text{convection}} - \underbrace{\frac{qF}{RT} DC \vec{\nabla} \phi}_{\text{migration}} \quad (1.10)$$

Where \vec{J} is the flux of the electroactive species, D is the diffusion coefficient of the species, $\vec{\nabla}$ is the vector differential operator, C is the concentration of electroactive species, \vec{V} is the velocity of the solution, q is the charge on the electroactive species, F is Faraday's constant, R is the gas constant, T is the temperature, and ϕ is the electrostatic potential.

- The first term in the right hand side of equation (1.10) represents diffusion, which is the natural movement of species due to concentration gradient [39].

¹The flux of species is the quantity of species (in mol or kg) passing through unit area in unit time

- The second term represent convection, which is the movement of species induced by external mechanical (forces stirring or hydrodynamic transport). In general, fluid flow happens because of natural convection (caused by density gradients) and forced convection (pumping, stirring...) [37].
- The last term refers to migration, which is the movement of species under the influence of an electrical field [37].

In order to simplify the mathematical treatment of electrochemical systems, it is important to decrease or eliminate the migration flux of the electroactive species, this is possible by adding excess of electrolyte to the solution [41, 42]. In our experiments, The electrolyte used was NaCl (0.5 M). As a result the current contribution due to migration is negligible within this thesis.

1.5.1 Diffusion controlled voltammetry

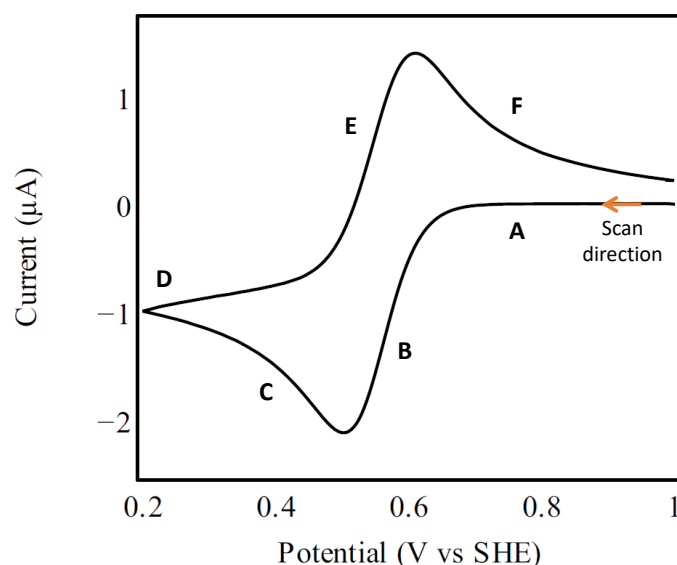


Fig. 1.5 Cyclic voltammetry for a redox species free to diffuse in solution, at a stationary electrode. The current is plotted against the potential. The labels from (A) to (F) are explained in the text. $[\text{Fe}(\text{CN})_6]^{4-}$ (1 mM) was used in NaCl electrolyte solution (0.5 M) at ambient temperature, scan rate = 0.1 V/s.

In the absence of convection in the solution (static electrode and static solution) and in the presence of a supporting electrolyte (migration is negligible), the transport of the electroactive species from the bulk towards the electrode is controlled only by diffusion. Fig 1.5 shows a CV of the reduction of ferricyanide into ferrocyanide (1.6) at a static disk electrode. We assume that we start with a bulk solution that contains only ferricyanide and all electrode's reactions are at equilibrium.

- When the potential is higher than E^0 , no reduction happens and therefore no current can be observed (fig 1.5.A).

- When the electrode potential approaches E^0 , ferricyanide starts to being reduced into ferrocyanide by taking electrons from the electrode (fig 1.5.B). This is measured as a negative current whose magnitude increases as the value of the potential decreases.
- The electrode reduces only the electroactive species at its vicinity which causes the depletion of ferricyanide at the surface. There, the magnitude of the current reaches the maximum then started to decrease again (fig 1.5.C) forming a peak.
- While the concentration of ferricyanide at the electrode surface is depleted, the produced ferrocyanide is being accumulated at the surface of the electrode and diffuses slowly towards the bulk.
- When the switching potential is reached, the scan direction is reversed. The current is still negative: ferricyanide is still being reduced since the electrode potential didn't reach the E^0 (fig 1.5.D).
- By approaching E^0 , the ferrocyanide that was accumulated at the electrode surface is started to being oxidized back to ferricyanide and a positive current is measured (fig 1.5.E).
- This current reaches its maximum then decrease while the concentration of ferrocyanide drops down (fig 1.5.F).

The reason of the existence of peaks i_p in the CV in fig 1.5 is that there are two competing processes: (i) the increase of the driving force which leads to the increase in the magnitude of the current; (ii) the decrease of electroactive species concentration at the electrode because of its consumption by the reaction which leads to the decrease in the current's magnitude. These peaks are proportional to bulk concentrations and the the square root of the scan rate v , this can be expressed by Randles-Sevcik equation [32]:

$$i_p = 0.4463nFAC \left(\frac{nFvD}{RT} \right)^{1/2} \quad (1.11)$$

This equation is very useful since it can be used to compute either the effective surface of the electrode or the diffusion coefficient from the slope of the plot $i_p = f(v^{1/2})$ as it will be shown in section 3.6 of chapter 3.

For a planar electrode (assuming an ideal infinite flat electrode in the molecular scale) under static flow (convection is neglected) and in the presence of supporting electrolyte (migration is neglected), for a unidirectional diffusion, equation (1.10) can be simplified to:

$$J = -D \frac{\partial C}{\partial z} \quad (1.12)$$

Since we have mass conservation, one can write:

$$\frac{\partial C}{\partial t} = -\frac{\partial J}{\partial z} \quad (1.13)$$

Combining equation (1.12) with equation (1.13) gives Fick's second law of diffusion which takes into consideration the changes of concentration over time for the diffusive species[37]:

$$\frac{\partial C}{\partial t} = D \frac{\partial^2 C}{\partial z^2} \quad (1.14)$$

Now, we consider that there is only ferricyanide in the solution at the beginning of the experiment ($t = 0$) with a concentration C_{Ox}^* and to simplify, we consider that the potential is taken in a single step to the lowest potential (now we are talking about CA and not CV).

Under the assumption of fast reaction at the electrode and high enough deriving force (low potential), all the ferricyanide that arrives to the electrode is reduced ($C_{Ox}(0, t) = 0$). Thus, the current measured over time is limited by diffusion of ferricyanide to the electrode. It is proportional to the flux that can be deduced from the relationship concentration-time. Now, I will present how to determine this relationship by solving equation (1.12) using the corresponding limiting boundaries.

Boundary conditions

$$\lim_{z \rightarrow \infty} C_{Ox}(z, t) = C_{Ox}^* \quad (1.15a)$$

$$C_{Ox}(z, 0) = C_{Ox}^* \quad (1.15b)$$

$$C_{Ox}(0, t) = 0 \quad (1.15c)$$

where: $C_{Ox}(0, t)$ is the concentration of ferricyanide at the electrode at time t and C_{Ox}^* is its concentration at the bulk far from the electrode.

- Condition (1.15a) means that at anytime during the experiment, the concentration at the bulk remains constant since it is not affected by what happens at the surface of the electrode.
- Condition (1.15b) means that at $t = 0$, the ferricyanide concentration is the same everywhere in the solution and equal to the bulk concentration.
- Condition (1.15c) means that at $t > 0$, the concentration at the electrode surface goes to 0 since ferricyanide is assumed to be totally consumed.

A Laplace transformation of (1.14) on the variable t yields:

$$s\bar{C}_{Ox}(z, s) - C_{Ox}^* = D \frac{d^2 \bar{C}_{Ox}(z, s)}{dz^2} \quad (1.16)$$

where s is the Laplace variable. Now, one should solve the ordinary differential equation:

$$\frac{d^2 \bar{C}_{Ox}(z, s)}{dz^2} - \frac{s}{D} \bar{C}_{Ox}(z, s) = -\frac{C_{Ox}^*}{D} \quad (1.17)$$

The solution of equation (1.17) can be written as:

$$\bar{C}_{Ox}(z, s) = \frac{C_{Ox}^*}{s} + A \exp\left(\left(-\frac{s}{D}\right)^{(1/2)} z\right) + B \exp\left(\left(\frac{s}{D}\right)^{(1/2)} z\right) \quad (1.18)$$

The first boundary condition (1.15a) can be transformed to:

$$\lim_{z \rightarrow \infty} \bar{C}_{Ox}(z, s) = \frac{C_{Ox}^*}{s} \quad (1.19)$$

For this condition: $B = 0$. Hence, equation (1.18) becomes:

$$\bar{C}_{Ox}(z, s) = \frac{C_{Ox}^*}{s} + A \exp\left(\left(-\frac{s}{D}\right)^{(1/2)} z\right) \quad (1.20)$$

Using the 3rd boundary condition (1.15c) allows to find $A = -\frac{C_{Ox}^*}{s}$. Thus:

$$\bar{C}_{Ox}(z, s) = \frac{C_{Ox}^*}{s} - \frac{C_{Ox}^*}{s} \exp\left(\left(-\frac{s}{D}\right)^{(1/2)} z\right) \quad (1.21)$$

Inverting equation (1.21) yields:

$$C_{Ox}(z, t) = C_{Ox}^* \left[1 - \operatorname{erfc}\left(\frac{z}{2(Dt)^{(1/2)}}\right) \right] \quad (1.22)$$

which is equivalent to:

$$C_{Ox}(z, t) = C_{Ox}^* \operatorname{erf}\left(\frac{z}{2(Dt)^{(1/2)}}\right) \quad (1.23)$$

The computed concentration profile is depicted in figure 1.6 at different values of time.

Since we have the expression of $C_{Ox}(z, t)$, the flux at the electrode can be obtained as a function of time.

Equation (1.12) can be written as:

$$J(0, t) = -D \left(\frac{\partial C_{Ox}(z, t)}{\partial z} \right)_{(z=0)} \quad (1.24)$$

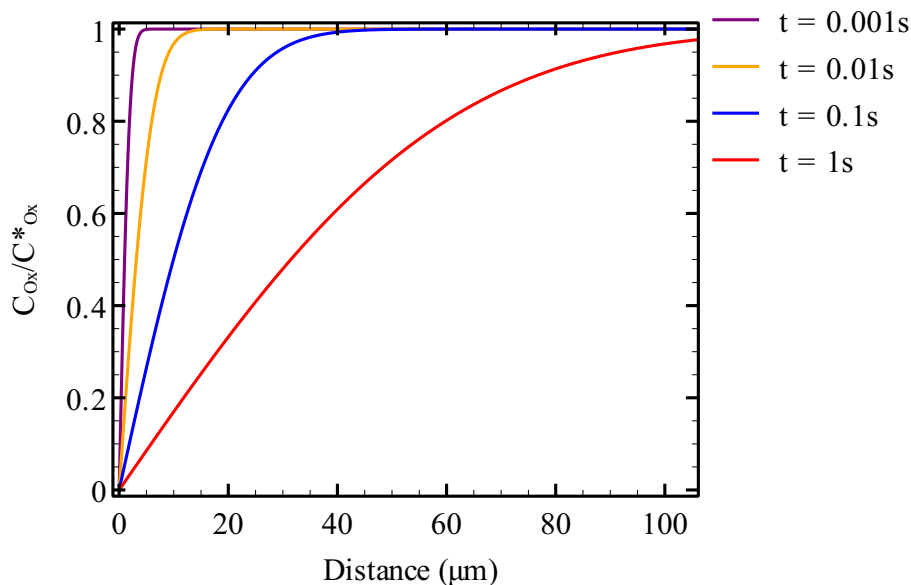


Fig. 1.6 The concentration profiles as a function of the distance from the electrode at several time values for ferricyanide reduction under diffusion conditions; The diffusion coefficient value is $1.088 \times 10^{-9} \text{ m}^2 \text{ s}^{-1}$. Adapted from ref 37.

Derivation of equation (1.23) at $z = 0$ then substituting in equation (1.24) yields:

$$J(0, t) = -\frac{D^{(1/2)}C^*_{Ox}}{\pi^{(1/2)}t^{(1/2)}} \quad (1.25)$$

Now, one can define a diffusion layer thickness δ , which corresponds to the distance from the electrode where the concentration starts to be affected by the electrode's reaction, by assuming a linear concentration gradient within it in such a way that:

$$J(0, t) = -D \frac{C^*_{Ox}}{\delta(t)} \quad (1.26)$$

where the diffusion layer thickness is expressed as [36]:

$$\delta = (\pi Dt)^{(1/2)} \quad (1.27)$$

The thickness of the diffusion layer depends on time. That is why it is never constant in the case of diffusion controlled regime.

1.5.2 Hydrodynamic controlled voltammetry

Hydrodynamic techniques require the use of forced convection on the solution in order to minimise the depletion of the electroactive species at the electrode. The most popular hydrodynamic system among electrochemists is the rotating disk electrode (RDE), which is an electrode that rotates along its axis in the solution. This create a convective movement

of the solution which helps to increase mass transport of the electroactive species from the bulk toward the electrode.

So, in this case, the diffusion layer is fixed, it is in fact imposed by the competition between the diffusion and the flow. As a consequence, the current evolves quickly to a stationary state until reaching a limiting value i_{lim} at high enough driving force [41, 34].

We consider ferricyanide reduction (1.6) at an RDE that rotates with a rotation rate ω . At high deriving force (low potential in this case), the concentration at the electrode is zero ($C_{Ox}^0 = 0$) and the current is limited by mass transport towards the RDE. This limiting current can be computed from the steady-state convection-diffusion equation, as it was first done by Levich taking into account the corresponding boundary conditions.

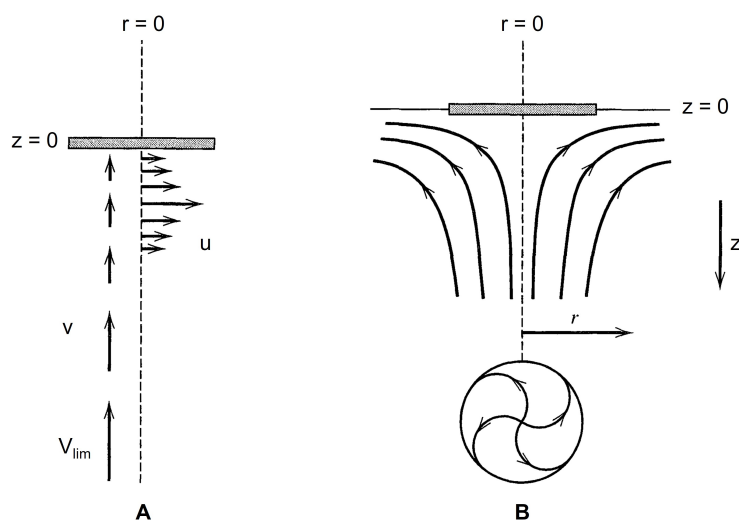


Fig. 1.7 (A) Vector representation of fluid velocities near a rotating disk, (B) Schematic resultant streamlines (or flows). Reprinted from ref 37.

For an infinite planar RDE rotating at an angular velocity ω , Von Karman and Cochran demonstrated that the axial (v) and the radial (u) velocities (see fig 1.7) for a stationary incompressible flow can be expressed as:

$$u = 0.51\omega^{(3/2)}\nu^{(-1/2)}rz \quad (1.28a)$$

$$v = -0.51\omega^{(3/2)}\nu^{(-1/2)}z^2 \quad (1.28b)$$

where z and r are the axial and the radial cylindrical coordinates. Note that the flow in the angular direction has no influence on the concentrations since the system is symmetric (invariant by rotation). v is the only component that matters for computing mass transport. More details about RDE's hydrodynamics will be discussed in chapter 2.

Using the velocity equations (1.28b), we can now solve the convective diffusion equation for the RDE.

Boundary conditions

$$\lim_{z \rightarrow \infty} C_{Ox}(z) = C_{Ox}^* \quad (1.29a)$$

$$C_{Ox}(0) = 0 \quad (1.29b)$$

Condition (1.29a) means that the concentration in the bulk is C_{Ox}^* and condition (1.29b) means that the the concentration at the electrode is 0.

We consider that the concentration is only dependant on the distance from the electrode so that C_{Ox} is only a function of z . In the steady-state conditions, equation (1.10) for C_{Ox} can be expressed as:

$$D_{Ox} \frac{d^2 C_{Ox}}{dz^2} - v \frac{dC_{Ox}}{dz} = 0 \quad (1.30)$$

Note that we only consider the steady state because as I have explained before, in case of hydrodynamic voltammetry, the system evolves quickly to a stationary regime.

Replacing v by its value from equation (1.28b) and rearranging yields:

$$\frac{d^2 C_{Ox}}{dz^2} = \frac{-z^2}{\Omega} \frac{dC_{Ox}}{dz} \quad (1.31)$$

where:

$$\Omega = \frac{D}{0.51\omega^{(3/2)}\nu^{(-1/2)}} \quad (1.32)$$

if we put $j = \frac{dC_{Ox}}{dz}$, equation (1.31) can be written as:

$$\frac{dj}{dz} = \frac{-z^2}{\Omega} j \quad (1.33)$$

After variable separation, we get:

$$\frac{dj}{j} = \frac{-z^2}{\Omega} dz \quad (1.34)$$

Equation (1.34) should be integrated between j_0 and j where $j_0 = \left(\frac{dC_{Ox}}{dz}\right)_{z=0}$.

$$\int_{j_0}^j \frac{dj}{j} = \int_0^z \frac{-z^2}{\Omega} dz \quad (1.35)$$

which yields:

$$j = j_0 \exp\left(\frac{-z^3}{3\Omega}\right) \quad (1.36)$$

which is equivalent to:

$$\frac{dC_{Ox}}{dz} = \left(\frac{dC_{Ox}}{dz}\right)_{z=0} \exp\left(\frac{-z^3}{3\Omega}\right) \quad (1.37)$$

The concentration profile can be obtained by integrating (1.37) between C_{Ox}^0 and C_{Ox} :

$$\int_{C_{Ox}^0}^{C_{Ox}} dC_{Ox} = C_{Ox}(z) - C_{Ox}^0 = \left(\frac{dC_{Ox}}{dz} \right)_{z=0} \int_0^z \exp\left(\frac{-z^3}{3\Omega}\right) dz \quad (1.38)$$

Equation (1.29b) can be written as:

$$C_{Ox}(z) = C_{Ox}^0 + \left(\frac{dC_{Ox}}{dz} \right)_{z=0} \int_0^z \exp\left(\frac{-z^3}{3\Omega}\right) dz \quad (1.39)$$

We make a variable change in the integral:

$$u = \frac{z}{(3\Omega)^{1/3}} \quad (1.40)$$

then:

$$u^3 = \frac{z^3}{3\Omega} \quad dz = du (3\Omega)^{1/3} \quad (1.41a)$$

Equation (1.39) becomes:

$$C_{Ox}(z) = C_{Ox}^0 + \left(\frac{dC_{Ox}}{dz} \right)_{z=0} (3\Omega)^{1/3} \int_0^{\frac{z}{(3\Omega)^{1/3}}} \exp(-u^3) du \quad (1.42)$$

Equation (1.42) is the expression of concentration profile. What is left is to determine $\left(\frac{dC_{Ox}}{dz} \right)_{z=0}$ which is the flux at the electrode (divided by D). We have:

$$C_{Ox}^* - C_{Ox}^0 = \left(\frac{dC_{Ox}}{dz} \right)_{z=0} (3\Omega)^{1/3} \int_0^\infty \exp(-u^3) du \quad (1.43)$$

Therefore:

$$\left(\frac{dC_{Ox}}{dz} \right)_{z=0} = \frac{C_{Ox}^* - C_{Ox}^0}{(3\Omega)^{1/3} \int_0^\infty \exp(-u^3) du} \quad (1.44)$$

Equation (1.42) becomes:

$$C_{Ox}(z) = C_{Ox}^0 + (C_{Ox}^* - C_{Ox}^0) \frac{\int_0^{\frac{z}{(3\Omega)^{1/3}}} \exp(-u^3) du}{\int_0^\infty \exp(-u^3) du} \quad (1.45)$$

with: $\int_0^\infty \exp(-u^3) du = 0.89298$.

Plotting equation (1.45) gives the concentration profile of an electroactive species towards RDE as shown in fig 1.8.

Now we determine the final expressions of the flux and of the mass transport coefficient at the electrode.

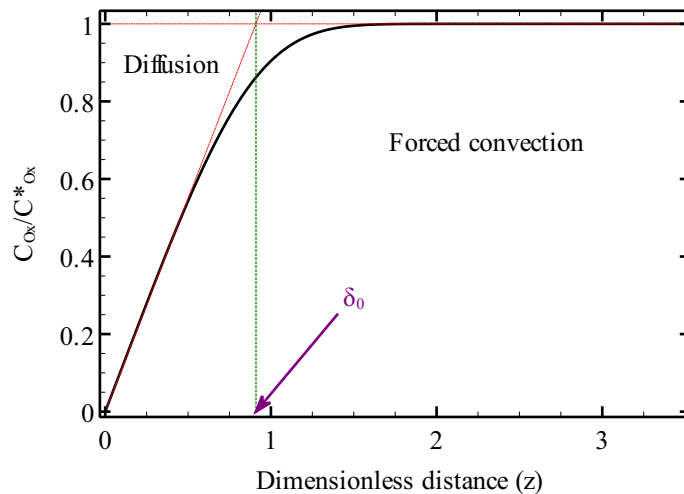


Fig. 1.8 Steady-state concentration profiles at the RDE, in the bulk region, δ_0 is the thickness of the stationary diffusion layer at the electrode surface where diffusion dominates. Adapted from ref 41.

The flux at the electrode is given by:

$$J = -D \left(\frac{dC_{Ox}}{dz} \right)_{z=0} = 0.62 \omega^{1/2} D^{2/3} \nu^{-1/6} (C_{Ox}^* - C_{Ox}^0) \quad (1.46)$$

In this example, the mass transport equation (1.9) that was described earlier can be expressed as:

$$m = \frac{J}{C_{Ox}^* - C_{Ox}^0} \quad (1.47)$$

By replacing J by its expression from (1.46) in equation (1.47), we obtain:

$$m = 0.62 \omega^{1/2} D^{2/3} \nu^{-1/6} \quad (1.48)$$

We can also find the expression of the limiting current i_{lim} :

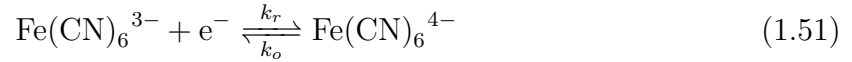
$$i_{lim} = nFAJ = 0.62nFA \omega^{1/2} D^{2/3} \nu^{-1/6} (C_{Ox}^* - C_{Ox}^0) \quad (1.49)$$

Equation (1.49) is known as Levich equation [43]. The diffusion layer thickness δ in this case is constant and only depends on the rotation rate:

$$\delta = 1.61 \nu^{1/6} D^{1/3} \omega^{-1/2} \quad (1.50)$$

1.6 Influence of electrode's kinetics

We consider again the reaction (1.6) but we don't assume anymore that the equation is very fast at the electrode.



The flux of Fe(CN)_6^{3-} transported from the bulk towards the electrode is expressed by equation (1.52):

$$J = m(C_{Ox}^* - C_{Ox}^0) \quad (1.52)$$

in which C_{Ox}^0 is the concentration of Fe(CN)_6^{3-} at the electrode.

The flux of species consumed by the electrode reaction at the surface takes the following form:

$$J_{reac} = k_r C_{Ox}^0 - k_o C_{Red}^0 \quad (1.53)$$

in which C_{Red}^0 is the concentration of Fe(CN)_6^{4-} at the electrode.

Since we have mass conservation, we can write:

$$C_{Ox}^* - C_{Ox}^0 = C_{Red}^0 \quad (1.54)$$

We consider that there is no accumulation of species at the surface of the electrode which is equivalent to: $J = J_{reac}$. So, we can have the expression of C_{Ox}^0 as following:

$$C_{Ox}^0 = \frac{C_{Ox}^*(m + k_o)}{m + k_o + k_r} \quad (1.55)$$

Substituting C_{Ox}^0 by its value from equation (1.55) in equation (1.53) yields:

$$J_{reac} = J = C_{Ox}^* \left(\frac{(m + k_o)}{m + k_o + k_r} (k_o + k_r) - k_o \right) \quad (1.56)$$

The current i can be expressed then as:

$$i = FAC_{Ox}^* \left(\frac{(m + k_o)}{m + k_o + k_r} (k_o + k_r) - k_o \right) \quad (1.57)$$

in which k_r k_o are described by several models and the simplest one is Butler-Volmer [39]:

$$k_r = k^0 e^{-\alpha f(E-E^{0'})} \quad (1.58a)$$

$$k_o = k^0 e^{(1-\alpha)f(E-E^{0'})} \quad (1.58b)$$

where $f = \frac{F}{RT}$ and α is the electron transfer coefficient ²

² α is a dimensionless parameter with values between 0 and 1, it is often assumed to be $\frac{1}{2}$.

1.7 Protein film Electrochemistry

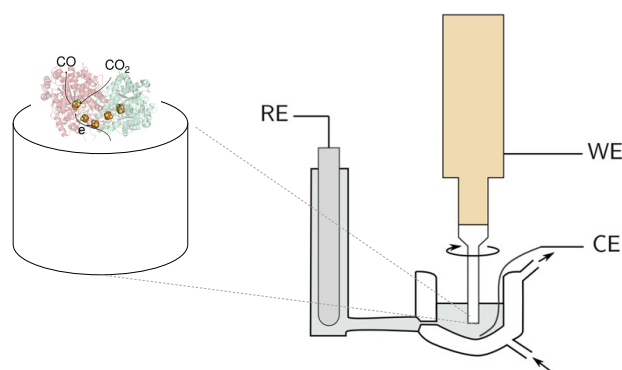


Fig. 1.9 Schematic representation of the classical setup (RDE as a working electrode) used in Protein Film Electrochemistry. A film of enzyme is immobilized on the rotating disk working electrode. Adapted from ref 44.

It was believed that the interaction between redox proteins and electrodes is impossible since the former are fragile and can be denatured when they are connected directly to a metallic surface [26]. Moreover, their active sites are located deeply inside which will make the direct transfer of electrons very difficult or impossible. However, in the 1970s, it was reported that direct electron transfer can occur between an electrode and redox proteins [45]. Since then, many studies of electrochemical investigation of catalytic enzymes have been published [46] and that paved the way to the development of a new technique that was called protein film electrochemistry [26, 34].

The principle of this technique is quite simple, it consists in adsorbing a film of enzyme at the surface of a suitable electrode (fig 1.9) in such a way that the redox active sites undergo fast and direct interfacial electron transfer then investigating the enzyme kinetics using different electrochemical experimental techniques such as CV and CA [47, 48].

The magnitude of the current generated from the exchange of electrons between the enzymes and the electrode is proportional to the turnover rate of the enzyme, which makes it possible to learn about various aspects of the reactivity of the immobilized enzyme [26, 44].

$$i = nFA\Gamma k_{cat}(C^0) \quad (1.59)$$

in which $A\Gamma$ is the total amount of adsorbed enzyme (electroactive coverage), k_{cat} is the catalytic rate and C^0 is the concentration of the substrate **at the electrode** because the concentration that matters is the one where the enzyme is located.

What makes this approach more informative than traditional solution assays is the ability to apply a controllable electrochemical potential which varies continuously or in steps to afford the required driving force that allows to catalysis to occur. This add another dimension to enzyme kinetics [26, 49].

Moreover, in PFE, any change in the catalytic activity can be immediately captured by observing the change of the current (with conditions that response is not obscured by transport limitation or electron transfer). Thus, we can determine how catalytic response evolves with time following an instant change in the experimental conditions (temperature, pH, concentrations of substrates and different inhibitors), this is very useful for studying activation, inactivation or inhibition of metalloenzymes, since these processes involve redox and redox-coupled transformations that happens in short time scales and are hence undetectable in standard activity assays [26].

PFE requires very small amounts of enzyme's sample (in the range of pmol/cm²) [50], which is an advantage for working with enzymes that are not always produced in large quantities. Furthermore, since the enzyme is adsorbed at an electrode, the same sample may be used over and over again with different conditions which saves both time and sample [34].

However, not all enzymes can be studied by PFE. Thus, it is essential that the enzyme has either an active site exposed to the surface, or a chain of redox centres that connect the active site to the surface like the Ni-CODHs. Also, the electroactive coverage should be enough so that it is possible to measure the current even with a small amount of adsorbed enzyme, and the substrate must not be oxidized or reduced directly on the electrode otherwise one can't discriminate between the direct reaction with the substrate and the enzymatic reaction [26].

With all the advantage that this technique brings, over the last two decades, PFE was widely applied for studying different aspects of the mechanism of redox enzymes such as coupled electron transfer in catalytic reactions [51], coupled proton transfer [52], substrate diffusion along gas channels [53], conformational changes [54], aerobic and anaerobic inactivation of different metalloenzymes [55–57, 20, 58]...

1.7.1 Which working electrode's material for PFE?

To study enzymes by PFE, the exchange of electrons between the electrode and the enzyme should be very quick and the interaction between them should be strong enough to maintain a stable film during the experiment [26]. Furthermore, the electrode should not change the enzyme's native properties. Therefore, the choice of the electrode material for PFE is a crucial step. The most used electrode in PFE is Pyrolytic Graphite Edge (PGE). Armstrong and co workers proposed a simple strategy that consists in immobilizing the enzyme on a freshly polished PGE by either cycling the the electrode in a dilute solution of enzyme or by painting the electrode with a small volume of concentrated enzyme's sample [59, 60]. There are also other electrodes that reported to be used successfully in PFE : glassy carbon [61–63]; carbon nanotubes treated with sulfuric acid were used with hydrogenases [64, 65]; Gold electrodes were used by Gorton et al with tobacco peroxidase [66] and laccase [67]; gold with self assembled mono layers of kanethiols was also used for immobilizing different cytochromes[68, 69]. However, since PGE is easy to

clean and usually doesn't require any supplementary treatment, it is favored to be used in PFE experiments.

1.7.2 Example of application: Determining Michaelis-Menten constant of molybdoenzyme *R.sphaeroides* periplasmic nitrate reductase

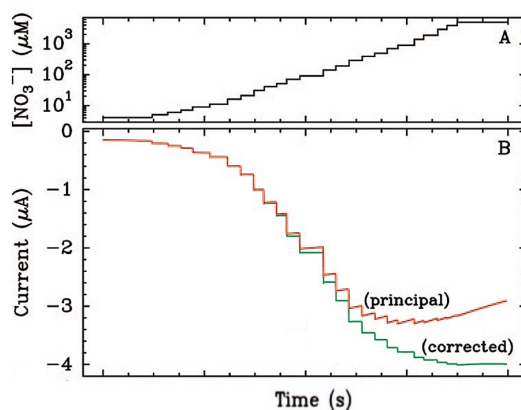
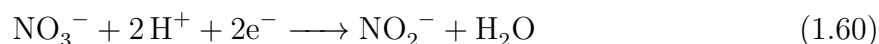


Fig. 1.10 (A) Concentration of Nitrate against time. (B) Raw and corrected chronoamperograms (red and green lines) for *R.sphaeroides* nitrate reductase (NapAB) adsorbed at a rotating disk electrode. The current is proportional to the rate of nitrate reduction. Each increase in current results from nitrate being added; $pH = 7$, $T = 25\text{ C}$, $\omega = 5\text{ krpm}$, $E = -510\text{ mV vs SHE}$. Reprinted from ref 70.

There are many different ways in which we can use PFE to learn about enzymes. Among the published works, I have chosen to demonstrate the technique by presenting how it can be employed to determine Michaelis-Menten constant K_m of redox enzymes, which is a constant that describes the affinity between the enzyme and its substrate. For this, I am taking the example of *Rhodobacter sphaeroides* NapAB, which is a dimeric enzyme that catalyzes the reduction of nitrate to nitrite.



The strategy consists in recording the catalytic current of nitrate reduction over time while adding concentrated solution of nitrate to the buffer (exposing the enzyme to concentrations of substrate that we increase in a stepwise fashion as shown in fig 1.10.A) at a fixed potential. The steady state current is then plotted against nitrate's concentration, and the K_m is simply computed by fitting Michaelis-Menten equation (1.61) to the plot of the plateau current as a function of nitrate's concentration (see fig 1.11). In the context of PFE, the Michaelis-Menten equation can be expressed as:

$$i = nF A \Gamma \frac{k_{cat}^{max}}{1 + \frac{K_m}{C^0}} = \frac{i_{max}}{1 + \frac{K_m}{C^0}} \quad (1.61)$$

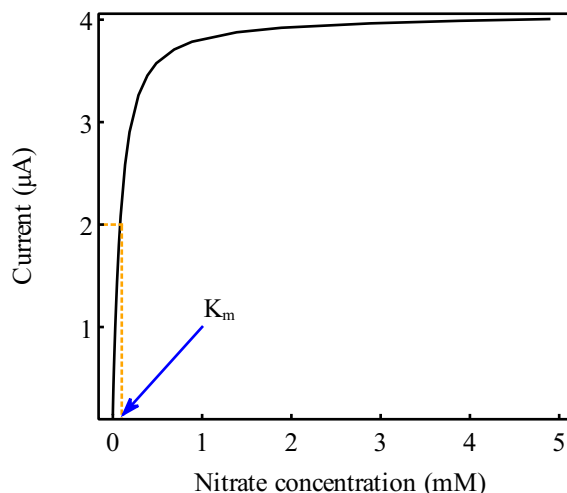


Fig. 1.11 The plot of the catalytic current (plateau) as function of the concentration of the substrate. K_m corresponds to the point with $y = i_{max}/2$.

where k_{cat}^{max} is the maximum catalytic rate, $A\Gamma$ is the total amount of adsorbed enzyme (electroactive coverage) and C^0 is the concentration of the substrate at the electrode. For the interpretation of the experimental results, we assume that the concentration at the electrode is the same as the one that we inject in the bulk. In general, the use of RDE is sufficient to ensure that this is true. But, this is not always the case and in section 1.8.1, I will show cases where this assumption can't stand anymore. Another behaviour can be detected when one look at the current steps in fig 1.10.B (red curve), which is the decrease of the current's magnitude over time. This can be explained by film loss that I will discuss in section 1.7.3. In this case, a correction is required and it can be performed using the method proposed by Fourmond et al [70] as it was done in fig 1.10.B (green curve).

1.7.3 Enzyme's film loss

As I mentioned above, the activity can be decreased over time due to film loss. This loss can have various causes such as enzyme's inactivation, molecules reorientation or the falling of the film from the electrode. Intuitively, we expect that the mechanical force that is exercised by the fluid at the surface of the electrode (shear stress) to have effects at least on the desorption [71]. Film loss can obscure important features in the catalytic response and introduce systematic errors that are difficult to evaluate [70]. Therefore, in chapter 4, I will address the relationship between the film loss and shear stress which is the strength of the fluid at the surface using chronoamperometry experiments on films of *Desulfovibrio desulfuricans* ATCC27774 cytochrome c nitrite reductase (ccNir).

1.8 Limitations of the classical setup of PFE

Although, the classical setup of PEE (fig 1.9) that consists in using a RDE as working electrode is practical and well characterized, it can present some limitations that can be encountered during the study of some metalloenzymes such as substrate transport limitation and the difficulty to control gaseous substrates and inhibitors concentrations.

1.8.1 In spite of the RDE, mass transport limitations can still occur

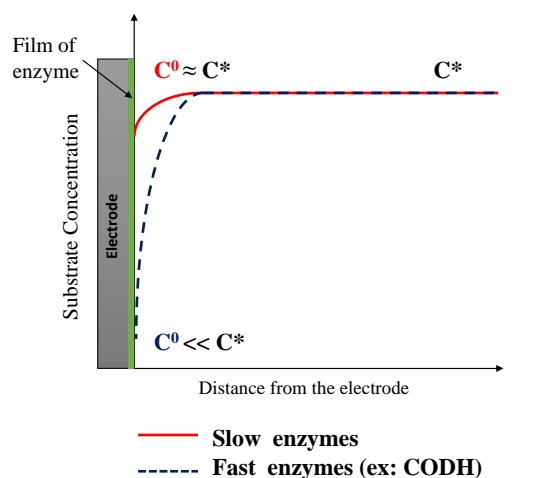


Fig. 1.12 Scheme of substrate's concentration profiles against the distance from the electrode for two different cases; case (a): red curve for slow enzymes and case (b): blue curve for fast enzymes.

In PFE, it is usually assumed that substrate transport by RDE is fast enough so that it doesn't limit the catalysis. However this is not the case for all the metalloenzymes.

Since the catalytic reaction which takes place at the surface of the electrode consumes the substrate, the RDE is used to create a convective motion in the buffer to bring fresh substrate to the electrode to compensate the consumed one so that the concentration at the electrode is maintained equal to the one at the bulk (red curve in fig 1.12). This was the case for most of the enzymes that my team (in BIP) was studying by PFE so far.

However, in the case of CO dehydrogenases which are extremely fast enzymes (turnover rates up to $4 \times 10^4 \text{ s}^{-1}$), the consumption of the substrate at the electrode is so fast which creates a significant difference between the injected concentration (at the bulk), and the one that the enzymes are exposed to (at the electrode), even at high rotation rate (blue curve in fig 1.12). In other words, we have no control of the concentration at the electrode C^0 , the only concentration that we can control is the one at the bulk C^* . Additionally, the determination of C^0 is difficult and this can greatly complicate the interpretation of data.

In this situation, it is wrong to assume that the concentration at the electrode is equal to the one at the bulk ($C^0 = C^*$) and to use it in equation (1.61) to determine K_m for

instance, as I will show in the example bellow; the assumption that there is no transport limitation ($C^0 = C^*$) led to overestimating K_m whereas using equation (1.61) taking into account mass transport limitation allowed to obtain better fits and eventually more reliable estimation of K_m .

Example: K_m of CODH from *Desulfovibrio vulgaris*

Here, I show a case example of the use of PFE for determining the K_m of CODH from *Desulfovibrio vulgaris* (Dv-CODH) where the recorded current was mass transport limited even when the rotation rate of the RDE was at it's maximum value (5 krpm) [72]. The experiment consists in injecting a solution saturated with the substrate CO then following the catalytic response as the current over time.

Figure 1.13 represents the response in the current of film of Dv-CODH (adsorbed on PGE electrode) after a single injection of 83 μM of CO under a constant potential. The CO concentration decreases exponentially over time due to the exchange between the buffer and the atmosphere. This exponential decrease permits to study the catalytic response over a large range of concentration in a single chronoamperometric run [15, 73]. The concentration can be expressed by equation (1.62).

$$C^* = \begin{cases} C_{inj} \exp\left(-\frac{t-t_0}{\tau}\right) & \text{if } t > t_0, \\ 0 & \text{otherwise.} \end{cases} \quad (1.62)$$

Where C^* is the concentration of the substrate in the bulk, C_{inj} is the injected concentration, t_0 is the time of the injection and τ is the time constant of the exponential decrease in substrate concentration.

By looking at fig 1.13, we can observe that before the injection, there is no substrate in the buffer and hence no current. Just at the injection ($t = 0$), the current instantly increases, it corresponds to the catalytic CO oxidation current, it remains constant for some time while the enzyme is still saturated with CO, then decreases exponentially when the concentration of CO drops below the value of K_m . In this study, two models were used to determine K_m value.

Model 01

In this model, it was assumed that the transport of the substrate from the bulk towards the electrode is fast enough so that the concentration at the electrode is equal to the one at the bulk ($C^0 = C^*$). Michaelis-Menten equation (1.61) was used with taking into consideration the fact that the concentration of the gaseous substrate decreases exponentially over time, according to equation (1.62).

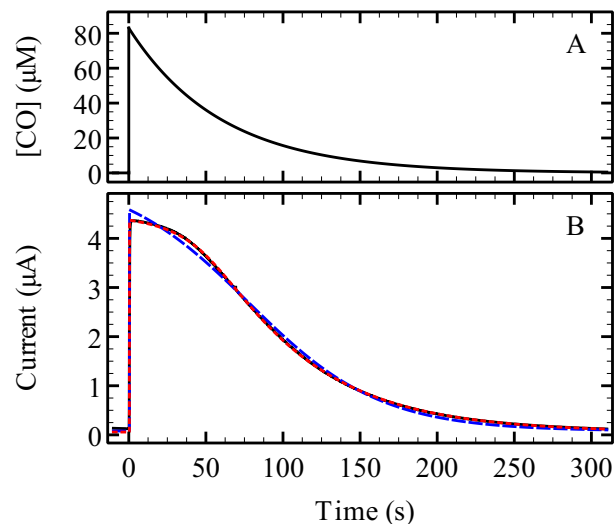


Fig. 1.13 The response in current of a film of Dv-CODH after a single injection of $83 \mu\text{M}$ CO. Panel A: Concentration of the injected CO as function of time. Panel B, black line: the response in current of a film of Dv-CODH after a single injection of $83 \mu\text{M}$ CO at $t = 0$, blue dashed line: fit of equation (1.65) (model 01) to the data with C^* given by (1.62); red dotted line: fit of equation (1.67) (model 02) to the data with C^* given by (1.62). Conditions: $T = 25^\circ\text{C}$, $pH = 7$, $\omega = 4 \text{krpm}$, $E = -310 \text{mV}$. Reprinted from ref 72.

The flux of substrate consumed by the catalytic reaction at the electrode surface J_c takes the following form [72]:

$$J_c = \Gamma \frac{k_{eff} C^0}{1 + \frac{C^0}{K_m}} \quad (1.63)$$

With Γ is the enzyme coverage concentration and k_{eff} is the catalytic efficiency expressed as:

$$k_{eff} = \frac{k_{cat}}{K_m} \quad (1.64)$$

where k_{cat} is the maximum catalytic rate. The current i is then given by:

$$i = nFAJ_c = nFA\Gamma \frac{k_{eff} C^*}{1 + \frac{C^*}{K_m}} = nFA\Gamma \frac{k_{cat} C^*}{1 + \frac{K_m}{C^*}} \quad (1.65)$$

This model (1.65) yielded in a poor fit of the experimental data as it can be seen in fig 1.13.B (blue dashed line).

Model 02

Here, the limitation by the transport of the substrate was taken into account. The flux of substrate imposed by the hydrodynamic flow J can be described as ([36, 74]:

$$J = m(C^* - C^0) \quad (1.66)$$

where C^0 is the concentration at the electrode and m is mass transport coefficient.

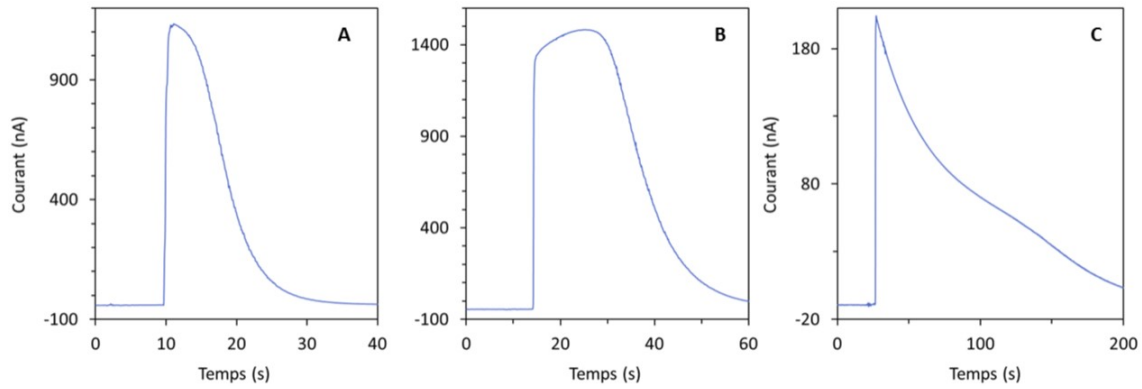


Fig. 1.14 Different forms of signals responses of CO dehydrogenase from *Desulfovibrio vulgaris* to a single CO injection in chronoamperometry experiments. Form 1 (A), Michaelis-Menten behaviour. Form 2 (B), activated by CO, and Form 3 (C) inhibited by CO. $T = 25\text{ }^{\circ}\text{C}$, $pH = 7$, $E = -360\text{ mV}$, $\omega = 4\text{ Krpm}$, $C_{inj} = 100\text{ }\mu\text{M}$ for (A) and (B) and $50\text{ }\mu\text{M}$ for (C). Reprinted from ref 75.

Assuming that there is no accumulation of CO at the electrode, $J_c = J$ (mass conservation):

$$m(C^* - C^0) = \Gamma \frac{k_{eff} C^0}{1 + \frac{C^0}{K_m}} \quad (1.67)$$

C^0 is obtained from equation 1.67 as:

$$C^0 = C^* \frac{\gamma + (\gamma^2 + 4\frac{K_m}{C^*})^{1/2}}{2} \quad (1.68)$$

where:

$$\gamma = 1 - \frac{K_m}{C^*} \left(1 + \frac{G}{m}\right) \quad (1.69)$$

with: $G = \Gamma k_{eff}$

As can be seen in fig 1.13.B (red dotted line) that model 02 (eq (1.67)) allowed to reliably reproduce the experimental data with a realistic mass transport coefficient.

As a conclusion from this example, mass transport in certain circumstances, and in particular in the case of CODH, should not be neglected and it have to be taken into consideration as it allows to estimate reliable values of (K_m).

However, the use of the mass transport model in the previous example was only possible because the catalytic response was simple and the variation of the activity of the enzyme according to the concentration of the substrate is known but this is not always the case. We don't always know how the enzyme behaves as function of substrate's concentration. For instance, CO dehydrogenase can exhibit different behaviors in its active form as shown in figure 1.14 [75]. Fig 1.14 shows different active forms of Dv-CODH that were studied (150 experiments) in my team under the same experimental conditions (same enzyme film, potential, temperature, injected CO concentration and pH) the active enzyme can have three different signal forms [75, 76].

- Signal 1 (fig 1.14.A) corresponds to the Michaelis-Menten behavior of the enzyme. The enzyme is first saturated by the substrate (plateau phase), then the current decreases sigmoidally.
- Signal 2 (fig 1.14.B) corresponds after injection to a slow increase in current followed by a slow decrease that eventually becomes exponential. This form of the signal probably corresponds to an activation of the enzyme by CO (fig 1.14.A).
- Signal 3 (fig 1.14.C) corresponds to a rapid decrease of the current and then the decrease slows down, this corresponds to a form of the enzyme that inactivates in the presence of CO.

As a conclusion, The mass transport model can't be always used as the relationship between the signal and substrate's concentration is not always understood and thus substrate's concentration at the electrode can't be always determined. Therefore, to solve this limitation we have to be able to control concentrations at the electrode. Hence, we have to achieve a situation where the concentration at the electrode is almost equal to the one at the bulk (same as in red curve in figure 1.12). This can't be solved using the RDE setup. Thus, another setup that provide better transport should be developed.

1.8.2 Imposing arbitrary concentrations/ Example: Study of Dv-CODH inhibition by oxygen

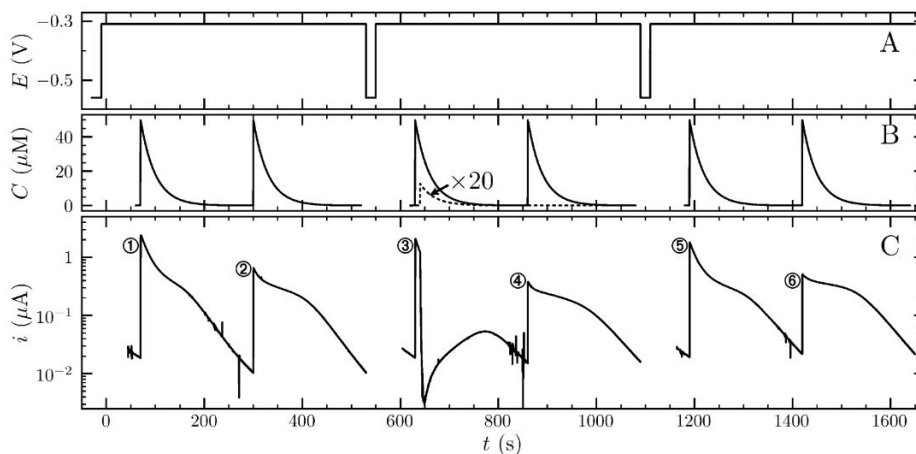


Fig. 1.15 Electrochemical response of a single film of Dv-CODH exposed to CO and O₂ injections. Panel A: Electrode potential (vs SHE) against time. Panel B: Concentration of CO (solid line) and O₂ (dotted line) against time, deduced from the amount injected and the time constant of the final exponential decrease of the current (the O₂ concentration is multiplied by 20 for clarity). Panel C: CO-oxidation current response (in log scale). Conditions: pH 7, T = 258 C, injected[O₂] = 0.6 μM, injected[CO] = 50 μM. Reprinted from ref 77.

Another issue that was encountered in the study of CODHs was the difficulty to control the concentrations of the gaseous substrates and inhibitors and that can be seen in the study of Merrouch et al where they investigated the reactivity of Dv-CODH [24] with O_2 using PFE [77].

Figure 1.15 shows the electrochemical response in current as a function of time of a film of Dv-CODH that was exposed to six injections of CO and one of O_2 . In panel A, the potential is plotted against time where it was kept in three steps at -310 mV (oxidative) preceded by a pulse of -590 mV (reductive) in which the current wasn't recorded. In panel B, the concentration of CO (solid line) and O_2 (dotted line) are plotted vs time. In panel C, the CO oxidation current response is plotted in a log scale over time.

The first injection of CO resulted in a CO catalytic oxidative current that has the same behaviour as the response from the experiment shown in fig 1.13 (typical Michaelian behaviour) and this was observed after each injections of CO. The current resulted from the second injection of CO is significantly lower than the first one, which is found to be due to anaerobic oxidative inactivation that is fully reverted by lowering the potential. The film was exposed to a third injection of CO which resulted in a current in which the maximum value is almost equal to i_1 (max value of first response). After 10 s, $0.6 \mu\text{M}$ of O_2 was injected, this led to a fast decrease of the current until reaching 0 A which can be explained by the total inhibition of CO oxidation by O_2 . This decrease was followed by a slow increase over time even though the CO concentration was decreasing, this indicates that CO oxidation activity was recovered after O_2 diffused away. The film was exposed again to CO and the observed current was 40% lower than the i_1 (a partial recovery). In the last step, the current after injection 5 is almost the same as i_1 and i_3 which indicates that all the activity that was lost after exposure to O_2 is recovered at a lower potential [77].

To sum up, with only one experiment, very valuable quantitative results have been obtained; it was concluded that Dv-CODH is inactivated rapidly and reversibly by O_2 and three inactive species were formed after the exposure to O_2 : one that reactivates spontaneously as O_2 is removed from the solution, one that reactivates at reductive potential and one that does not reactivate at all [77].

However, the issue here is that all we can obtain from this experiment are these qualitative conclusions. It is extremely complicated to get any quantitative results since the modeling in this case is very difficult as there are too many variables: both concentration are changing exponentially and they are very difficult to control (gas diffusion). Moreover, to make the situation even worst, the concentrations that are injected in the bulk are different than the ones at the vicinity of the electrode (see section 1.8.1).

For these reasons, a strategy that ensures control of concentrations of substrates and inhibitors in the cell is needed. For example, it can be useful to maintain a constant concentration of CO and have a short constant exposure to O_2 .

1.9 New electrochemical cell to solve transport limitation

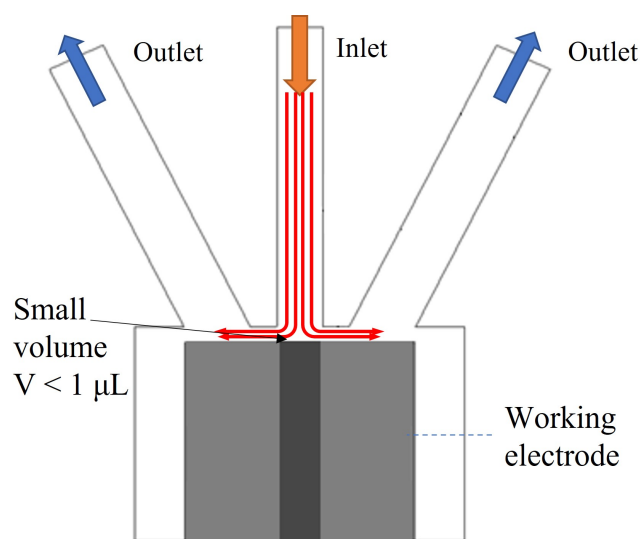


Fig. 1.16 Schematic representation of the built wall-tube electrode cell. Adapted from ref 78.

In section 1.8, I showed that in our experimental studies of some metalloenzymes, by using PFE in the classical setup of the RDE, we encountered two main limitations: (i) we had difficulty to control the concentration at the electrode and (ii) we even had difficulty to control the concentration at the bulk.

The first limitation led us to think about changing completely the setup and design a different geometry of electrochemical cells with improved transport. Thus, the team screened different cell geometries by means of numerical simulation (CFD) [79]. Then, selected and built one with promising transport properties.

The built cell is based on the configuration of wall-tube electrodes (more details about the configuration are described in 2.4.1) in which the electrode is stationary and the buffer is pumped towards it (figure 1.16). Simulations showed that this cell can provide three times higher mass transport coefficient than the one of RDE [78] (figure 1.17). However, that wasn't enough for our application for studying highly active metalloenzymes by PFE. Therefore, the transport in the cell should be further improved and this is one of the objectives of this thesis.

Additionally, the new cell may solve the second limitation (section 1.8.2). Since the volume between the jet and the electrode is very small ($< 1 \mu\text{L}$), the cell offers the possibility to change its contents by just changing what it is pumped in. So, we can imagine that by using multiple pumps to pump buffers with different compositions (concentrations, pH, temperature..), imposing arbitrary changes in concentrations, pH, or/and temperature would be possible.

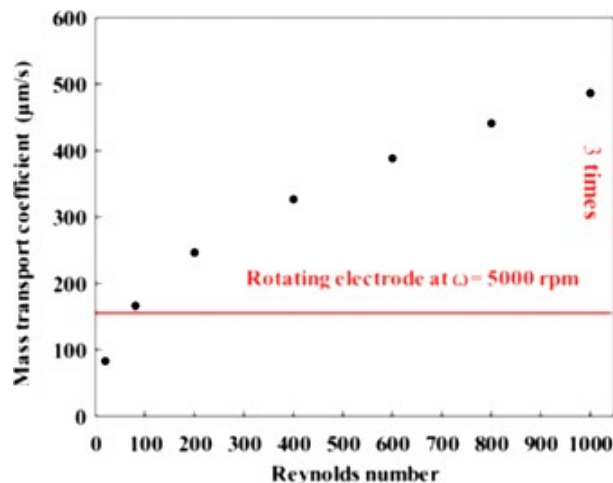


Fig. 1.17 Comparison of the transport in the two different geometries: horizontal line corresponds to RDE at maximum reliable rotation rate 5 Krpm corresponds to $Re=3500$. The black dots symbol corresponds to the numerical results of the built wall-tube electrode cell. Reprinted from ref 80.

Figure 1.18 shows a scheme of concentration profiles that would be possible to achieve in the new cell. We can for example maintain a constant concentration of CO and have a transient exposure to O₂. This setup can also be useful to control dissolved substrate (or inhibitors) concentration (fig 1.19).

1.10 Thesis objectives

This thesis has two main objectives:

1. Optimizing mass transport in the cell built by M.Fadel (ref 78) with satisfying four criteria:
 - A high mass transport to avoid substrate depletion at the electrode;
 - The mass transport should be as homogeneous as possible, to avoid heterogeneity of substrate concentration on the electrode, which would complicate the studies as the enzymatic response is highly non linear in function of the substrate concentration.
 - Since the cell will be used by immobilizing enzymes on the surface of the working electrode, a particular interest should be given to the forces applied by the fluid at the surface (shear stress) as it could be one of the main reasons for the loss of the film of enzyme [81].
 - The pressure drop ³ in the circuit (pipes+cell) should be maintained as low as possible to prevent high pressure inside (should be much more smaller than 1×10^5 Pa).

³Pressure Drop is the difference in pressure between two points in the circuit. It occurs when flow resistance resulting in frictional forces acts on the fluid while it is flowing through the circuit

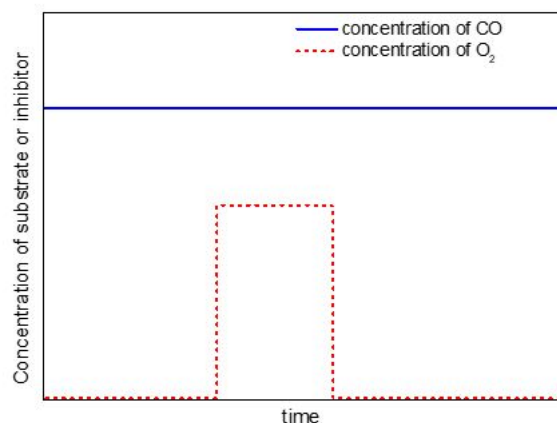


Fig. 1.18 schematic representation of substrate CO (blue solid line) and inhibitor O_2 (dotted red line) concentrations profiles that may be possible to achieve in the wall-tube electrode cell.

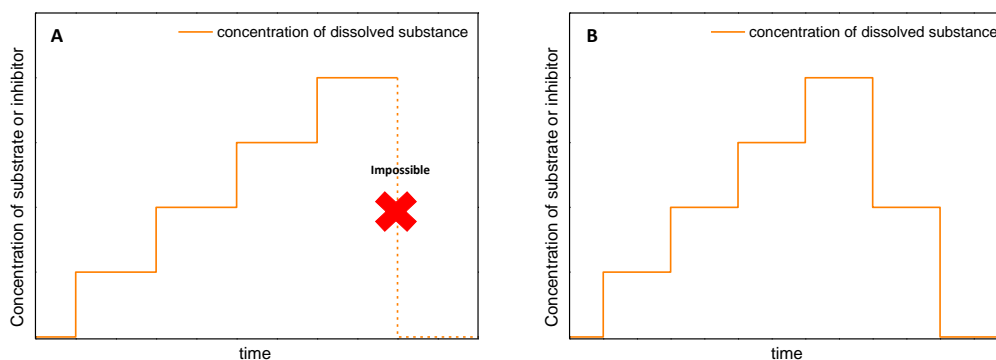


Fig. 1.19 Schematic representation of the possibility to control dissolved substrates and inhibitors concentrations in the wall-tube electrode cell.

2. Design new cells that allow to impose arbitrary changes of concentrations basing on the following criteria:

- Fast changes of concentrations (we aim ultimately for a changing time that is smaller than 0.1 s).
- Possibility to switch back to concentration = 0
- Low pressure drop in the setup.

For both objectives, This work consists of designing, building and using new cells for electrochemical studies of enzymes. That's why we proceed in a succession of iterations between two approaches:

- Computational exploration of geometries using computational fluid dynamics (CFD);
- Experimental validation and characterization of the cell.

In this insight, the rest of chapters will be organized as following:

In chapter 2, I will present the different hydrodynamic electrochemical cells highlighting their hydrodynamics and mass transport in each category.

Chapter 3 is devoted to describe the approaches adopted in order to optimize the previously designed cell (wall-tube). Herein, CFD was used in two steps, in the first one, we conducted a sensitivity study to identify the most influencing parameters on mass transport coefficient and shear stress and in the second one, we performed an in-depth study using simulations with a greater resolution for the most influencing parameters to explore their impact more systematically. We used these data to propose semi-empirical formula for both the mass-transport coefficient and the shear stress on the electrode. We then validated our predictions experimentally.

In chapter 4, I will outline the effect of shear stress on the loss of the biological film that is wired to the electrode basing on chronoamperometry experiments that were carried out using experiments on films of *Desulfovibrio desulfuricans* ATCC27774 cytochrome c nitrite reductase (ccNir).

In Chapter 5, I will show that the possibility to impose arbitrary concentrations in the built cell was tested experimentally by using the standard electrochemical reaction (1.6) (ferricyanide reduction). For that, we were pumping and mixing two solutions with different concentrations of ferricyanide but the mixing wasn't efficient enough to ensure quick changes of concentrations. Thus, we had to design new types of cells that provide better mixing.

Finally, in chapter 6, I will summarise the conclusions from chapters 3 to 5, and I will propose some future work suggestions.

Chapter 2

Mass transport in hydrodynamic electrochemical cells

Hydrodynamic electrochemical cell configurations are based on the convective transport of the electroactive species towards the working electrode. They are widely used in electrochemistry to decrease depletion of the electroactive species at the electrode. There are different techniques to generate and control forced convection to the electrode. They can be mainly classified into two categories [37, 82]:

- An electrode that moves with respect to the solution such as rotating electrodes;
- A static electrode and a moving solution such as channel, tubular and impinging jet electrodes.

In this section, I will provide a summary about the main hydrodynamic electrodes, highlighting for each one their theory, some of their applications and their limitations but first, I will start by presenting some useful concepts to understand flow behaviour in hydrodynamic electrodes.

2.1 Useful concepts in hydrodynamics and mass transport

2.1.1 Laminar and Turbulent flow

Generally, fluid flow regimes can be sorted into two categories: laminar and turbulent.

In laminar flows, the fluid flows in parallel layers at different speeds with no mixing between them; these layers have definite and observable paths or streamlines 2.1.A. (non-crossing streamlines) [84, 85].

Turbulent flows are characterized by chaotic and complex motion of the fluid and by the presence of eddies and swirls that move in random directions 2.1.B [84, 85].

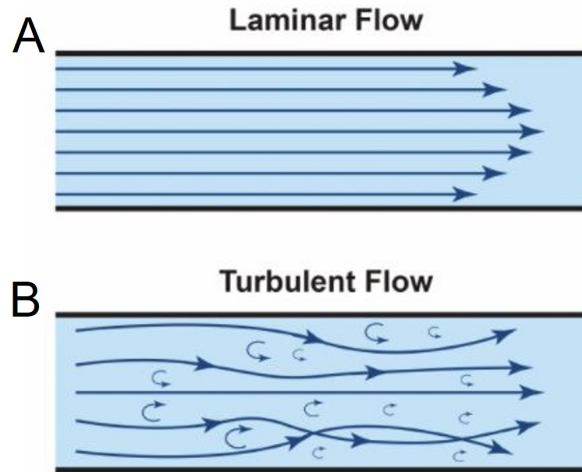


Fig. 2.1 Schematic representation of the two flow regimes: laminar and turbulent within a pipe. Reprinted from 83.

When the regime is stationary; in laminar flow, the instantaneous velocity at any point has a steady value and does not fluctuate whereas in turbulent flow the instantaneous velocity is time dependent [86].

2.1.2 Dimensionless numbers

To reduce the number of variables in the solution of mass transport problems and to help with understanding the physics of the flows, several dimensionless numbers are used [87]:

Reynolds number

The Reynolds number (Re) is defined by the ratio of inertial forces to viscous forces as follows:

$$Re = \frac{VL_c}{\nu} \quad (2.1)$$

where ρ is the density, V is the average velocity, L_c is the characteristic dimension (ex: the diameter of the pipe, the diameter of the jet for the cell that we are studying...), and ν is the kinematic viscosity.

Re plays an important role in predicting the patterns of a fluid's behavior as it helps to discriminate between laminar and turbulent flow as following:

$$\text{Laminar regime} \quad Re < Re_c \quad (2.2a)$$

$$\text{Transition regime} \quad Re_c < Re < Re'_c \quad (2.2b)$$

$$\text{Turbulent regime} \quad Re > Re'_c \quad (2.2c)$$

Re_c and Re'_c are characteristic values of Re that they allow to identify the transition between laminar and turbulent regimes. They depends on the geometry, for instance, in a pipe, they are around 2000 and 4000 respectively.

Schmidt number

The Schmidt number Sc is a fluid property which is defined as the ratio between the momentum diffusivity and mass diffusivity. It compares the size of the hydrodynamic boundary layer to the size of the diffusion boundary layer and describes whether momentum or diffusion will dominate mass transport. Sc is determined as follows:

$$Sc = \frac{\nu}{D} \quad (2.3)$$

in which ν is the kinematic viscosity and D is the diffusion coefficient. In all the cases that we are studying within this thesis, $\nu \gg D$, so Sc is much larger than 1 ($Sc \approx 720$).

Unlike Re , Sc does not depend on the way we design the experiment. It is fixed by the physical properties of the fluid.

2.1.3 Navier-Stokes equations

As mentioned earlier, hydrodynamic electrochemical systems involve flow of the electrolytic solution. The velocity field of the latter can be determined from the Navier-Stokes equations which are the partial differential equations that describe the flow of Newtonian fluids and are widely used to model the flow in different systems.

The Navier–Stokes equations mathematically express conservation of momentum and conservation of mass for Newtonian fluids.

Conservation of momentum

On the base of Newton's second law of motion, the rate of change of momentum of a fluid element is equal to the sum of the forces applied. Here the forces are the pressure gradient, the stress in the fluid, and the force of gravity:

$$\underbrace{\frac{\partial(\rho \vec{V})}{\partial t} + \vec{\nabla} \cdot \rho(\vec{V} \otimes \vec{V})}_{\text{rate of change of momentum}} = \underbrace{-\vec{\nabla} P}_{\text{pressure gradient}} + \underbrace{\mu \nabla^2 \vec{V}}_{\text{stress}} + \underbrace{\rho \vec{g}}_{\text{force of gravity}} \quad (2.4)$$

where ρ is the density of water, \vec{V} is the velocity vector, $\vec{\nabla}$ is the vector differential operator, \otimes is the tensor product, \vec{P} is the pressure vector, μ is the dynamic viscosity and \vec{g} is the gravity vector.

Conservation of mass

The conservation of mass is expressed by the continuity equation:

$$\frac{\partial \rho}{\partial t} + \vec{\nabla} \cdot (\rho \vec{V}) = 0 \quad (2.5)$$

Under the assumptions of incompressible fluid flowing in laminar stationary regime, equation (2.5) becomes:

$$\vec{\nabla} \cdot \vec{V} = 0 \quad (2.6)$$

2.2 Rotating disk electrodes

Among the hydrodynamic electrodes, the most popular ones are the rotating electrodes and the most common geometry is Rotating Disk Electrode (RDE) which consists of a disk of a conductive material surrounded by an insulating material. The disk is attached to a motor that insures the rotation at a certain frequency with an axis perpendicular to the surface of the electrode. This movement of rotation drags the solution upward then throwing it outward from the center due to the centrifugal force in a radial direction (fig 2.2) [37, 88].

The RDE has been massively used in a wide variety of experimental studies [89–92], such as studying electrode reaction kinetics and mechanisms [93]. The reason for the popularity of this electrode is that it has a well described flow and a well known analytical solution (as shown in section 1.5.2). Moreover, it provides well defined and controllable mass transport of species to and from the electrode. Unlike other types of electrodes, the mass transport in RDE depends only on the rotation rate which make it very appealing to use [94, 95]. Furthermore, it is easy to construct with a variety of materials [93].

In addition to RDE, there are other forms of rotating electrodes such as rotating cylinder electrode (RCE), rotating rod electrode (RRE) that are not widely used and the most employed one after the RDE is the rotating ring disk electrode (RRDE) [37].

RRDE consists on an RDE with an additional conductive ring around the disk [96, 97]. The advantage of this electrode is that the ring collects the products of the reaction that occurs in the disk and they can be directly monitored electrochemically [98]. However, the difficulty of using RRDE is that the geometry is

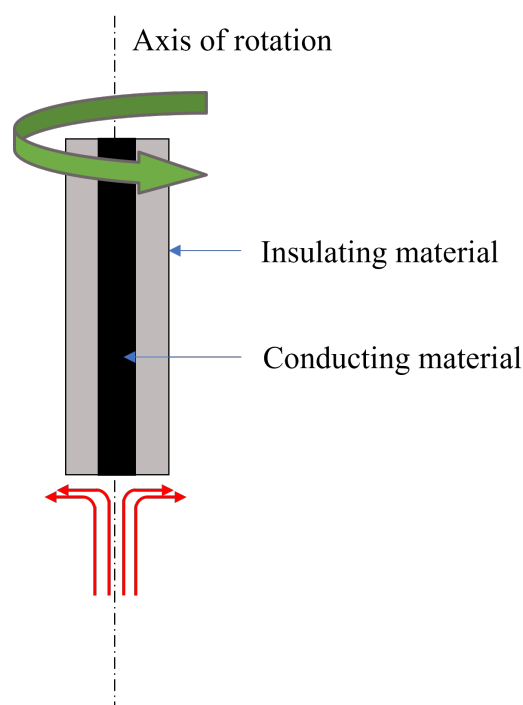


Fig. 2.2 Schematic representation of Rotating Disk Electrode

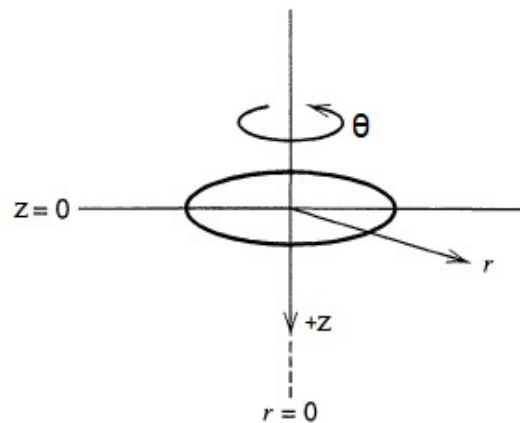


Fig. 2.3 Cylindrical coordinates for the rotating disk. Reprinted from ref 37.

critical to the quality of the results and it is difficult to construct accurate ring disk assemblies [39].

2.2.1 Theory of rotating disk electrode

Hydrodynamic and mass transport properties of RDE are well characterized, the flow to a rotating disk in a viscous fluid was solved by Von Karman [99] and Cochran [100].

Considering the steady flow of an incompressible fluid caused by the rotation of a large disk about an axis through its center, the cylindrical coordinates r , θ , and z are used, where r is the radial distance from the axis of rotation z is the perpendicular distance from the disk and θ is the angular coordinate (fig 2.3).

In cylindrical coordinates, the equation of continuity for incompressible flow at a steady state (2.6) is written as:

$$\frac{1}{r} \frac{\partial}{\partial r} (ru) + \frac{1}{r} \frac{\partial w}{\partial \theta} + \frac{\partial v}{\partial z} = 0 \quad (2.7)$$

in which u , w , and v are respectively the radial, the angular and the axial components of velocity.

Under the assumption of the absence of gravitational effects and no special flow effects at the edge of the disk, the velocity at the surface ($z = 0$) is:

$$u = 0 \quad (2.8a)$$

$$w = r\omega \quad (2.8b)$$

$$v = 0 \quad (2.8c)$$

this implies that the solution is dragged along at the surface of the disk with the angular velocity ω .

In the bulk solution ($z \rightarrow \infty$):

$$u = 0 \quad (2.9a)$$

$$w = 0 \quad (2.9b)$$

$$v = -v^0 \quad (2.9c)$$

thus, far from the disk, there is no flow in the r and θ directions, but the solution flows at a limiting velocity v^0 towards the disk, with v^0 determined by the solution of the problem [37].

Von Karman and Cochran suggested a solution of the velocities in the form of infinite series based on the dimensionless variable γ , where $\gamma = \left(\frac{\omega}{\nu}\right)^{1/2} z$

For small values of z ($\gamma \ll 1$)

$$u = r\omega F(\gamma) = r\omega \left(0.51023\gamma - \frac{\gamma^2}{2} + \frac{1}{3}0.6159\gamma^3 + \dots \right) \quad (2.10a)$$

$$w = r\omega G(\gamma) = r\omega \left(1 - 0.6159\gamma + \frac{1}{3}0.51023\gamma^3 + \dots \right) \quad (2.10b)$$

$$v = (\omega\nu)^{1/2} H(\gamma) = (\omega\nu)^{1/2} \left(-0.51023\gamma^2 + \frac{\gamma^3}{3} + \frac{-0.6159\gamma^4}{6} + \dots \right) \quad (2.10c)$$

The flow in the angular direction has no influence on the concentrations because the system is symmetric (invariant by rotation). So only u and v are important here.

Near the surface, $z \rightarrow 0$ ($\gamma \rightarrow 0$), u and v are expressed as:

$$u = r\omega(a\gamma) = 0.51\omega^{3/2}\nu^{-1/2}rz \quad (2.11a)$$

$$v = (\omega\nu)^{1/2}(-a\gamma^2) = -0.51\omega^{3/2}\nu^{-1/2}z^2 \quad (2.11b)$$

For computing the mass transport to the rotating disk electrode, only v matters. Thus, as I showed in section 1.5.2, by using the expression of v (2.11b) and the transport equation (1.14), the species flux and the mass transport expressions of RDE were obtained.

The analytical solution of RDE is based on the assumptions of an infinite electrode diameter within an infinite bath as assumed by Von-Karman and Cochran [100]. In the 1950s and 1960s, some studies [101, 102] began to question whether these simplifying assumptions are valid for real RDEs and to which extent non-idealities such as electrode's shape, electrode's immersion depth and an infinite bath can affect mass transport to the surface of the electrode [94]. These considerations were explored by some groups such as Blurtorn et al in 1962 and 1965 [103, 102] where they investigated experimentally the effect of the shape of the electrode on the transport properties. Overall, they found less than 10% difference between the predicted mass transport from Levich equation (1.49) and the one they measured using different electrodes shapes [102]. Following that, in 1966, Prater et al showed that electrode immersion depth has no effect on mass transport [104].

In more recent works, CFD simulations were used to study flow characteristics of RDEs in confined cells. Mandin et al [105] and later, other groups [106, 107, 94] addressed by means of finite volume method the impact of the confined volume of the cell on the overall flow. Despite the significant deviation that they found in the flow behavior from the one described by Cochran in the bulk, their results at the vicinity of the electrode are reasonably in agreement with the predicted ones. Experimental measurement of local velocities with Doppler laser anemometry [105] or with magnetic resonance [93] imaging showed similar results.

The homogeneity of mass transport to RDE was also addressed. Albery et al showed that RDE is uniformly accessible which means that the local mass transport coefficient is almost the same at all points on the surface of RDE [108].

2.2.2 Applications and limitations of rotating disk electrode

Since the mass transport to the electrode surface is uniform and controllable, the RDEs has been widely used in electrochemistry for investigating reactions kinetics [109, 110] and they have been successfully utilized to study enzyme kinetics by PFE [26, 48, 58]. Moreover, they proved very useful for investigating fuel cell catalysts [111, 112].

However, RDE has also some drawbacks like the limited transport due to the limited rotation rate that can be practically reached, this is because it is difficult to access to high rotation rates while keeping an electrical contact [113]. It was also shown that some defects of RDE that can be originated during manufacturing, polishing or during mounting the experimental setup [114] can increase significantly the heterogeneity of mass transport. This can greatly complicates the calculation of kinetic parameters from measurements of the total current especially in the case of adsorbed enzymes where the response is not linear with respect to the concentration [114].

2.3 Tubular and channel electrodes

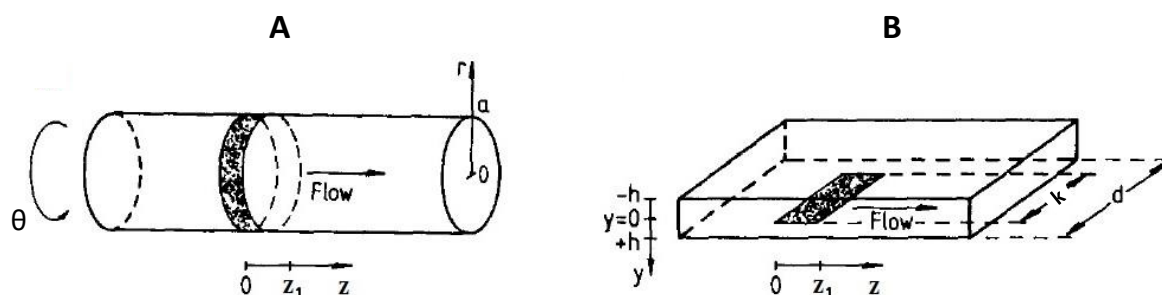


Fig. 2.4 Geometry of tubular electrode (A) where a is the radius of the electrode. Geometry of channel electrode (B) where d is the width of the channel and k is the length of the electrode. Reprinted from ref 115.

Tubular (TE) (fig 2.4.A) and channel (CE) (fig 2.4.B) electrodes consist respectively of an electrode placed within a cylindrical pipe [116] or embedded in the wall of a rectangular duct through which electrolyte flows [117, 118]. The interest on these electrodes has grown in first place with the development of flow injection analysis [119] and liquid chromatography with electrochemical detection [120, 121].

2.3.1 Theory of tubular and channel electrodes

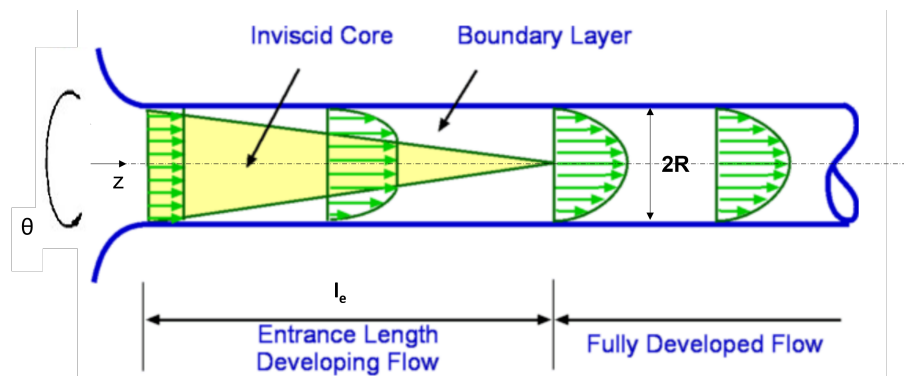


Fig. 2.5 Establishment of Poiseuille flow and diffusion layer under laminar flow in a tube. Adapted from 115.

Hydrodynamic and mass transport under laminar flow conditions in tubular and channel electrodes are well characterized since there is a precisely defined, parabolic hydrodynamic flow regime (Poiseuille flow 2.3.1) and the dimensions of the cell are accurately determinable [116]. The direction of flow is designated as the z -direction, r is the radial direction (for TE) and y is the direction normal to the electrode (for CE) [116, 122]. TE is characterized by the radius of the tube a and CE by the channel height $2h$ (see fig 2.4).

In TE and CE, Poiseuille flow should be established which requires an entry length, l_e (fig 2.5) [43, 123], that is described by the following expressions [115]:

$$\text{In TE} \quad l_e \approx 0.1aRe \quad (2.12a)$$

$$\text{In CE} \quad l_e \approx 0.1hRe \quad (2.12b)$$

Poiseuille flow For incompressible and Newtonian fluid in laminar flow flowing through a long cylindrical pipe of constant cross section, the velocity profile across the section has a parabolic shape with a maximum velocity at the centre. This velocity decreases with the radial distance [84, 85].

Let us consider a flow in a cylindrical pipe of radius R and length L . The liquid flows in the z direction, under the assumptions of laminar regime at steady state conditions and

axial symmetry, velocity components can be written as:

$$u = 0 \quad v = v(r) \quad w = 0 \quad (2.13a)$$

using the assumptions stated above, continuity equation (2.6) in a cylindrical coordinates system can be simplified to:

$$\frac{\partial v}{\partial z} = 0 \quad (2.14)$$

and momentum equation (2.4) can be simplified to:

Component r

$$-\frac{\partial P}{\partial r} = 0 \quad (2.15)$$

Component z

$$-\frac{\partial P}{\partial z} + \mu \left[\frac{1}{r} \frac{\partial}{\partial r} \left(r \frac{\partial v}{\partial r} \right) \right] = 0 \quad (2.16)$$

Integration of equation (2.16) from 0 to r yields:

$$\frac{dv}{dr} = \frac{dP}{dz} \frac{r}{2\mu} \quad (2.17)$$

in (2.17), we switched from partial to total derivative because v depends only on r and P depends only on z . We arrange the variables and we integrate further between 0 and v knowing that at $r = R$; $v = 0$:

$$\int_0^v dv = \int_R^r \frac{dP}{dz} \frac{1}{2\mu} r dr \quad (2.18)$$

this leads to:

$$v = \frac{dP}{dz} \left(\frac{r^2 - R^2}{4\mu} \right) \quad (2.19)$$

as mentioned earlier, the velocity at the center is the maximal velocity (at $r = 0$; $v = v^0$), so:

$$v^0 = -\frac{dP}{dz} \frac{R^2}{4\mu} \quad (2.20)$$

thus, equation (2.12) for a poiseuille flow can be written as:

$$v = v^0 \left(\frac{1 - r^2}{R^2} \right) \quad (2.21)$$

In TE and CE, downstream of the entrance l_e (fully developed flow), the steady state flow can be expressed using equation (2.21) as follows:

$$\text{In TE} \quad v = v^0(1 - r^2/a^2) \quad (2.22a)$$

$$\text{In CE} \quad v = v^0(1 - y^2/h^2) \quad (2.22b)$$

h is assumed to be significantly smaller than d and k is sufficiently smaller than d for edge effects to be neglected.

Leveque gave approximations of the parabolic velocity profile by a linear one near to the electrode [124]:

$$\text{In TE} \quad v = v^0(1 - r^2/a^2) \approx 2v^0(1 - r/a) \quad \text{for : } r \approx \pm a \quad (2.23a)$$

$$\text{In CE} \quad v = v_z^0(1 - r^2/h^2) \approx 2v^0(1 - y/h) \quad \text{for : } y \approx \pm h \quad (2.23b)$$

Under the assumption of neglected axial diffusion [122], the steady state convective-diffusion equation (transport equation) for TE and CE respectively is given by:

$$\text{In TE} \quad D \frac{1}{r} \frac{\partial^2 C}{\partial r^2} - v \frac{\partial C}{\partial z} = 0 \quad (2.24a)$$

$$\text{In CE} \quad D \frac{\partial^2 C}{\partial y^2} - v \frac{\partial C}{\partial z} = 0 \quad (2.24b)$$

where C is the electroactive species concentration, D is the diffusion coefficient. Levich solved equations (2.24) at the electrode using the velocity approximation made by Levêque (2.23) and proposed the following expressions for the the local mass transport coefficient m_l as function of the distance z_l from the beginning of the electrode [43]:

$$\text{In TE} \quad m_l = 1.73 D^{\frac{2}{3}} Q_v^{\frac{1}{3}} a^{-1} z_l^{-\frac{1}{3}} \quad (2.25a)$$

$$\text{In CE} \quad m_l = 0.925 D^{\frac{2}{3}} \left(\frac{Q_v}{h^2 d} \right)^{\frac{1}{3}} z_l^{-\frac{2}{3}} \quad (2.25b)$$

where Q_v is the volume flow rate and a is the radius of the tube. Q_v is the volume flow rate and a is the radius of the tube.

2.3.2 Applications and limitations of tubular and channel electrodes

The tubular electrodes have been widely used in low concentration detection [125–127], they have also been used in studying reaction's kinetics using electron spin resonance (ESR) [128].

The channel electrodes have been also used in many applications: in analytical studies where they provide the ability to continuously monitor the flow such in chromatography [129, 130], in investigating electrode processes by voltammetric methods [131, 132, 87, 133, 134], in photoelectrochemistry [118, 135–137] and recently the well characterization of these electrodes made them very attractive for the wide application in microfluidic systems devices [138, 139], in the simultaneous spectroscopic measurements [123, 140].

Despite the advantages provided by TE and CE, as every system, they have several drawbacks: cleaning the working electrode is difficult compared to other cell configurations; Moreover, the mass transport in TE and CE is highly non uniform (heterogeneous) as it decreases with the distance from the beginning of the electrode (2.25a), and this limitation complicates greatly the interpretation of the process that occurs at the electrode [108]. This makes them in particular non suitable for our application in studying enzyme's kinetics which requires uniformly accessible electrodes.

2.4 Impinging jet electrodes

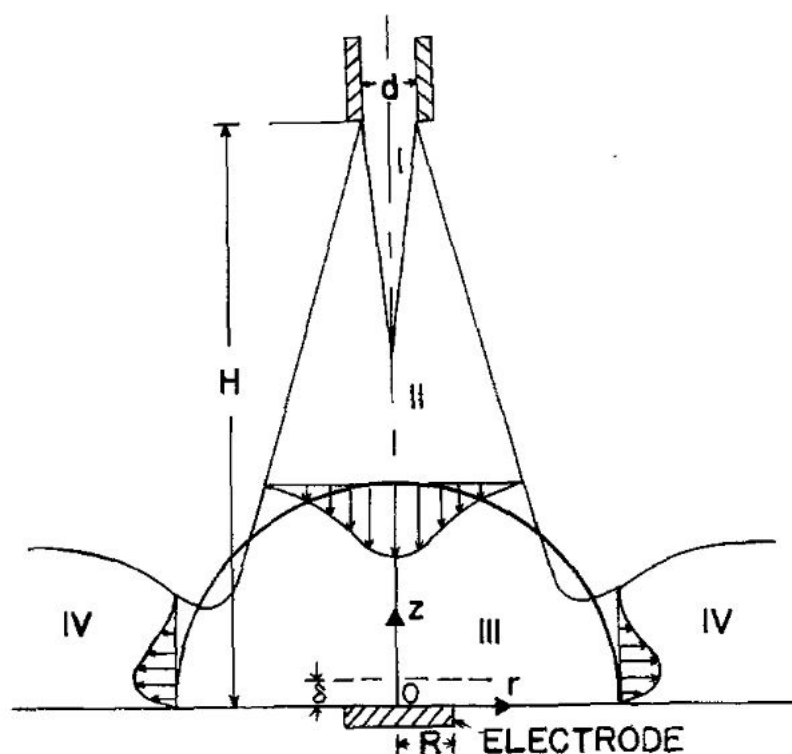


Fig. 2.6 The flow behaviour within an impinging jet electrode with different regions:(I) the potential core region; (II) established flow region; (III) a stagnation region(IV) a developed radial flow region. Reprinted from ref 141.

Impinging jets (IJ) came out as an alternative to the RDE and have been one of the most important tools that were used in electrochemical investigation since they ensure

high and controllable mass transport [142, 143]. They are electrochemical cells in which the flow impinges normally from an inlet toward a fixed disk electrode than it spreads out radially away from the center [144]. In terms of flow profile within an impinging jet, four regions can be identified (figure 2.6):

- I. The *potential core* where the fluid leaves the nozzle and the velocity profile changes from pipe flow to a free jet flow. In this region, the electrolyte starts to mix with the neighboring fluid then the width of the mixing zone develops along with direction of the jet which creates a conical potential core in which the fluid velocity is constant. The length of this region is between 4.7 to 7.7 nozzle diameters [145].
- II. The *established flow region* where the velocity profile is well developed and the magnitude of the center-line velocity is inversely proportional to the distance from the nozzle, the height of this region from the plate is about 1.6 to 2.2 nozzle diameters [141].
- III. The *stagnation region*, located just above the plate in which the jet is deflected from the axial direction and it has a radius that ranges between 0.6 to 1.4 nozzle diameters which is consistent with the results that we show in section 3.6. In this region, the thickness of the hydrodynamic boundary layer is found to be relatively independent of the radial position from the stagnation point [146].
- IV. The *developed radial flow zone*, where fluid flows outwards with a decreasing radial velocity and an increasing thickness of the boundary layer as a function of the radial position. Two sublayers can be identified in this region: an inner layer in which the flow is mostly influenced by the wall and an outer layer in which the flow is impacted by the surrounding fluid [141, 142].

Impinging jets can be classified into two types depending on the size of the electrode with respect to the size of the jet (figure 2.7):

- wall-jet (WJE) [148], in which the diameter of the electrode is bigger than the one of the jet. WJE is widely applied for the electrochemical detection in liquid chromatography [149, 150].
- wall-tube (WTE) [151], in which the diameter of the electrode is smaller or equal to the diameter of the jet. WTE provides uniform mass transport coefficient [152, 108].

2.4.1 Theory of flow in impinging jets

The flow from a jet to a an infinite plate is very similar to the one at the RDE. Homann et al [153] developed a mathematical solution to describe the boundary layer flow in the *stagnation region* of a uniform flowing field on an infinite plate [153]. Considering a

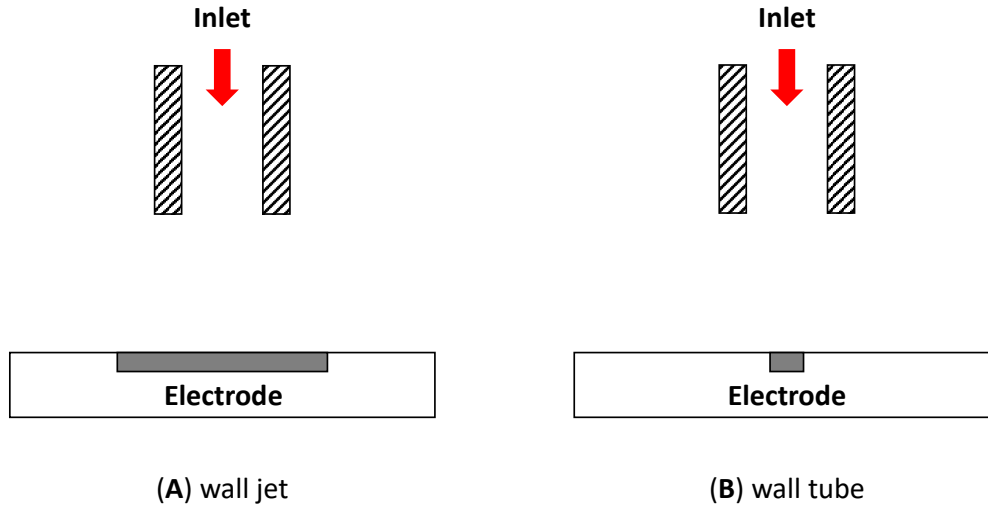


Fig. 2.7 The two limiting forms of the impinging jet electrode geometry. Adapted from ref 147

stationary incompressible flow from a circular jet. According to Homann [153], the axial (v) and the radial (u) velocities in the stagnation region can be written under the following forms:

$$u = ar\phi'(\eta) \quad (2.26a)$$

$$v = -2\sqrt{a\nu}\phi(\eta) \quad (2.26b)$$

in which a is a constant, called the *hydrodynamic constant* and it depends on the flow rate and the geometry of the jet, η is the dimensionless axial coordinate that is defined as $\eta = z\sqrt{a/\nu}$, and $\phi(\eta)$ is a function. Frossling proposed a Taylor expansion for the function $\phi(\eta)$ [154, 141]:

$$\phi(\eta) = 0.656 \times \eta^2 + \dots \quad (2.27)$$

Using (2.27), equations (2.26) can be expressed as:

$$u = 2\alpha a^{3/2}\nu^{-1/2}rz \quad (2.28a)$$

$$v = -2\alpha a^{3/2}\nu^{-1/2}z^2 \quad (2.28b)$$

The velocities expressions (2.28) near to the surface of the electrode at the **stagnation region** in case of impinging jets are very similar to those of RDE (1.28) which explains the similarities in the flow between the impinging jets and RDE. For instance in both cases, the u is proportional to r and the v is proportional to z^2 . The main difference is in the angular velocity but as I mentioned earlier, in section 2.2.1, the flow in the angular direction in the RDE system has no influence on the concentrations (invariant by rotation) and thus on mass transport.

Mass transport to the wall-jet electrode The transport in WJE was first addressed by Glauert et al in 1956 [142] then by Matsuda et al in 1971 [155] who proposed a formula that predicts the average mass transport within a circular WJE:

$$m = 0.318D^{2/3}\nu^{-5/12}Q_V^{3/4}d_{jet}^{-1/2}r_{elec}^{-5/4} \quad (2.29)$$

where m is the mass transport coefficient, Q_V is the volumetric mass flow rate, d_{jet} is the diameter of the jet's nozzle and r_{elec} is the radius of the electrode.

Regarding the homogeneity of the transport, Albery et al showed that the mass transport coefficient to the working electrode in WJE is not uniform. It varies with the radius, being largest at the center and decreasing as the radius increases (see equation (2.29)) [152].

Mass transport to the wall-tube electrode Mass transport in the wall-tube electrodes (WTE) was first studied by Chia et al who demonstrated that the mass transport rate at the impinged surface is relatively uniform in the case of WTE [156]. They solved the steady state convective diffusion equation using Hommann solution (2.26). Chin et al used experimental data to propose their semi-empirical formula that predict mass transport coefficient within a WTE configuration [141] in both laminar and turbulent conditions. For laminar flows ($Re < 2000$, and $0.2 < r_{jet}/h < 1$)

$$m = 0.6244D^{2/3}\nu^{-1/6} \left(\frac{Q_v}{r_{jet}^3} \right)^{0.5} \left(\frac{r_{jet}}{h} \right)^{0.054} g(Sc) \quad (2.30)$$

For turbulent flows ($4000 < Re < 16000$, and $0.2 < r_{jet}/h < 2$)

$$m = 0.4631D^{2/3}\nu^{-1/6} \left(\frac{Q_v}{r_{jet}^3} \right)^{0.5} \left(\frac{r_{jet}}{h} \right)^{0.057} g(Sc) \quad (2.31)$$

in which r_{jet} is the jet's nozzle radius and $g(Sc)$ is an asymptotic series whose development is [141]:

$$g(Sc) = 1 - 0.084593Sc^{-1/3} - 0.0016368Sc^{-2/3} - 0.0057398Sc^{-1} + 0.0014288Sc^{-3/4} + \dots \quad (2.32)$$

Other semi-empirical formulas of mass transport coefficient within the WTE are stated in chapter 3, section 3.6, table 4. We also derived an expression using the same approach as Chin but basing on CFD data. We found very slightly different results. More details about the approach and our results are given in chapter 3, section 3.6.

In 2003, Rees et al [157] started to question the validity of equations 2.30 and 2.31, they stated five possible limitations that based on the assumptions made by Chin et al [141] and can be different for real WTE systems.

- The assumption of laminar parabolic inlet flow seems to break down in less viscous fluids. Rees et al observed that the measured currents using less viscous fluid are significantly smaller than those predicted by chin et al [141]. This can be explained by the existence of a plug-flow profile in the nozzle and not a fully developed parabolic flow as it was assumed [157].
- The radial diffusion which was neglected can have a significant effect on mass transport in case of micro electrodes of radius $< 25 \mu\text{m}$ [157, 158].
- The cell geometry of WTE was found to have important effects on the measured limiting currents [158, 158]. In particular, the nozzle wall thickness should be greater than 0.1625 cm in order for the limiting current to be independent of it [158].
- The precise centering of the electrode under the nozzle can have a noticeable effect in case of micro-electrodes [113, 151].
- The existence of recirculation zones within the electrode chamber was noticed in case of large values of the distance between the nozzle and the electrode. This can have an impact on mass transport [159, 158, 151].

Based on the cited points, it became clear that in order to use the WTE with reliability either for kinetics or for other applications, it is necessary to know the nature of the hydrodynamics for the specific cell designs [157].

2.4.2 Micro-jet electrodes

The micro jet electrode (MJE) is a miniaturized version of the wall-tube electrode. It consists in a jet of solution that contains electroactive species impinging at a high velocity (up to 25 ms^{-1}) from a nozzle whose diameter ranges between $25 \mu\text{m}$ and $100 \mu\text{m}$ onto the surface of an ultramicroelectrode (UME) in which the diameter is mainly smaller or equal to $25 \mu\text{m}$ [108, 32, 160, 113]. MJEs are characterized by defined and very high mass transport rates which makes them a suitable tool for studying fast electrode kinetics [160, 161].

Most of the studies of MJE used the same semi-empirical model of the WTE electrode [141] basing on the assumption that the rate of forced convection is sufficient for the diffusional edge effect at the UME to be neglected and for the mass transport to the electrode to be uniform [161]. However, simulated (using finite element method) and experimental results obtained by Melville et al showed a significant deviation from equation (2.30). They suggest that this particular empirical treatment by Chin et al at conventional sized WTEs is inappropriate for the MJE scale [151] for the same reasons cited in section 2.4.1.

2.4.3 Application and limitations of impinging jet electrode

The different forms of IJE geometries (WJE, WTE and MJE) have proven to be powerful electroanalytical devices.

From one side, WJE have been used in variety of analytical techniques [162] such as anodic stripping voltammetry [163, 164], flow-injection analysis [165–167] and high performance liquid chromatography (HPLC) [168, 169, 147].

On the other side, with the high and uniform mass transport rate that they provide, WTE and in particular MJEs found applications in measurement of fast kinetics mechanism [170] and fast heterogeneous electron-transfer processes [171]. They have been also used in HPLC detection [172] and in electronic microchips as a cooling device [173, 174].

However, the main limitation of IJEs is that they are difficult to fabricate and less practical to use compared to the RDE.

Additionally, in the case of WJEs, the mass transport to the electrode is not uniform [152] which justifies their limited application in the study of electrode reaction mechanisms [162] since the non uniformity of transport is not a favored property when it comes for studying electrode kinetics [152].

2.5 New cell based on wall-tube configuration for enzyme kinetics studies

As shown in the previous sections, hydrodynamics electrode afford high mass transport. However, only RDE and WTE (including the miniaturised version MJE) are shown to provide a uniform mass transport which make them suitable for studying kinetics. The downside about the RDE is that it can't surpass a certain value of rotation rate (5 Krpm) otherwise, the quality of the moving contact will decrease. This limits the mass transport that can be reached within an RDE setup which was the case when we wanted to study fast enzymes (particularly CODH) using PFE (see section 1.8).

Therefore, to address this limitation, the previous PhD student M.FADEL and with the collaboration of both teams (IUSTI/BIP) designed a new electrochemical cell based on the wall-tube configuration that provides high and uniform mass transport coefficient. In a first step, they screened using the commercial Computational Fluid Dynamic (CFD) software Starccm⁺ several geometries of channel and jet electrodes. It is important to note that in their study, MJEs were not considered since they are difficult to construct with high accuracy using 3D printing and making a PGE micro-electrode is very challenging. Moreover, mass transport in MJE system is highly sensitive to the lateral displacement of the nozzle electrode [113, 175].

Their results confirmed that the channel cells provide non uniform mass transport which makes them non suitable for our application. In the other hand, wall-tube electrode

showed the best uniformity of transport. Based on these results, a wall-tube geometry with two outlets was designed.

In a second step, the designed cell was built using 3D printing then tested experimentally employing the simple redox couple $\text{Fe}(\text{CN})_6^{3-}/\text{Fe}(\text{CN})_6^{4-}$. The experimental results showed that the new cell can provide 3 times higher transport than the RDE. However, this improvement is still not sufficient for studying enzymes with high turnover rates. Thus, we performed an optimization study of the wall-tube electrode cell. This study will be explained in chapter 3.

2.5.1 The experimental setup

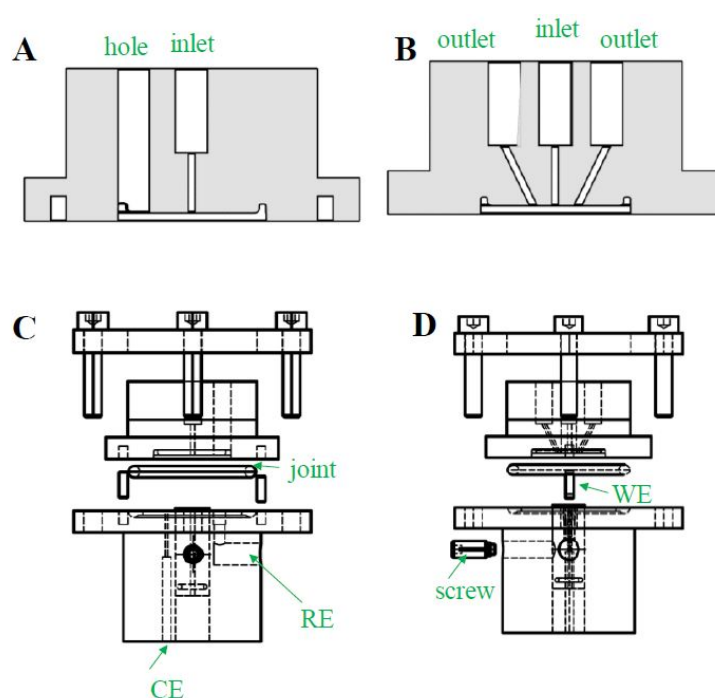


Fig. 2.8 The design of the wall-tube cell : (A) is the view along the upper part of the cell to show the hole, (B) is the view along the upper part of the cell that includes the inlet and two symmetric outlets, (C) is the view of the two assembly parts of the cell along the side that shows the part of the reference electrode (RE) and counter electrode (CE), and (D) is the view of the tow assembly parts of the cell the working electrode (WE) and the screw that fix it. Reprinted from 80.

The built cell is composed of two parts (fig 2.8):

- the bottom part: consists of epoxy shell that was machined with traditional workshop techniques and hosts the three electrodes: the working electrode which is made of PGE, the reference is an Ag/AgCl, and the counter electrode is a platinum wire.
- the upper part: which includes the inlet and the two outlets, it was printed using stereolithography to make it easier to change its geometry, this allows for easy

changes in the configuration of the flow (position of the inlet/outlets, nozzle to electrode distance...).

The two parts were screwed together and a large O-ring was used to seal the system. Also, two centering rods were employed to ensure the inlet and electrode alignment.

In order to make the solution flow to the cell, a flow system that is composed of pump, pipes and reservoir was used. This is of a great importance because these elements are bringing their own set of constraints of complications.

During this thesis, I started working with the previous setup that included a peristaltic pump but many complications were encountered such as the presence of flow fluctuations, the difficulty to regulate and measure the flow rate. Therefore, I tried to improve the the setup by looking for different possibilities of pumping systems. Syringe pumps showed good qualities like reliability, less fluctuations... However, they have several disadvantages. For instance, the syringes have a limited volume which may cause interruptions during the experiment and they can also be broken at high pressure. The present setup includes syringe pumps and shows less fluctuations but the flow system still needs further improvement.

Chapter 3

Enhancing mass transport in the wall-tube electrode

In this chapter, I will address the first objective of the thesis which is to optimize the transport within the designed wall-tube electrode cell. This chapter is built around a published (see section 3.6) in *Electrochimica Acta* journal [176].

As I mentioned earlier in chapter 1, our first objective is to optimize mass transport in the cell built by M.Fadel (ref 78) with satisfying four criteria::

- The transport of the substrate from the bulk towards the electrode should be controllable and uniform in order to guarantee that the concentration to which the enzyme is exposed to is homogeneous over the surface of the electrode and not significantly different from the concentration in the bulk.
- The enzyme's film should be relatively stable during the experiment. Thus, a particular attention should be given to shear stress. However, in the end, we found that this is less critical than what we initially thought. This point will be discussed further in chapter 4.
- Another point that should be monitored in the system is the pressure drop. It should be kept in an acceptable range (much smaller than 10×10^5 Pa) because the higher it is in the line, the greater the amount of energy needed to maintain the desired flow rate requiring a higher pumping energy. Moreover, when there is an over-pressure inside the system, the seals used in the cell and in the pump can be degraded or deformed, causing leaks. This can also cause stalls of and/or potential syringe damage.

With this in mind and since there are many design parameters that can affect the hydrodynamics and therefore mass transport, shear stress and pressure drop; in a first part, we investigated by CFD the effects of the design parameters on the properties mentioned above. For this, the design of experiment (DoE) approach was applied on six parameters which are: inlet radius, the distance between the inlet and the outlets, the diameter of the

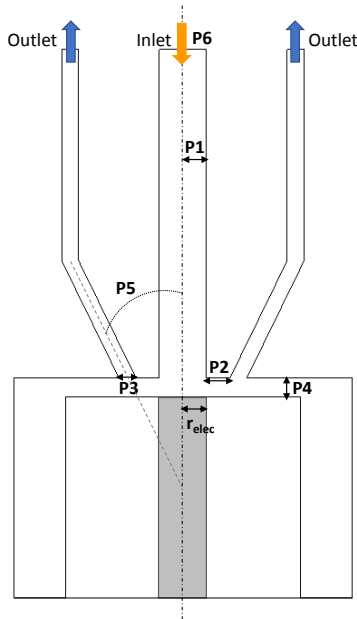


Fig. 3.1 Schematic representation of the geometry of the cell, indicating the 6 parameters varied in the systematic approach. The detailed meaning and values of the parameters are given in table 3.1

Parameter	Inlet radius (P1) mm	Distance inlet-outlet (P2) mm	Outlet thickness (P3) mm	distance nozzle-electrode (P4) mm	inlet-outlet angle (P5) °	Flow rate (P6) mL/min
Low level	0.1	0.05	0.1	0.1	10	1
High level	0.5	1	1	0.5	80	5

Table 3.1 Values of the low and high levels of the parameters varied in the sensitivity studies. The definition of the parameters is in figure 3.1.

outlets, the distance between the inlet and the electrode, the angle of the outlets and the input flow rate (see fig 3.1).

In a second part, after identifying the most influencing parameters, we performed an in-dept study using CFD simulations with a greater number of values for each one of these impacting parameters to explore more systematically their influence.

We then used the results from the in-depth study along side with the theoretical equations of velocity at the stagnation region to propose semi-empirical formulas that predict mass transport coefficient and shear stress at the electrode.

Finally, we chose a cell with high and uniform mass transport coefficient (*homogeneity* > 90%) and built it by 3D printing. We then used it in hydrodynamic voltammetry experiment of ferricyanide reduction (1.6) to validate our formulas. It is important to have these formulas since we can't afford to make a simulation for every single possibility cell/flow rate combinations.

Before passing to section 3.6 that includes the paper, I will start by introducing a brief background about the CFD simulation and the quantities that we used for characterizing

the performance of the cell, including mass transport, shear stress and pressure drop. I will also define the terminology necessary to understand the fundamental concept of the DoE approach, that we used in the first part of the study.

3.1 Numerical and physical model

Numerical simulations were performed using the commercial finite volume code Starccm⁺ from CD Adapco. As detailed in chapter 2, CFD have been largely used to address hydrodynamics and transport phenomena in electrochemical systems [94, 106, 107]. In our study, using Starccm⁺ allowed us to test easily different geometries and compute rapidly many simulations to study the impact of each design's parameters.

Starccm⁺ is based on finite volume method (FVM) [177], which has been used successfully for different laminar fluid heat and mass transport simulation and proved particularly useful for studying hydrodynamic electrodes such as in the case of RDEs and jet electrodes [161, 178, 179]. The FVM method consists in numerically solving partial differential equations over a defined domain. In our study, they are the Navier-Stokes equations (conservation of momentum (equation (2.4)) and mass (equation (2.5)) coupled with transport equation of a scalar, which is temperature in heat transfer and species concentration in mass transfer (equation (1.14)). The studied domain is subdivided into small cells, which are the finite volumes in which values such as velocity, flux...are assumed to be uniform.

Conservation equations are integrated within each volume element associated with boundary conditions on the limits of the domain. This leads to a set of linear algebraic equations where unknowns are the values of the velocity, pressure and the transported scalar, which is in our case the species concentration. The total number of unknowns in each equation system corresponds to the number of volumes in the grid.

The equations are solved using a segregated flow solver based on algebraic iterative methods ([see link](#)). One of the main advantage of Starccm⁺ is its ability to easily parallelize the computations on many processors. It offers a massive gain in calculation's time by cutting the mesh ¹ in equal parts. Each of these parts is computed by a processor or a core of processor.

Boundary conditions and the mesh properties that were used in our simulations are explained in details in section 3.7 in fig.S1 and fig.S2.

3.2 From 3D to 2D axis symmetric

The model that was used in the previous study was 3D and it was validated experimentally [78]. However, since the mesh density is high next to the electrode where we have a gradient of concentration, the time of calculations is long (almost 12 hours using 30 parallel cores). So, in order to decrease the computation time and utilize a better refined

¹A mesh divides a geometry into many elements or cells of small volumes

mesh that allows to get much smoother data, we used a 2D axisymmetric model (mesh size 10 times smaller and calculation time is about 4 h per 30 PC.) We show in section 3.7. S2 (and in figure S3) that the two models predict the same flux within less than 10% for values of electrode's radius between 0 and at least the value of the inlet radius at different velocities for the previously printed geometry.

3.3 Simulation's results and studied quantities

From each simulation, a file of raw data is exported. This file contains the properties of all the finite volumes at the surface of the electrode with the position and all the quantities that we are interesting in. These quantities are then analysed depending on our objectives.

Rather than simulating several electrode sizes (the region in which the concentration is set to be 0), we have chosen to simulate only a single large value for the electrode radius, and change the effective electrode radius r_{elec} by just considering the studied quantities within the $r \leq r_{elec}$ region. This allows for a continuous variation of the effective electrode size with the results of a single simulation.

3.3.1 Local and average mass transport

From each simulation, we characterised the amount of mass transport to the electrode surface by an average value of the mass transport coefficient m_{avg} which was computed as following:

$$m_{avg} = \frac{\sum m_i A_f}{\sum A_f} \quad (3.1)$$

where m_i is the cell's face value of mass transport coefficient (which represents the local mass transport coefficient) and A_f is the face area. Starccm⁺ reports transport in terms of mass flux J_m , and so in order to get the local mass transport coefficient, we had to divide the simulated mass flux J by the density:

$$m_i = \frac{J_m}{\rho(C^* - C^0)} \quad (3.2)$$

in which ρ is the density of water, C^* and C^0 are respectively the dimensionless concentrations at the bulk and at the electrode. Their values are set as boundary conditions: $C^* = 1$ and $C^0 = 0$.

The non homogeneity of mass transport coefficient H_m was calculated as following:

$$H_m = \frac{m_{max} - m_{min}}{m_{avg}} \quad (3.3)$$

with m_{max} and m_{min} are respectively the maximum and the minimum values of the local mass transport coefficient.

3.3.2 Shear Stress

Shear stress τ_w at the electrode is extracted directly from the fluid flow simulation. However, since it depends on the radial position (r) at the electrode (not constant), to validate our formula, we compared the slope (a') from eq (3.4) where this equation can be written as:

$$\tau = a'r \quad (3.4)$$

to the one computed from the simulations using the following expression:

$$a' = \frac{1}{r} \frac{\sum \tau_i A_f}{\sum A_f} \quad (3.5)$$

3.3.3 Pressure drop

Pressure drop ΔP within the cell was characterised by simply computing the difference between the value of the pressure at the inlet P_{in} and the one at the outlet P_{out} :

$$\Delta P = P_{in} - P_{out} \quad (3.6)$$

3.4 Design of experiment

As I mentioned in the beginning of this chapter, we used design of experiments (DoE) approach to systematically study the influence of six parameters on mass transport, shear stress and pressure drop in the cell.

DoE is a methodology that is based on the process of planning, designing and analysing the experiments or the simulations in order to effectively and efficiently draw valid conclusions. This approach can be applied to research or industry in different disciplines from the moment we look for a relationship between the output y and the key input variables x_1, \dots, x_n (or factors) [180].

$$y = f(x_1, \dots, x_n) \quad (3.7)$$

Performing DoE requires to intentionally and systematically perturb input variables then observe the impact in the output. In this manner, one can identify and classify the most impacting input variables and the non influencing ones [181]. In our study, input variables are referred to as parameters and outputs as responses.

So basically, experiments or simulations are run at different parameter's values, called levels. Each run of an experiment or a simulation involves a combination of the levels of the investigated parameters. When there is an important number of parameters (k) to investigate, it is difficult to use many levels (F) because the number of the experiments or

simulations that should be conducted would be very high (F^k), in this sense, the two level 2^k factorial design proved to be a very powerful tool as it provides the smallest number of runs with which the impact of all the k parameters can be studied [182].

In our numerical studies, since there are many parameters to explore and each simulation requires about 4 h per 30 PC, we chose to use a full factorial design with 6 parameters (described in details in section (3.6)) and 2 levels each. We basically limited the variations of each parameter between two limits. The lower limit is the low level and the upper bound is the high level. Then, all combinations were performed by running 64 simulations.

3.5 DoE data analysis

3.5.1 Determining the main effects of factors

A main effect is the single influence of each parameter on the average response value, it can be determined using the expression:

$$E_f = \bar{F}_{(+1)} - \bar{F}_{(-1)} \quad (3.8)$$

Where: $\bar{F}_{(+1)}$ is the average response at high level of a factor and $\bar{F}_{(-1)}$ is the average response at low level of a factor.

The sign of a main effect informs us about the direction of the effect (ex: a negative main effect means that by increasing the value of the parameter, the average response value decreases). The magnitude informs us about the impact of the parameter (The greater the effect (in absolute value), the more impact the parameter has on the response) [181].

3.5.2 Determining the interaction effects

The interaction between two parameters (P1 and P2) can be computed using the following equation:

$$I_{P1,P2} = \frac{1}{2} \left(E_{(P1,P2)(+1)} - E_{(P1,P2)(-1)} \right) \quad (3.9)$$

where $E_{(P1,P2)(+1)}$ is the effect when parameters P1 and P2 have high or low levels together, and $E_{(P1,P2)(-1)}$ is the effect when and they have opposite levels [181].

3.6 Optimizing the mass transport of wall-tube electrodes for protein film electrochemistry

This section includes the text of the paper that we have recently published in light of the study that was conducted to improve mass transport in the first prototype.



ELSEVIER

Contents lists available at ScienceDirect

Electrochimica Acta

journal homepage: www.elsevier.com/locate/electacta

Optimizing the mass transport of wall-tube electrodes for protein film electrochemistry

Asmaa Hadj Ahmed^{a,b}, Jean-Vincent Daurelle^b, Vincent Fourmond^{a,*}^a Aix-Marseille Université, CNRS, BIP UMR 7281, 31 Chemin J. AIGUIER, CS70071, Marseille Cedex 20 F-13402, France^b Laboratoire IUSTI (UMR AMU-CNRS 7343) Polytech Marseille, Dpt Mécanique Energétique (ME), Technopôle de Chateau Gombert, 5 rue Enrico Fermi, Marseille cedex 13 13453, France

ARTICLE INFO

Article history:

Received 29 July 2021

Revised 29 October 2021

Accepted 29 October 2021

Available online 7 November 2021

Keywords:

Hydrodynamic electrode

Wall-tube

Computational fluid dynamics

Protein film electrochemistry

ABSTRACT

Protein Film Electrochemistry (PFE) is a technique in which an enzyme is directly wired to an electrode and its catalytic turnover rate is measured under the form of an electrical current. This technique has proved useful for the study of a number of enzymes, but requires fast transport of the enzymatic substrate towards the electrode. In a previous work (Fadel *et al.*, *Phys. Chem. Chem. Phys.*, 2019, **21**, 12360), we have proposed a new design based on the wall-tube electrode that provides better transport than the rotating disc electrode, which is usually employed for PFE studies. In the present work, we use computational fluid dynamics to explore the effects of the various parameters of the cell, and propose a semi-empirical formula suitable to predict the mass-transport coefficient and the wall shear stress on the electrode. We use a 3D-printed cell to experimentally validate our predictions.

© 2021 Elsevier Ltd. All rights reserved.

1. Introduction

Protein Film Electrochemistry (PFE) is an electrochemical technique that is used for studying the mechanism of redox enzymes. It consists in immobilizing a film of enzymes on an electrode in a configuration where the electron transfer is direct, and measuring the response in current to changes in conditions [1,2]. The current generated from the exchange of electrons between the enzymes and the electrode is proportional to the turnover rate of the enzyme, which makes it possible to learn about various aspects of the reactivity of the immobilized enzyme [3–5]. As the enzymatic substrate is consumed at the electrode by the catalytic reaction, PFE requires fast transport of the substrate towards the electrode. Sometimes, the enzymatic reaction is slow enough that passive diffusion suffices [6]; however, most enzymes require faster transport, which is usually provided by using a rotating disc electrode (RDE) as working electrode [7]. However, our group has recently reached a limitation of the RDE setup while working on CO dehydrogenases, the enzymes which catalyze the reversible oxidation of CO to CO₂ [8]: these enzymes are so fast that even at the highest practical rotation rates, mass-transport of CO is limiting [9,10], which greatly complicates the study of this enzyme.

To overcome this limitation, we have chosen to design a new electrochemical cell with improved transport properties. The mass transport should be as homogeneous as possible, to avoid the presence of heterogeneity of substrate concentration on the electrode, which would greatly complicate the studies as the enzymatic response is highly non-linear in function of the substrate concentration. This property is known as “uniform accessibility” [11]. Moreover, since the cell will be used by immobilizing enzymes on the surface of the working electrode, a particular interest should be given to the forces applied by the fluid at the surface (the shear stress) since it could be one of the main reasons for the desorption of the film of enzyme [12,13]. Jet electrodes, in which the flow impinges normally from an inlet toward a disk electrode [14], are good candidates for solving the transport limitation since they ensure high and controllable mass transport [15]. The jet electrodes can be divided into two sub-types depending on the size of the electrode with respect to the size of the inlet: the “wall jet” configuration [16], in which the diameter of the inlet is smaller than the one of the electrode, which is widely applied for electrochemical detection in liquid chromatography [17,18], and the “wall tube” configuration [19], in which the electrode is smaller than the inlet. Only the latter provides uniform accessibility [11,20].

After an initial screening of a number of geometries using computational fluid dynamics, we have recently proposed a design based on wall-tube electrodes [21], which provides a factor-of-three improvement with respect to the classical RDE setup (assuming a rotation rate of 5000 rpm). However, in our previous

* Corresponding author.

E-mail addresses: jean-vincent.daurelle@univ-amu.fr (J.-V. Daurelle), vincent.fourmond@imm.cnrs.fr (V. Fourmond).

work, we relied only on computational fluid dynamics simulations to predict the mass transport in given conditions. This contrasts with the ease of use of the RDE, for which a reliable analytical formula is available for predicting the mass transfer properties [22]. Hydrodynamics in impinging jets have been addressed by many studies in mass and in heat transfer [23,24]. Homann and coworkers developed a mathematical solution to describe the boundary layer flow in the stagnation region of a uniform flowing field on an infinite plate [25]. This solution was extended to the case of a uniform impinging jet, where it was proved that a boundary layer of a constant thickness is present in the stagnation region. Chia and coworkers demonstrated that the mass transfer rate at the impinging surface is relatively uniform in the case of wall-tube electrodes [26]. Semi-empirical solutions of mass transport in a uniform impinging jet were developed in previous studies [11,27–29] but they were limited to certain configurations. In spite of the amount of studies about the mass transport in jet electrodes, very few addressed shear stress.

In this work, we have developed semi-empirical formulas suitable to predict the mass-transport properties and the shear stress for wall-tube cells such as the one we have previously proposed [21]. We have used an approach based on computational fluid dynamics, using first a systematic sensitivity study to determine the most influencing parameters, and then focusing on them to propose an analytical formula that reproduces our data within 10%. We then demonstrate the validity of our formulas by verifying them experimentally using the reduction of ferricyanide in a 3D-printed cell.

2. Results

Figure 1 represents a schematic view of the experimental setup, similar to the one we have used in our previous work [21]. The fluid comes through the inlet in the center of the scheme (orange downward arrow), impinges on the working electrode (the gray area at the bottom) and is evacuated via symmetric outlets that are initially inclined with respect to the vertical axis (blue upward arrows). The reference and counter electrodes are near the working

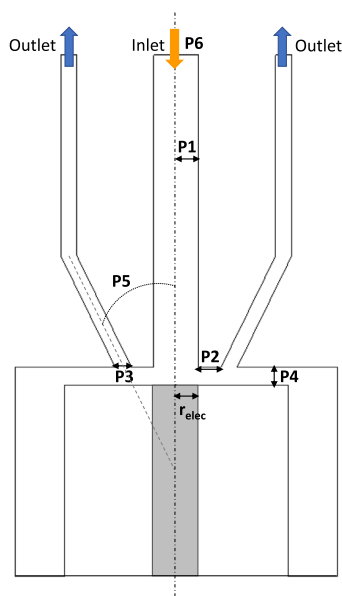


Fig. 1. Schematic representation of the geometry of the cell, indicating the 6 parameters varied in the systematic approach. The detailed meaning and values of the parameters are given in Table 1.

electrode (they are not represented in Fig. 1). The cell is designed in two parts, one with the inlet and outlets, and the other with the electrodes. For more detailed information, see ref. [21].

Numerical simulations were performed using commercial finite volumes modelling package STAR-CCM+ from CD Adapco to study the flow and transport properties of the cells in silico. We used a physical model that is based on a laminar incompressible flow at steady state regime in a 2D axis symmetric domain with a mesh of a base size of 50 μm . The size of the mesh cells decrease when approaching the working electrode so we can properly model the strong gradient of concentration in this zone (diffusion layer). The boundary conditions that were used are as following: we imposed a given velocity and a fixed concentration in the inlet of the cell, a split value condition at the outlets, a non slip condition on the walls. At the working electrode, we assumed an infinitely fast catalytic reaction that consumes all the reaction's substrate, so its concentration is zero at the surface of the electrode. More details about the meshing and the boundary conditions can be found in supplementary section S1.

These simulations were used to compute the velocity profiles in order to determine the value of the wall shear-stress at the electrode, but, most importantly, to compute the flux of electroactive species towards the electrode, in order to determine the mass-transport coefficient m , defined by:

$$j = m \times (c(\infty) - c(0)) \quad (1)$$

in which j is the flux of species at the electrode, $c(\infty)$ the concentration of species in the upstream flow and $c(0)$ the concentration of species at the electrode (in our case, $c(0) = 0$).

In contrast to our previous work [21], we simplified the 3D design into a 2D design with a rotational invariance, which provided both finer grained results, less discretization artifacts, and faster computation time. We show in supplementary section S2 (and figure S3) that the two models predict the same flux within less than 10% for values of r between 0 and at least the value of the inlet radius.

2.1. Sensitivity study

In a first part, we studied the influence of the design parameters of the setup on the properties of the cell. We chose to focus on six parameters (Fig. 1): P1, the inlet radius, P2, the distance between the center of the cell and the center of the outlets, P3, the diameter of the outlets, P4, the distance between the inlet and the electrode, P5, the angle of the outlets, and P6, the input flow rate. The electrode radius plays also a very important role in the properties of the setup, but as it can be varied at will by just changing the size of the region in which the flux is considered (see below), we haven't included it as a parameter.

We used a design of experiments approach to systematically study the influence of these six parameters on the mass-transport properties of the cell. We used a full-factorial design with two levels [30], which consists in defining a "low" and a "high" level for all the parameters and running simulations for all the possibilities (here, $2^6 = 64$ combinations). For the levels, we used values that correspond to the limits of what we could experimentally build (see Table 1).

We ran the 64 simulations, extracted the mass-transport coefficient (Eq. (1)) and applied the statistical treatment described in ref. [30]. The results of this treatment are "effects" for each parameter (and combination of parameters), which are the difference between the average values of all the "high level" simulations and the average values of the "low level" simulations. The greater the effect (in absolute value), the more impact the parameter has on the mass transport. Table 2 lists all the single-parameter effects. It shows that, out of the six parameters, only three have a significant

Table 1

Values of the low and high levels of the parameters varied in the sensitivity studies. The definition of the parameters is in Fig. 1.

Parameter	Inlet radius (P1) mm	Inlet-outlet distance (P2) mm	Outlet thickness (P3) mm	Nozzle-electrode distance (P4) mm	Inlet-outlet angle (P5) °	Flow rate (P6) mL/min
Low level	0.1	0.05	0.1	0.1	10	1
High level	0.5	1	1	0.5	80	5

Table 2

The single effects of all parameters on the simulated mass transport coefficient from the sensitivity study for $r_{elect} = 0.1$ mm. Average is the average of the mass-transport coefficient over all the 64 simulations. The list of all the effects including multi-parameter changes is found in supplementary table S1 (section S3).

Parameters	Effects (mm.s ⁻¹)
Inlet radius (P1)	-1.26953
Inlet-outlet distance (P2)	0.00194
Outlet thickness (P3)	0.00509
Nozzle-electrode distance (P4)	-0.11021
Inlet-outlet angle (P5)	-0.00073
Flow rate (P6)	0.58171
Average	0.73959

influence: P1, P4 and P6, respectively the inlet radius, the inlet-to-electrode distance and the flow rate (the full list of effects, including the effect of jointly changing two or more parameters can be found in supplementary Table S1, section S3). The inlet radius has a strong negative effect, the flow rate a slightly smaller positive effect, and the inlet-electrode distance has about 10 times less effect as the inlet radius. The effects of the other parameters, are at least one order of magnitude smaller than that of the inlet-electrode distance. These results are in line with other works, which found that the inlet diameter, the flow rate and the distance between inlet and electrode were the most important parameters [16,29].

2.2. Derivation of semi-empirical formulas

In a second step, we proceeded to propose semi-empirical formulas to predict the values of the mass-transport coefficient and the wall shear-stress, restricting ourselves to the dependence on the most influencing parameters determined in the first step.

Theoretical background: the hydrodynamic constant We consider a stationary incompressible flow. According to Homann [25], the axial (v) and the radial (u) velocities in the stagnation region can be written under the following forms:

$$u = ar\phi'(\eta) \quad (2a)$$

$$v = -2\sqrt{av}\phi(\eta) \quad (2b)$$

in which a is a constant, called the "hydrodynamic constant" (of dimension the reciprocal of time), η is the dimensionless axial coordinate, and $\phi(\eta)$ is a function. η is defined as:

$$\eta = z\sqrt{a/\nu} \quad (3)$$

where ν is the kinematic viscosity.

Frossling proposed a Taylor expansion for the function $\phi(\eta)$ [31]. For the purposes of this article, we have truncated the expansion to its first term[29]:

$$\phi(\eta) = 0.656 \times \eta^2 \quad (4)$$

This expression is very general since it has been applied to wall-jet cells [29] but it is also valid in the case of the rotating disc

electrode. We first demonstrate that the knowledge of the value of a is sufficient to determine the mass-transport coefficient and the shear stress; we then focus on extracting the values of a from the simulations and deriving an empirical formula for the prediction of a . Note that the actual value of the coefficient in equation (4) has little importance here, since changing the coefficient is equivalent to changing the value of a ; we have used 0.656 to be consistent with previous studies [31].

We now compute the concentration profile c of the electroactive species in the solution. The electroactive species is consumed at the electrode, with a rate supposed to be sufficiently fast that $c = 0$ at the electrode surface. Similarly to what has been done before [29], we assume that the concentration is independent of the radial coordinate, so that c is only a function of η . Under this hypothesis, and using the expression of the velocities in (2), the steady-state convection-diffusion equation for c can be expressed as:

$$\frac{d^2c}{d\eta^2} + 2\mathcal{S}\phi(\eta)\frac{dc}{d\eta} = 0 \quad (5)$$

where we have introduced the Schmidt number,

$$\mathcal{S} = \nu/D \quad (6)$$

Double integration of (5) yields:

$$\frac{c(\infty) - c(0)}{\kappa_0} = \int_0^\infty \exp(-2\mathcal{S}\Phi(\eta))d\eta \quad (7)$$

in which κ_0 is an integration constant (the value of the first derivative of c at 0), $c(0)$ is the concentration at the electrode, $c(\infty)$ at a large distance from the electrode (in the bulk), and Φ is a primitive of ϕ defined by:

$$\Phi(\eta) = \int_0^\eta \phi(\eta')d\eta' \quad (8)$$

Equation (1) for the mass-transport coefficient m can be rewritten thus:

$$D\frac{dc}{dz} = m \times (c(\infty) - c(0)) \quad (9)$$

Integrating of (7) using the expression of $\phi(\eta)$ given in (4) and injecting the result into Eq. (9) yields:

$$m = \beta a^{1/2} D^{2/3} \nu^{-1/6} \quad (10)$$

where $\beta = 0.85002$. Note that Eq. (10) is formally identical to the equation giving the mass transport coefficient for a rotating disc electrode, if one uses $a = 0.533 \times \omega$, in which ω is the angular velocity of the RDE.

The wall shear stress τ_w is defined as:

$$\tau_w = \rho\nu \times \left. \frac{du}{dz} \right|_{z=0} \quad (11)$$

Using the expressions of u and $\phi(\eta)$ from Eqs. (2) and (4), we obtain:

$$\tau_w = 1.312 \times \rho\nu^{1/2} a^{3/2} r \quad (12)$$

Equations (12) and (10) show that it is possible to deduce m and τ_w from the value of the hydrodynamic constant a .

Determination of the hydrodynamic constant as a function of the parameters

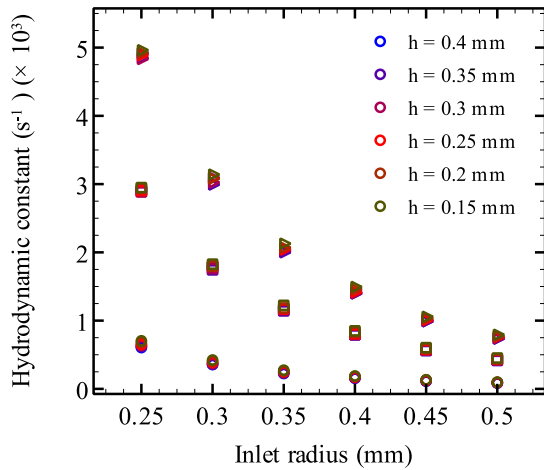


Fig. 2. Values of the hydrodynamic constant a determined from the simulations for the 108 combinations of parameters from Table 3, as a function of the radius of the inlet, r_{jet} . The different symbol shapes correspond to different values of Q_v : 1 mL/min for circles, 5 mL/min for squares and 10 mL/min for triangles. The different values of h are color-coded, as indicated in the graph itself. The other parameters were: distance inlet-outlet ($P2 = 1$ mm), outlet thickness ($P3 = 0.36$ mm), inlet-outlet angle ($P5 = 26^\circ$). The value of the electrode radius has no influence on the hydrodynamic parameters.

Table 3

Values of the different parameters used for the determination of the hydrodynamic constant. All the $6 \times 6 \times 3 = 108$ combinations were used.

Inlet radius r_{jet} (mm)	Inlet-electrode distance h (mm)	Inlet flow rate Q_v (mL/min)
0.25	0.15	1
0.30	0.20	5
0.35	0.25	10
0.40	0.30	
0.45	0.35	
0.5	0.40	

With the aim of determining the dependence of the hydrodynamic constant a on the flow rate Q_v , the inlet diameter r_{jet} and h the distance nozzle-electrode, we ran a series of $6 \times 6 \times 3 = 108$ simulations with all the possible combinations of the parameter values listed in Table 3. For all these simulations, we have extracted the value of a by fitting either Eq. (2a) or (2b) to the values of the velocities in a neighbourhood of the electrode (see supplementary figures S4 and S5 in supplementary section S4 for more information). Fig. 2 shows the 108 values of a , plotted as a function of the inlet radius r_{jet} .

The data show a clear decrease of a as r_{jet} increases, along with a strong increase as Q_v increases (the different values of Q_v are distinguished by the shape of the points). The dependence on h is less marked, but it is nevertheless visible that a decrease in h leads to a slight increase in a .

To remove the largest part of the influence of the parameters on a , we have worked on a dimensionless hydrodynamic constant a^* defined this way:

$$a^* = \frac{a \pi r_{jet}^3}{Q_v} \quad (13)$$

We consider here that the hydrodynamic constant only depends on four dimensional parameters: r_{jet} , Q_v , h , and the kinematic viscosity ν , that have two independent dimensions in total (time and distance). The π theorem therefore states that it can be expressed as a function of two independent dimensionless parameters. We

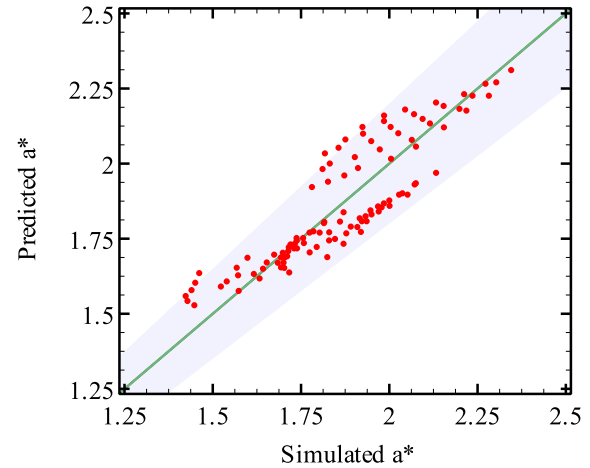


Fig. 3. Values of a^* predicted from Eq. (15) as a function of the value of a^* determined from the simulations. The line corresponds to $y = x$. The shaded region corresponds to $y = x \times (1 \pm 0.1)$.

have chosen the following:

$$\alpha_1 = \frac{r_{jet}}{h} \quad (14)$$

$$\alpha_2 = \frac{Q_v}{\nu h}$$

We sought an approximation for a^* in the form of a simple power law:

$$a^* = \sigma \times \alpha_1^{\beta_1} \times \alpha_2^{\beta_2} \quad (15)$$

in which σ , β_1 and β_2 are constants to determine. We used a simple systematic search to find the values of σ , β_1 and β_2 that yield the minimum root mean squared difference between the predicted and measured values of a^* . We found:

$$\sigma = 3.04993, \beta_1 = 0.1685, \beta_2 = -0.0995 \quad (16)$$

Fig. 3 represents the values of the a^* predicted from Eq. (15) with the coefficients in (16) as a function of the values of a^* determined from the simulations. The data show that all the points from the simulations lie in the 10% region on either side of the $y = x$ line, showing that the formula can predict hydrodynamic constants with a high accuracy.

Expressions for the mass-transport coefficient and the shear stress Substituting (15) back into Eqs. (10) and (12) yields the following expressions:

$$m = 0.83753D^{2/3}\nu^{-0.11692}Q_v^{0.45025}h^{-0.0345}r_{jet}^{-1.41575} \quad (17a)$$

$$\tau_w = 1.255\rho\nu^{0.64925}Q_v^{1.35075}h^{-0.1035}r_{jet}^{-4.24725}r \quad (17b)$$

Figure 4 and supplementary figure S6 show that the above expressions correctly predict the values of m and of τ_w deduced from the simulations. While this is not surprising, considering that the values of m , τ_w , and a are all deduced from the same velocity profiles, the quality of the predictions confirm the derivations above, and show that the semi-empirical formulas (17) reliably predict the results of our 2D simulations. The dependency on a of Eq. (10) and (12) imply that a 10 % error on a corresponds to a 5 % error on m and a 15 % error on τ_w .

2.3. Homogeneity of the mass transport

For the cell to be used for electrochemical studies of enzymes, it is important that the flux is homogeneous, so that the concentration of the enzymatic substrate at the electrode is homogeneous

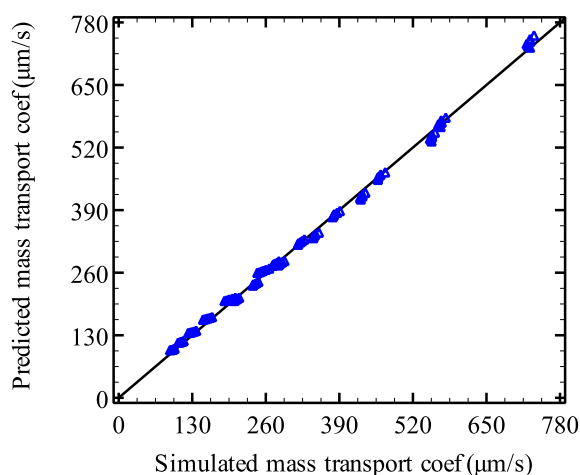


Fig. 4. Comparison between simulated mass transport coefficient and the predicted one from equation (17) for the 108 simulations.

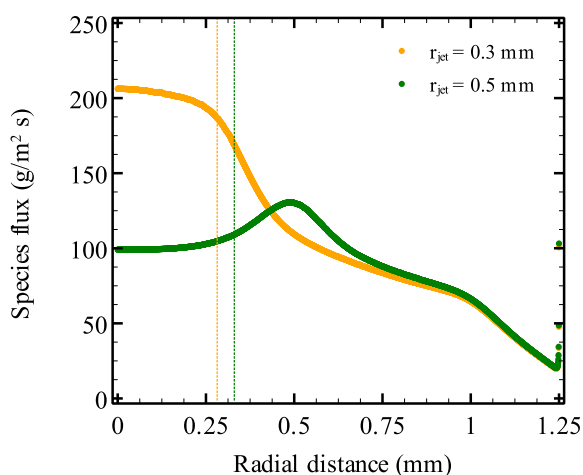


Fig. 5. Simulated mass flux profiles at the electrode as a function of the radial distance from the center of the electrode for two geometries with different inlet radius at the same flow rate (1 mL/min) where the radius of the electrode is $r_{elec} = 1.25$ mm: the curve in orange represents the mass flux where $r_{jet} = 0.3$ mm and $h = 0.15$ mm; the curve in green represents the mass flux where $r_{jet} = 0.5$ mm and $h = 0.15$ mm; the dotted vertical lines represent the limits where the non homogeneity of species flux is below 10%. (For interpretation of the references to colour in this figure legend, the reader is referred to the web version of this article.)

[21]. In the simulations, we have used a very large electrode surface ($r_{elec} = 1.25$ mm) over which we assumed $c = 0$. This made it possible to systematically probe the flux over a large surface and determine the maximum radius of the electrode which receives a homogeneous flux. We assume that electrode parts further away from the axis cannot influence the flux in electrode parts closer to the axis. This assumption is compatible with the direction of the flow, since it seems very unlikely that consumption of the electroactive species further downstream has any influence on the concentration of species upstream. We have verified that this is the case in supplementary section S5.

Figure 5 shows the flux of species at the electrode as a function of the distance from the axis for two different simulations. The yellow curve (for which $r_{jet} = 0.3$ mm and $h = 0.15$ mm) shows the typical behaviour observed in most of the simulations. The flux hardly changes between $r = 0$, and a certain value, here $r \approx r_{jet} = 0.3$ mm, and it then decreases with r . On the other hand, the green

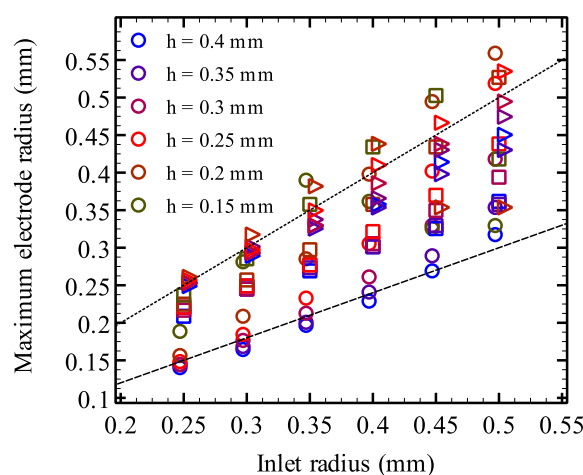


Fig. 6. r_{max} , the maximal value of the electrode radius for which the values of the flux for $0 \leq r \leq r_{max}$ do not vary more than 10% as a function of the inlet radius, for different values of h and Q_v . The values of h can be deduced from the color of the symbol (see the legend inside the graph), while the shape of the symbols correspond to different values of Q_v : $Q_v = 1$ mL/min for the circles, $Q_v = 5$ mL/min for the squares and $Q_v = 10$ mL/min for the triangles. The dot and the dash lines correspond respectively to $y = x$ and $y = 0.6x$.

curve (for $r_{jet} = 0.5$ mm) is less common, but was found in a few simulations, especially at high values of r_{jet}/h ratio. In this case, after a region in which the flux varies little, it first increases significantly around $r = 0.4$ mm $< r_{jet}$, peaking at about $r = r_{jet}$ at a value 30% higher than the value at $r = 0$ before decreasing slowly at higher values of r .

For each of the simulations, we have determined the value r_{max} for which the flux does not vary more than 10% between $r = 0$ and $r = r_{max}$. The values are plotted in Fig. 6 as a function of r_{jet} , and for the different values of h and Q_v used in the simulations. Overall, the points follow a linear relationship as a function of r_{jet} , as is attested by the fact that they mostly lie between the $y = 0.6x$ and $y = x$ lines. In general, increasing the flow rate increases r_{max} : the circles (for which $Q_v = 1$ mL/min) correspond to the lowest values of r_{max} , while the triangles ($Q_v = 10$ mL/min) correspond to the highest values of r_{max} .

However, the individual dependence of r_{max} on r_{jet} can sometimes be more complex, as is attested by data for $h = 0.15$ mm and $Q_v = 1$ mL/min in Fig. 6. For $r_{jet} \leq 0.4$ mm, the value of r_{max} increases with r_{jet} , but for larger values of r_{jet} , the value of r_{max} decreases; this behaviour is related to the occurrence of the “atypical” behaviour discussed above in which the flux increases significantly about $r = r_{jet}$, before decreasing again (green curve in Fig. 5).

From the overall data in Fig. 6, we can conclude that the requirement that the variation in flux (or mass-transport coefficient) remains smaller than 10% is fulfilled when the radius of the electroactive area is smaller than $0.6 \times r_{jet}$.

2.4. Experimental validation

To validate the relevance of the prediction of Eq. (10) in a real experimental setting, we built, using 3D-printing, a cell corresponding to $r_{jet} = 0.3$ mm and $h = 0.35$ mm. We performed cyclic voltammetry of a $K_3Fe(CN)_6$ solution for a number of flow rates. The results are plotted in Fig. 7. Fig. 7(A) shows the raw voltammograms, which show plateaus at low potential that are typical of a transport-limited reduction process. The fluctuations visible are linked to the argon flux necessary to keep the system as anaerobic as possible. From the values of the plateau current, it is possible to

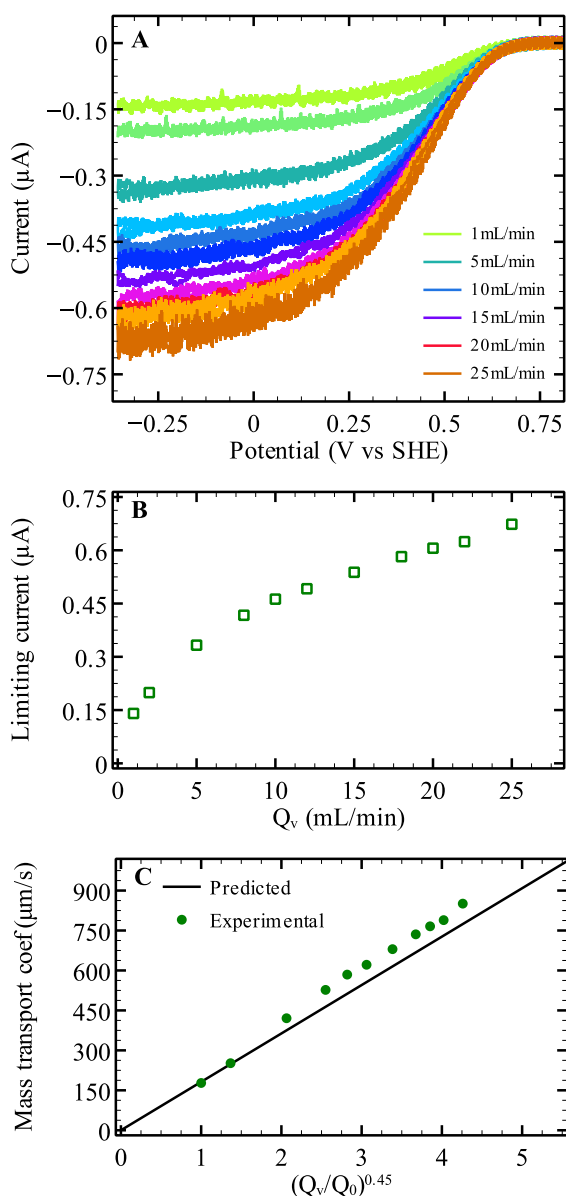


Fig. 7. Experimental validation of the transport properties of one of the promising electrochemical cells ($r_{\text{jet}} = 0.3$ mm; $h = 0.35$ mm): (A) Cyclic voltammetry for the reduction of $\text{Fe}(\text{CN})_6^{3-}$ at a graphite electrode of diameter $100\mu\text{m}$ at $\nu = 100$ $\text{mV}\cdot\text{s}^{-1}$. The experiments were conducted at volume flow rate that ranged from 1 mL/min to 25 mL/min at room temperature, under degassed system with argon. (B) the limiting current (in absolute value) as a function of the flow rate. (C) Comparison of mass transport coefficient ($m = I/nFA$) extracted from the cyclic voltammetry experiments of the reduction of $\text{Fe}(\text{CN})_6^{3-}$ (green circles) with the predicted mass transport coefficient from equation (17) (black line), $Q_v = 1$ mL/min. Conditions: $[\text{Fe}(\text{CN})_6^{3-}] = 1$ mM, electrolyte: 0.5 M NaCl, room temperature. We determined the working electrode's surface to be 8.2×10^{-9} m^2 . (For interpretation of the references to colour in this figure legend, the reader is referred to the web version of this article.)

deduce the mass-transport coefficient. We have plotted it against the power 0.45 of the flow rate in Fig. 7B (circles), along with the prediction of Eq. (10). The agreement is excellent, fully validating the whole approach.

3. Discussion

In this article, we have built upon our previous work, in which we have described a wall-tube cell designed for the stud-

ies of very fast enzymes [21]. Although we demonstrated that the cell was already improving upon the mass-transport properties of the RDE, which is commonly used for studying enzymes [1,2], our previous work relied on CFD simulations for predicting the mass-transport properties of the cell, which is far too time- and resource-consuming for practical uses. Instead, for practical operation of the cell, and fine-tuning of its properties (geometric parameters), analytical formulas are required. The present work arises from attempts to i) validate the previously proposed formulas (or propose new ones) to accurately predict the mass-transport in our configuration; ii) verify the conditions under which the mass transport can be considered homogeneous and iii) propose formulas for predicting the shear stress, which has not been addressed in the literature before. The computation of the shear stress is important because it is likely that excessive shear stress could lead to washing of the enzymatic film [13], which has to be prevented as much as possible.

We used a two step approach to provide semi-empirical formula for predicting both the mass-transport coefficient and the shear stress values. First, with a coarse sensitivity study using a design of experiments approach applied to mass-transport values determined from simulations, we showed that only the flow rate, the jet radius and the distance between the inlet and the electrode have significant influence on the mass transport coefficient. Then, in a second approach, we use finer grained simulations with a greater number of parameter values to explore more systematically the parameter space. We used these data to propose semi-empirical formulas for both the mass-transport coefficient and the shear stress in the system. These formulas were able to reproduce simulated mass-transport coefficients and shear stress values with good accuracy, and were also very accurate to predict the experimental current obtained in a 3D-printed cell (Fig. 7).

Table 4 summarizes some of the formulas available in the literature for the prediction of the mass-transport coefficient in wall-tube or wall-jet geometries, along with the smallest errors, the largest errors and the root-mean-squared deviation between the predicted value of mass transport and that measured on the 108 simulations of the second step of this work. For most of the formulas, the root-mean-squared deviation is in the order of 10% or significantly more, while the root-mean-squared deviation with respect to Eq. (17) is less than 3%. Only the prediction of Chin and Tsang comes reasonably close to our proposition, with less than 5% error in average, and a maximum error not much above that of (17).

We could not find formulas that predict the wall shear stress in wall-jet and wall-tube electrodes in the literature, perhaps because the main objective of the published works is to predict the value of the current that one can obtain from a given experimental setup, but also probably because it is experimentally more challenging to measure the wall shear-stress, and it is hence harder to verify the given formulas experimentally. Rather than using an analytical formula to predict the shear stress, Esteban and coworkers use a combination of Eqs. (10) and (12) to predict the shear stress from an experimentally determined mass-transport coefficient [12], in the context of corrosion studies. Here, we provide an analytical formula for predicting the shear stress. Although we could not validate our predictions for the shear stress experimentally, considering that both the mass-transport coefficient and the shear stress are derived from the same equations, based on the determination of the hydrodynamic constant a , we are confident that a good accuracy in the prediction of experimental mass-transport coefficients is an indication of the quality of the prediction of the shear stress too. It should be noted that, provided the Eqs. (10) and (12) are valid (which is the case for both the wall-tube electrode and the RDE), the shear stress is related to the

Table 4

Standard deviation and maximum deviation of the difference between the predicted and the simulated mass-transport coefficient for the case of the 108 simulations. $g(\mathcal{X})$ is an asymptotic series whose development is: $g(\mathcal{X}) = 1 - 0.084593\mathcal{X}^{-1/3} - 0.0016368\mathcal{X}^{-2/3} - 0.0057398\mathcal{X}^{-1} + 0.0014288\mathcal{X}^{-3/4} + \dots$

Mass transport formula	Flow regime	Minimum error	Maximum error	Deviation	Ref.
$0.4648D^{2/3}\nu^{-1/6}\left(\frac{Q_v}{r_{jet}^3}\right)^{0.5}\left(\frac{h}{r_{jet}}\right)^{-0.057}g(\mathcal{X})$	turbulent	0.202	0.315	0.276	[29]
$0.318D^{2/3}\nu^{-5/12}Q_v^{3/4}d_{jet}^{-1/2}r_{elec}^{-5/4}$	laminar (wall jet)	6.2	26.9	16.2	[27]
$1.2021\frac{D}{d_{jet}}Re^{1/2}\mathcal{X}^{1/3}\left[2.464 - 1.0629\left(\frac{h}{r_{jet}}\right) + 1.5794\left(\frac{h}{2r_{jet}}\right)^2\right]^{1/2}g(\mathcal{X})$	laminar	0.013	0.306	0.135	[28]
$0.194D^{2/3}\nu^{-1/6}\left(\frac{Q_v}{r_{jet}^3}\right)^{0.5}g(\mathcal{X})$	laminar	2.25×10^{-3}	0.158	0.078	[11]
$0.6244D^{2/3}\nu^{-1/6}\left(\frac{Q_v}{r_{jet}^3}\right)^{0.5}\left(\frac{r_{jet}}{h}\right)^{0.054}g(\mathcal{X})$	laminar	1.26×10^{-3}	0.082	0.046	[29]
(17)	laminar	6.99×10^{-5}	0.073	0.029	(this work)

mass-transport coefficient through the following formula:

$$\tau_w = 2.13 \times \frac{\rho \nu r}{D^2} \times m^3 \quad (18)$$

so that the shear stress scales as the cube of the mass transport coefficient. Therefore, the only way to greatly increase the mass-transport coefficient without a significant increase in the shear stress is to decrease the electrode size, since the shear stress is proportional to the distance from the rotational symmetry axis.

An important requirement to conduct protein film electrochemistry studies is the need for uniform accessibility: the mass-transport should be homogeneous across the whole surface of the electrode, so that the concentration of substrate perceived by all the molecules of enzymes is homogeneous. The rule-of-thumb found in the literature is that uniform accessibility is obtained in a wall-jet system when the electrode is smaller than the inlet [12]; this configuration is known as wall-tube. However, our data (Fig. 5) suggests that there can be significant heterogeneity even when the wall-tube condition is satisfied, and that for a more homogeneous mass-transport coefficient, a condition of $r_{electrode} \leq 0.6 \times r_{jet}$ is necessary. Our data also show that, under certain conditions, the center of the electrode does not correspond to the maximum of the mass transport coefficient, but that the transport increases slightly up to the size of the inlet, before decreasing (Fig. 5, green curve). MacPherson and coworkers experimentally observed a similar behaviour on a microjet electrode, which is similar to the setup we propose here, save for the smaller dimensions. Using electrodes significantly smaller than the inlet size, they could use a micropositioning device to map the mass transport coefficient as a function of the position of the electrode, and they also observed a slight increase when moving away from the center of the inlet [32].

Other works have emphasized the presence of recirculation patterns in wall-jet or wall-tube setups, in particular in the so-called “wall-jet” region, in which the radial velocity starts to decrease. These were predicted in some simulations [33], also in the case of the RDE [34], and observed experimentally in the case of the microjet electrode [35]. In the case of our simulations, we could not find traces of recirculation patterns in all the simulations (see for instance supplementary figure S10). Presumably, this is due to the fact that the horizontal flow proceeds in a restricted space of height h comparable or even smaller than the inlet diameter, which leaves little space for recirculation patterns to occur.

Equation (17) shows that there cannot be an “optimal” setup, since the mass-transport coefficient can be made arbitrarily large by decreasing the size of the inlet. A practical setup must therefore be a compromise between the mass-transport capacities obtained at a given flow rate and the practicality of building a cell with a small inlet diameter, and an even smaller electrode diameter. The possibility to make very thin platinum electrodes were exploited by MacPherson and coworkers to build a microjet setup with an electrode size of 25 μ m and a nozzle diameter in the 80 to 120 μ m range, with the highest mass-transport reported

to date with a wall jet system [36]. However, this system requires a horizontal micropositioning device to ensure that the electrode is centered with respect to the inlet. With the application to PFE in mind, larger electrodes will have to be used, because the electrode of choice for PFE studies is the pyrolytic graphite edge electrode [1,2,7], which cannot easily be machined to sizes below 0.4 mm. Together with the practical implications of using 3D-printed parts for the inlet, this sets a reasonable size of the inlet diameter around 0.6 mm, which is what we have used in the experimental validation of Fig. 7. However, the formulas and guidelines proposed in this article are likely valid for even smaller ranges, which means they could be used for much smaller electrodes.

The motivation of this work is to provide faster mass-transport than the setup usually employed for PFE studies, the RDE, as this setup, even used at very high rates, wasn't enough to prevent depletion for studying fast enzymes like the CO dehydrogenase [9]. For both the RDE and the wall-tube, the mass-transport is given by equation (10), with only the value of a changing from one setup to the other. Therefore, the factor of increase of the transport over the RDE is given by:

$$\frac{m_{WT}}{m_{RDE}} = \left(\frac{a_{WT}}{a_{RDE}}\right)^{1/2} = 1.35 \frac{\nu^{0.04975} Q_v^{0.45025}}{h^{0.0345} r_{jet}^{1.41575} \omega^{1/2}} \quad (19)$$

in which the quantities indexed with RDE correspond to the RDE while those indexed with WT refer to the wall-tube electrode. Assuming a reasonable maximum value of 5 krpm for the rotation rate of the RDE, using the values of $r_{jet} = 0.5$ mm and $h = 0.35$ mm and $Q_v = 37$ mL/min as described in our previous work [21] yields the factor of 3 described previously. Using $r_{jet} = 0.3$ mm, the flow rate required for a factor-of-three improvement drops to $Q_v = 10$ mL/min. As was noted above (Eq. (18)), the wall-tube design in itself does not provide an advantage over the RDE with respect to the shear stress, since both setups share the same relationship between mass-transport coefficient and shear-stress. However, while for the RDE, the only possibility for increasing mass-transport is to increase the rotation rate, but practical rates for rotating disc electrodes seldom go above 5krpm. On the contrary, to increase the transport in the case of the wall tube electrode, one can either decrease the jet size or increase the flow rate, which provides more flexibility to achieve high mass transport coefficients.

Credit Author Statement

The authors have all participated in the design of the experiments/simulations, their analysis and the writing of the article.

Declaration of Competing Interest

The authors have no conflict of interest to declare.

Acknowledgements

The authors acknowledge support from CNRS, Aix-Marseille Université, Agence Nationale de la Recherche (ANR-15-CE05-0020, ANR-17-CE11-002), and the Excellence Initiative of Aix-Marseille University - A*MIDEX, a French "Investissements d'Avenir" programme (ANR-11-IDEX-0001-02), and the ANR-DFG project SHIELDS (PL 746/2-1). They also wish to acknowledge expert help from Alain Grossi and Sady Noel in preparing the 3D-printed cell and the electrodes, and Gaëlle Coustillier and Philippe Delaporte from the laboratory "Lasers, Plasmas et Procédés Photoniques" in Marseille for their preparation of graphite samples of very small size, and finally Jérôme Vicente for insightful discussions and comments. AHA and VF are part of FrenchBIC (<http://frenchbic.cnrs.fr>).

Supplementary material

Supplementary material associated with this article can be found, in the online version, at [10.1016/j.electacta.2021.139521](https://doi.org/10.1016/j.electacta.2021.139521)

References

- [1] C. Léger, P. Bertrand, *Chem. Rev.* 108 (2008) 2379–2438.
- [2] V. Fourmond, C. Léger, *Adv. Biochem. Eng. Biotechnol.* 158 (2016) 1–41.
- [3] M. del Barrio, V. Fourmond, *ChemElectroChem* 6 (2019) 4949–4962.
- [4] J. Hirst, *Biochim. Biophys. Acta* 1757 (2006) 225–239.
- [5] F.A. Armstrong, N.A. Belsey, J.A. Cracknell, G. Goldet, A. Parkin, E. Reisner, K.A. Vincent, A.F. Wait, *Chem. Soc. Rev.* 38 (2009) 36–51.
- [6] T. Zeng, S. Leimkühler, U. Wollenberger, V. Fourmond, *J. Am. Chem. Soc.* 139 (2017) 11559–11567.
- [7] F.A. Armstrong, H.A. Heering, J. Hirst, *Chem Soc Rev* 26 (1997) 169–179.
- [8] M. Can, F.A. Armstrong, S.W. Ragsdale, *Chem. Rev.* 114 (2014) 4149–4174.
- [9] M. Merrouch, J. Hadj-Saïd, C. Léger, S. Dementin, V. Fourmond, *Electrochim. Acta* 245 (2017) 1059–1064.
- [10] L. Domnik, M. Merrouch, S. Goetzl, J.-H. Jeoung, C. Léger, S. Dementin, V. Fourmond, H. Dobbek, *Angew. Chem. Int. Ed.* 56 (2017) 15466–15469.
- [11] W.J. Albery, S. Bruckenstein, *J Electroanal Chem Interfacial Electrochem* 144 (1983) 105–112.
- [12] J. Esteban, G. Hickey, M. Orazem, *Corrosion* 46 (1990) 896–901.
- [13] G. Binyamin, A. Heller, *J. Electrochem. Soc.* 146 (1999) 2965.
- [14] S.G. Weber, W.C. Purdy, *Anal. Chem.* 54 (1982) 1757–1764.
- [15] M. Glauert, *J Fluid Mech* 1 (1956) 625–643.
- [16] J. Yamada, H. Matsuda, *J Electroanal Chem Interfacial Electrochem* 44 (1973) 189–198.
- [17] H.M. Elbardsy, E.M. Richter, R.D. Crapnell, M.P. Down, P.G. Gough, T.S. Belal, W. Talaat, H.G. Daabees, C.E. Banks, *Anal. Methods* 12 (2020) 2152–2165.
- [18] B. Fleet, C. Little, *J Chromatogr Sci* 12 (1974) 747–752.
- [19] J.L. Melville, B.A. Coles, R.G. Compton, N. Simjee, J.V. Macpherson, P.R. Unwin, *The Journal of Physical Chemistry B* 107 (2003) 379–386.
- [20] W.J. Albery, *J Electroanal Chem Interfacial Electrochem* 191 (1985) 1–13.
- [21] M. Fadel, J.-V. Daurelle, V. Fourmond, J. Vicente, *PCCP* 21 (2019) 12360–12371.
- [22] B. Levich, *Acta Physicochim USSR*, 17 (1942) 257.
- [23] G.M. Carlomagno, A. Ianaro, *Exp. Therm Fluid Sci.* 58 (2014) 15–35.
- [24] J. Seyed-Yagoobi, *Drying Technol.* 14 (1996) 1173–1196.
- [25] F. Homann, *Forsch. Ing. Wes* 7 (1936) 1.
- [26] C.-J. Chia, F. Giralt, O. Trass, *Industrial & Engineering Chemistry Fundamentals* 16 (1977) 28–35.
- [27] H. Matsuda, J. Yamada, *J Electroanal Chem Interfacial Electrochem* 30 (1971) 261–270.
- [28] M.T. Scholtz, O. Trass, *AIChE J.* 16 (1970) 82–90.
- [29] D.-T. Chin, C.H. Tsang, *J Electrochem Soc* 125 (1978) 1461.
- [30] J. Antony, *Design of experiments for engineers and scientists*, Elsevier, 2014.
- [31] N. Frossling, *Lunds. Univ. Arsskr. NF Avd 2* (1940) 35.
- [32] J.V. Macpherson, M.A. Beeston, P.R. Unwin, *J. Chem. Soc., Faraday Trans. 91* (1995) 899–904.
- [33] J. Melville, N. Simjee, P.R. Unwin, B.A. Coles, R.G. Compton, *J. Phys. Chem. B* 106 (2002) 2690–2698.
- [34] A. Alexiadis, A. Cornelli, M. Dudukovic, *J. Electroanal. Chem.* 669 (2012) 55–66.
- [35] E. Bitziou, N.C. Rudd, M.A. Edwards, P.R. Unwin, *Anal. Chem.* 78 (2006) 1435–1443.
- [36] J.V. Macpherson, S. Marcar, P.R. Unwin, *Anal. Chem.* 66 (1994) 2175–2179.

3.7 Supplementary information

Optimizing the mass transport of wall-tube electrodes for protein film electrochemistry

Supplementary information

Asmaa Hadj-Ahmed, Jean-Vincent Daurelle, Vincent Fourmond

S1 Numerical methods

For the numerical simulations, we used the commercial finite volumes modelling package starccm+ from CD Adapco. The equations used are Navier stocks for momentum balance (eq S1) and continuity equation (eq S2).

$$\rho V \cdot \nabla V = -\nabla(P + \mu(\nabla V + (\nabla V)^T)) \quad (\text{S1})$$

$$\nabla \cdot V = 0 \quad (\text{S2})$$

Where ρ is the density of water, V is the velocity vector, P is the pressure, μ is the dynamic viscosity of water, and T is the matrix transpose operator. The field of study was considered as 2D axisymmetric. Fig S1 shows a scheme of the domain studied with the the boundary conditions that were used.

- Boundary 1: the axis of rotational symmetry.
- Boundary 2: the inlet of the cell, an inlet velocity and passive scalar conditions were used (velocity was a variable and passive scalar=1 (corresponds to the dimensionless concentration)).
- Boundary 3: the outlet of the cell, a split ratio condition was imposed.
- Boundary 4: is the electrode where we set a passive scalar condition (we assumed that the reaction at the electrode is infinite so that the passive scalar = 0 there).
- Boundaries from 5 to 14 are the walls of the cell and are set to have a no slip boundary condition.

The calculations were performed at a steady state flow regime, under laminar flow conditions ($Re < 2000$) with the thermal-physical parameters:

- Dynamic viscosity: $\mu = 8.89 \times 10^{-4}$ Pa.s
- Diffusion coefficient: $D = 1.25 \times 10^{-9}$ m².s⁻¹
- Density: $\rho = 997.561$ Kg.m⁻³

S1.1 Meshing parameters

The meshing models fig S2 that were used are:

- Polyhedral mesher
- Prism layer mesher

With the following parameters:

- The base mesh size is 5×10^{-5} m
- The mesh size of Volume control 1 is 5×10^{-6} m
- The mesh size of Volume control 2 is 5×10^{-7} m

For the 3D meshing model, the base sizes for all volume control were 10 times higher than the ones in 2D axisymmetric.

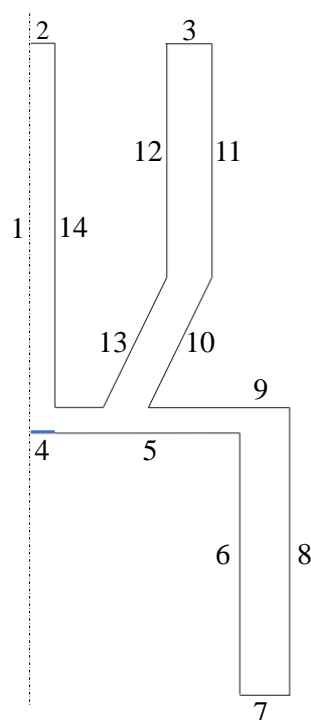


Figure S1: A scheme representing the domain of study and the boundary conditions used. 1: the axis of rotational symmetry; 2: the inlet of the cell; 3: the outlet of the cell; 4: the working electrode ; boundaries from 5 to 14 are the walls

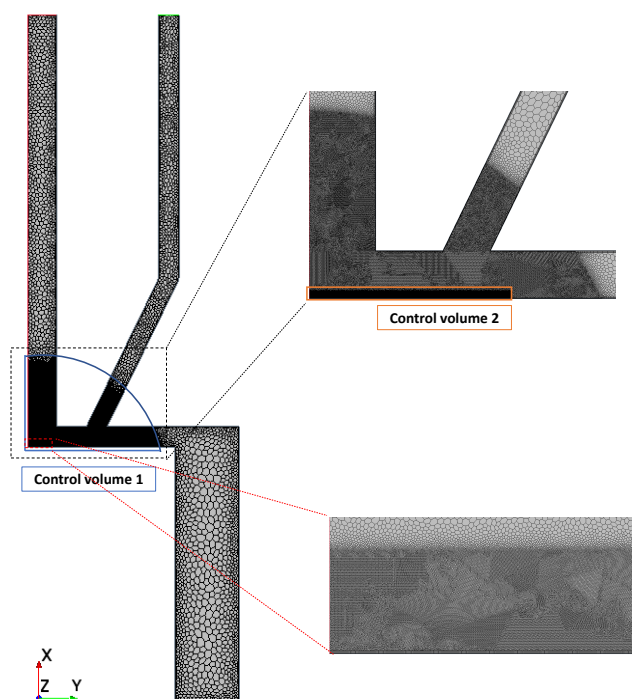


Figure S2: Representation of the mesh used in the 2D axisymmetric model with close ups of the two volume controls where the mesh is more refined compared to the rest of the volume. Volume control 1 : mesh size = 5×10^{-6} m; Volume control 2 : mesh size = 5×10^{-7} m

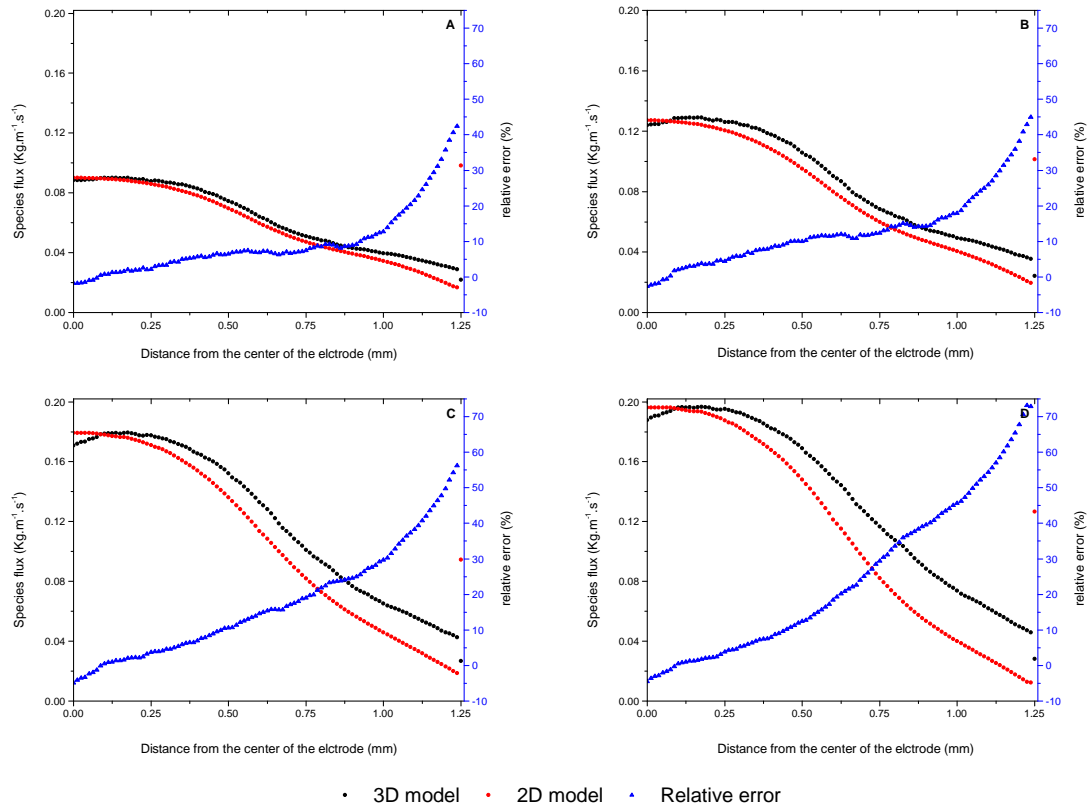


Figure S3: comparison of species flux profiles between 3D and 2D axis symmetry models: the graph represents the local mass flux as a function of the radial distance from the center of the electrode in two models (3D (in black); 2D axis symmetry (in red)) and the relative error (in blue) for four different values of inlet's velocity (A: 0.02 m/s ; B: 0.04 m/s; C: 0.08 m/s ; D: 0.1 m/s)

S2 Comparison between 3D and 2D axis symmetric

The model that was used in the previous study was 3D and it was validated experimentally [1]. However, since the mesh density is high near to the electrode where we have a gradient of concentration, the time of calculations is long (almost 12 hours using 30 parallel cores not including the time of the execution of the mesh). So, in order to decrease the computation time and utilize a better refined mesh, we used a 2D axisymmetric model. The latter was validated by comparing mass flux between the 2D and the 3D model at different velocities for the previously printed geometry, for which the simulations were also validated by the experimental determination of the mass-transport coefficient [1].

Fig S3 shows the comparison of simulated species flux profiles using 3D and 2D axisymmetric (refined mesh) at different inlet velocities. For all the cases, it can be seen that at very small radial distance from the center (below 0.1 mm), the flux is slightly higher in the 2D model with a difference that is lower than 5%. Moving radially outward, the flux becomes more important in the 3D model than in the 2D axisymmetric and the difference between them increases with the distance. For a radial distance of 0.5 mm, which is equal to the radius of the working electrode in the simulated cell, the error is increasing with the velocity however it remains under 10%. For higher distances from the center, the error becomes significant especially for high velocities such as 0.1 m.s^{-1} where it reaches about 75% for $r = 1.25 \text{ mm}$.

For this study, only small radii of the working electrode were taking into consideration since the highest and uniform fluxes are located near to the center and that is what interests us. As shown before, for small electrodes such as $r = 0.5 \text{ mm}$, the difference is not very significant. Therefore, the 2D axisymmetric model can be used for the rest of the study.

S3 The effects of all the parameters on mass transport coefficient from the sensitivity study

Table S1 shows the effects for all the parameters, classified from the least influencing to the most influencing. This is an extension of table 1 in main text.

Parameters	Effects (mm.s ⁻¹)	Parameters	Effects (mm.s ⁻¹)
P1*P2*P3*P5	9.10712×10^{-5}	P1*P3*P6	1.37059×10^{-4}
P1*P2*P3	-2.8814×10^{-4}	P1*P3	4.20184×10^{-4}
P1*P2*P3*P6	4.517×10^{-4}	P1*P2*P3*P5*P6	5.37783×10^{-4}
P2*P3*P4*P6	-6.27015×10^{-5}	P2*P3*P6	-6.79501×10^{-4}
P5	-7.3071×10^{-4}	P1*P2*P3*P4*P6	7.71242×10^{-4}
P1*P3*P5	8.03499×10^{-4}	P2*P3*P4*P5	9.86119×10^{-4}
P2*P3*P4	-0.00111	P2*P3	0.00112
P1*P3*P5*P6	0.0012	P3*P4*P5	0.00123
P3*P4*P5*P6	0.00131	P2*P6	-0.00162
P2*P3*P4*P5*P6	0.00169	P1*P3*P4*P6	0.00185
P1*P2*P3*P4*P5*P6	0.00186	P2	0.00194
P1*P3*P4*P5*P6	0.00199	P5*P6	-0.00208
P3*P5*P6	0.00217	P1*P2*P3*P4*P5	0.00223
P1*P2*P3*P4	0.00226	P1*P3*P4	0.00227
P2*P3*P5*P6	0.00242	P3*P4	0.00261
P3*P4*P6	0.0027	P3*P5	0.00277
P1*P3*P4*P5	0.00284	P4*P5	-0.00292
P4*P5*P6	-0.00375	P2*P3*P5	0.00392
P3*P6	0.00423	P1*P2*P4	-0.00449
P2*P4*P6	-0.00463	P1*P4*P5	-0.00507
P3	0.00509	P1*P2*P5	0.00523
P1*P2*P4*P5	0.00561	P1*P4*P5*P6	-0.00567
P1*P2*P5*P6	0.00575	P1*P2*P4*P5*P6	0.00635
P1*P5*P6	-0.00658	P2*P4	-0.00703
P1*P2*P4*P6	-0.00822	P2*P5*P6	0.00834
P1*P5	-0.00845	P2*P4*P5*P6	0.00861
P2*P4*P5	0.00876	P2*P5	0.01009
P1*P2*P6	-0.01256	P1*P2	-0.01262
P1*P4	0.03213	P4*P6	0.04561
P1*P4*P6	-0.06719	P4	-0.11021
P1*P6	-0.48647	P6	0.58171
P1	-1.26953	Residual	0.73959

Table S1: The effects of all parameters on the simulated mass transport coefficient from the sensitivity study

S4 Computing the hydrodynamic constant from the in-depth simulations

According to Homann [2], the axial (v) and the radial (u) velocities in the stagnation region can be written under the forms:

$$u = ar\phi'(\eta) \quad (\text{S3a})$$

$$v = -2\sqrt{av}\phi(\eta) \quad (\text{S3b})$$

$\phi(\eta)$ can be put under the following form:

$$\phi(\eta) = 0.656 \times \eta^2 \quad (\text{S4})$$

Introducing equation (S4) in (S3a) and in (S3b) yields:

$$u = 2\alpha a^{3/2} v^{-1/2} r z \quad (\text{S5a})$$

$$v = -2\alpha a^{3/2} v^{-1/2} z^2 \quad (\text{S5b})$$

in which $\alpha = 0.656$.

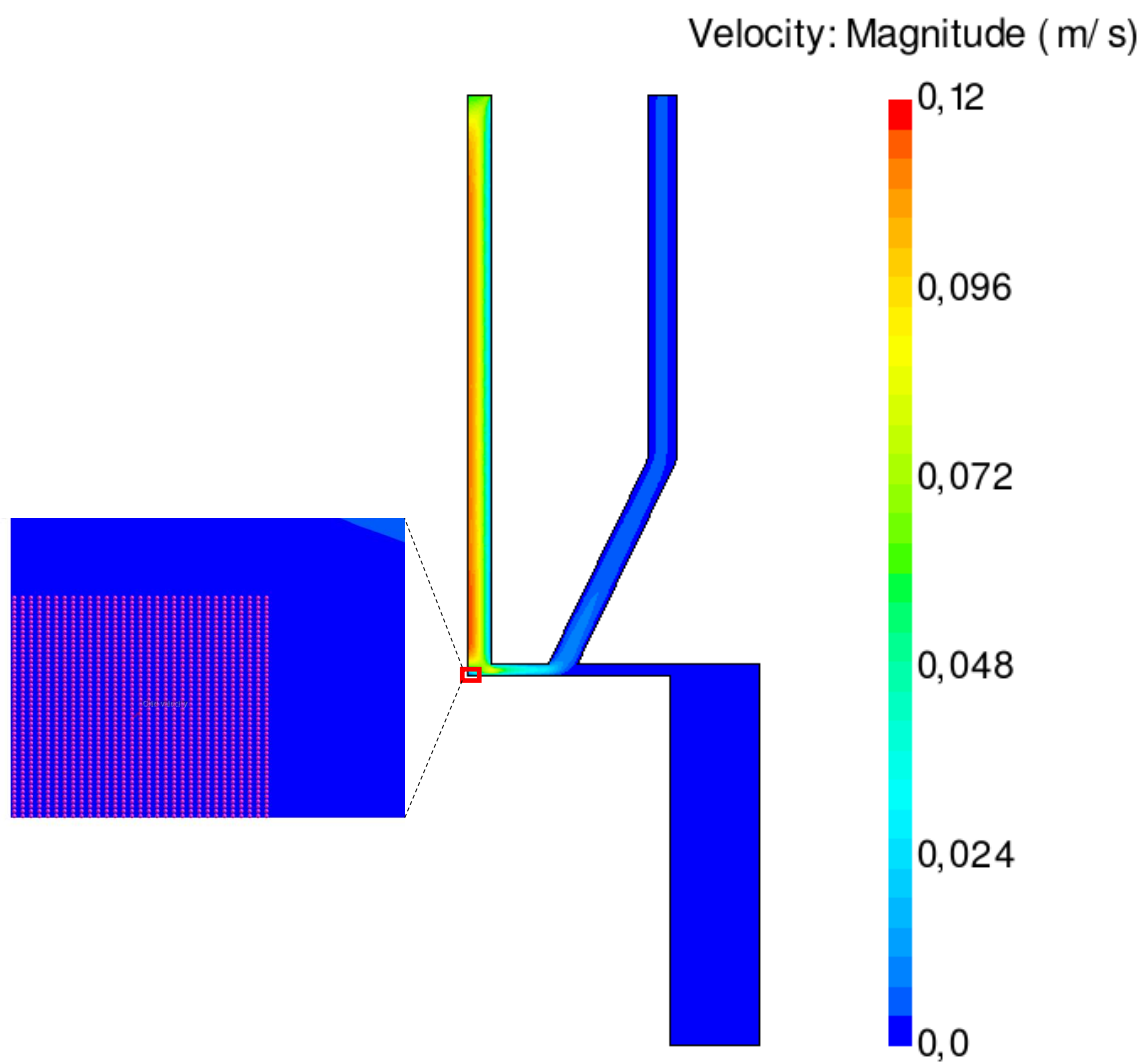


Figure S4: Velocity profile in the jet flow cell for $r_{jet} = 3$ mm, $h = 0.15$ mm and $Q_v = 1$ mL.min⁻¹ and a close up of the stagnation region ($r = 1.3 \times 10^{-5}$ m and $z = 5 \times 10^{-6}$ m) where u and v values were extracted

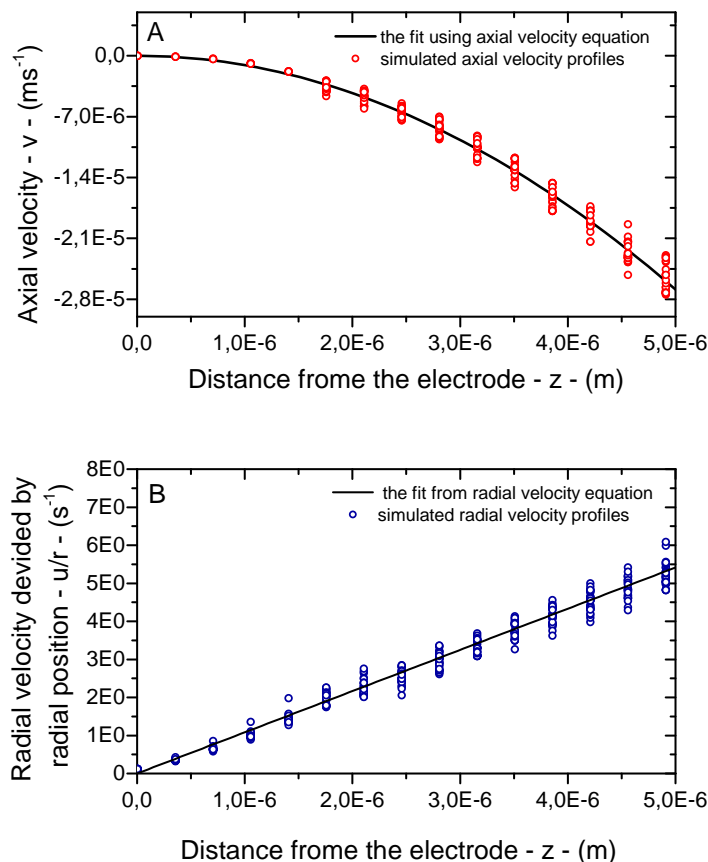


Figure S5: An example of extracting the values of the hydrodynamic constant a from the results of the in-depth simulations. A: axial velocity as a function of the radial distance from the electrode for all the finite volumes in the region $r < 1.3 \times 10^{-5}$ m, $z_{min} < z < z_{min} + 5 \times 10^{-6}$ m for the simulation Opt 72 ($r_{jet} = 0.5$ mm, $h = 0.4$ mm, $Q_v = 1$ mL/min). The green line is a fit of equation (S5b) to the data, which yields a value of $a = 84.25$ s $^{-1}$; B: radial velocity as a function of the radial distance from the electrode for all the finite volumes in the same region and the same conditions as for panel A. The black line is a fit of equation S5a to the data, which yields a value of $a = 84.68$ s $^{-1}$

For each simulation, we extracted the profiles of the axial and the radial velocities as a function of r and z respectively in a small region around the center of the electrode inside the stagnation region (the zoomed area in red frame in red in fig S4).

We determined a by fitting the data to both equations (S5a) and (S5b) as in the example in fig S5. The values of a that were obtained using both equations were almost the same and this can be seen by looking at the relative deviation, which is smaller than 1% for all the simulations (see table S2).

S5 Varying the effective electrode size

Rather than simulating several electrode sizes (the region in which the concentration is forced to be 0), we have chosen to simulate only a single large value for the electrode radius, and change the effective electrode radius r_{elec} by just considering the mass-transport and shear stress of the large electrode within the $r \leq r_{elec}$ region. This allows for a continuous variation of the effective electrode size with the results of a single simulation.

This assumption seems reasonable, while the portion of the “large” electrode that is ignored is “downstream” of the flux, so it is not expected to influence the portion that is considered. However, we wanted to check this by simulating the effect of changing the real electrode size in a given configuration. Figure S7 shows the species flux as a function of the radial distance from the center of the electrode for three real electrode sizes. All the plots are superimposed, which confirms our assumption that electroactive parts further away from the axis cannot

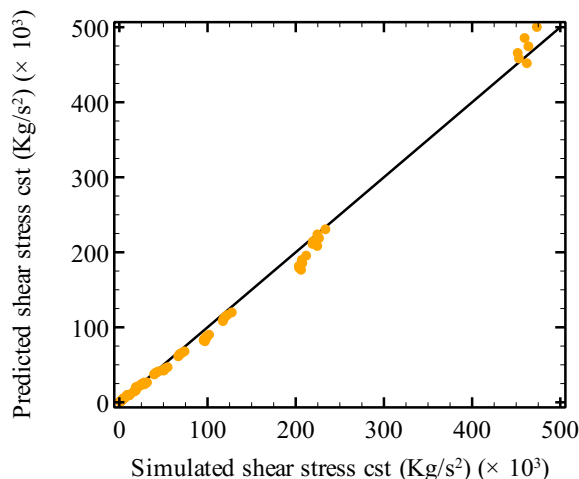


Figure S6: Comparison between simulated shear stress and the prediction from equation (17b) in text. As the latter predicts the shear stress is proportional to r , the distance from the electrode axis, the values plotted is are the values of the A as the constant was determined by dividing the shear stress by the radial distance ($r = 50 \mu\text{m}$) from the center of the electrode.

influence the mass flux at the electroactive parts closer to the axis. The few divergent points correspond to boundary effect artifacts.

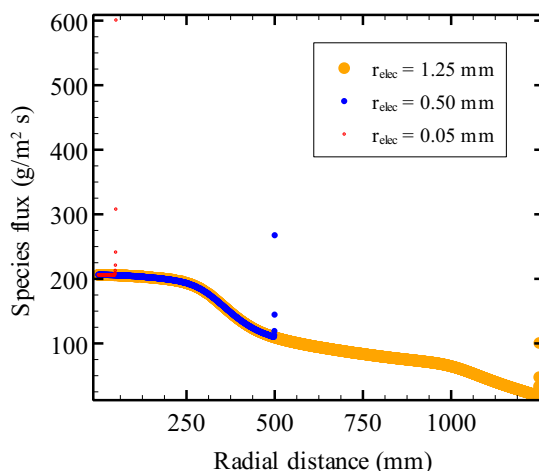


Figure S7: Comparison of species flux profiles in 2D axis symmetry between geometries with three different electrode radius: the graph represents the species flux as a function of the radial distance from the center of the electrode for three electrode sizes ($r_{elec} = 1.25 \text{ mm}$ in orange; $r_{elec} = 0.5 \text{ mm}$ in blue and $r_{elec} = 0.05 \text{ mm}$ in red). The other parameters are: $r_{jet} = 0.3 \text{ mm}$; $h = 0.15 \text{ mm}$ and $Q_v = 1 \text{ mL/min}$.

S6 Experimental results from ferricyanide reduction

Figure S8 shows the raw cyclic voltammograms of ferricyanide reduction (A) and the blank (B). The voltammograms were cut at $E = -0.356 \text{ V}$, which is where oxygen reduction started.

Figure S9 shows the voltammograms in the absence of any flow that were used to determine the diffusion coefficient of $\text{Fe}(\text{CN})_6^{3-}$ in our conditions.

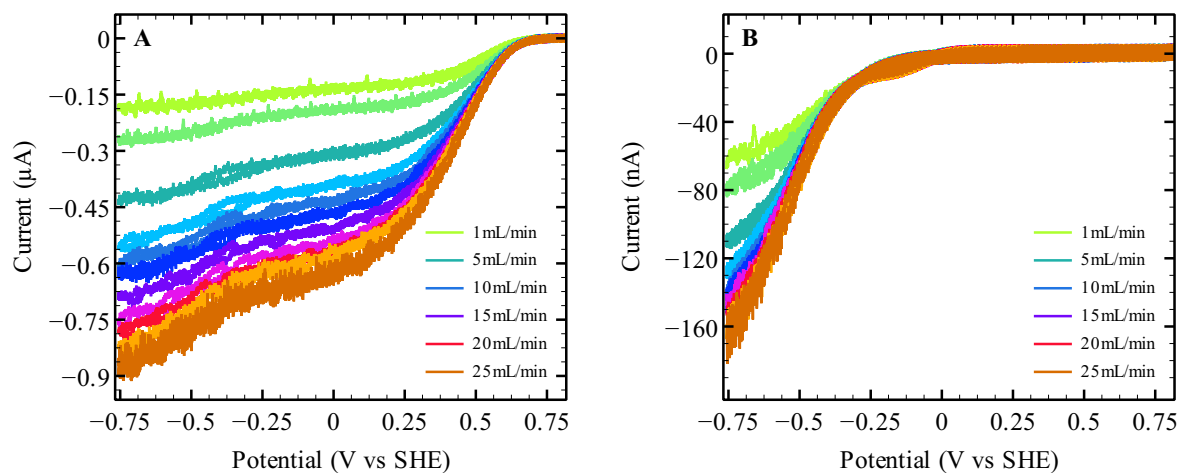


Figure S8: raw Cyclic voltammograms for (A) the reduction of $Fe(CN_6)^{3-}$ (1 mM) in an electrolyte solution of 0.5 M NaCl in the electrochemical cell where $r_{jet} = 0.3$ mm; $h = 0.35$ mm with graphite electrode of $100 \mu m$ diameter at $\nu = 100$ $mV \cdot s^{-1}$. (B) NaCl cyclic voltammograms at the same conditions. The experiments were conducted at volume flow rate that ranged from 1 ml/min to 25 ml/min at room temperature, under degassed system with argon.

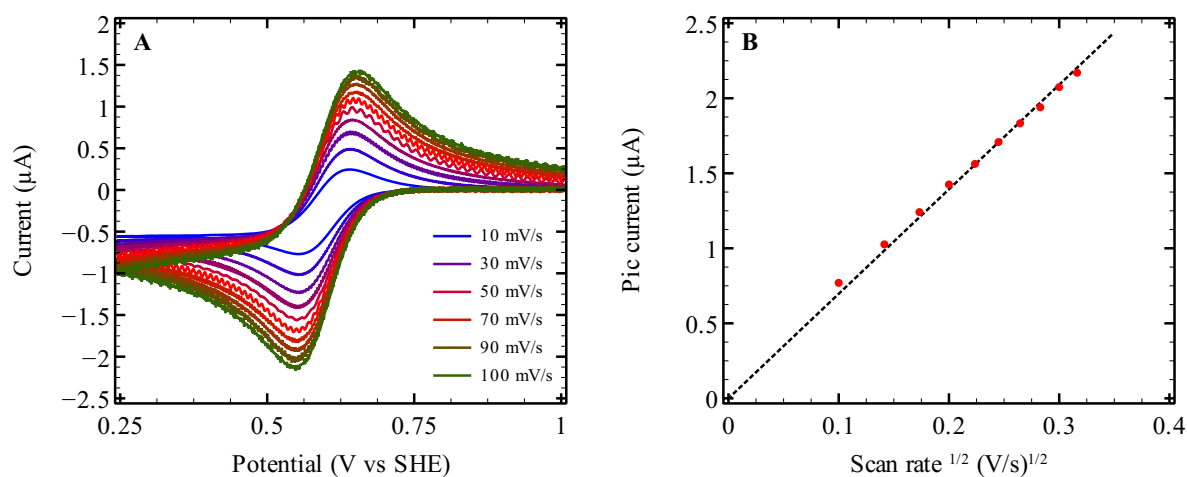


Figure S9: (A) Cyclic voltammograms of $Fe(CN_6)^{3-}$ (1 mM) in an electrolyte solution of 0.5 M NaCl at a range of scan rates (10 mV/S to 100 mV/s); (B) Reduction peak current (in absolute value) as a function of scan rate; the straight line corresponds to $i = -6.96736 \times 10^{-6} \nu^{-1/2}$, where ν is the scan rate. This slope yields a diffusion coefficient of $1.088 \times 10^{-9} m^2 \cdot s^{-1}$. Experiments were conducted at room temperature right after the experiments shown in S8. The diameter of the graphite electrode that was used is 1 mm.

Sim	r_{jet} (mm)	h (mm)	Q_V (mL/min)	a_{axial} (s^{-1})	a_{radial} (s^{-1})	$a_{average}$ (s^{-1})	Error (s^{-1})	Rel. error (%)
Opt 01	0.25	0.15	5	2949.4	2925.35	2937.38	12.025	0.41
Opt 02	0.3	0.15	5	1827.74	1826.43	1827.09	0.655	0.04
Opt 03	0.35	0.15	5	1223.87	1214.93	1219.4	4.47	0.37
Opt 04	0.4	0.15	5	850.353	842.749	846.551	3.802	0.45
Opt 05	0.45	0.15	5	604.051	604.757	604.404	0.353	0.06
Opt 06	0.5	0.15	5	452.529	452.999	452.764	0.235	0.05
Opt 07	0.25	0.2	5	2937.29	2916.97	2927.13	10.16	0.35
Opt 08	0.3	0.2	5	1797.59	1781.34	1789.46	8.125	0.45
Opt 09	0.35	0.2	5	1185.45	1174.27	1179.86	5.59	0.47
Opt 10	0.4	0.2	5	829.194	822.941	826.067	3.1265	0.38
Opt 11	0.45	0.2	5	590.252	589.662	589.957	0.295	0.05
Opt 12	0.5	0.2	5	439.635	442.217	440.926	1.291	0.29
Opt 13	0.25	0.25	5	2904.35	2895.6	2899.97	4.375	0.15
Opt 14	0.3	0.25	5	1797.28	1785.16	1791.22	6.06	0.34
Opt 15	0.35	0.25	5	1169.82	1160.18	1165	4.82	0.41
Opt 16	0.4	0.25	5	808.045	805.889	806.967	1.078	0.13
Opt 17	0.45	0.25	5	577.728	575.998	576.863	0.865	0.15
Opt 18	0.5	0.25	5	432.287	432.449	432.368	0.081	0.02
Opt 19	0.25	0.3	5	2886.77	2853.27	2870.02	16.75	0.58
Opt 20	0.3	0.3	5	1762.79	1744.57	1753.68	9.11	0.52
Opt 21	0.35	0.3	5	1161.98	1147.25	1154.62	7.365	0.64
Opt 22	0.4	0.3	5	796.76	792.378	794.569	2.191	0.28
Opt 23	0.45	0.3	5	566.667	564.438	565.553	1.1145	0.20
Opt 24	0.5	0.3	5	424.412	424.511	424.462	0.0495	0.01
Opt 25	0.25	0.35	5	2889.99	2863.15	2876.57	13.42	0.47
Opt 26	0.3	0.35	5	1743.25	1742.11	1742.68	0.57	0.03
Opt 27	0.35	0.35	5	1142.17	1140.57	1141.37	0.8	0.07
Opt 28	0.4	0.35	5	791.411	789.075	790.243	1.168	0.15
Opt 29	0.45	0.35	5	562.631	560.533	561.582	1.049	0.19
Opt 30	0.5	0.35	5	417.631	418.58	418.106	0.4745	0.11
Opt 31	0.25	0.4	5	2914.11	2895.72	2904.91	9.195	0.32
Opt 32	0.3	0.4	5	1792.28	1784.64	1788.46	3.82	0.21
Opt 33	0.35	0.4	5	1157.15	1144.97	1151.06	6.09	0.53
Opt 34	0.4	0.4	5	795.568	785.442	790.505	5.063	0.64
Opt 35	0.45	0.4	5	563.487	558.181	560.834	2.653	0.47
Opt 36	0.5	0.4	5	418.041	418.951	418.496	0.455	0.11
Opt 37	0.25	0.15	1	704.739	704.828	704.784	0.0445	0.01
Opt 38	0.3	0.15	1	423.359	425.817	424.588	1.229	0.29
Opt 39	0.35	0.15	1	274.486	273.915	274.201	0.2855	0.10
Opt 40	0.4	0.15	1	189.16	188.296	188.728	0.432	0.23
Opt 41	0.45	0.15	1	134.074	134.719	134.397	0.3225	0.24
Opt 42	0.5	0.15	1	99.5306	99.9498	99.7402	0.2096	0.21
Opt 43	0.25	0.2	1	680.725	681.748	681.236	0.5115	0.08
Opt 44	0.3	0.2	1	405.5	404.439	404.97	0.5305	0.13
Opt 45	0.35	0.2	1	261.715	260.596	261.155	0.5595	0.21
Opt 46	0.4	0.2	1	182.255	181.658	181.957	0.2985	0.16
Opt 47	0.45	0.2	1	130.152	130.492	130.322	0.17	0.13
Opt 48	0.5	0.2	1	96.4415	97.3103	96.8759	0.4344	0.45
Opt 49	0.25	0.25	1	648.937	652.518	650.727	1.7905	0.28
Opt 50	0.3	0.25	1	387.68	387.598	387.639	0.041	0.01
Opt 51	0.35	0.25	1	250.614	249.838	250.226	0.388	0.16
Opt 52	0.4	0.25	1	173.611	173.881	173.746	0.135	0.08
Opt 53	0.45	0.25	1	125.391	125.46	125.425	0.0345	0.03
Opt 54	0.5	0.25	1	93.8761	94.1983	94.0372	0.1611	0.17
Opt 55	0.25	0.3	1	635.799	633.821	634.81	0.989	0.16
Opt 56	0.3	0.3	1	373.791	372.34	373.065	0.7255	0.19
Opt 57	0.35	0.3	1	241.128	239.307	240.217	0.9105	0.38
Opt 58	0.4	0.3	1	166.1	165.883	165.992	0.1085	0.07

Sim	r_{jet} (mm)	h (mm)	Q_V (mL/min)	a_{axial} (s^{-1})	a_{radial} (s^{-1})	$a_{average}$ (s^{-1})	Error (s^{-1})	Rel. error (%)
Opt 59	0.45	0.3	1	120.514	120.456	120.485	0.029	0.02
Opt 60	0.5	0.3	1	90.4987	90.793	90.6458	0.14715	0.16
Opt 61	0.25	0.35	1	620.108	619.663	619.885	0.2225	0.04
Opt 62	0.3	0.35	1	359.863	361.978	360.921	1.0575	0.29
Opt 63	0.35	0.35	1	229.681	230.552	230.117	0.4355	0.19
Opt 64	0.4	0.35	1	159.628	159.835	159.731	0.1035	0.06
Opt 65	0.45	0.35	1	115.562	115.534	115.548	0.014	0.01
Opt 66	0.5	0.35	1	86.7837	87.241	87.0123	0.22865	0.26
Opt 67	0.25	0.4	1	604.668	606.169	605.418	0.7505	0.12
Opt 68	0.3	0.4	1	355.82	356.69	356.255	0.435	0.12
Opt 69	0.35	0.4	1	224.899	223.701	224.3	0.599	0.27
Opt 70	0.4	0.4	1	155.48	154.157	154.819	0.6615	0.43
Opt 71	0.45	0.4	1	112.008	111.345	111.677	0.3315	0.30
Opt 72	0.5	0.4	1	84.2513	84.6884	84.4699	0.21855	0.26
Opt 73	0.25	0.15	10	4962.54	4896.37	4929.45	33.085	0.67
Opt 74	0.3	0.15	10	3140.39	3125.13	3132.76	7.63	0.24
Opt 75	0.35	0.15	10	2128.51	2106.01	2117.26	11.25	0.53
Opt 76	0.4	0.15	10	1494.32	1476.9	1485.61	8.71	0.59
Opt 77	0.45	0.15	10	1057.22	1056.09	1056.65	0.565	0.05
Opt 78	0.5	0.15	10	793.846	793.125	793.486	0.3605	0.05
Opt 79	0.25	0.2	10	4924.15	4864.81	4894.48	29.67	0.61
Opt 80	0.3	0.2	10	3080.48	3040.28	3060.38	20.1	0.66
Opt 81	0.35	0.2	10	2071.11	2044.81	2057.96	13.15	0.64
Opt 82	0.4	0.2	10	1457.31	1442.39	1449.85	7.46	0.51
Opt 83	0.45	0.2	10	1032.81	1029.49	1031.15	1.66	0.16
Opt 84	0.5	0.2	10	770.227	773.297	771.762	1.535	0.20
Opt 85	0.25	0.25	10	4888.55	4848.47	4868.51	20.04	0.41
Opt 86	0.3	0.25	10	3088.16	3054.9	3071.53	16.63	0.54
Opt 87	0.35	0.25	10	2045.16	2021.68	2033.42	11.74	0.58
Opt 88	0.4	0.25	10	1420.79	1413.22	1417.01	3.785	0.27
Opt 89	0.45	0.25	10	1011.61	1006.38	1009	2.615	0.26
Opt 90	0.5	0.25	10	757.636	756.522	757.079	0.557	0.07
Opt 91	0.25	0.3	10	4832.33	4751.77	4792.05	40.28	0.84
Opt 92	0.3	0.3	10	3024.98	2981.72	3003.35	21.63	0.72
Opt 93	0.35	0.3	10	2032.08	1999.79	2015.93	16.145	0.80
Opt 94	0.4	0.3	10	1403.31	1391.9	1397.61	5.705	0.41
Opt 95	0.45	0.3	10	998.579	992.494	995.536	3.0425	0.31
Opt 96	0.5	0.3	10	745.225	744.035	744.63	0.595	0.08
Opt 97	0.25	0.35	10	4849.65	4780.07	4814.86	34.79	0.72
Opt 98	0.3	0.35	10	2992.37	2978.52	2985.44	6.925	0.23
Opt 99	0.35	0.35	10	1999.96	1990.71	1995.34	4.625	0.23
Opt 100	0.4	0.35	10	1395.98	1388.14	1392.06	3.92	0.28
Opt 101	0.45	0.35	10	988.754	982.951	985.852	2.9015	0.29
Opt 102	0.5	0.35	10	735.42	735.748	735.584	0.164	0.02
Opt 103	0.25	0.4	10	4915.73	4859.2	4887.47	28.265	0.58
Opt 104	0.3	0.4	10	3091.38	3065.64	3078.51	12.87	0.42
Opt 105	0.35	0.4	10	2020.01	1992.34	2006.17	13.835	0.69
Opt 106	0.4	0.4	10	1403.59	1382.04	1392.82	10.775	0.77
Opt 107	0.45	0.4	10	991.949	980.49	986.219	5.7295	0.58
Opt 108	0.5	0.4	10	737.851	738.102	737.976	0.1255	0.02

Table S2: List of all the simulations with their respective parameters and the the values of a deduced from the axial (a_{axial}) and radial (a_{radial}) velocity profiles, their average, and the absolute and relative error between the two.

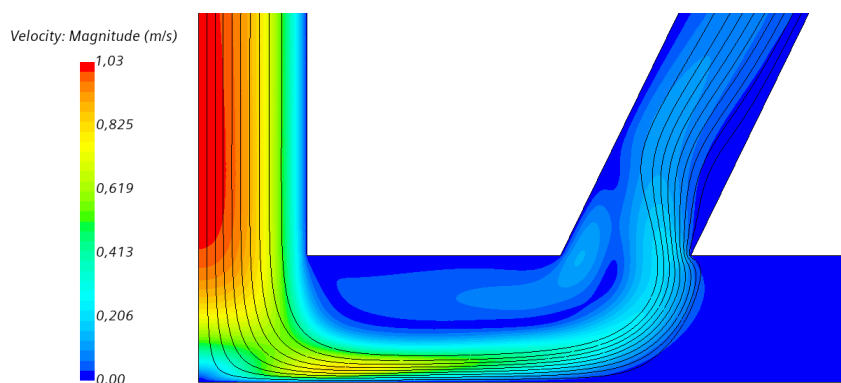


Figure S10: Flow streamlines (in black) and velocity profile in the jet flow cell for $r_{jet} = 0.3$ mm, $h = 0.35$ mm and $Q_v = 10$ mL.min⁻¹

References

- [1] M. Fadel, J.-V. Daurelle, V. Fourmond and J. Vicente, *Physical Chemistry Chemical Physics*, 2019, **21**, 12360–12371.
- [2] F. Homann, *Forschg. Ing. Wes*, 1936, **7**, 1.

3.8 Additional results from DoE

3.8.1 Shear stress

Figure 3.2 shows that the inlet radius and the flow rate have the most significant impact on shear stress. There is also a minor influence of the distance between the nozzle and the electrode while the other parameters have negligible impact. These results are qualitatively in agreement with the formula (17.b) that we proposed in section 3.6 to predict shear stress at the electrode.

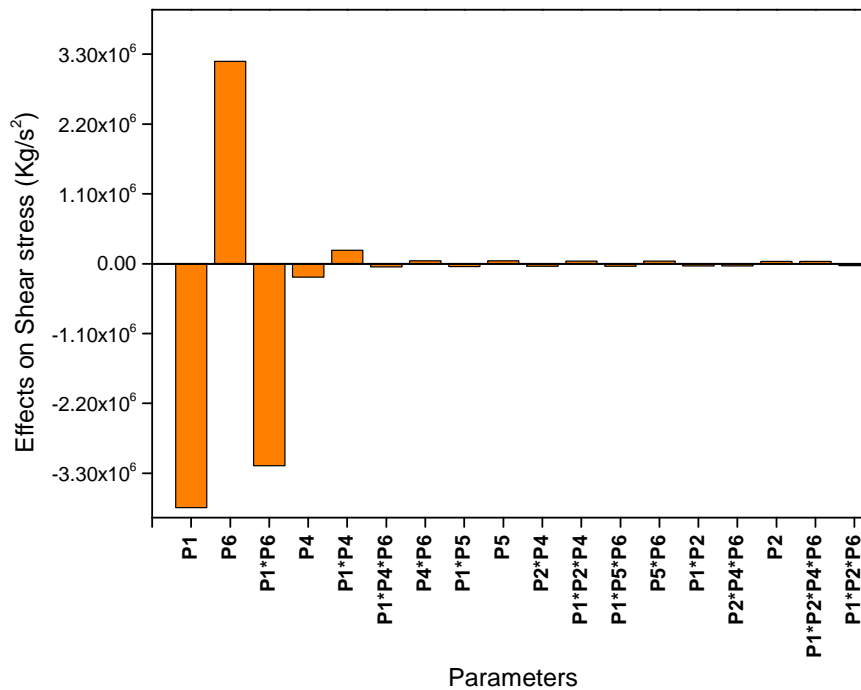


Fig. 3.2 The single and the interaction effects of the parameters on the simulated slope of shear stress for 64 combinations of parameters from table 3.1.

3.8.2 Pressure drop

From figure 3.3, it can be seen that excepted the distance between the inlet and the outlet, the pressure drop is affected by all the other parameters with uneven degrees. The most impactful ones are inlet radius and the flow rate then comes the outlet radius. In particular, this means that pressure drop is much difficult to predict.

Contrary to the shear stress and the mass transport that are local properties, which means that they are independent of the details of the flow. The pressure drop is a global property that depends on all the parameters of the cell.

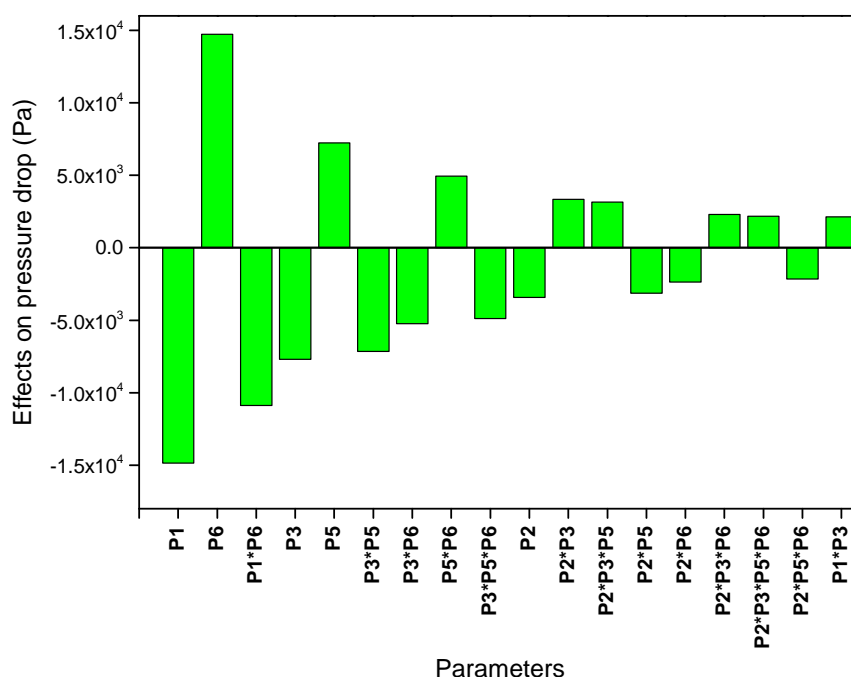


Fig. 3.3 The single and the interaction effects of the parameters on the simulated pressure drop for 64 combinations of parameters from table 3.1.

3.9 Experimental setup

With the aim of validating the numerical and the analytical approaches that were adopted in the paper, we used an experimental setup (described schematically in fig.3.4) that consists of a solution tank, a syringe pump, and the electrochemical cell that was selected from the in-depth simulation. This cell showed high and uniform mass transport ($H \leq 10\%$), it was selected then printed using stereolithography. The pump that was used is a syringe pump (Fusion 4000) from Chemyx. the tubing of PVC with (1/16" inner diameter and (1/16" outer diameter) and the tube fittings and connections are from Fisher Scientific. Argon was bubbled in the solution tank for an hour and thirty minutes prior to the experiment with a pressure of 1 bar. Then, its flow was maintained constant during the whole experiment in order to prevent the diffusion of oxygen from outside to the setup. A potentiostat (PGSTAT101) from (Metrohm France) was used to control the applied potential through the cell and to record the measured current.

The solution used was composed of 1 mM of potassium ferricyanide and 0.5 M of NaCl as a supporting electrolyte. The working electrode was polished with diamond paste (3 μm , 1 μm) then with alumina 1 μm .

Cyclic voltammograms were recorded at different flow rates in order to obtain the limiting current vs the flow rate. Experimental mass transport coefficient (m_{exp}) was calculated using equation (1.9) [37].

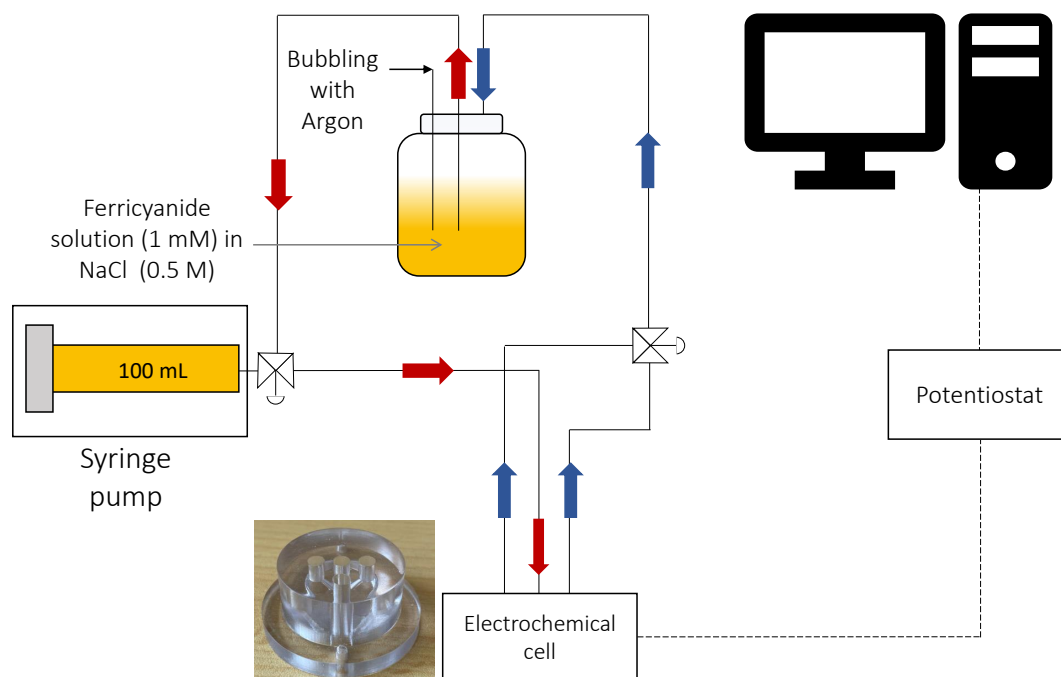


Fig. 3.4 Schematic representation of the experimental setup used to record the limiting current at different flow rate in the wall-tube cell.

3.9.1 Optimization of the pumping system

In previous works, we used to use a peristaltic pump (PERIMAX 12) of 12 rollers. However, some technical problems were encountered and the most significant one was the fluctuations of the flow due to the rotation of the rollers. To solve this issue, we changed the pumping system and switched to syringe pump. This pump allows precise volumes to be pumped by the movement of a piston in the pump cylinder.

Figure 3.5 shows the comparison between the recorded CVs of ferricyanide reduction at different flowrates using the two pumping systems. The amplitude of the fluctuations caused by the syringe pump are almost 10 times lower than those caused by the peristaltic pump.

3.10 Conclusion

In this chapter, I showed that by using CFD and DoE approach, we were able to identify the main influencing parameters on the cell's performances. These parameters are: inlet's flow rate, jet radius and the distance between the inlet and the electrode. High resolution simulations with a greater number of parameter values allowed us to explore more sys-

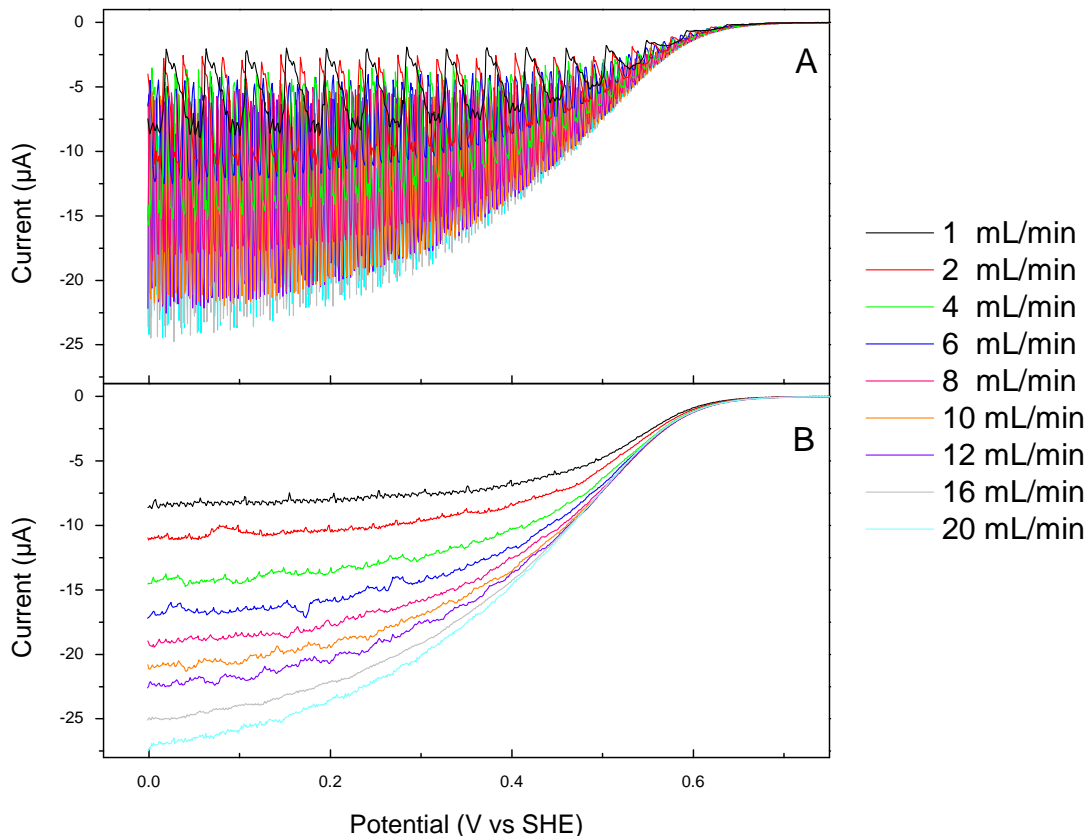


Fig. 3.5 Comparison of the flow fluctuations induced by using the peristaltic pump and the syringe pump: Cyclic voltammograms for the reduction of $\text{Fe}(\text{CN})_6^{3-}$ at a graphite electrode of diameter 1 mm at $\nu = 20 \text{ mV s}^{-1}$. Electrochemical cells parameters/ $r_{jet}=1 \text{ mm}$; $h=0.3 \text{ mm}$. The experiments were conducted at volume flow rate that ranged from 1 mL/min to 20 mL/min using: (A) the peristaltic pump, (B) the syringe pump. Conditions: $[\text{Fe}(\text{CN})_6^{3-}] = 1 \text{ mM}$, electrolyte: 0.5 M NaCl.

tematically the parameter space. We used the obtained data to propose semi-empirical formulas to predict mass transport and shear stress at the electrode.

The formula of mass transport was in good agreement with the one proposed by Chin et al [141] and with the experimental results from ferricyanide reduction.

In contrast to mass transport coefficient formula, verifying the wall shear stress formula is more challenging because measuring the wall shear stress experimentally is not simple. Therefore, in this work, our predictions for the shear stress couldn't be validated experimentally. However, since both the mass transport coefficient and the shear stress are derived from the same equations and they are both dependent on the hydrodynamic constant a , the experimental validation of the predicted mass transport coefficient can be considered as an indication of the quality of the prediction of the shear stress.

we now have a formula that can be used to determine mass transport whenever we use the cell, including when we change parameters like the inlet diameter.

Chapter 4

Shear stress and film loss on the electrode

This chapter addresses the relationship between shear stress and film loss on the electrode. It is built around a short communication that will be submitted soon (section 4.1).

As shown in chapter 1, section 1.7.3, during PFE experiments, a continuous decrease in the catalytic current of redox enzymes over time is often encountered, this phenomenon is called “film loss”. This loss may obscure important features and introduce systematic errors that are difficult to evaluate, which limits the accuracy of the measurements. Therefore, during data analysis, a correction is applied to minimize the effects of film loss to allow quantitative data analysis [70].

Although not well understood, film loss is frequently and intuitively associated with the physical desorption of the enzyme. It is thought to be caused by the mechanical force (shear stress) applied by the flow of the solution on the surface of the electrode. However, this hypothesis has never been addressed before, and in the literature, there are only few studies that connected shear stress and film loss, such as the one conducted by Binyamin et al, where they showed that thick polymer films containing glucose oxidase were washed away from the surface immediately after the the RDE started to rotate [71].

In our study (section 4.1), the wall-tube cell that we have built and experimentally characterized (described in chapter 2), was used to investigate the relationship between shear stress and the rate of film loss on films of *Desulfovibrio desulfuricans* ATCC27774 cytochrome c nitrite reductase (ccNir). Contrary to our expectations, we found that, an increased shear stress is associated with slower film loss.

4.1 Mechanical stress does not cause film loss in protein film electrochemistry

Mechanical stress does not (necessarily) cause film loss in protein film electrochemistry

Asmaa Hadj-Ahmed^{a,b}, Anna Aldinio-Colbachini^{a,b}, Americo G. Duarte^c, Jean-Vincent Daurelle^b, Vincent Fourmond^{a*}

^aAix-Marseille Université, CNRS, BIP UMR 7281, 31 Chemin J. AIGUIER, CS70071, Marseille Cedex 20 F-13402, France

^bLaboratoire IUSTI (UMR AMU-CNRS 7343) Polytech Marseille, Dpt Mécanique Energétique (ME), Technopôle de Château Gombert, 5 rue Enrico Fermi, Marseille cedex 13 13453, France

^cInstituto de Tecnologia Química e Biológica António Xavier/Universidade Nova de Lisboa, Av. da República, Estação Agronómica Nacional, 2780-157 Oeiras, Portugal.

*vincent.fourmond@imm.cnrs.fr

Abstract

Film loss refers to the continuous loss of catalytic current of redox enzymes immobilized on an electrode. It is often associated with enzyme desorption, and as such, is thought to be induced by mechanical stress (shear stress), in particular with hydrodynamic electrodes, like the rotating disc electrode, in which the electrochemical buffer flows along the electrode. We have used a wall-tube electrode that we have recently described and fully characterized to study the relationship between shear stress and the rate of film loss for films of cytochrome *c* nitrite reductase, and found that, contrary to expectations, film loss decreases when the shear stress increases.

The discovery that it is possible to immobilize redox enzymes onto electrodes in a configuration in which fast and direct electron transfer can be achieved opened several completely new fields, with the construction of biosensors[1,2], relying on the sensitivity and specificity of enzymes, bioelectrodes for use in energy conversion, for instance in biofuel cells[3], but also it led to the possibility of taking advantage of the direct connexion to study the enzymes. This approach is known as Protein Film Electrochemistry[4–7], and relies on the fact that the electrical current passing through the electrode is generally proportional to the enzymatic activity. This technique has been successfully applied to the study of many different aspects of the functioning of metalloenzymes like hydrogenases[8] or molybdenum enzymes[9].

As a general rule, the catalytic reaction leads to the consumption of the enzyme's substrate in the vicinity of the electrode, so, unless the catalytic reaction is very slow, active transport of the substrate is required to avoid mass-transport limitations[4]. This is usually performed using a rotating disc electrode (RDE).

It was also noticed early on that the enzymatic films are not that stable on the electrode, leading to a decrease of the catalytic current over time. This phenomenon is called "film loss", and is very variable, from films lasting days down to a complete loss of the catalytic current in minutes. The effects of film loss are generally multiplicative, which means that, unless it is so fast that no experiments are possible, strategies based on division by a possibly synthetic control signal are successful to minimize or even eliminate the effects of film loss to allow quantitative data analysis[10].

Irreversible losses of activity are generally hard to understand using protein PFE, because precisely the enzymes that lost activity do not contribute anymore to the current and therefore cannot be studied. However, film loss is often associated with the idea of desorption, the physical removal of the enzyme from the electrode[4]. In that respect it is also believed that it is caused by mechanical stress, i.e. by the effect of the shear stress induced by the flow of the electrochemical buffer on the surface of the electrode. However, there is very little data in the literature connecting shear stress and film loss. Binyamin and Heller found that thick polymer films containing glucose oxidase were immediately removed upon the application of rotation, unless they used cross-linkers to consolidate the film[11]. To the best of our knowledge, no study so far has concentrated on the effect of shear stress on monolayers or sub-monolayers of enzymes immobilized on electrodes.

We have recently designed an electrochemical cell, based on a wall-tube design, to act as a replacement of the RDE, but with the possibility to produce larger mass-transport coefficients[12]. We have fully characterized the properties of the flow and provided semi-empirical formulas to compute both the mass-transport and shear stress[13].

Here, we use this new cell to investigate the effect of shear stress on films of *Desulfovibrio desulfuricans* ATCC27774 cytochrome *c* nitrite reductase (ccNir), which catalyzes the 6-electron reduction of nitrite to ammonium[14], immobilized onto pyrolytic graphite “edge” electrodes; we show that, contrary to the expectations, increased shear stress is correlated to slower film loss.

Figure 1 shows the current produced by a film of Dd ccNir immobilized on a pyrolytic graphite edge electrode inside the wall-tube cell we have designed. The electrode is exposed to a jet of a buffer solution of nitrite, providing the enzyme with its substrate, and the electrode is poised at a constant potential, allowing catalytic reduction of nitrite into ammonium. The electrode is maintained under a flow for the whole duration of the experiment, but the value of the flow rate is varied step-wise during the experiment. Each change in flow rate results in an instant change of the current, reflecting a small contribution of mass-transport limitation to the overall current (see SI section 4 for a discussion of mass-transport limitation).

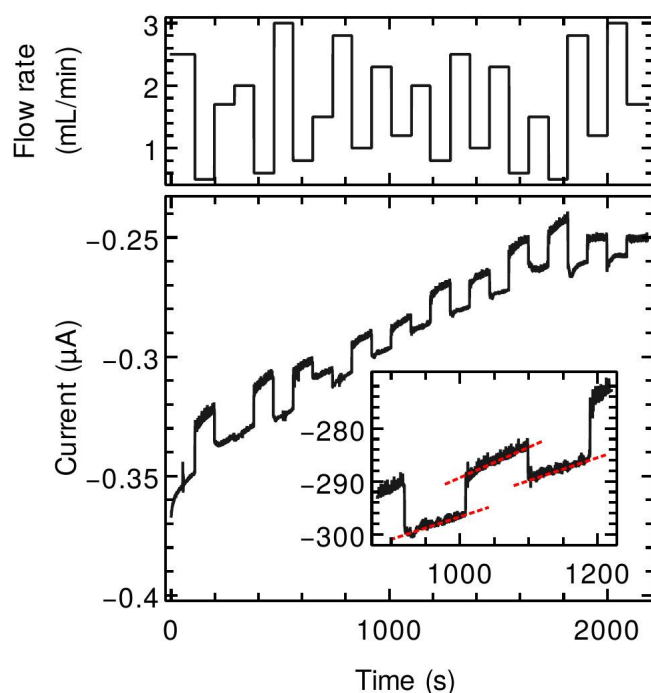


Figure 1 response of a film of ccNir to an exposure to constant 40 μM nitrite with variations in the flow rates. Panel A: flow rates as a function of time. Panel B: resulting catalytic current. Inset:

zoom of the response, together with linear fits (dotted red lines) of the current of the three steps corresponding to effective first order rate constant of film loss of respectively 1.4, 2.0 and 1.5 $\times 10^{-4}$ s^{-1} . The corresponding flow rates are 2.3, 1.2 and 2 mL/min . Conditions: room temperature, pH 7.

The global trend of the data is a slow decrease of the magnitude of the current, reflecting film loss, the irreversible loss of the enzymatic activity over time. To quantify the effect, we determined the effective first order rate constant of film loss by fitting a linear regression and using the identity:

$$i_0 \exp(-k_\ell(t - t_0)) \approx i_0 - k_\ell i_0(t - t_0)$$

Such linear fits are shown in the inset of figure 1: the evolution of the current over time is well represented by a linear trend, consistent with the fact that film loss is rather slow. The inset shows the effect for three different flow rates, the intermediate one being the smallest. A very surprising feature of this data is that the film loss rate constant deduced from the intermediate step is larger than that for the other two steps, although they correspond to a significantly higher flow rate (and thus larger shear stress).

Film loss is very variable from one experiment to another, but we observed this increase in film loss rate many times upon a decrease in the flow rate. To better quantify this effect, we repeated chronoamperometry experiments, testing systematically 12 different flow rates twice, such as in figure 1 and determined the average rate of film loss as a function of flow rate. The results are shown in figure 2, panel A. They show an overall decrease of the average value of the film loss rate constant when the flow rate increases, with the notable exception of the value at 2.5 mL/min , which was systematically the first point in all of the experiments and for which we always observed much higher film loss. However, the standard error on the rate of film loss itself is too large to be conclusive, pointing to a large variability of the film loss rate constant.

To ascertain whether the non-reproducibility comes from an inherent variability of the dependence of film loss on flow rate, or if it comes from a variability between experiments, we divided the film loss in each experiment by the average film loss over the experiment duration, and plotted the average and standard deviation over all the experiments in the panel B of figure 2. With this data treatment, the standard deviation is significantly smaller (in relative values), showing that an important part of the non-reproducibility comes from a variation between experiments. These data show without ambiguity that the data points at low flow rates are in average higher than the data points at high flow rate, with an average slope of -0.36 ± 0.16 per mL/min , demonstrating that, under our conditions at least, contrary to the expectations an increase in flow rate, and thus an increase in shear stress, leads to a decrease in the rate of film loss (under our conditions, the shear stress scales as the power 1.35 of the flow rate[13], see also supplementary figure S3).

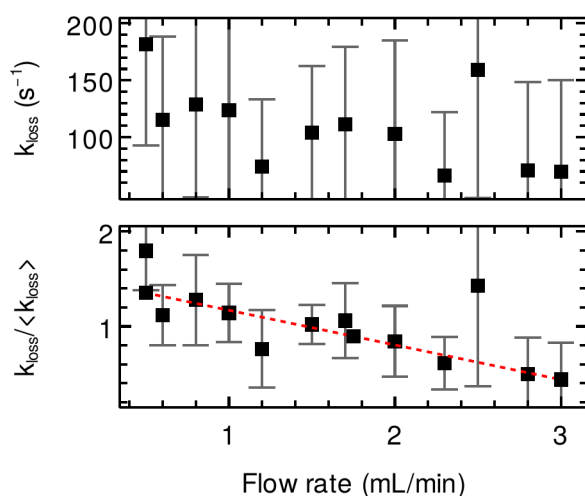


Figure 2: dependency of film loss rate constant as a function of flow rate. Panel A: average and standard deviation of the film loss determined as in the inset of figure 1, for a total of 11 different measures. Panel B: same data but this time first divided by the average film loss over a series before averaging and taking the standard deviation. The line corresponds to a linear fit taking into account the standard deviation. The same data are plotted as a function of average shear stress or average pressure in supplementary figure S3.

Film loss, the process by which an enzymatic electroactive film slowly loses activity over time, is often described as desorption, the simple removal of the enzymes from the electrode surface[4]. Under such assumption, it seems that an increasing mechanical stress exerted by the electrochemical buffer (under the form of shear stress) should hasten the removal process, and thus increase the rates of film loss. However, contrary to expectations, our experiments show that, increased flow rate (and thus increased shear stress) leads to moderately decreased rates of film loss. This observation cannot be an artifact from mass-transport limitation, first because the contribution from mass-transport limitation is relatively small (see SI section 4), but also because if that were the case, one would expect hardly any change at all of the current for the lower flow rates, since the mass-transport limited current is not affected by changes in the concentration of enzyme. However, we observed the contrary.

There is no doubt that shear stress causes the removal of micrometer-sized elements from surfaces. Wall-jet setups like the ones we used here have been used to measure the adhesion strength of bacteria to surfaces[15,16] or the resistance of anti-corrosion protective films to shear stress[17]. In all of these examples, increasing the flow rates (and thus the shear stress) leads to more efficient removal. However, it is unclear if shear stress still has a significant effect at the scale of the immobilized enzymes, which are a couple of nanometers thick.

“Film loss” is in fact very likely to be the result of many different processes, out of which only one is the physical desorption of the enzymes from the surface of the electrode. If the various processes are independent, the total rate constant for film loss is the sum of the individual rate constants. In the case of multicopper oxidases, a number of studies combining in situ electrochemical methods and surface characterization techniques such as ellipsometry[18], quartz microbalance[19,20] and surface plasmon resonance[21] showed that the catalytic current decreases even if the global enzyme coverage remains mostly constant. Singh and coworkers observed a correlation between the dissipation of a quartz microbalance and the catalytic current produced by a bilirubin oxidase, and concluded that film loss in that case is probably due to dehydration of the enzyme layer[19].

Conversely, there are also clearly identified cases in which covalent grafting, which greatly limits desorption, decreases film loss. This was for instance observed for NiFe[22,23] and FeFe[24] hydrogenases, glucose oxidase[25], cellobiose dehydrogenase[26,27], and laccase[28].

In some cases, it is clear that film loss is chemical inactivation, like in the case the irreversible part of the oxidative inactivation of FeFe hydrogenases[29].

In the present case, the cause of film loss is unclear. Our data show that at least one of the contributions to film loss in the case of ccNir decreases with the increase in flow rate. Changing the flow rate affects not only the value of the shear stress, but also the pressure on the electrode. We have used numerical simulations to compute the average pressure over the surface of the electrode and compared the result to the values of the shear stress extracted from the same simulations. Supplementary figure S3 show that under our conditions, the average pressure and shear stress behave similarly as a function of flow rate, but that the pressure is about 2 to 3 times larger than the shear stress (both have the same units). Based on these data, we can imagine that the dominant effect under our conditions is a compression effect that increase the adherence of the enzyme to the electrode, rather than a tearing effect.

In any case, the main conclusion from our data is that shear stress is probably a much less significant issue than was previously anticipated for running Protein Film Electrochemistry experiments – at least in the case of ccNir.

Acknowledgments

The authors acknowledge support from CNRS, Aix-Marseille Université, Agence Nationale de la Recherche (ANR-15-CE05-0020, ANR-17-CE11-0027), and the Excellence Initiative of Aix-Marseille University - A*MIDEX, a French “Investissements d’Avenir” programme (ANR-11-IDEX-0001-02), and the ANR-DFG project SHIELDS (PL 746/2-1). They also wish to acknowledge expert help from Alain Grossi and Sady Noel in preparing the 3D-printed cell and the electrodes. AHA, AAC, and VF are part of the FrenchBIC (<http://frenchbic.cnrs.fr>). Funding by Fundação para a Ciência e Tecnologia (Portugal) through project PTDC/BIA-BQM/29118/2017.

Supplementary material

The supplementary information contains the methods: protein purification, experimental procedures, and the scripts for the data analysis using the open-source software QSoas[30]. It contains the supplementary figures S1 to S4.

- [1] D. Grieshaber, R. MacKenzie, J. Vörös, E. Reimhult, Electrochemical biosensors - sensor principles and architectures, *Sensors* . 8 (2008) 1400–1458.
- [2] J. Wang, Electrochemical glucose biosensors, *Chem. Rev.* 108 (2008) 814–825.
- [3] X. Xiao, H.-Q. Xia, R. Wu, L. Bai, L. Yan, E. Magner, S. Cosnier, E. Lojou, Z. Zhu, A. Liu, Tackling the Challenges of Enzymatic (Bio)Fuel Cells, *Chem. Rev.* 119 (2019) 9509–9558.
- [4] C. Léger, P. Bertrand, Direct electrochemistry of redox enzymes as a tool for mechanistic studies, *Chem. Rev.* 108 (2008) 2379–2438.
- [5] F.A. Armstrong, N.A. Belsey, J.A. Cracknell, G. Goldet, A. Parkin, E. Reisner, K.A. Vincent, A.F. Wait, Dynamic electrochemical investigations of hydrogen oxidation and production by enzymes and implications for future technology, *Chem. Soc. Rev.* 38 (2009) 36–51.
- [6] J. Hirst, Elucidating the mechanisms of coupled electron transfer and catalytic reactions by protein film voltammetry, *Biochim. Biophys. Acta.* 1757 (2006) 225–239.
- [7] M. Del Barrio, M. Sensi, C. Orain, C. Baffert, S. Dementin, V. Fourmond, C. Léger, Electrochemical Investigations of Hydrogenases and Other Enzymes That Produce and Use Solar Fuels, *Acc. Chem. Res.* 51 (2018) 769–777.
- [8] M. Sensi, M. del Barrio, C. Baffert, V. Fourmond, C. Léger, New perspectives in hydrogenase direct electrochemistry, *Curr. Opin. Electrochem.* 5 (2017) 135–145.
- [9] V. Fourmond, Direct electrochemistry of molybdenum and tungsten enzymes, in: *Encyclopedia of Interfacial Chemistry*, Elsevier, 2018: pp. 477–488.
- [10] V. Fourmond, T. Lautier, C. Baffert, F. Leroux, P.-P. Liebgott, S. Dementin, M. Rousset, P. Arnoux, D. Pignol, I. Meynial-Salles, P. Soucaille, P. Bertrand, C. Léger, Correcting for electrocatalyst desorption and inactivation in chronoamperometry experiments, *Anal. Chem.* 81 (2009) 2962–2968.
- [11] G. Binyamin, A. Heller, Stabilization of wired glucose oxidase anodes rotating at 1000 rpm at 37°C, *J. Electrochem. Soc.* 146 (1999) 2965–2967.
- [12] M. Fadel, J.-V. Daurelle, V. Fourmond, J. Vicente, A new electrochemical cell with a uniformly accessible electrode to study fast catalytic reactions, *Phys. Chem. Chem. Phys.* 21 (2019)

- 12360–12371.
- [13] A. Hadj Ahmed, J.-V. Daurelle, V. Fourmond, Optimizing the mass transport of wall-tube electrodes for protein film electrochemistry, *Electrochim. Acta.* 403 (2022) 139521.
- [14] M.G. Almeida, C.M. Silveira, B. Guigliarelli, P. Bertrand, J.J.G. Moura, I. Moura, C. Léger, A needle in a haystack: the active site of the membrane-bound complex cytochrome c nitrite reductase, *FEBS Lett.* 581 (2007) 284–288.
- [15] K.J. Bundy, L.G. Harris, B.A. Rahn, R.G. Richards, Measurement of fibroblast and bacterial detachment from biomaterials using jet impingement, *Cell Biol. Int.* 25 (2001) 289–307.
- [16] S. Bayouhd, L. Ponsonnet, H.B. Ouada, A. Bakhrouf, A. Othmane, Bacterial detachment from hydrophilic and hydrophobic surfaces using a microjet impingement, *Colloids Surf. A Physicochem. Eng. Asp.* 266 (2005) 160–167.
- [17] J.M. Esteban, G.S. Hickey, M.E. Orazem, The impinging jet electrode: Measurement of the hydrodynamic constant and its use for evaluating film persistency, *Corrosion.* 46 (1990) 896–901.
- [18] D. Pankratov, J. Sotres, A. Barrantes, T. Arnebrant, S. Shleev, Interfacial behavior and activity of laccase and bilirubin oxidase on bare gold surfaces, *Langmuir.* 30 (2014) 2943–2951.
- [19] K. Singh, T. McArdle, P.R. Sullivan, C.F. Blanford, Sources of activity loss in the fuel cell enzyme bilirubin oxidase, *Energy Environ. Sci.* 6 (2013) 2460.
- [20] Y. Kamitaka, S. Tsujimura, T. Ikeda, K. Kano, Electrochemical Quartz Crystal Microbalance Study of Direct Bioelectrocatalytic Reduction of Bilirubin Oxidase, *Electrochemistry.* 74 (2006) 642–644.
- [21] C. Gutierrez-Sanchez, A. Ciaccafava, P.Y. Blanchard, K. Monsalve, M.T. Giudici-Ortoni, S. Lecomte, E. Lojou, Efficiency of enzymatic O₂ reduction by *Myrothecium verrucaria* bilirubin oxidase probed by surface plasmon resonance, PMIRRAS, and electrochemistry, *ACS Catal.* 6 (2016) 5482–5492.
- [22] O. Rüdiger, J.M. Abad, E.C. Hatchikian, V.M. Fernandez, A.L. De Lacey, Oriented immobilization of *Desulfovibrio gigas* hydrogenase onto carbon electrodes by covalent bonds for nonmediated oxidation of H₂, *J. Am. Chem. Soc.* 127 (2005) 16008–16009.
- [23] E. Lojou, X. Luo, M. Brugna, N. Candoni, S. Dementin, M.T. Giudici-Ortoni, Biocatalysts for fuel cells: efficient hydrogenase orientation for H₂ oxidation at electrodes modified with carbon nanotubes, *J. Biol. Inorg. Chem.* 13 (2008) 1157–1167.
- [24] C. Baffert, K. Sybirna, P. Ezanno, T. Lautier, V. Hajj, I. Meynial-Salles, P. Soucaille, H. Bottin, C. Léger, Covalent attachment of FeFe hydrogenases to carbon electrodes for direct electron transfer, *Anal. Chem.* 84 (2012) 7999–8005.
- [25] M. Pellissier, F. Barrière, A.J. Downard, D. Leech, Improved stability of redox enzyme layers on glassy carbon electrodes via covalent grafting, *Electrochem. Commun.* 10 (2008) 835–838.
- [26] F.A. Al-Lolage, M. Meneghello, S. Ma, R. Ludwig, P.N. Bartlett, A flexible method for the stable, covalent immobilization of enzymes at electrode surfaces, *ChemElectroChem.* 4 (2017) 1528–1534.
- [27] F. Tasca, W. Harreither, R. Ludwig, J.J. Gooding, L. Gorton, Cellobiose dehydrogenase aryl diazonium modified single walled carbon nanotubes: enhanced direct electron transfer through a positively charged surface, *Anal. Chem.* 83 (2011) 3042–3049.
- [28] M. Sosna, J.-M. Chrétien, J.D. Kilburn, P.N. Bartlett, Monolayer anthracene and anthraquinone modified electrodes as platforms for *Trametes hirsuta* laccase immobilisation, *Phys. Chem. Chem. Phys.* 12 (2010) 10018–10026.
- [29] V. Fourmond, C. Greco, K. Sybirna, C. Baffert, P.-H. Wang, P. Ezanno, M. Montefiori, M. Bruschi, I. Meynial-Salles, P. Soucaille, J. Blumberger, H. Bottin, L. De Gioia, C. Léger, The oxidative inactivation of FeFe hydrogenase reveals the flexibility of the H-cluster, *Nat. Chem.* 6 (2014) 336–342.
- [30] V. Fourmond, QSoas: A Versatile Software for Data Analysis, *Anal. Chem.* 88 (2016) 5050–5052.

Mechanical stress does not (necessarily) cause film loss in protein film electrochemistry

Supplementary information

Asmaa Hadj-Ahmed^{a,b}, Anna Aldinio-Colbachini^{a,b}, Americo G. Duarte^c, Jean-Vincent Daurelle^b, Vincent Fourmond^{a*}

^aAix-Marseille Université, CNRS, BIP UMR 7281, 31 Chemin J. AIGUIER, CS70071, Marseille Cedex 20 F-13402, France

^bLaboratoire IUSTI (UMR AMU-CNRS 7343) Polytech Marseille, Dpt Mécanique Energétique (ME), Technopôle de Château Gombert, 5 rue Enrico Fermi, Marseille cedex 13 13453, France

^cInstituto de Tecnologia Química e Biológica António Xavier/Universidade Nova de Lisboa, Av. da República, Estação Agronómica Nacional, 2780-157 Oeiras, Portugal.

*vincent.fourmond@imm.cnrs.fr

1. Enzyme preparation

Cytochrome c Nitrite reductase (ccNir) was purified from *Desulfovibrio desulfuricans* ATCC 27774 cells as previously described for the homologous protein from *Desulfovibrio vulgaris*[1]. Briefly, the membrane protein content was extracted with n-dodecyl-d-maltoside (DDM). The crude membrane extract was loaded in a Q-Sepharose High Performance column (GE Healthcare) equilibrated with 50 mM Tris-HCl pH 7.6, 10 % (v/v) glycerol, 0.1% (w/v) DDM. The fractions eluted between 50 and 100 mM NaCl were concentrated, buffer exchanged and applied in the same column using the same buffers. In this chromatographic step, the fraction eluted before the start of the gradient containing ccNir was loaded in a Sephacryl S-300 equilibrated with 10 mM Tris-HCl pH 7.6, 100 mM NaCl, 0.03 % (w/v) DDM. ccNir purity was constantly evaluated by UV-visible spectrum and SDS-PAGE electrophoresis stained with Coomassie blue and heme staining[2].

Before use, the enzyme was thawed inside the glove box, diluted 10 times until a final concentration of 2.9 mM and stored in a fridge inside the glove box fridge.

2. Electrochemical setup

All the experiments were carried out at room temperature inside a glove box (Jacomex), filled with N₂ (O₂ < 1 ppm), located in a climate room. All solutions were previously degassed with Ar in order to remove any trace of O₂.

We employed a three-electrode electrochemical cell of our conception, projected on a wall-tube electrode, still lacking for thermostatic control. The device, 3D-printed in ABS-like material, comprises two modules: the top part, with the inlet and the outlets and the bottom part, with the electrodes. Further information about the design and optimization of the cell can be found in our previous works[3,4].

A solution of NaNO_2 40 μM dissolved in mixed buffer containing 5 mM each of MES, sodium acetate, HEPES, TAPS and CHES, and 0.1 M NaCl at pH 7, was impinged towards a film of Dv ccNir (0.5 μL of enzyme 2.9 mM) immobilized on a pyrolytic graphite “edge” electrode by means of a syringe pump (Chemix), manually controlled. The nozzle-electrode distance was calibrated at 0.3 mm using a spacer. An Ag/AgCl saturated electrode was used as reference: the reference electrode chamber was fulfilled with the solution flowing, in order to prevent any shift in potential along the experiment duration, due to the pore-size of our frit. A platinum wire was employed as counter electrode.

The potential control was performed by means of a potentiostat connected to GPES software. A current was recorded.

All blanks were obtained using the same buffer, but devoid of nitrite.

Meticulous attention to prevent air bubble formation was paid over the entire setup. In particular, the frit was delicately wetted, the cell internal volume was filled and all the pipes were controlled before starting the flow.

In spite of our best efforts, some small bubbles were still present at times. Their influence on the flow rate was minimized by avoiding all kinds of movement that could change the pressure inside the glove box.

Each measurement was reproduced 11 times in order to make our conclusions statistically significant, using a series of 6 experiments. The Ag/AgCl reference electrode we used was drifting significantly from day to day, so we used an internal reference for calibrating the potential. At the beginning of each experiment, a cyclic voltammogram was recorded (flow rate of 1 mL/min, scan rate = 0.1 V/s) and the position of the intermediate peak was determined (see the star in figure S1). The potential used for the chronoamperometric experiments was 350 mV below this point. We also recorded CVs at the end of the experiments to make sure the potential had not drifted during the experiment. This approach allowed to decrease as much as possible the influence of artifacts coming from the instability of the reference electrode.

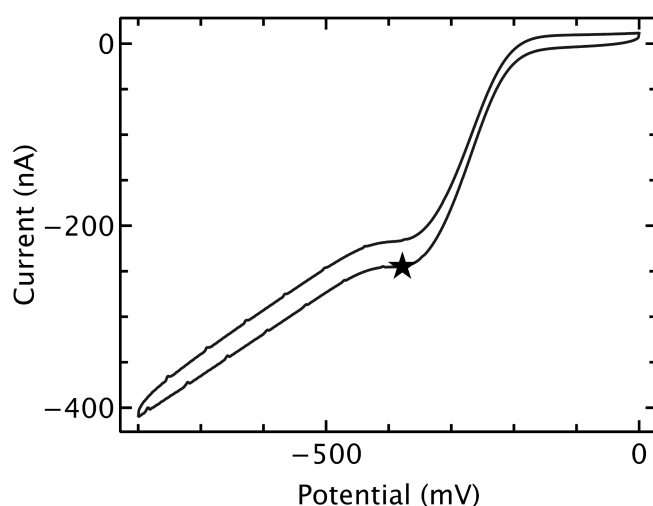


Figure S1. cyclic voltammogram of the response of a film of ccNir to an exposure to 40 μM nitrite with a flow rate of 1 mL/min (scan rate = 0.1 V/s). The star indicates the reduction peak we used

as a benchmark to fix the potential (350 mV below) to record the chronoamperograms (see Figure 1, panel B).

The small peak-like regular fluctuations, visible on the voltammogram below the value of potential corresponding to the star, presumably come from the periodic flow rate and pressure fluctuations originating from the stepper motor of our syringe-pump. (10.1109/FPM.2015.7337207, 10.1039/c3lc51176f) [5,6]

Then, the value of the potential was fixed to record a chronoamperogram. 12 different flow rates were imposed twice for 90 seconds each, with a fixed order: 2.5, 0.5, 1.7, 2, 0.6, 3, 0.8, 1.5, 2.8, 1, 2.3, 1.2, 2, 0.8, 2.5, 1, 2.3, 0.6, 1.5, 0.5, 2.8, 1.2, 3, and 1.7 mL/min. The flow rate range was kept in between 0.5 mL/min and 3 mL/min to minimize syringe pump-induced pressure fluctuations[7].

Finally, a second cyclic voltammogram with exactly the same parameters as the first one, was recorded to ensure the reference electrode potential didn't shift during the procedure.

3. Data analysis

All data were analyzed with QSoas software[8]. We considered all measurements recorded in the chronoamperograms, except the second round of 12 of a single experiment: the background noise's fluctuations were too large to manipulate it.

Each file was analyzed performing manually the linear regression of the time intervals at constant flow rate (see SCRIPT 2). The output files contain the information of the K_{eff} in function of the flow rate (*.dat).

The information about each series of 12 consecutive different measurements was isolated in a single file, obtaining 11 different output files.

Panel A of Figure 2 was plotted after averaging the values of the effective rate constant (k_{eff}) computed for a certain flow rate in all experiments and calculating the standard deviation on the values averaged (see SCRIPT 3).

Panel B of Figure 2 was plotted after normalizing the values of k_{eff} by the average of all k_{eff} estimated along that experiment, then averaging the values and calculating the standard deviation as for Panel A of the same figure.

SCRIPT 1:

reg

SCRIPT 2:

chop *all intervals duration (number) separated by one space each* /set-segments=true

a *file name*

save

set-meta *name* /type=number-list *all flow rates in order, separated by commas, without spaces*

segments-chop /expand-meta=*name*

flag *all buffers corresponding to a segment* /flags=*flag*

output /meta=*name*

```
run-for-datasets SCRIPT1.cmds flagged manual regression: pick bounds (left and right), write to output file  
(command: spacebar), next buffer (command: n)
```

```
apply-formula x=y6
```

```
tweak-columns /select=x,y3
```

```
save
```

```
SCRIPT 3;
```

```
load ${1}
```

```
apply-formula y2=y**2 /extra-columns=1
```

```
flag /flags=flag2
```

```
SCRIPT 4:
```

```
run-for-each SCRIPT3.cmds *.dat
```

```
average flagged:flag2
```

```
apply-formula (y2=y2-y**2)**0.5
```

```
dataset-options /yerrors=y2]
```

4. Mass transport limitation

Despite the apparent change in current when changing the flow rate, the current is far from being limited by mass transport. Looking at the first transition in figure 1 of main text, the current goes from about -350 nA down to -330 nA (about 6 % difference) for a change from 2.5 mL/min to 0.5 mL/min. If the current was mass-transport limited, the current should be proportional to the mass-transport coefficient, which scales as the power 0.45 of the flow rate. One would therefore expect a decrease of 51 %. That the decrease is almost an order of magnitude proves that the mass transport has only limited control on the current.

5. Numerical simulations

Numerical simulations with the different values of the flow rates were performed exactly in the same way as described in ref [4]. We extracted the values of the pressure and shear stress along the electrode (plotted in figure S2), and averaged them over the whole surface of the electrode to obtain figure S3, the plot of the average shear stress and pressure as a function of flow rate. These data were used to reinterpret the data plotted as a function of flow rate in figure 2 in text to plot them as a function of average shear stress and pressure in figure S4.

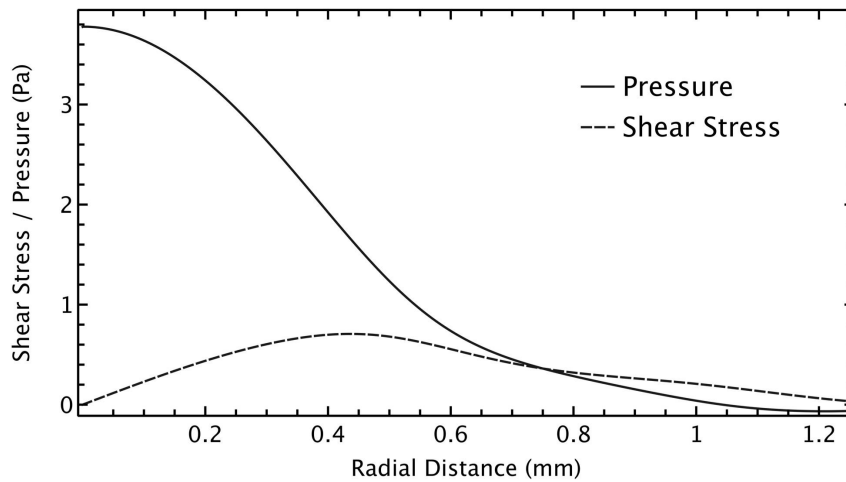


Figure S2: Simulated profile of (normal) pressure and shear stress along the electrode as function of the radial distance from its rotational symmetry axis, for a flow rate of 1.7 mL/min. Determined under the same conditions as in ref[4]. The data show that the pressure on the electrode is maximal at the center of the electrode and decreases with the distance from the symmetry axis, while the shear stress increases linearly up to a certain distance (about 0.5 mm). Both have similar magnitudes, the pressure being 2-3 times larger than the shear stress.

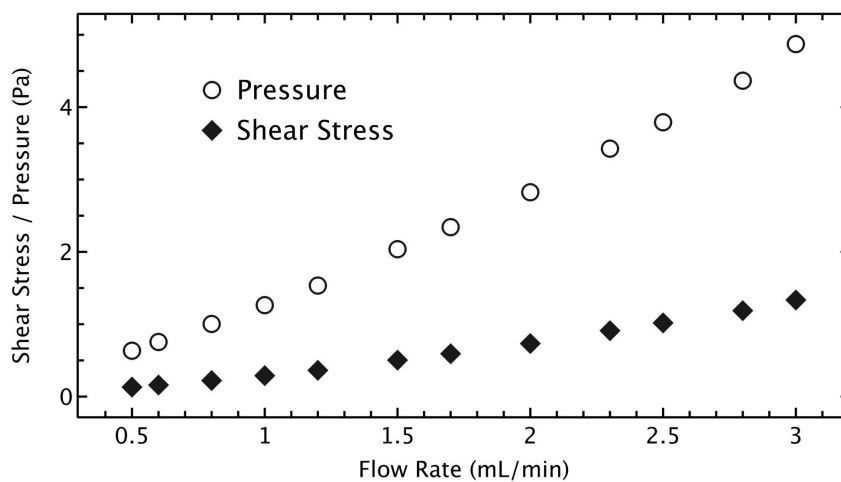


Figure S3: Simulated average (normal) pressure and shear stress on the electrode surface ($r=0.5$ mm) as function of flow rate, obtained after numerical simulation. Determined under the same conditions as in ref [4].

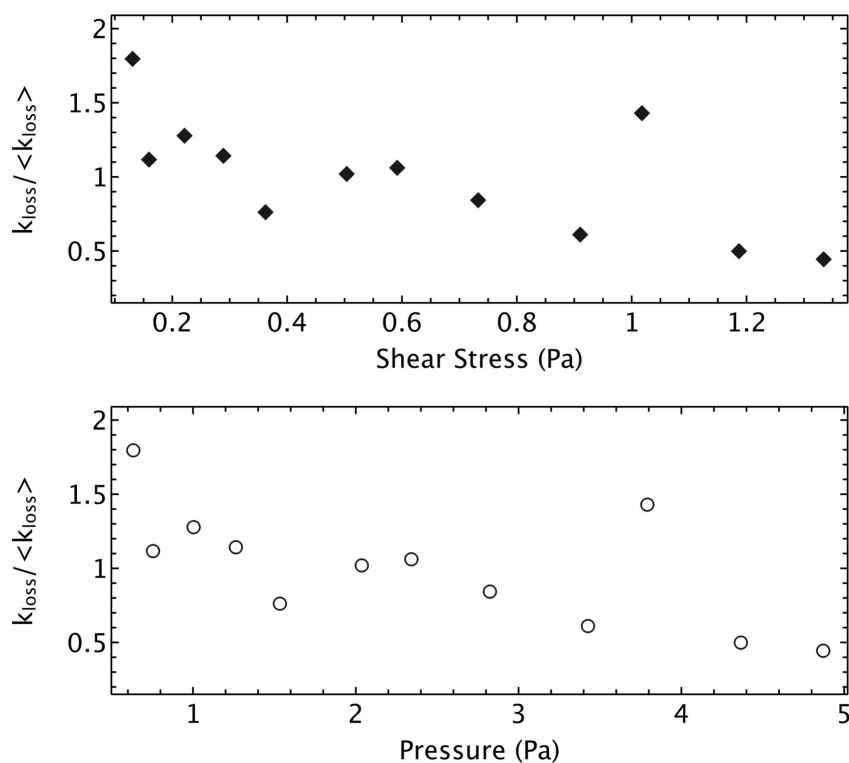


Figure S4: Dependency of relative experimental film loss rate constant (as plotted in figure 2 of text) as a function of the average simulated shear stress (panel A, see also diamonds in figure S4) and average (normal) pressure (panel B, see also circles in figure S4). Electrode size: $r=0.5$ mm.

- [1] M.L. Rodrigues, T. Oliveira, P.M. Matias, I.C. Martins, F.M.A. Valente, I.A.C. Pereira, M. Archer, Crystallization and preliminary structure determination of the membrane-bound complex cytochrome c nitrite reductase from *Desulfovibrio vulgaris* Hildenborough, *Acta Crystallogr. Sect. F Struct. Biol. Cryst. Commun.* 62 (2006) 565–568. <https://doi.org/10.1107/S1744309106016629>.
- [2] R.T. Francis Jr, R.R. Becker, Specific indication of hemoproteins in polyacrylamide gels using a double-staining process, *Anal. Biochem.* 136 (1984) 509–514. [https://doi.org/10.1016/0003-2697\(84\)90253-7](https://doi.org/10.1016/0003-2697(84)90253-7).
- [3] M. Fadel, J.-V. Daurelle, V. Fourmond, J. Vicente, A new electrochemical cell with a uniformly accessible electrode to study fast catalytic reactions, *Phys. Chem. Chem. Phys.* 21 (2019) 12360–12371. <https://doi.org/10.1039/c9cp01487j>.
- [4] A. Hadj Ahmed, J.-V. Daurelle, V. Fourmond, Optimizing the mass transport of wall-tube electrodes for protein film electrochemistry, *Electrochim. Acta.* 403 (2022) 139521. <https://doi.org/10.1016/j.electacta.2021.139521>.
- [5] W. Zeng, S. Li, Z. Wang, Characterization of syringe-pump-driven versus pressure-driven microfluidic flows, in: 2015 International Conference on Fluid Power and Mechatronics (FPM), IEEE, 2015. <https://doi.org/10.1109/fpm.2015.7337207>.
- [6] Z. Li, S.Y. Mak, A. Sauret, H.C. Shum, Syringe-pump-induced fluctuation in all-aqueous microfluidic system implications for flow rate accuracy, *Lab Chip.* 14 (2014) 744–749. <https://doi.org/10.1039/c3lc51176f>.
- [7] W. Zeng, I. Jacobi, D.J. Beck, S. Li, H.A. Stone, Characterization of syringe-pump-driven induced pressure fluctuations in elastic microchannels, *Lab Chip.* 15 (2015) 1110–1115. <https://doi.org/10.1039/c4lc01347f>.
- [8] V. Fourmond, QSoas: A Versatile Software for Data Analysis, *Anal. Chem.* 88 (2016) 5050–5052. <https://doi.org/10.1021/acs.analchem.6b00224>.

Chapter 5

Mixing in the new cell: a means to control concentrations

This chapter addresses the second aim of the thesis which is to develop a setup that provides a much greater flexibility for changing the concentration of the species that the immobilized enzyme is exposed to. To address this objective, we first tested the control of concentrations in the first prototype of wall-tube cell (described in fig 1.16) by mixing two solutions with different concentrations of ferricyanide and recording the reduction current which is proportional to the average concentration as a function of time. The preliminary results showed that we succeeded in changing (or controlling) the concentration arbitrarily. However two issues were encountered:

- the response time was long;
- the concentration of the mixture was spatially heterogeneous.

Following that, we tried to identify the origins of these problems in order to propose appropriate solutions. Thus, in the next sections, I will explain the sources of these issues and the possible solutions that we proposed.

5.1 Characterize the mixing in the first prototype

Chronoamperometry experiments were used to test the control of concentration in the setup as it is explained bellow.

5.1.1 Mixing using Y and T junctions

We used an experimental setup (5.1) that is composed of:

- The wall-tube cell.
- Two syringe pumps of (100 mL): one is filled with the electrolyte NaCl (0.5 M) and the other one is filled with $\text{Fe}(\text{CN})_6^{3-}$ (5 mM) that is dissolved in NaCl (0.5 M).

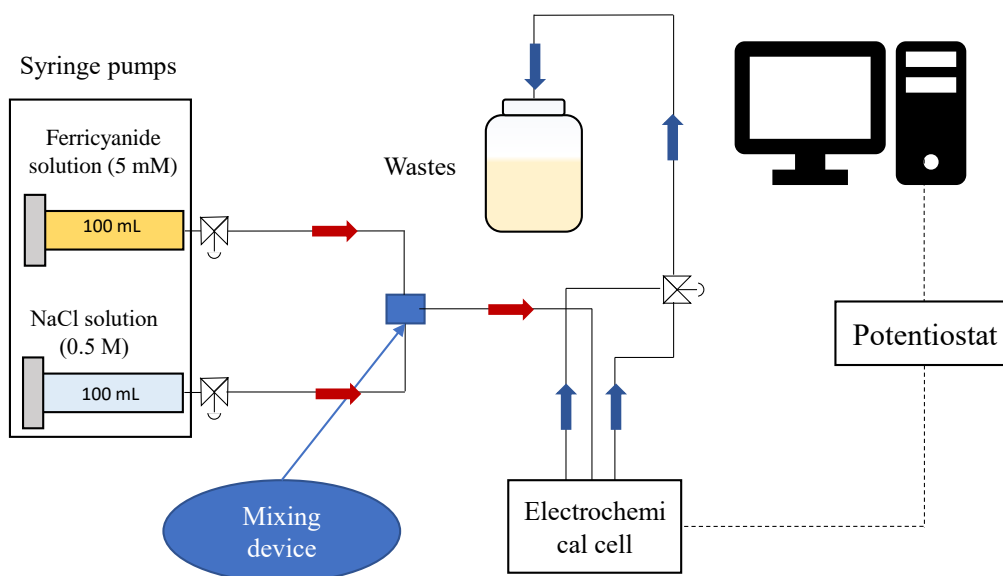


Fig. 5.1 Schematic of the experimental setup

- Simple mixing tools (T or Y fitting tubes).
- Waste container.
- Pipes and fitting tubes for connection.

During the experiments, we fixed the potential and we recorded the ferricyanide reduction current over time while changing the concentration by mixing the solutions from the syringes in the mixing tool.

The principle here is that if we mix two fluids with a given flow rate Q_i and if they are mixed perfectly, the concentration that we expect to get (C_{expect}) is the weighted average of the initial concentrations (5.1):

$$C_{expect} = \frac{\sum C_i Q_i}{\sum Q_i} \quad (5.1)$$

The total flow rate should be maintained constant so that mass transport is constant. When this is true, the measured current will depend only on the actual concentration that arrives to the electrode. In fact, the current will be proportional to the actual concentration.

Figs 5.2.A,B,C represent the results of the current of ferricyanide reduction as function of time at different concentrations using respectively the fitting tubes (T,Y and Y with obstacles) as mixing tools and figs 5.2.D,E,F show the plateau current from the chronoamperograms 5.2.A,B,C as a function of the expected concentration of ferricyanide that was obtained by mixing the two solutions (ferricyanide (50 mM) and NaCl (0.5 M)) inside the mixing tools.

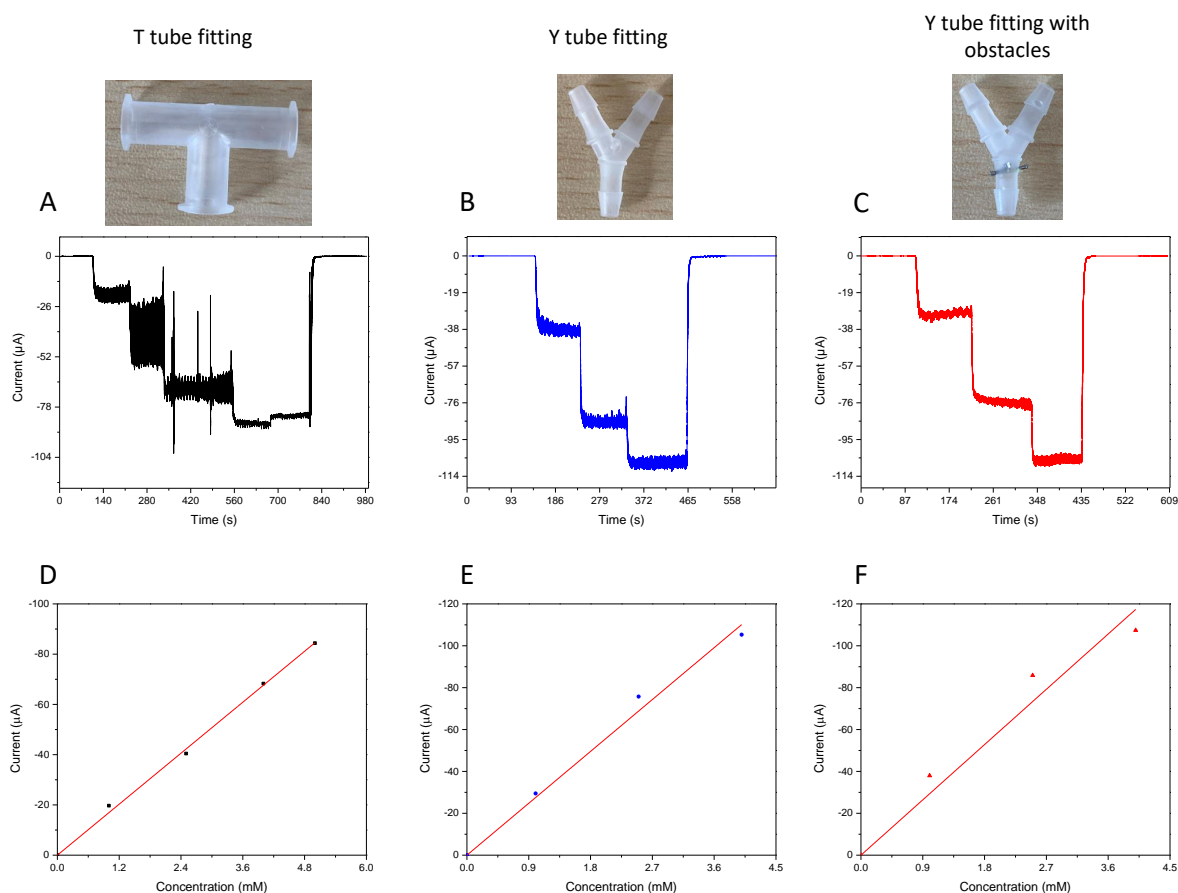


Fig. 5.2 Mixing with different type of fitting tubes. A,B,C: current of ferricyanide reduction as function of time at different concentrations using respectively the depicted fitting tubes T,Y and Y with obstacles. D,E,F: The plateau current as a function of ferricyanide expected concentration (equation (1.62)) that was obtained by mixing two solutions (ferricyanide (5 mM) and NaCl (0.5 M)) in the depicted mixing tools. The total flow rate was maintained at 10 mL/min

The overall results from fig 5.2.A,B,C shows that increasing the concentration and even removing ferricyanide completely from the cell was achieved in a continuous experiment by just controlling the relative flow rates. Note that is impossible to remove the electroactive species from the RDE cell without stopping the experiment to empty the cell and fill it again.

The plateau current in fig 5.2.D,E,F is proportional to the expected concentration of ferricyanide. From this, we can conclude that the current, and therefore the concentration, is what we think it should be according to how we expect the mixing to work, which means that the setup can be used to achieve arbitrary changes of concentration by just mixing solutions with different concentrations.

Moreover, the fact that the current is proportional to the expected concentration, will allow us to characterise the mixing and the response time of the system by just looking at the behaviour of the recorded current. However, if one look closely to one of the steps in the recorded current (fig 5.3), two problems can be detected:

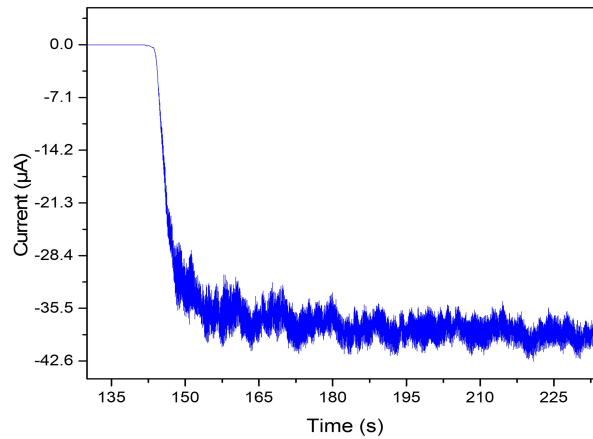


Fig. 5.3 Inset from the the first step of current in fig 5.2.B.

- The response time is too long (about 10 s);
- There are fluctuations in the recorded current.

In the rest of the chapter, I will present the possible origins of the two issues that we have identified during the experiments and the solutions that we propose for solving them.

5.1.2 Possible origins of the delay

If we consider a flow entering a pipe with a uniform velocity, when the flow is laminar, the axial velocity has a parabolic profile. This can be explained by the fact that the fluid particles in the layer in contact with the surface of the pipe are not moving due to friction with the wall, and thus the fluid particles in the adjacent layers slow down gradually as a result of friction between the layers. As a consequence, the velocity becomes non uniform along the section of the pipe in the radial direction (fig 5.4.A). Therefore, particles of the fluid in the center of the pipe will exit much sooner than the ones close to the walls.

The velocity of the fluid at any point in the tube, v , can be described by the Poiseuille equation (2.19) that I have already shown in chapter 2:

$$v = \frac{dP}{dz} \frac{1}{4\mu} (r^2 - R^2) \quad (5.2)$$

We assume that we managed to change instantaneously the concentration at the mixing point (black dashed line in fig 5.4.B). So, we consider a solution $S1$ with a uniform dimensionless concentration ($C_1 = 1$) that will be leaving the mixing point at $t = t_0$. The rest of the tube is assumed to be filled with a solution $S0$ of concentration $C_0 = 0$. We also consider a section at the end of the pipe (equivalent to the jet section above the electrode

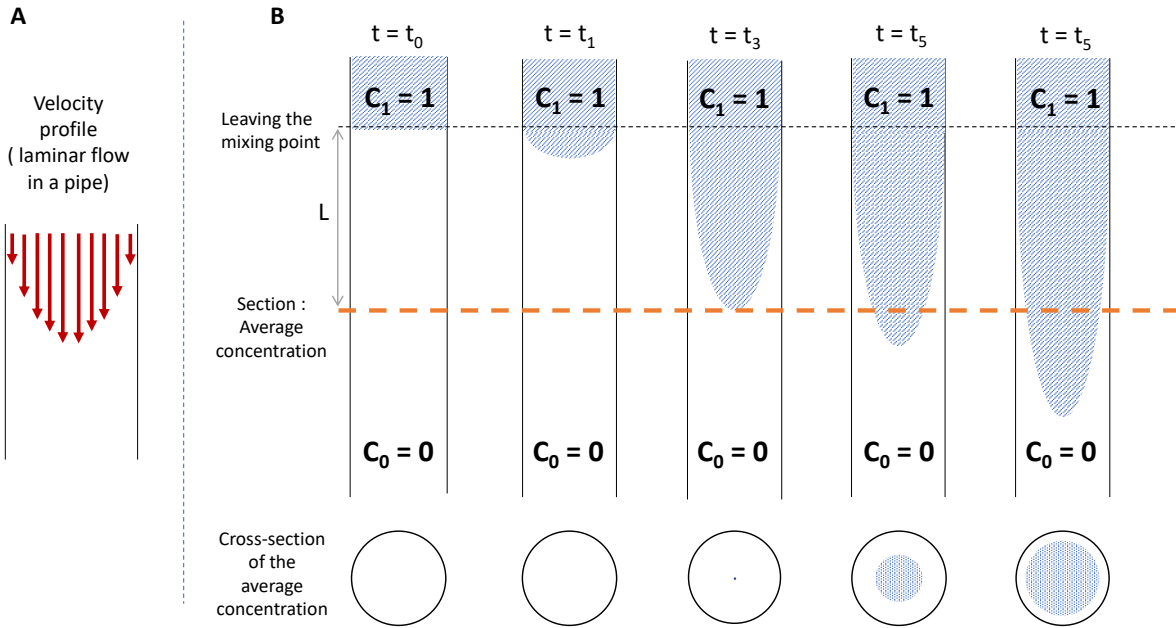


Fig. 5.4 A: velocity profile in a pipe at laminar flow regime. B: schematic representation of the development of the average concentration in the section above the electrode over time.

in our setup) where we follow the development of the concentration. We assume that the distance between this section and the mixing point is L .

By looking at the radial cross view of this section in fig 5.4.B. It is clear that before some time, there is only solution S_0 . Starting from t_3 , solution S_1 arrives with a narrow parabolic shape due to the behaviour of the pipe flow. The area of section of the paraboloid A_1 , grows with time (blue circle in fig 5.4.B) and thus the average concentration C increases over time as shown in fig 5.5. This concentration is the average of the initial concentrations C_1 and C_0 weighted by the areas A_1 and A_0 (A_0 is the area occupied by solution S_0 at the measuring section):

$$C = \frac{C_1 \times A_1 + C_0 \times A_0}{A_1 + A_0} \quad (5.3)$$

taking into account that $C_0 = 0$ and $A_1 + A_0 = A_p$ where A_p is the section area of the pipe, equation (5.3) can be simplified to:

$$C = C_1 \frac{A_1}{A_p} \quad (5.4)$$

Going from this, and with neglecting diffusion, we computed the average concentration in the cross-section over time.

Since the distance between the mixing point and the cross-section is L , we can write:

$$\int_0^L \frac{dP}{dz} = \frac{\Delta P}{L} \quad (5.5)$$

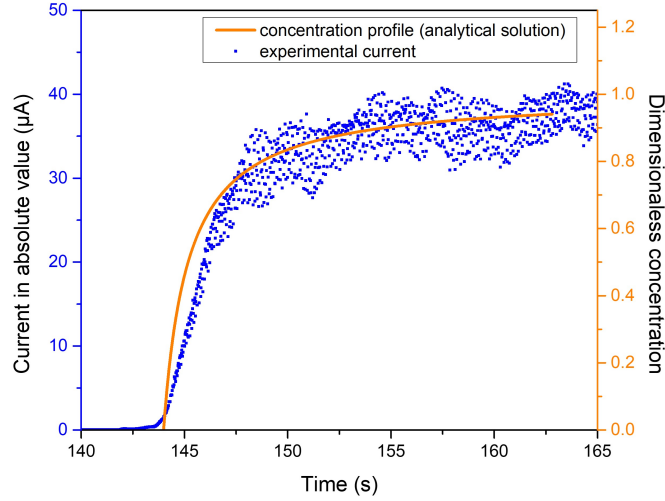


Fig. 5.5 Orange plot: Average concentration profile at the section (in the dashed orange section shown in fig 5.4.B) over time. Blue plot: The experimental current from fig 5.3 over time.

then equation (5.2) becomes:

$$v = \frac{\Delta P}{4\mu L}(r^2 - R^2) \quad (5.6)$$

in which ΔP is the pressure drop, r is the radial distance and R is the radius of the pipe.

We have $vt = L$, then:

$$L = \frac{\Delta P t}{4\mu L}(r_c^2 - R^2) \quad (5.7)$$

in which r_c is the the radius of the section occupied by solution $S1$ at the measuring point.

$$r_c^2 = \frac{4\mu L^2}{\Delta P} \times \frac{1}{t} + R^2 \quad (5.8)$$

then, equation (5.4) becomes

$$\frac{C}{C_1} = \frac{r_c^2}{R^2} = \left(\frac{4\mu L^2}{\Delta P R^2} \times \frac{1}{t} + 1 \right) \quad (5.9)$$

equation (5.9) can be written as:

$$\frac{C}{C_1} = 1 - \frac{\tau_0}{t} \quad (5.10)$$

with

$$\tau_0 = -\frac{4\mu L^2}{\Delta P R^2} \quad (5.11)$$

Equation (5.10) is true only after the solution $S1$ reaches the measuring section, which can be expressed to $t \geq \tau_0$.

Equation (5.10) is a hyperbolic function which means that it takes a long time to reach the final concentration (fig 5.5).

By superposing the experimental current from fig 5.3 with the dimensionless concentration calculated by equation (5.10) (using the real experimental dimensions ($R = 0.79$ mm and $L = 200$ mm)), the two plots fit, which confirm our initial hypothesis that the delay observed experimentally is mainly caused by the behaviour of the pipe flow. It is proportional to the square of the distance between the mixing point and the electrode.

As a conclusion, even if we manage to have a perfect mixing in our experiment, we will have a delay that is proportional to square of the distance between the mixing tool and the jet. Therefore, to reduce this delay, the mixing tool have to be placed as close as possible to the jet and therefore to the electrode.

5.1.3 Possible sources of fluctuations

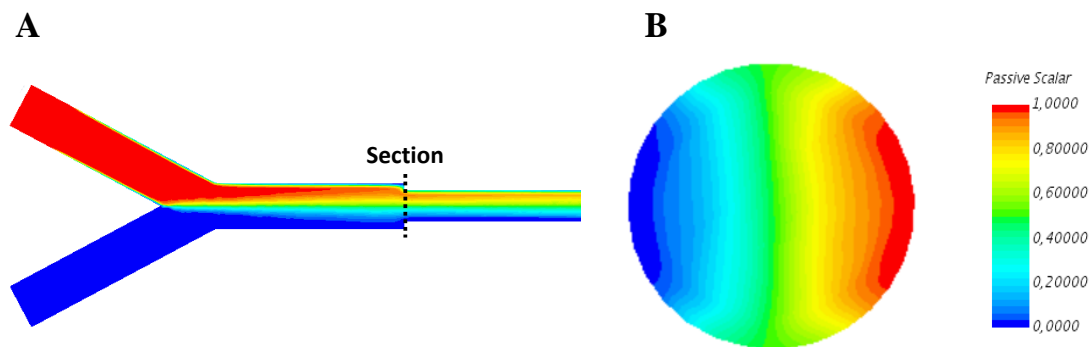


Fig. 5.6 Mixing in the Y fitting tube. A: Map of axial concentration field in a Y fitting tube after injecting two liquids with same physical properties and different concentration $C_1 = 0$ and $C_2 = 1$. B: Radial concentration field's map in the section of the outlet of the Y fitting tube.

The fluctuations observed in the recorded current can be caused by different phenomena:

- The syringe plunger can induce regular fluctuations in the flow;
- The two pumps are not working exactly in the same way;
- Possibly there are some fluctuations when the two relative flow rates are not equal...

When we investigated the sources of fluctuations, we realized that the mixing is not sufficient, and it seemed reasonable to assume that because of the poor mixing, all the small defects such as the ones that I have listed above are going to be more pronounced in the recorded current.

In fact, the mixing is not good with the tools that we used in our experiments. To investigate that, we conducted simulation of mixing in the Y fitting tube. Fig 5.6.A shows a map of axial concentration field in a Y fitting tube after injecting two liquids with same

physical properties and different concentration $C_1 = 0$ and $C_2 = 1$ with a total flow rate 10 mL/min. Fig 5.6.B shows the radial concentration field's map in the exit section of the Y fitting tube. It can be seen that there is almost no mixing inside the Y fitting tube and thus the concentration is significantly heterogeneous at the outlet section.

One should also note that this is ideal world simulation, which means that in reality, mixing would certainly be less bad as it appears in simulation because of disymetries and imperfections.

Although we didn't actually simulate this hypothesis, we suspect that any small fluctuations in the flow rate are going to be amplified by the heterogeneity of concentration and they hence going to appear as significant current fluctuations.

Eventually, the problem is not really the fluctuations, but the fact that we're not mixing. This means that the local concentration of the species that arrive to the electrode is very heterogeneous and this can't be measured experimentally because the the current that we record is only proportional to the average concentration.

A large heterogeneity is incompatible with the aim of using the cell to study enzymes, because we need highly homogeneous concentrations in this case. Therefore, mixing tools that allows better mixing and thus less heterogeneity of concentrations should be used.

To overcome the limitations explained in sections 5.1.2 and 5.1.3, we chose to design better mixing devices that ensure homogeneous concentration, and to reduce the response time, this devices have to be placed as close as possible to the electrode. This led us to design new cells with integrated mixers.

Since we need to make efficient mixing, it's crucial to have idea about the different strategies that are used to achieve that. For this reason, before passing to show the cells that we designed, I will give a brief presentation of the mixers available in literature. I will speak particularly about laminar mixing. Turbulent mixing is very good, but it can't be used in our case, because turbulence means fluctuations and we want to avoid them at all costs.

5.2 Literature review of laminar mixing processes

Fluids mixing is an essential step in many processes such as chemical reactions, DNA purification, mass transfer, heat transfer... Clearly, it is easier to mix fluids in turbulent flows (high Re). However, it is extremely difficult to mix them when the flow is laminar (low Re) as stream layers are parallel to each other.

Laminar mixing became a hot topic for academic research in the recent years since it is an important process for many engineering applications where turbulence cannot be used or generated (viscous, pressure drop, practical complication...). For instance, this problem is often encountered in pharmaceutical, cosmetic, agri-food, charged fluid particles and biological applications where low flow rates are imposed or using shear-sensitive cell cultures or substances are involved [183].

5.2.1 Laminar micromixers

In the last three decades, and due to the development of microfluidic field, mixing in small scales gained a great importance and since then it have been widely applied in various applications that involve chemical reactions where, most often, the diffusion in fluids is very low so that without the help of mixing, the reaction time can be extremely long.

To improve mixing at micro scale, different types of micromixers have been developed, they can be mainly classified into two categories: active [184–186] and passive micromixers [187–190].

- Active micromixers where external sources of energy are used such as vibrations, acoustics, pressure disturbance, electric and magnetic fields [191].
- Passive micromixers which don't involve the use of an external force and only depends on the geometry of the flow passage [191]. They are simply based on the splitting, stretching, folding and breaking of the flow in order to produce complex flow fields to increase mixing efficiency [192].

In this thesis, active mixers were not considered since we are limited in terms of space and it would very complicated to add parts that move as they need regular maintenance and require additional source of power. Additionally, They could have a bad effect on the film of enzymes too.

Therefore, I only focus on passive mixers as they are simple to integrate in the wall-tube cell and they don't need maintenance.

Passive micromixers can be classified into two categories [191]:

- Multi-lamination-based micromixers;
- Chaotic advection based micromixers.

Multi-lamination-based micromixers

The principle of multi-lamination is splitting a fluid stream into several sub-streams and therefore increasing the interface between the liquids. In this case, the latter interpenetrate more effectively and the size of the diffusion layer between them will be reduced [191].

Buchegger et al developed a horizontal multi-lamination micromixer based on wedge-shaped channels. They showed experimentally that this configuration allowed to achieve uniform mixing in the millisecond range [194].

Tofteberg et al proposed a design that enabled a 90° rotation of the flow before being splitted into several channels (fig 5.7). In each channel, the flow was rotated of 90° then being recombined. Basically, the splitting and recombination process was repeated until the desired degree of mixing was achieved [193].

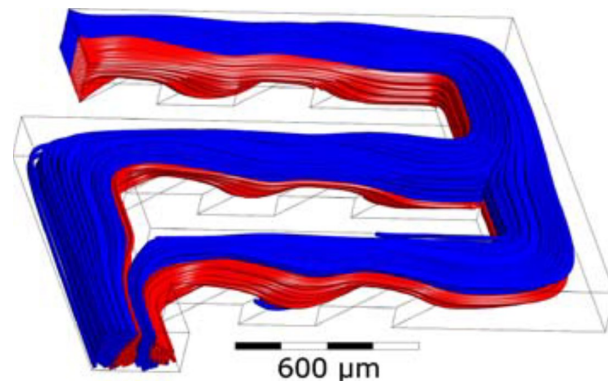


Fig. 5.7 Simulated flow field in one mixing module showing lamination in the Stokes flow regime. The two fluids enter in the upper left corner. The interfacial area between the two has approximately tripled at the exit in the lower left corner. Reprinted from 193

Chaotic advection based micromixers

At low Reynolds number, advection¹ is often parallel to the main flow direction, and not contributing in the radial mixing. Therefore, to improve mixing, chaotic advection is induced by special geometries [195]. The basic idea is to modify the shape of the channel in a way that it forces the flow to be split, stretched, folded and broken [196].

Embedded barriers This method is based on inserting obstacles into the mixing channel to create chaotic advection [197–200].

Tseng et al [198] showed by simulation that inserting diamond-shaped obstacles in a microchannel improved mixing by inducing intense vortices and secondary flows in the spanwise planes.

Fang et al [201] developed a micromixer with embedded geometric features. The experimental and simulation results showed that after 28 period mixing units, the mixing was uniform however it required a relatively long channel.

Intersecting channels Intersecting channels geometries are based on splitting, reorganizing then recombining the fluid flows [203, 189, 202].

Ansari et al [203] showed by means of numerical simulation and experimental investigation in fluids where Re was ranging from 10 to 80 that the mixing was improved in a microchannel by inducing unbalanced splits collisions of fluid streams then combining due to formation of some flow structures with rotating motion in the bending areas of the microchannel. These structures are called Dean vortices.

A modified version of the micromixer of Ansari was developed by Li et al [202], it was based on the principle of planar asymmetric split-and-recombine(P-SAR) mixing with dislocation sub-channels (fig. 5.8). They investigated the mixing quality experimentally and by simulation at Re between 1 and 100. A good mixing efficiency was achieved due

¹advection is the transport of a substance or a quantity by fluid motion.

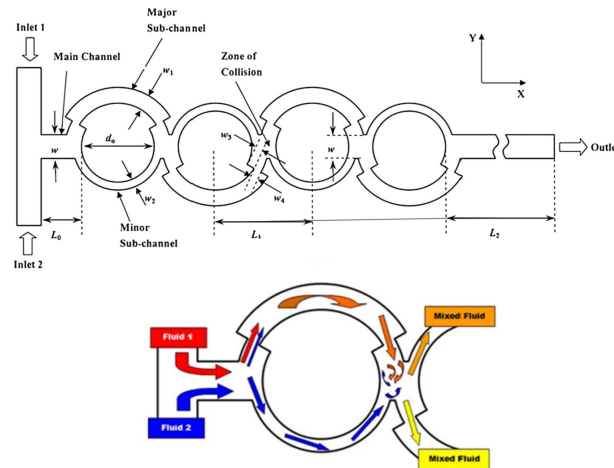


Fig. 5.8 Schematic illustrations of modified Planar Asymmetric Split-and-Recombine (P-SAR) micromixer with dislocation sub-channels. Reprinted from ref 202

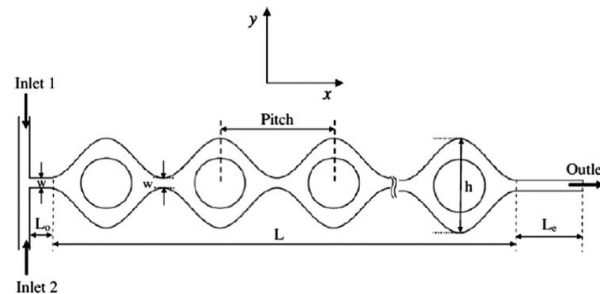


Fig. 5.9 Schematic illustration of the passive split and recombine (P-SAR) micromixer with convergent–divergent walls. Reprinted from ref 204

to the combination of unbalanced collision of the fluid streams by sub-channels and also by multi-directional vortices and collision-induced flow in the mixing cavities between neighboring two-looped structures.

Convergent–divergent channels Afzal and Kim [204] designed a passive split and recombine (P-SAR) micromixer with convergent-divergent walls, in which the main channel was separated into two sub-channels and then recombined at periodic intervals along the microchannel length (fig. 5.9). They carried out numerical simulations to investigate the mixing and the flow behaviour at Re ranging between 10 and 70. The results showed that for all Re values, the mixing effect was enhanced by the secondary flows induced in the sub-channels. In addition, at higher Re , symmetric double vortex pairs were formed at the throat of each convergent-divergent channel, which resulted in a further improvement in mixing. The optimal mixing performance was obtained at a Re of 70 in a mixer containing eight sinusoidal channel wall cycles.

The mixing in passive micromixer containing convergent-divergent sinusoidal microchannels with different amplitude-to-wavelength ratios for Re in the range between 0.2 and 50 were studied by Parsa et al [205] numerically and experimentally. They found that for Re

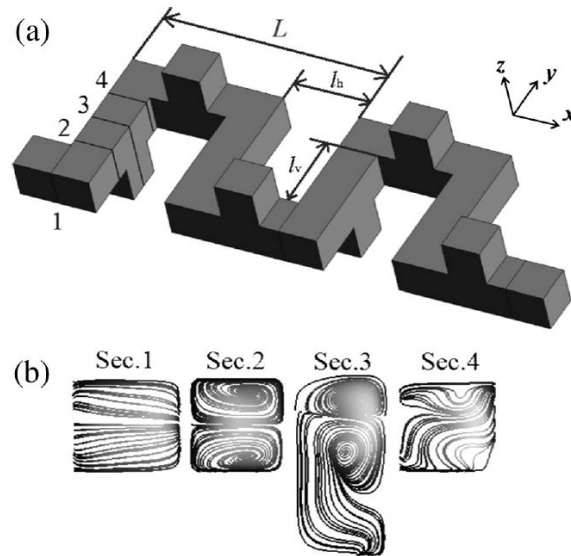


Fig. 5.10 (a) Schematic of micromixer flow path. Parameter L denotes the span of each element along x -axis direction, while l denotes length of each straight section. Subscript h indicates horizontal section (i.e., section along x -axis), while v indicates vertical section (i.e., section along y -axis). (b) CFD simulation results for streamlines at four cross-sections ($Re = 64$). Reprinted from ref 206

lower than 10, mixing was dominated by diffusion. However, as the Re was increased from 10 to 20, the mixing performance improved due to the motion induced by the centrifugal force. For Re greater than 20, the mixing performance was even better due to the formation Dean vortices.

Three-dimensional structures So far, the mixers that I have described are planar, they are widely used in microfluidics since the geometries are restricted by monolayers design. However, we are not constrained to this limitation. Therefore, we can be inspired by those designs with taking the advantage of having three dimensional patterns.

In the rest of this section, I will present some of the 3D micromixers in which the most known configurations are three dimensional spiral and serpentine shapes.

An interesting design was developed by Lin et al [206], it consisted in a periodic combination of square-wave structures and cubic grooves (fig 5.10). The square-wave structure caused laminar recirculation, and the cubic grooves induced flow stretching, resulting in significantly enhanced mixing over a wide range of Re . The mixing quality found to be enhanced with rising the flow rate, and approximated to a constant beyond a $Re = 220$. This micromixer is recommended for in line processes where the Re range between 30 and 220 [206].

Yang et al [207] presented a three-dimensional spiral micromixer consisting of two spiral channels overlapped in the vertical direction so as to produce, enhance and sustain Dean vortices. The experimental results indicated that the erect channel connecting the

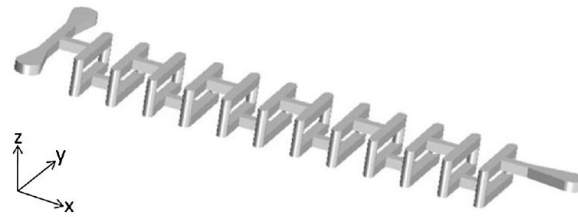


Fig. 5.11 Schematic illustration of H-shaped micromixer. Reprinted from ref 208

two spiral channel layers played an essential role in promoting mixing. Furthermore, it was shown that a very high mixing efficiency could be achieved by increasing the flow rate.

Nimafar et al [208] presented a passive micromixer based on a split and recombine (SAR) process within H-shaped sub-channels (figure 5.11). It was shown experimentally that the mixing ($Re = 0.083$).

5.2.2 Industrial static mixers

In industry, static mixers are commercialised under the name of “in-line mixers”, they have no moving elements and they are basically used for mixing fluids in continuous flow industrial systems.

Depending on the flow regime and mixing efficiency, a wide range of static mixers have been developed for specific applications. Thakur et al [209], in their review, reported the existence of 2000 US patent on static mixers.

Static mixers are employed in different applications, such as in polymer processing, chemical reactions, food processing, paints, pharmaceuticals, and water treatment [210] for industrial processes such as gas-liquid and liquid-liquid surface generation, liquid-solid dispersion, mixing of miscible fluids and heat transfer [209]. They are mostly used because unlike the mechanical agitators, they require smaller space, lower energy consumption as well as reduced construction and maintenance costs [209–211]. Generally, industrial static mixers have the same design concept as passive micromixers [196]. The basic idea is to induce chaotic advection by implementing motionless mixing elements such as blades or corrugated plates to make changes in the fluid streamlines. The most used mechanism for mixing is the split-and-recombine (SAR) which is based on splitting the incoming fluid into layers then recombining the layers in a new sequence.

Many static mixers were developed since the 70s. The most known models commercially are: SMX, SMV, HEV and Kenics mixers (fig 5.12), their concept is based on placing a number of motionless mixing elements in a pipe or channel. For instance, the SMX and SMV mixer (5.12.A) consist of a grids that are implemented in a tube. The grid is composed of inclined cross bars which repeatedly divide the flows into layers and spread them over the entire cross-section of the pipe which allow to achieve high mixing within short lengths [213]; the Kenics KM mixer (5.12.C) contains a helical mixing elements that direct the flow radially toward the pipe walls and back to the center which increases mixing

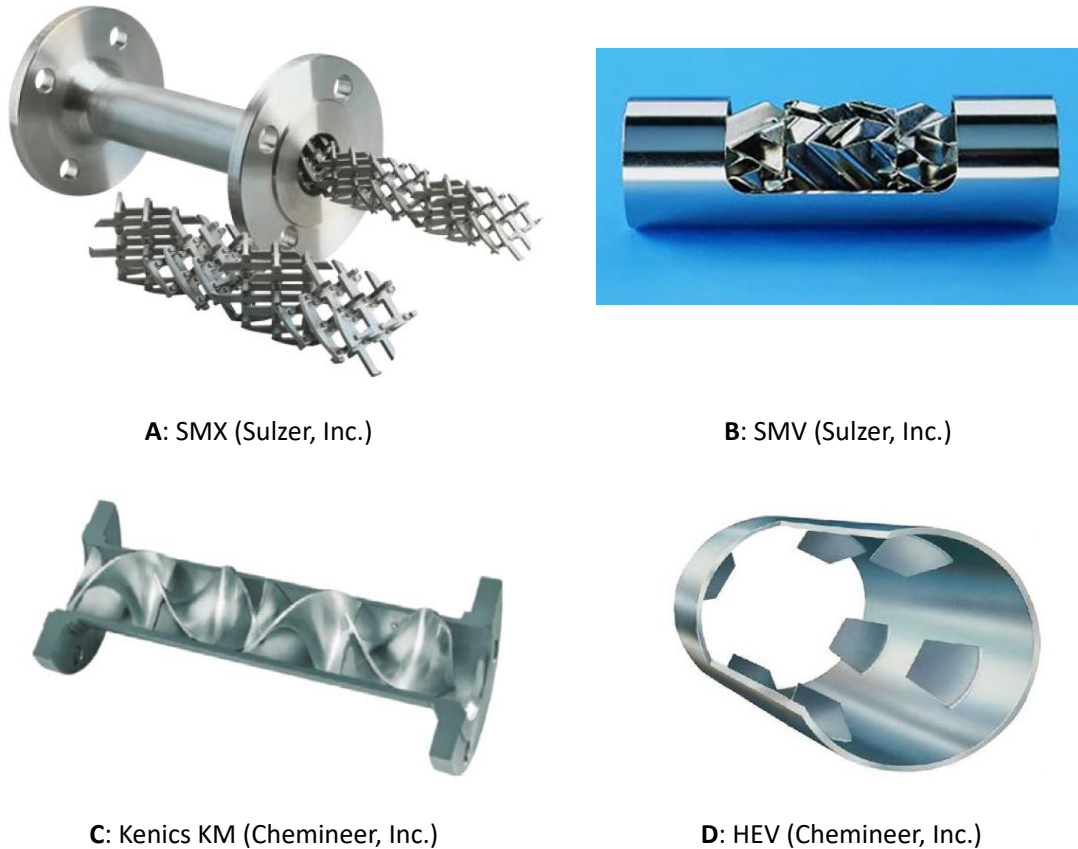


Fig. 5.12 Some of the available commercial mixers. Reprinted from ref 212.

efficiency ([see link](#)), the HEV mixer (5.12.D) includes elements that are implemented on its wall. These elements generate vortex structure which allow to accomplish the mixing. HEV provides pressure drop up to 75% lower than other conventional static mixers. However, its mixing efficiency is low ([see link](#)).

Over the last years, numerous studies have addressed the flow behaviour and mixing quality in these commercial static mixers.

Zalc et al [214] investigated the mixing performances and the flow behaviour of a Newtonian fluid in a SMX static mixer that contains four elements under Re ranging between 10^{-4} and 100. They found that the flow is independent of Re for $Re \leq 1$, while substantial deviations happened at higher Re where inertial forces are significant [214].

Sazlai and al [215] reported that only the twist angle affects mixing performance of SMX mixers at low flow rates ($Re = 1$), and both the element aspect ratio and the twist angle are shown to be important at high flow rates ($Re \leq 1000$).

By means of CFD, Liu et al [216] investigated the impact of the geometry element stacking in SMX static mixers for mixing laminar flows. They showed that mixing elements with 10 and 8 crossbars provided the best mixing quality (fig 5.13).

More specific models were developed by other researchers. Carriere [217] proposed a model consisting of a series of converging-diverging T's (fig 5.14) and based on this

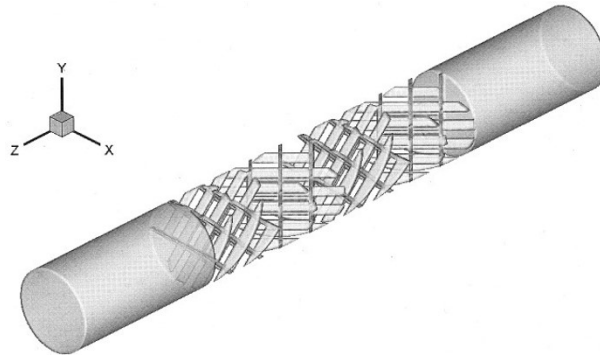


Fig. 5.13 Geometry of SMX mixing elements with eight crossbars. Reprinted from ref 216

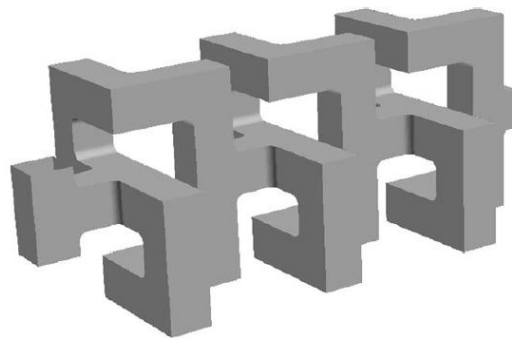


Fig. 5.14 Carriere's mixing system in a three basic elements configuration. Reprinted from ref 217

concept, Creyssels et al [218] designed a multi-level laminating mixer (MLLM) where the degree of mixing depends on the length of the pipe and on the number of elements.

A static mixer with semicircular baffles elements was designed by Al-Atabi et al [219]. Flow visualisation studies suggest that the baffles improved the mixing (two laminar streams of brine (25% NaCl, w/w) and water) at Re ranging between 50 and 700 by inducing a non-laminar turbulent like flow conditions even when the flow upstream of the baffles is in laminar regime. The enhanced mixing was accompanied by a slight increase in pressure drop. This simple model offers considerable mixing efficiency compared to more established static mixers such as SMX [219].

Hesseini et al [210] designed four blade static mixer for in-line mixing of Newtonian fluids at Re ranging from 700 to 6800. The mixer consists of four equally spaced blades mounted on cylindrical housing with 45° rotation (fig 5.15). It was tested in three different compartments of 6, 8 and 10 mixing elements; each element rotated 45° relative to the adjacent one. For the case of 10 mixing elements, a good mixing performance was achieved.

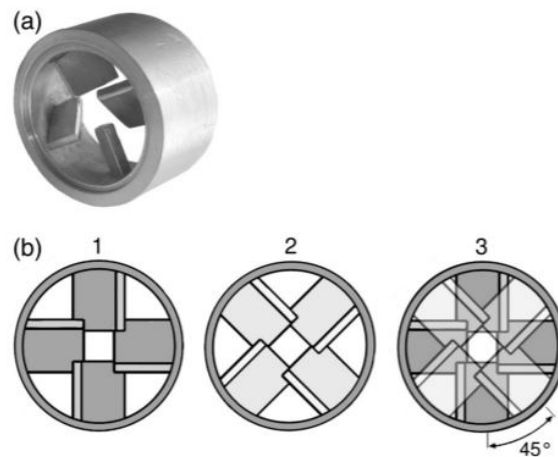


Fig. 5.15 The four-blade mixing element. (a) Fabricated mixing element (aluminum alloy) and (b) arrangement of two adjacent elements. Reprinted from ref 210

5.3 Design of electrochemical cells with integrated mixers

As I showed previously in sections 5.1.2 and 5.1.3, two limitations were encountered during the mixing experiments:

- Delay in the response time;
- Insufficient mixing.

To overcome these limitations, we chose to design new cells with integrated mixers. Thus, we have explored different designs.

In these designs, the wall-tube compartment from the first prototype (fig 1.16) was conserved and a mixing chamber was integrated just upstream the jet.

To design the mixing chambers, we were inspired by some of the mixers that I have mentioned in section 5.2 such as the 3D serpentine micromixers, Kinecs KM, HEV... basing on the following criteria:

- Homogeneous concentration or efficient mixing (the heterogeneity of the mixture should be lower than 10%);
- Low pressure drop in the setup (should be much smaller than 1×10^5 Pa);
- Feasibility: we are constrained by the volume and thus it is important to choose designs with elements that can easily be implemented in the cell.

We tested many configurations of cells with integrated static mixers using 3D-CFD simulations. In each configuration, the fluids enter the cell through two inlets with dimensionless concentrations of 0 and 1 and equal flow rates of 5 mL/min then leave through the two outlets after passing by the electrode.

Each configuration was characterized by:

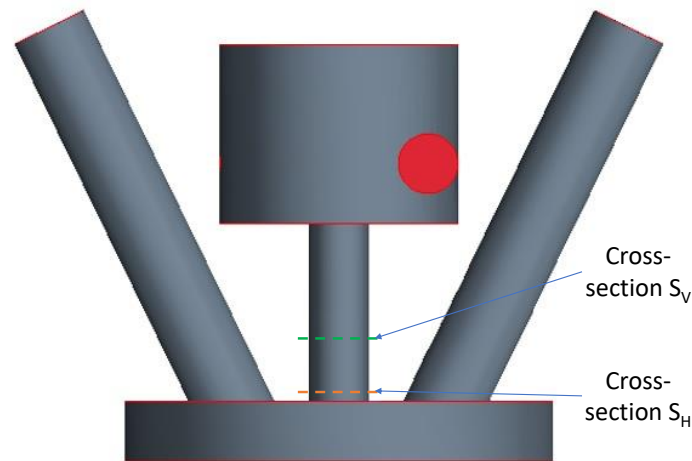


Fig. 5.16 Scheme of cell with integrated mixers with the sections S_H and S_V in which heterogeneity of concentration and non-verticality of the flow were computed respectively.

- Heterogeneity of concentration H at the radial cross-section S_H that is located just above the jet (see fig 5.16). It was computed using equation:

$$H = \frac{C_{max} - C_{min}}{C_{avg}} \times 100 \quad (5.12)$$

in which: C_{max} , C_{min} and C_{avg} are respectively the maximum, minimum and the average dimensionless concentrations at the cross-section S_H .

- Pressure drop throughout the cell ΔP . It was determined as in chapter 3, section 3.3.3 using equation (3.6).

In some geometries especially in the complex ones, we have noticed that the flow streamlines in the jet channel are not vertical (to the xy plane) and we presumed that this would cause an issue. Therefore, we integrated a porous medium in those geometries to decrease this non-verticality. In the end, we have tried several variants of those but we didn't have a clear idea about the actual physical medium that we could be using for this. Moreover, the simulations we made showed that the porous medium introduce very high pressure drop. Therefore, we didn't follow that direction as we thought that it wouldn't be interesting.

In this thesis, I will present only one example with porous medium and I will compare its performance to the main geometry (without porous) in terms of heterogeneity, non-verticality and pressure drop. The non-verticality V was computed in the cross section S_V

(see fig 5.16) using equation (5.13):

$$V = \frac{\sqrt{v_x^2 + v_y^2}}{\frac{\sqrt{v_x^2 + v_y^2 + v_z^2} \times A_i}{\sum_{i=1}^n A_i}} \quad (5.13)$$

in which: v_x , v_y , v_z are the velocity components in x,y and z axis. A_i is the surface area of the meshing cell's face.

Overall, the mixing cells that we designed can be classified into three categories.

5.3.1 Cells with vortex mixer

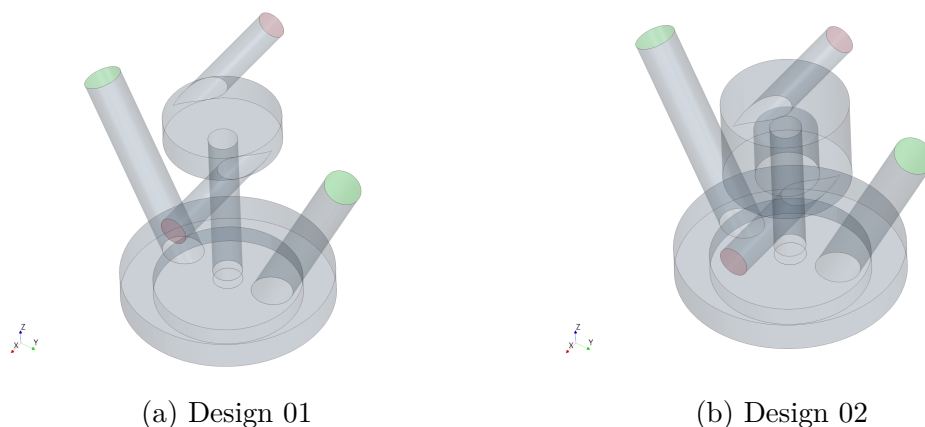


Fig. 5.17 The main geometries of the cell with integrated vortex mixers.

The concept is to generate vortices to increase the surface of exchange between both fluids and thus promote mixing.

The main part in the mixing compartment is a cylinder with two opposing inlets. A swirling winding begins in this chamber and the resulting mixture is evacuated to the electrochemical compartment through the jet channel.

Figure 5.17a shows the basic geometry of the cell with the integrated vortex mixer. It consists of two opposite inputs with a diameter of 1 mm, a mixing chamber with a diameter of 4 mm and a depth of 1 mm and finally the jet channel with a diameter of 1 mm and a length of 6.5 mm.

Figure 5.18a illustrates the flow streamlines in the cell from the inlets to the outlets. These streamlines were obtained from simulations using 25 massless particles that were seeded in the sections of each inlet, and the trajectory that they would take moving with the flow field was visualized as streamlines colored with the values of species concentration. This allows to follow the path of the fluids and how they mix together.

The fluids enter the cell through the inlets and due to the opposing positions of the latter and to the curved walls, a swirling flow is formed under the influence of the

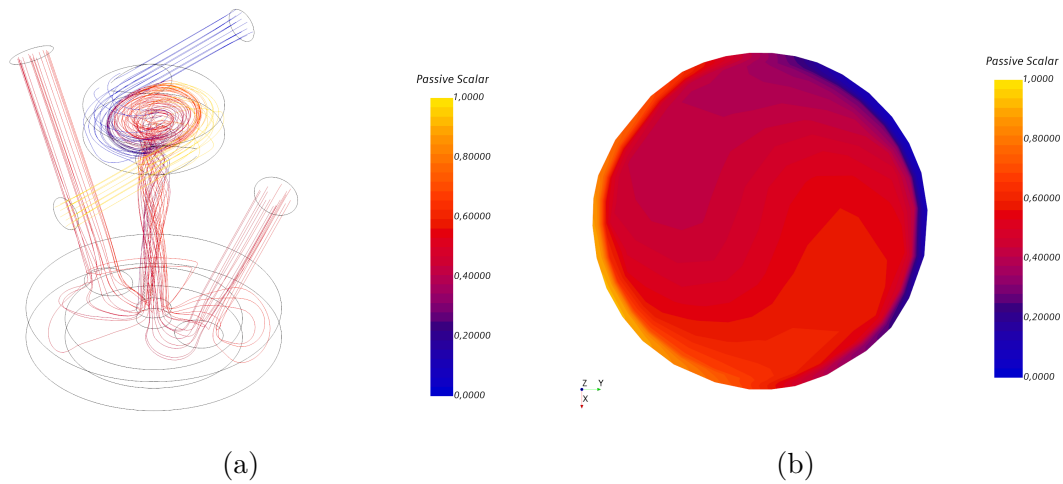


Fig. 5.18 a: The streamlines colored with species concentration in Design 01. b: Concentration map at the cross section S_H in Design 01 (5.17a)

centrifugal force which permits the two fluids to mix. The mixture then leaves the mixing chamber from the jet to impinge directly on the electrode and finally leaves the cell from the two symmetrical outlets.

The concentration field at the jet radial cross-section is shown in fig 5.18b. It is significantly heterogeneous with a $H = 166\%$.

An alternative configuration is shown in fig 5.17b where the mixing chamber is annular and the hole from which the mixture leaves to the wall-tube compartment is placed 1.5 mm higher than the base of the chamber. The reason for adding this small detail is to force the fluids to stay longer in the circular path to improve mixing. This actually helped to slightly reduce the heterogeneity of concentration ($H = 132\%$). However, the mixing is still not sufficient.

Some variants of configuration 5.17b are illustrated in figure 5.19. They were designed by adding obstacles in the cylindrical chamber or in the jet channel.

- Design 03 (5.19a) include conical base instead of a planar circular one.
- Design 04 (5.19b) includes triangular obstacles inserted into the mixing chamber.
- Design 05(5.19c) includes a hollow plate in the jet channel.
- Design 06 (5.19d) includes cylindrical obstacles inserted into the jet channel (embedded rods perpendicular to the inside wall of the channel).
- Designs 07 (5.19e) and 08 (5.19f) includes respectively 6 an 8 elements of a shape of half circles implemented in the jet channel. The elements are inclined and perpendicular to each other.

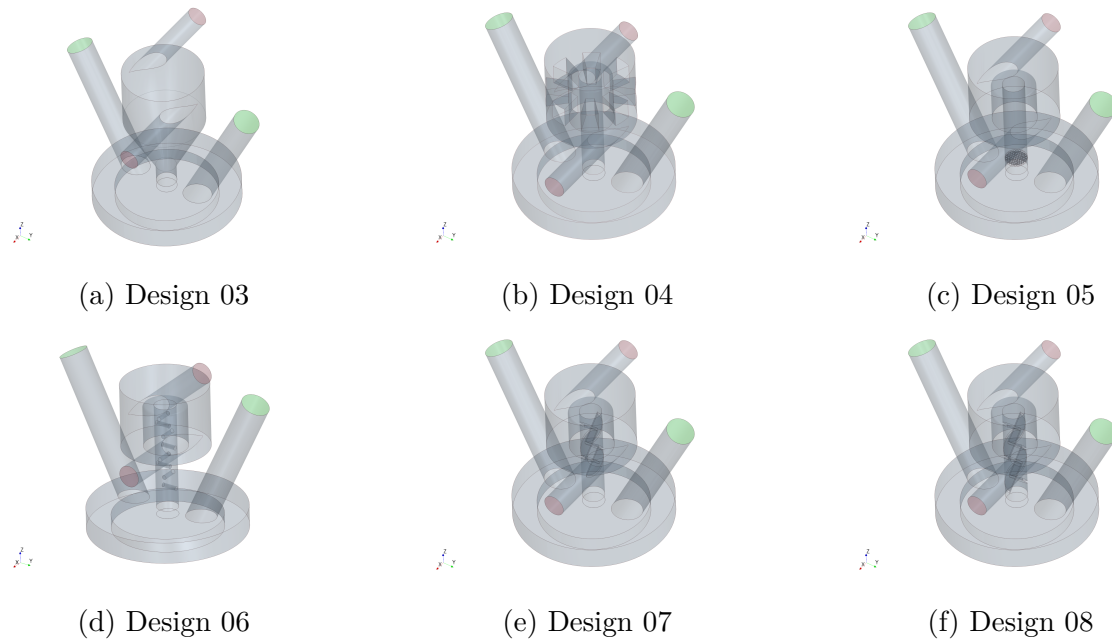


Fig. 5.19 The different variants of the configuration with integrated vortex mixer.

Design	Reference	Properties	Heterogeneity (%)	Pressure drop (Pa)
Design 01	5.17a	no elements inserted	166.06	167
Design 02	5.17b	mixing chamber has an annular shape	132.25	127
Design 03	5.19a	conical base	169.01	84.4
Design 04	5.19b	triangular obstacles in the mixing chamber	146.78	124
Design 05	5.19c	a hollow plate in the jet channel	103.77	288
Design 06	5.19d	cylindrical obstacles in the jet channel	123.96	259
Design 07	5.19e	6 circular elements in the jet channel	5.52	1301
Design 08	5.19f	8 circular elements in the jet channel	7.89	1679

Table 5.1 Comparison of the cells with integrated vortex.

Conclusion Table 5.1 shows the results obtained from the simulations of the cells with vortex mixers.

Except the designs 07 (5.19e) and 08 (5.19f), all the designs of vortex mixers showed very high heterogeneity of concentration ($H > 100\%$) and low pressure drop around ($\Delta P < 300$ Pa). Even if the pressure drop is low, their mixing quality is very poor. The designs 07 and 08 provide low heterogeneity ($H < 8\%$). However implementing the mixing elements in the jet channel is very complicated.

5.3.2 Cells with mixing plates

In this configuration, the mixing compartment comprises an annular chamber that is divided by horizontal plates of 0.2 mm thickness. Several variants that include different numbers and forms of the plates were screened. Among them, the configuration that showed the best mixing performances (design 09) consists of one plate that divides the mixing

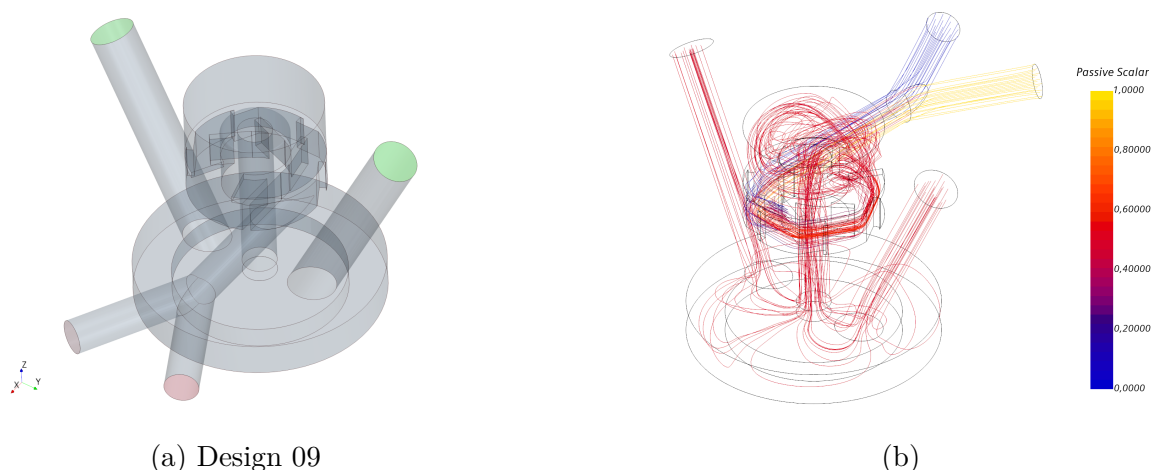


Fig. 5.20 a: The main geometry of the cell with mixing plates. b: The streamlines colored with species concentration in Design 09.

compartment into two floors. The first floor is equipped with 7 obstacles implemented in the wall (fig 5.20a). This geometry was inspired by the industrial static mixer HEV (see fig 5.12.B).

Figure 5.20b shows the streamlines of the flow in this cell. The fluids meet in a Y intersection before the mixing chamber. Once they enter to the latter together, they flow in a circular path in anti-clockwise direction due to the curved wall and due to the vertical wall that is placed in the entrance, the latter doesn't allow the fluid to flow in the other direction. From the streamlines fig 5.20b), we can also observe that the obstacles induce local vortices in the flow which leads to promote the mixing.

Some variants of design 09 (fig 5.20a) were proposed:

- Design 10 (5.21a) consists of two plates with two 45° openings in each. the second plate was rotated by 90°.
- Design 11 (5.21b) has the same configuration as design 10 but with tangential inlets.
- Design 12 (5.21c) has also two plates but with 8 rectangular openings (0.2 mm × 0.2 mm) at each plate.
- Design 13 (5.21d) consists of two plates with two 23° openings in each.
- Design 14 (5.21e) has the same configuration as design 13 but the first plate was rotated by 90°.
- Design 15 (5.21f) consists of three plates with two 45° openings in each.

Conclusion Table 5.2 shows the results obtained from the simulations of the cells with mixing plates.

Designs 11 (5.21b), 12 (5.21f) and 15 (5.21c) provided very poor mixing ($H > 120\%$). Design 13 wasn't much better ($H = 80\%$). Designs 10 (5.21a) and 14 (5.21e) showed a

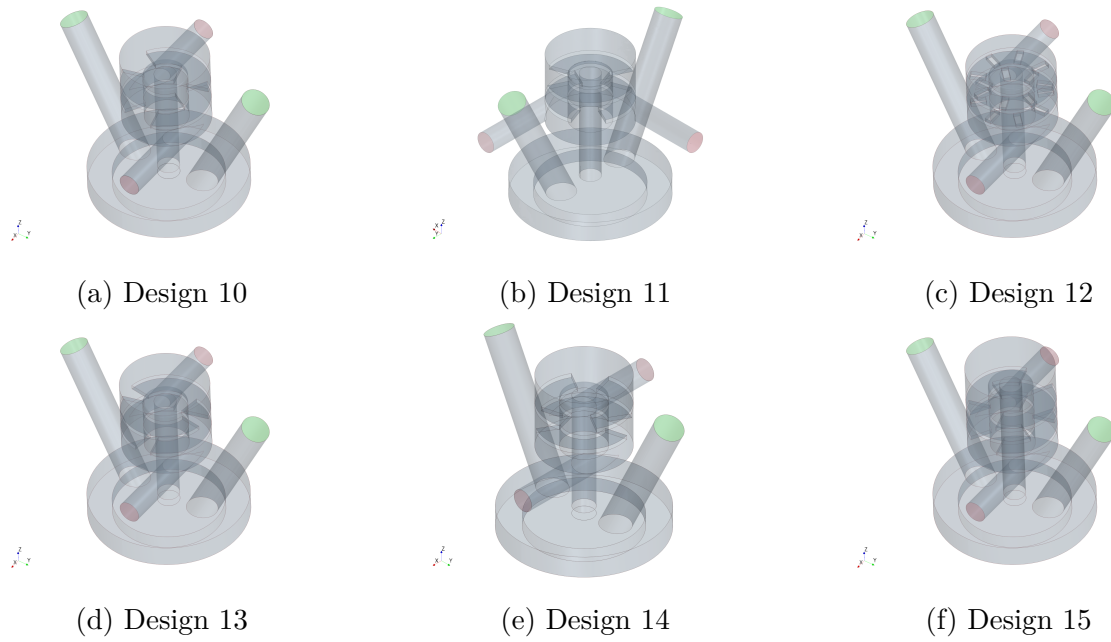


Fig. 5.21 The different variants of the configuration with integrated mixing plates.

Design	Reference	Properties	Heterogeneity (%)	Pressure drop (Pa)
Design 09	5.20a	1 plate, 1 opening (45°) and 7 obstacles	3.07	743
Design 10	5.21a	2 plates with 2 (45°) openings. the second plate is rotated by 90°	27.90	139
Design 11	5.21b	same configuration as design 10 but with tangential inlets	178.46	134
Design 12	5.21c	2 plates with 8 rectangular openings	143	158
Design 13	5.21d	2 plates with 2 openings (23°)	80.44	169
Design 14	5.21e	same configuration as design 13 but the first plate was rotated by 90°	26.73	140
Design 15	5.21f	3 plates with 2 openings (45°)	121.11	165

Table 5.2 Comparison of the cells with mixing plates.

relatively good mixing performance ($H < 28\%$). Design 09 (5.20a) showed best mixing quality with $H = 3.07\%$. All the variants were found to cause an acceptable pressure drop. Design 09 presents the best candidate to be printed and tested experimentally.

5.3.3 Cell with mixing channel of a square duct

The basic geometry is inspired from the 3D-serpentine square-wave micromixers 5.10. It consists in a channel with a square duct of 1 mm. Several variants were screened. The one that provides the best mixing is presented in fig 5.22a.

Figure 5.22b shows that the fluids enter the mixing chamber together and they follow the channel path. The 90° twisting allows to create local vortices which promote mixing.

The variants of design (fig 5.22a) are presented in fig 5.23:

- Design 17 (5.23a) has the same configuration as design 16 (5.22a) but the inlets were placed in a lower level.

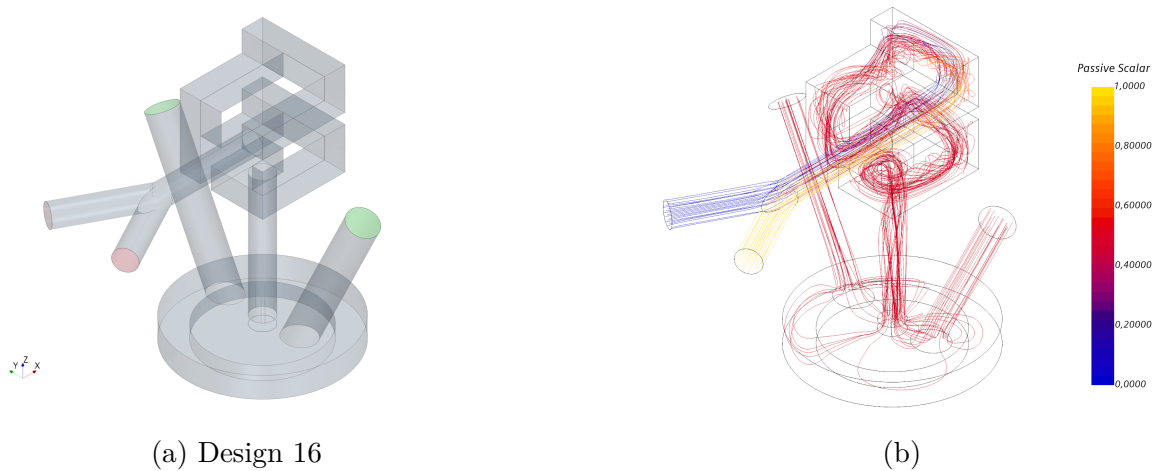


Fig. 5.22 a: The main geometry of the cell with mixing channel of a square duct. b: The streamlines colored with species concentration in Design 16.

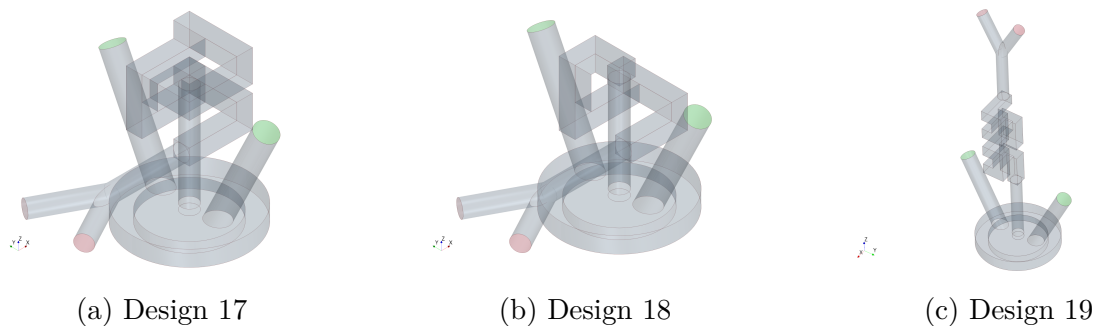


Fig. 5.23 The different variants of the configuration with mixing channel of a square duct.

- Design 18 (5.23b) has the same configuration as design 17 but the path is smaller with less twisting.
- Design 19 (5.23c) consists of combination of square-wave structures that are stacked vertically.

Conclusion Table 5.3 shows the results obtained from the simulations of the cells with mixing channel of a square duct.

All the configuration presented provide excellent mixing $H < 3\%$ with moderate pressure drop $\Delta P < 600$ Pa. However, some of them such as design 19 (5.23c) is not very suitable in terms of space. The rest can be practically implemented in the cell.

Design	Reference	Properties	Heterogeneity (%)	Pressure drop (Pa)
Design 16	5.22a	channel of a square duct	0.16	509
Design 17	5.23a	inlets are placed in a lower level	0.26	529
Design 18	5.23b	smaller path with less twisting	3.14	381
Design 19	5.23c	square waves stacked vertically	0.99	477

Table 5.3 Comparison of the cells with mixing channel of a square duct.

Design 16 (5.22a) present another excellent candidate.

5.3.4 Geometries with porous medium

As explained above, we have tested some geometries with a porous medium to reduce the non verticality of the flow. Here, I am showing an example of design 16 with a porous medium (with a thickness of 0.5 mm and a porosity of 0.8) that was implemented in the jet channel.

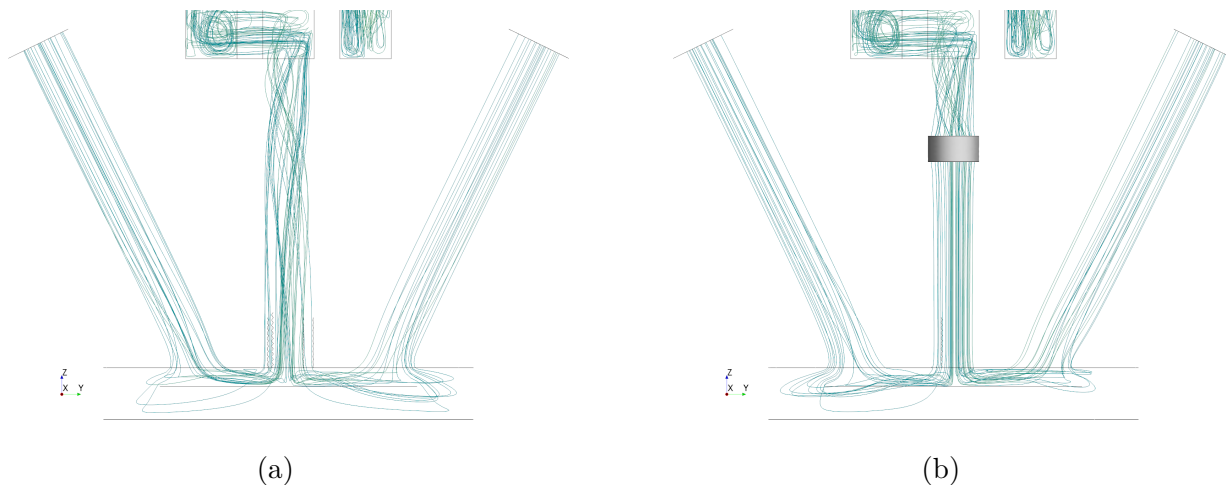


Fig. 5.24 The flow streamlines before (a) and after (b) adding the porous medium to the design 16 at the jet channel

Figures 5.24a and 5.24b illustrate the streamlines in the design 16 (5.22a) before and after adding a porous medium in the jet channel. It can be clearly observed that the streamlines became vertical after adding the porous medium.

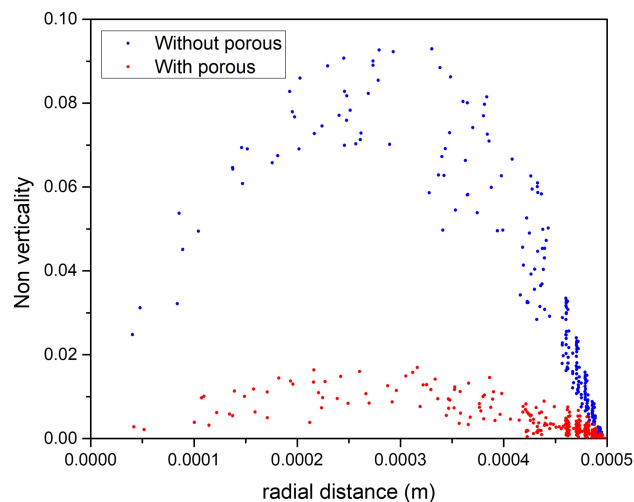


Fig. 5.25 Non-verticality of the flow at section S_V as a function of the radial distance from the electrode for design 16 (5.22a).

Figure 5.25 shows the non-verticality of the flow at the cross-section S_V (see fig 5.16) as a function of the radial distance from the electrode before (5.20a) and after (5.22a) adding the porous medium to design 16.

The porous medium helped to reduce the non-verticality V 5 times. However, it introduced almost 100 times higher pressure drop: pressure drop increased from 743 Pa to 78 300 Pa after adding the porous medium.

Indeed, the porous medium has a calming effect on the flow (makes the layers of the flow parallel). However, this is accompanied with a very high cost of pressure drop.

In this work, since we are not sure that the non-verticality would actually cause problems and since the pressure drop introduced by porous mediums is very high, we preferred to avoid investigating this any further (non-verticality).

5.4 Printed cell

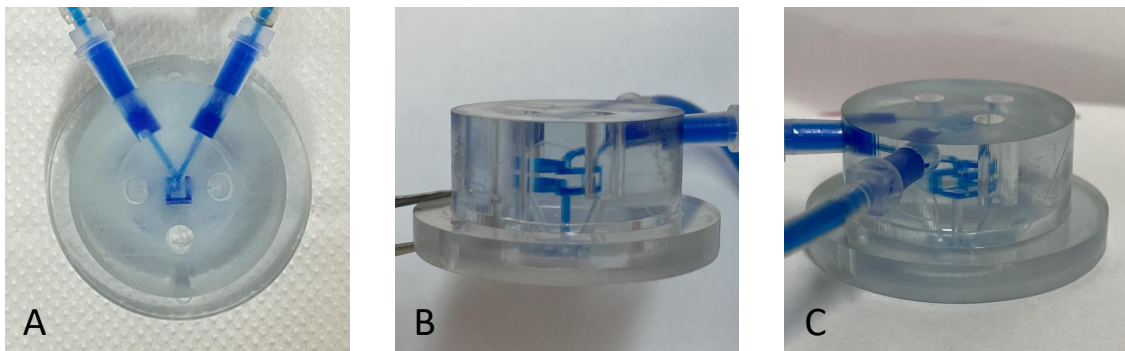


Fig. 5.26 (A) top view, (B) lateral view and (C) of the printed cell of the design 16 (5.22a). The cell was filled with a solution of methylene blue to better visualize the flow path.

We chose to print and test designs 09 (5.20a) and 16 (5.22a) as they showed excellent mixing performances and acceptable pressure drop. The prototypes were printed using stereolithography.

Figure 5.26 shows an image of the prototype of design 16 (5.22a). The cell was filled with methylene blue for visualization. The prototypes have not been tested yet due to recent technical problems with the syringe pumps.

5.5 Conclusion

In this chapter, I showed that the new setup seems to work for achieving arbitrary concentrations. However, two problems were identified: the delay in the response time due to the pipe flow behaviour and the fluctuations that are caused by different technical problems and amplified due to the poor mixing.

Therefore, in order to improve the mixing and to reduce the delay, we had to design better mixers and place them as close as possible to the electrode which led us to design new types of cells with integrated mixers. We explored a broad range of designs based on: simplicity, literature and also explored other possibilities that include porous medium to help with the non-verticality of the flow and mixing but that wasn't investigated further up because we found that it is not promising for pressure drop and it complicates the actual building of the cell.

Two of the most promising designs with low heterogeneity of concentration ($H < 4\%$) and acceptable pressure drop ($\Delta P < 800$ Pa) were chosen and built with 3D printing. Unfortunately, we couldn't test them yet because we encountered some technical problems with the syringe pumps but they will be tested as soon possible.

Chapter 6

General conclusion and perspectives

The first part of this thesis was devoted to the optimization of mass transport in the wall-tube electrode cell that was designed and built for studying highly active enzymes [78]. Although this cell have already been characterized with improved mass transport properties compared to the RDE, which is commonly used for studying enzymes in PFE, the previous work relied on CFD simulations to predict mass transport and shear stress in the cell, which is time consuming. However, for practical operation of the cell, and fine-tuning of its properties, analytical formulas are required.

In chapter 3, I showed that, by using CFD and Design of Experiments approach, we were able to perform a sensitivity study that allowed us to identify the main influencing parameters on the performances of the cell. Following that, by using high resolution simulations with a greater number of parameter values, we were able to explore more systematically the parameter space. Then, we used the obtained data to propose semi-empirical formulas that were successfully able to reproduce simulated mass transport coefficients and shear stress values with good accuracy. They were also very accurate to predict the experimental current obtained in a 3D-printed cell.

In this part, we also addressed the homogeneity of mass transport to the wall-tube electrode since it's an important requirement to conduct protein film electrochemistry studies. We showed that a ratio of $r_{electrode}/r_{jet} \leq 0.6$ is necessary for a homogeneous mass transport coefficient (homogeneity $\geq 90\%$).

We took advantage of the analytical formula for the shear stress derived in chapter 3 to investigate the relationship shear stress/film loss in chapter 4. We have found that for films of *Desulfovibrio desulfuricans* ATCC27774 cytochrome c nitrite reductase (ccNi), immobilized onto pyrolytic graphite edge electrodes, unexpectedly, the increase in shear stress is associated with slower film loss. This means that shear stress is likely to be a much less significant issue (at least for ccNi) than was previously expected for performing Protein Film Electrochemistry experiments.

The second part of the thesis covered the design of electrochemical cells that allow fast control of concentrations.

In chapter 5, I have shown that the new setup seems to work to achieve arbitrary concentrations. However, two issues have been identified: a long response time due to the laminar pipe flow behavior and current's fluctuations that are caused by various technical problems and amplified by poor mixing. In order to solve these limitations, we had to design better mixers and place them as close as possible to the electrode, which led us to design new types of cells with integrated mixers.

The bibliographic study we have proposed showed that many original solutions have been developed to improve laminar mixing. From our side, we have been particularly interested in the designs that are capable of achieving efficient mixing, without requiring a large space to be implemented. Based on that, we explored a broad range of designs with two main objectives in mind: low heterogeneity of concentration and low pressure drop. At the end, we chose two of the most promising designs and built them using 3D printing. It was unfortunately not possible to test them during this thesis due to issues with the pumps.

It is also worth mentioning, that there were many technical problems in the setup during experiments:

- Flow fluctuations due to the pumping system limitations.
- The presence of small bubbles inside the cell.
- Difficulties with using the cell: long time to open/close and also to calibrate the electrode...

Finally, I would like to conclude by proposing some of the future work suggestions, noting that this project is being continued by the PhD student A.Aldinio-Colbachini:

- Further improvement in the pumping system to reduce fluctuations.
- Optimizing the cell's assembly, in particular, the closing system, (screwing the top and bottom parts) for more practicality of the cell.
- Addressing the issue of bubbles: using bubbles trap, surface treatment to increase the hydrophilicity inside the cell.
- Using the setup (which includes in particular the cells with integrated mixers) to study different enzymes (inhibition...).

References

- [1] Aaron M Appel, John E Bercaw, Andrew B Bocarsly, Holger Dobbek, Daniel L DuBois, Michel Dupuis, James G Ferry, Etsuko Fujita, Russ Hille, Paul JA Kenis, et al. Frontiers, opportunities, and challenges in biochemical and chemical catalysis of co₂ fixation. *Chemical reviews*, 113(8):6621–6658, 2013.
- [2] Christof Knocke and Jennefer Vogt. Biofuels—challenges & chances: how biofuel development can benefit from advanced process technology. *Engineering in Life Sciences*, 9(2):96–99, 2009.
- [3] Peter J le B Williams and Lieve ML Laurens. Microalgae as biodiesel & biomass feedstocks: Review & analysis of the biochemistry, energetics & economics. *Energy & Environmental Science*, 3(5):554–590, 2010.
- [4] Derek Abbott. Keeping the energy debate clean: How do we supply the world’s energy needs? *Proceedings of the IEEE*, 98(1):42–66, 2009.
- [5] Olivia Langhamer, Kalle Haikonen, and Jan Sundberg. Wave power—sustainable energy or environmentally costly? a review with special emphasis on linear wave energy converters. *Renewable and Sustainable Energy Reviews*, 14(4):1329–1335, 2010.
- [6] Michele Aresta and Angela Dibenedetto. Carbon dioxide fixation into organic compounds. In *Carbon dioxide recovery and utilization*, pages 211–260. Springer, 2003.
- [7] Gabriele Centi, Siglinda Perathoner, Gauthier Winè, and Miriam Gangeri. Electrocatalytic conversion of co₂ to long carbon-chain hydrocarbons. *Green Chem.*, 9:671–678, 2007.
- [8] Miriam González-Castaño, Bogdan Dorneanu, and Harvey Arellano-García. The reverse water gas shift reaction: a process systems engineering perspective. *Reaction Chemistry & Engineering*, 6(6):954–976, 2021.
- [9] Alexis T Bell, Bruce C Gates, Douglas Ray, and Michael R Thompson. Basic research needs: catalysis for energy. Technical report, Pacific Northwest National Lab.(PNNL), Richland, WA (United States), 2008.
- [10] Marta Meneghello, Christophe Léger, and Vincent Fourmond. Electrochemical studies of co₂-reducing metalloenzymes. *Chemistry—A European Journal*, 2021.
- [11] Arren Bar-Even, Elad Noor, and Ron Milo. A survey of carbon fixation pathways through a quantitative lens. *Journal of experimental botany*, 63(6):2325–2342, 2012.
- [12] Georg Fuchs. Alternative pathways of carbon dioxide fixation: insights into the early evolution of life? *Annual review of microbiology*, 65:631–658, 2011.

- [13] Stephen W Ragsdale and Elizabeth Pierce. Acetogenesis and the wood–ljungdahl pathway of co₂ fixation. *Biochimica et Biophysica Acta (BBA)-Proteins and Proteomics*, 1784(12):1873–1898, 2008.
- [14] VA Svetlichny, TG Sokolova, M Gerhardt, M Ringpfeil, NA Kostrikina, and GA Zavarzin. Carboxydotherrmus hydrogenofmans gen. nov., sp. nov., a co-utilizing thermophilic anaerobic bacterium from hydrothermal environments of kunashir island. *Systematic and Applied Microbiology*, 14(3):254–260, 1991.
- [15] Christophe Orain, Laure Saujet, Charles Gauquelin, Philippe Soucaille, Isabelle Meynial-Salles, Carole Baffert, Vincent Fourmond, Hervé Bottin, and Christophe Léger. Electrochemical measurements of the kinetics of inhibition of two fefe hydrogenases by o₂ demonstrate that the reaction is partly reversible. *Journal of the American Chemical Society*, 137(39):12580–12587, 2015.
- [16] Vincent Fourmond, Nicolas Plumeré, and Christophe Léger. Reversible catalysis. *Nature Reviews Chemistry*, 5(5):348–360, 2021.
- [17] Fangting Yu, Virginia M Cangelosi, Melissa L Zastrow, Matteo Tegoni, Jefferson S Plegaria, Alison G Tebo, Catherine S Mocny, Leela Ruckthong, Hira Qayyum, and Vincent L Pecoraro. Protein design: toward functional metalloenzymes. *Chemical reviews*, 114(7):3495–3578, 2014.
- [18] Paul Kaufmann, Benjamin R Duffus, Christian Teutloff, and Silke Leimkuhler. Functional studies on oligotropha carboxidovorans molybdenum–copper co dehydrogenase produced in escherichia coli. *Biochemistry*, 57(19):2889–2901, 2018.
- [19] Mehmet Can, Fraser A Armstrong, and Stephen W Ragsdale. Structure, function, and mechanism of the nickel metalloenzymes, co dehydrogenase, and acetyl-coa synthase. *Chemical reviews*, 114(8):4149–4174, 2014.
- [20] Alison Parkin, Javier Seravalli, Kylie A Vincent, Stephen W Ragsdale, and Fraser A Armstrong. Rapid and efficient electrocatalytic co₂/co interconversions by carboxydotherrmus hydrogenofmans co dehydrogenase i on an electrode. *Journal of the American Chemical Society*, 129(34):10328–10329, 2007.
- [21] Vincent C-C Wang, Mehmet Can, Elizabeth Pierce, Stephen W Ragsdale, and Fraser A Armstrong. A unified electrocatalytic description of the action of inhibitors of nickel carbon monoxide dehydrogenase. *Journal of the American Chemical Society*, 135(6):2198–2206, 2013.
- [22] Vincent C-C Wang, Shams TA Islam, Mehmet Can, Stephen W Ragsdale, and Fraser A Armstrong. Investigations by protein film electrochemistry of alternative reactions of nickel-containing carbon monoxide dehydrogenase. *The Journal of Physical Chemistry B*, 119(43):13690–13697, 2015.
- [23] Jae-Hun Jeoung and Holger Dobbek. Carbon dioxide activation at the ni, fe-cluster of anaerobic carbon monoxide dehydrogenase. *Science*, 318(5855):1461–1464, 2007.
- [24] Jessica Hadj-Saïd, Maria-Eirini Pandelia, Christophe Léger, Vincent Fourmond, and Sébastien Dementin. The carbon monoxide dehydrogenase from desulfovibrio vulgaris. *Biochimica Et Biophysica Acta (BBA)-Bioenergetics*, 1847(12):1574–1583, 2015.
- [25] Fraser A. Armstrong. Insights from protein film voltammetry into mechanisms of complex biological electron-transfer reactions. *J. Chem. Soc., Dalton Trans.*, pages 661–671, 2002.

- [26] Christophe Léger and Patrick Bertrand. Direct electrochemistry of redox enzymes as a tool for mechanistic studies. *Chemical Reviews*, 108(7):2379–2438, 2008.
- [27] Melisa Del Barrio, Matteo Sensi, Christophe Orain, Carole Baffert, Sébastien Dementin, Vincent Fourmond, and Christophe Léger. Electrochemical investigations of hydrogenases and other enzymes that produce and use solar fuels. *Accounts of chemical research*, 51(3):769–777, 2018.
- [28] Vincent Fourmond, Claudio Greco, Kateryna Sybirna, Carole Baffert, Po-Hung Wang, Pierre Ezanno, Marco Montefiori, Maurizio Bruschi, Isabelle Meynial Salles, Philippe Soucaille, Jochen Blumberger, Hervé Bottin, Luca De Gioia, and Christophe Léger. The oxidative inactivation of FeFe hydrogenase reveals the flexibility of the H-cluster. *Nature Chemistry*, 6(4):336 – 342, 2014.
- [29] Melisa del Barrio, Matteo Sensi, Christophe Orain, Carole Baffert, Sébastien Dementin, Vincent Fourmond, and Christophe Léger. Electrochemical Investigations of Hydrogenases and Other Enzymes That Produce and Use Solar Fuels. *Accounts of Chemical Research*, 51(3):769 – 777, March 2018.
- [30] Marta Meneghello, Ana Rita Oliveira, Aurore Jacq-Bailly, Inês A.C. Pereira, Christophe Léger, and Vincent Fourmond. Formate dehydrogenases reduce CO₂ rather than HCO₃⁻ : an electrochemical demonstration. *Angewandte Chemie International Edition*, February 2021.
- [31] Richard G Compton and Giles HW Sanders. *Electrode potentials*. Number 544.62 COM. 1998.
- [32] Christopher Brett and Ana María Oliveira Brett. *Electrochemistry: principles, methods, and applications*. Number 544.6 BRE. 1993.
- [33] György Inzelt. Electrode potentials. In *Handbook of Reference Electrodes*, pages 1–24. Springer, 2013.
- [34] Vincent Fourmond and Christophe Léger. An introduction to electrochemical methods for the functional analysis of metalloproteins. In *Practical Approaches to Biological Inorganic Chemistry*, pages 325–373. Elsevier, 2020.
- [35] Heike Kahlert. Reference electrodes. In *Electroanalytical methods*, pages 291–308. Springer, 2010.
- [36] Allen J Bard, Larry R Faulkner, et al. Fundamentals and applications. *Electrochemical methods*, 2(482):580–632, 2001.
- [37] J Bard Allen and R Faulkner Larry. *Electrochemical methods fundamentals and applications*. John Wiley & Sons, 2001.
- [38] James J Van Benschoten, Jane Y Lewis, William R Heineman, Daryl A Roston, and Peter T Kissinger. Cyclic voltammetry experiment. *Journal of Chemical Education*, 60(9):772, 1983.
- [39] Cynthia G Zoski. *Handbook of electrochemistry*. Elsevier, 2006.
- [40] Richard G Compton and Giles HW Sanders. *Electrode Potentials (Oxford Chemistry Primers)*. Oxford University Press Oxford, UK, 1996.
- [41] D. Pletcher. *A First Course in Electrode Processes*. Royal Society of Chemistry, 2019.

- [42] Fritz Scholz et al. *Electroanalytical methods*, volume 1. Springer, 2010.
- [43] V. G. LEVICH. Physicochemical hydrodynamics. pages 689–700, 1962.
- [44] V Fourmond and C Leger. Protein electrochemistry: Questions and answers. *Adv. Biochem. Eng. Biotechnol.*, 158:1–41, September 2016.
- [45] Mark J Eddowes and H Allen O Hill. Electrochemistry of horse heart cytochrome c. *Journal of the American Chemical Society*, 101(16):4461–4464, 1979.
- [46] Chi-Woo Lee, Harry B Gray, Fred C Anson, and Bo G Malmström. Catalysis of the reduction of dioxygen at graphite electrodes coated with fungal laccase a. *Journal of electroanalytical chemistry and interfacial electrochemistry*, 172(1-2):289–300, 1984.
- [47] Fraser A Armstrong, Hendrik A Heering, and Judy Hirst. Reaction of complex metalloproteins studied by protein-film voltammetry. *Chemical Society Reviews*, 26(3):169–179, 1997.
- [48] Fraser A Armstrong, Raúl Camba, Hendrik A Heering, Judy Hirst, Lars JC Jeuken, Anne K Jones, Christophe Léger, and James P McEvoy. Fast voltammetric studies of the kinetics and energetics of coupled electron-transfer reactions in proteins. *Faraday discussions*, 116:191–203, 2000.
- [49] Carole Baffert, Sébastien Dementin, Vincent Fourmond, and Christophe Léger. L'électrochimie, un outil pour étudier les mécanismes enzymatiques. *L'actualité chimique*, 392:9–15, 2015.
- [50] Hendrik A Heering, Frank GM Wiertz, Cees Dekker, and Simon de Vries. Direct immobilization of native yeast iso-1 cytochrome c on bare gold: Fast electron relay to redox enzymes and zeptomole protein-film voltammetry. *Journal of the American Chemical Society*, 126(35):11103–11112, 2004.
- [51] Judy Hirst. Elucidating the mechanisms of coupled electron transfer and catalytic reactions by protein film voltammetry. *Biochimica et Biophysica Acta (BBA)-Bioenergetics*, 1757(4):225–239, 2006.
- [52] Kaisheng Chen, Judy Hirst, Raul Camba, Christopher A Bonagura, C David Stout, Barbara K Burgess, and Fraser A Armstrong. Atomically defined mechanism for proton transfer to a buried redox centre in a protein. *Nature*, 405(6788):814–817, 2000.
- [53] Fanny Leroux, Sébastien Dementin, Bénédicte Burlat, Laurent Cournac, Anne Volbeda, Stéphanie Champ, Lydie Martin, Bruno Guigliarelli, Patrick Bertrand, Juan Fontecilla-Camps, Marc Rousset, and Christophe Léger. Experimental approaches to kinetics of gas diffusion in hydrogenase. *Proceedings of the National Academy of Sciences*, 105(32):11188–11193, 2008.
- [54] Ting Zeng, Silke Leimkuhler, Ulla Wollenberger, and Vincent Fourmond. Transient catalytic voltammetry of sulfite oxidase reveals rate limiting conformational changes. *Journal of the American Chemical Society*, 139(33):11559–11567, 2017.
- [55] A Kubas, C Orain, D De Sancho, L Saujet, M Sensi, C Gauquelin, I Meynial-Salles, P Soucaille, H Bottin, C Baffert, et al. Mechanism of o₂ diffusion and reduction in fe₂ hydrogenases. *nat chem* 9: 88–95, 2017.

- [56] Abbas Abou Hamdan, Pierre-Pol Liebgott, Vincent Fourmond, Oscar Gutiérrez-Sanz, Antonio L De Lacey, Pascale Infossi, Marc Rousset, Sébastien Dementin, and Christophe Léger. Relation between anaerobic inactivation and oxygen tolerance in a large series of nife hydrogenase mutants. *Proceedings of the National Academy of Sciences*, 109(49):19916–19921, 2012.
- [57] Abbas Abou Hamdan, Bénédicte Burlat, Oscar Gutiérrez-Sanz, Pierre-Pol Liebgott, Carole Baffert, Antonio L De Lacey, Marc Rousset, Bruno Guigliarelli, Christophe Léger, and Sébastien Dementin. O 2-independent formation of the inactive states of nife hydrogenase. *Nature chemical biology*, 9(1):15–17, 2013.
- [58] Vincent Fourmond, Claudio Greco, Kateryna Sybirna, Carole Baffert, Po-Hung Wang, Pierre Ezanno, Marco Montefiori, Maurizio Bruschi, Isabelle Meynial-Salles, Philippe Soucaille, et al. The oxidative inactivation of fefe hydrogenase reveals the flexibility of the h-cluster. *Nature chemistry*, 6(4):336–342, 2014.
- [59] Biljana Sljukic, Craig E. Banks, Chris Salter, Alison Crossley, and Richard G. Compton. Electrochemically polymerised composites of multi-walled carbon nanotubes and poly(vinylferrocene) and their use as modified electrodes: Application to glucose sensing. *Analyst*, 131:670–677, 2006.
- [60] Christopher F Blanford and Fraser A Armstrong. The pyrolytic graphite surface as an enzyme substrate: microscopic and spectroscopic studies. *Journal of Solid State Electrochemistry*, 10(10):826–832, 2006.
- [61] Julea N Butt, Marian Filipiak, and Wilfred R Hagen. Direct electrochemistry of megasphaera elsdonii iron hydrogenase: Definition of the enzyme’s catalytic operating potential and quantitation of the catalytic behaviour over a continuous potential range. *European journal of biochemistry*, 245(1):116–122, 1997.
- [62] Wilfred R HAGEN. Direct electron transfer of redox proteins at the bare glassy carbon electrode. *European journal of biochemistry*, 182(3):523–530, 1989.
- [63] Nobutaka Fujieda, Megumi Mori, Kenji Kano, and Tokuji Ikeda. Spectroelectrochemical evaluation of redox potentials of cysteine tryptophylquinone and two hemes c in quinoxinoprotein amine dehydrogenase from paracoccus denitrificans. *Biochemistry*, 41(46):13736–13743, 2002.
- [64] AA Karyakin, SV Morozov, EE Karyakina, SD Varfolomeyev, NA Zorin, and S Cosnier. Hydrogen fuel electrode based on bioelectrocatalysis by the enzyme hydrogenase. *Electrochemistry Communications*, 4(5):417–420, 2002.
- [65] AA Karyakin, SV Morozov, EE Karyakina, NA Zorin, VV Perelygin, and S Cosnier. Hydrogenase electrodes for fuel cells, 2005.
- [66] Elena E Ferapontova, John Castillo, Dmitri Hushpulian, Vladimir Tishkov, Tatiana Chubar, Irina Gazaryan, and Lo Gorton. Direct electrochemistry of recombinant tobacco peroxidase on gold. *Electrochemistry communications*, 7(12):1291–1297, 2005.
- [67] Marcos Pita, Sergey Shleev, Tautgirdas Ruzgas, Víctor M Fernández, Alexander I Yaropolov, and Lo Gorton. Direct heterogeneous electron transfer reactions of fungal laccases at bare and thiol-modified gold electrodes. *Electrochemistry communications*, 8(5):747–753, 2006.

- [68] Tao Ye, Ravinder Kaur, Xin Wen, Kara L Bren, and Sean J Elliott. Redox properties of wild-type and heme-binding loop mutants of bacterial cytochromes c measured by direct electrochemistry. *Inorganic chemistry*, 44(24):8999–9006, 2005.
- [69] Lea V Michel, Tao Ye, Sarah EJ Bowman, Benjamin D Levin, Megan A Hahn, Brandy S Russell, Sean J Elliott, and Kara L Bren. Heme attachment motif mobility tunes cytochrome c redox potential. *Biochemistry*, 46(42):11753–11760, 2007.
- [70] Vincent Fourmond, Thomas Lautier, Carole Baffert, Fanny Leroux, Pierre-Pol Liebgott, Sébastien Dementin, Marc Rousset, Pascal Arnoux, David Pignol, Isabelle Meynial-Salles, et al. Correcting for electrocatalyst desorption and inactivation in chronoamperometry experiments. *Analytical chemistry*, 81(8):2962–2968, 2009.
- [71] Gary Binyamin and Adam Heller. Stabilization of wired glucose oxidase anodes rotating at 1000 rpm at 37°C. *J. Electrochem. Soc.*, 146(8):2965, 1999.
- [72] Meriem Merrouch, Jessica Hadj-Saïd, Christophe Léger, Sébastien Dementin, and Vincent Fourmond. Reliable estimation of the kinetic parameters of redox enzymes by taking into account mass transport towards rotating electrodes in protein film voltammetry experiments. *Electrochimica Acta*, 245:1059–1064, 2017.
- [73] Christophe Léger, Sébastien Dementin, Patrick Bertrand, Marc Rousset, and Bruno Guigliarelli. Inhibition and aerobic inactivation kinetics of desulfovibrio fructosovorans nife hydrogenase studied by protein film voltammetry. *Journal of the American Chemical Society*, 126(38):12162–12172, 2004.
- [74] John Newman and Karen E Thomas-Alyea. *Electrochemical systems*. John Wiley & Sons, 2012.
- [75] Meriem Merrouch. *Mécanisme, maturation et biodiversité d'une enzyme à cofacteur NiFe, importante dans le contexte de l'énergie et de l'environnement: la carbone monoxyde déshydrogénase*. PhD thesis, Aix-Marseille, 2017.
- [76] Jessica Hadj-Saïd. *La CO déshydrogénase de Desulfovibrio vulagris*. PhD thesis, Aix-Marseille, 2015.
- [77] Meriem Merrouch, Jessica Hadj-Saïd, Lilith Domnik, Holger Dobbek, Christophe Léger, Sébastien Dementin, and Vincent Fourmond. O₂ inhibition of ni-containing co dehydrogenase is partly reversible. *Chemistry—A European Journal*, 21(52):18934–18938, 2015.
- [78] Mariam Fadel, Jean-Vincent Daurelle, Vincent Fourmond, and Jérôme Vicente. A new electrochemical cell with a uniformly accessible electrode to study fast catalytic reactions. *Physical Chemistry Chemical Physics*, 21(23):12360–12371, 2019.
- [79] Fadel Mariam, Daurelle Jean-Vincent, Fourmondj Vincent, and Vicente Jerome. Enhancing mass transport in jet electrode to study highly active enzymes. 2017.
- [80] Mariam Fadel. *Designing a new electrochemical cell for the study of enzyme that reduces CO₂*. PhD thesis, Aix-Marseille, 2018.
- [81] JM Esteban, GS Hickey, and ME Orazem. The impinging jet electrode: measurement of the hydrodynamic constant and its use for evaluating film persistency. *Corrosion*, 46(11):896–901, 1990.
- [82] WJ Blaedel and GW Schieffer. Turbulent tubular electrode. *Analytical Chemistry*, 46(11):1564–1567, 1974.

- [83] Yunus A Cengel. *Fluid mechanics*. Tata McGraw-Hill Education, 2010.
- [84] HEAT TRANSFER THERMODYNAMICS. Doe fundamentals handbook. 1992.
- [85] Yasuki Nakayama. *Introduction to fluid mechanics*. Butterworth-Heinemann, 2018.
- [86] RP Chhabra and V Shankar. *Coulson and Richardson's Chemical Engineering: Volume 1A: Fluid Flow: Fundamentals and Applications*. Butterworth-Heinemann, 2017.
- [87] Richard G Compton and Matthew BG Pilkington. Channel-electrode voltammetry. waveshape analysis of the current–voltage curves of ec 2 and disp2 processes. *Journal of the Chemical Society, Faraday Transactions 1: Physical Chemistry in Condensed Phases*, 85(8):2255–2271, 1989.
- [88] J Nikolic, E Expósito, J Iniesta, José González-García, and V Montiel. Theoretical concepts and applications of a rotating disk electrode. *Journal of Chemical Education*, 77(9):1191, 2000.
- [89] Han Cheng Kuo and Dieter Landolt. Rotating disc electrode study of anodic dissolution of iron in concentrated chloride media. *Electrochimica Acta*, 20(5):393–399, 1975.
- [90] G Maurin and A Lavanant. Electrodeposition of nickel/silicon carbide composite coatings on a rotating disc electrode. *Journal of Applied Electrochemistry*, 25(12):1113–1121, 1995.
- [91] KJJ Mayrhofer, D Strmcnik, BB Blizanac, V Stamenkovic, M Arenz, and NM Markovic. Measurement of oxygen reduction activities via the rotating disc electrode method: From pt model surfaces to carbon-supported high surface area catalysts. *Electrochimica Acta*, 53(7):3181–3188, 2008.
- [92] Gustav KH Wiberg, Karl JJ Mayrhofer, and Matthias Arenz. Investigation of the oxygen reduction activity on silver—a rotating disc electrode study. *Fuel cells*, 10(4):575–581, 2010.
- [93] Mariela Carpinella, Manuel I Velasco, Emilia V Silletta, Juan M Ovejero, Sergio A Dassie, and Rodolfo H Acosta. Determination of flow patterns in a rotating disk electrode configuration by mri. *Journal of Electroanalytical Chemistry*, 750:100–106, 2015.
- [94] Alessio Alexiadis, Ann Cornell, and MP Dudukovic. Comparison between cfd calculations of the flow in a rotating disk cell and the cochran/levich equations. *Journal of Electroanalytical Chemistry*, 669:55–66, 2012.
- [95] Stanley Bruckenstein and Barry Miller. Unraveling reactions with rotating electrodes. *Accounts of Chemical Research*, 10(2):54–61, 1977.
- [96] AN Frumkin and LN Nekrasov. On the ring-disk electrode. *Dok. Akad. Nauk SSSR*, 126:115, 1959.
- [97] IB Ivanov and VG Levich. Investigation of unstable intermediary products of electrode reactions by means of a rotating disc electrode. *Doklady Akademii Nauk SSSR*, 126(5):1029–1032, 1959.
- [98] Wyndham John Albery, Michael L Hitchman, and Wyndham John Albery. *Ring-disc electrodes*. Clarendon Press Oxford, 1971.

- [99] Th v Kármán. Über laminare und turbulente reibung. *ZAMM-Journal of Applied Mathematics and Mechanics/Zeitschrift für Angewandte Mathematik und Mechanik*, 1(4):233–252, 1921.
- [100] WG Cochran. The flow due to a rotating disc. In *Mathematical Proceedings of the Cambridge Philosophical Society*, volume 30, pages 365–375. Cambridge University Press, 1934.
- [101] Nigel Gregory, John Trevor Stuart, and WS Walker. On the stability of three-dimensional boundary layers with application to the flow due to a rotating disk. *Philosophical Transactions of the Royal Society of London. Series A, Mathematical and Physical Sciences*, 248(943):155–199, 1955.
- [102] KF Blurton and AC Riddiford. Shapes of practical rotating disc electrodes. *Journal of Electroanalytical Chemistry (1959)*, 10(5-6):457–464, 1965.
- [103] Shaukat Azim and AC Riddiford. A new type of rotating disk electrode. *Analytical Chemistry*, 34(8):1023–1025, 1962.
- [104] KB Prater and RN Adams. A critical evaluation of practical rotated disk electrodes. *Analytical Chemistry*, 38(1):153–155, 1966.
- [105] Ph Mandin, Th Pauporté, Ph Fanouillère, and D Lincot. Modelling and numerical simulation of hydrodynamical processes in a confined rotating electrode configuration. *Journal of Electroanalytical Chemistry*, 565(2):159–173, 2004.
- [106] Qingbo Dong, Shriram Santhanagopalan, and Ralph E White. A comparison of numerical solutions for the fluid motion generated by a rotating disk electrode. *Journal of the Electrochemical Society*, 155(9):B963, 2008.
- [107] Jesus Gonzalez, Cesar Real, Luis Hoyos, Raul Miranda, and Francisco Cervantes. Characterization of the hydrodynamics inside a practical cell with a rotating disk electrode. *Journal of electroanalytical chemistry*, 651(2):150–159, 2011.
- [108] W John Albery and Stanley Bruckenstein. Uniformly accessible electrodes. *Journal of Electroanalytical Chemistry and Interfacial Electrochemistry*, 144(1-2):105–112, 1983.
- [109] A Frumkin, L Nekrasov, B Levich, and Ju Ivanov. Die anwendung der rotierenden scheibenelektrode mit einem ringe zur untersuchung von zwischenprodukten elektrochemischer reaktionen. *Journal of Electroanalytical Chemistry (1959)*, 1(1):84–90, 1959.
- [110] Takeyoshi Okajima, Takeo Ohsaka, Osamu Hatozaki, and Noboru Oyama. Electrode kinetics of [ru (nh₃)₆]^{3+/2+} couple confined in montmorillonite clay/poly (vinyl alcohol) composite films on graphite electrodes and film permeation of electroactive solution species. *Electrochimica acta*, 37(10):1865–1872, 1992.
- [111] Sang-Eun Bae, Karen L Stewart, and Andrew A Gewirth. Nitrate adsorption and reduction on cu (100) in acidic solution. *Journal of the American Chemical Society*, 129(33):10171–10180, 2007.
- [112] Matthew S Thorum, Jessica Yadav, and Andrew A Gewirth. Oxygen reduction activity of a copper complex of 3, 5-diamino-1, 2, 4-triazole supported on carbon black. *Angewandte Chemie*, 121(1):171–173, 2009.

- [113] Julie V Macpherson, Mark A Beeston, and Patrick R Unwin. Imaging local mass-transfer rates within an impinging jet and studies of fast heterogeneous electron-transfer kinetics using the microjet electrode. *Journal of the Chemical Society, Faraday Transactions*, 91(5):899–904, 1995.
- [114] Mariam Fadel, Jean-Vincent Daurelle, Jérôme Vicente, and Vincent Fourmond. Impact of alignment defects of rotating disk electrode on transport properties. *Electrochimica Acta*, 269:534–543, 2018.
- [115] Christopher MA Brett and Ana Maria CF Oliveira Brett. Hydrodynamic electrodes. In *Comprehensive chemical kinetics*, volume 26, pages 355–441. Elsevier, 1986.
- [116] Richard G Compton and Patrick R Unwin. Channel and tubular electrodes. *Journal of electroanalytical chemistry and interfacial electrochemistry*, 205(1-2):1–20, 1986.
- [117] Jonathan A Cooper and Richard G Compton. Channel electrodes—a review. *Electroanalysis: An International Journal Devoted to Fundamental and Practical Aspects of Electroanalysis*, 10(3):141–155, 1998.
- [118] R COMPTON and R DRYFE. Photoelectrochemical studies. *Progress in Reaction Kinetics*, 20(3), 1995.
- [119] Craig B Ranger. Flow injection analysis. principles, techniques, applications, design. *Analytical Chemistry*, 53(1):20A–32A, 1981.
- [120] Daryl A Roston, Ronald E Shoup, and Peter T Kissinger. Liquid chromatography/electrochemistry: thin-layer multiple electrode detection. *Analytical Chemistry*, 54(13):1417A–1434A, 1982.
- [121] Craig E Lunte, Peter T Kissinger, and Ronald E Shoup. Difference mode detection with thin-layer dual-electrode liquid chromatography/electrochemistry. *Analytical Chemistry*, 57(8):1541–1546, 1985.
- [122] John A Alden and Richard G Compton. Hydrodynamic voltammetry with channel microband electrodes: Axial diffusion effects. *Journal of Electroanalytical Chemistry*, 404(1):27–35, 1996.
- [123] Barry A Coles and Richard G Compton. Photoelectrochemical esr: Part i. experimental. *Journal of Electroanalytical Chemistry and Interfacial Electrochemistry*, 144(1-2):87–98, 1983.
- [124] MA Lévêque. The laws of heat transmission by convection. *Les Annales des Mines: Memoires*, 12(13):201–299, 1928.
- [125] WJ Blaedel, Carter L Olson, and LR Sharma. The tubular platinum electrode. *Analytical Chemistry*, 35(13):2100–2103, 1963.
- [126] WJ Blaedel and SL Boyer. Submicromolar concentration measurements with tubular electrodes. *Analytical Chemistry*, 43(12):1538–1540, 1971.
- [127] WJ Blaedel and DG Iverson. Study of the steady-state current at tubular electrodes in the micromolar concentration region. *Analytical Chemistry*, 49(11):1563–1566, 1977.
- [128] W John Albery, Andrew T Chadwick, Barry A Coles, and Noel A Hampson. The tube electrode and esr: Second order kinetics. *Journal of Electroanalytical Chemistry and Interfacial Electrochemistry*, 75(1):229–239, 1977.

- [129] RG Compton, JC Ball, and JA Cooper. J. electroanal. chem., 1993.
- [130] Stephen G Weber. Digital simulation of the channel flow-through electrochemical cell: A theoretical study of the determination of solute adsorption on modified electrodes. *Journal of electroanalytical chemistry and interfacial electrochemistry*, 222(1-2):117–128, 1987.
- [131] Patrick R Unwin. The ece-disp1 problem: general resolution via double channel electrode collection efficiency measurements. *Journal of electroanalytical chemistry and interfacial electrochemistry*, 297(1):103–124, 1991.
- [132] Richard G Compton and Patrick R Unwin. Linear sweep voltammetry at channel electrodes. *Journal of electroanalytical chemistry and interfacial electrochemistry*, 206(1-2):57–67, 1986.
- [133] Adrian C Fisher and Richard G Compton. The ec mechanism: Split waves at the channel electrode. *Electroanalysis*, 4(3):311–315, 1992.
- [134] Wayne M Leslie, John A Alden, Richard G Compton, and Toomas Silk. Ece and disp processes at channel electrodes: Analytical theory. *The Journal of Physical Chemistry*, 100(33):14130–14136, 1996.
- [135] Adrian C Fisher, Barry A Coles, Richard G Compton, Donald Bethell, and Sadhana Tripathi. The photo-ce mechanism: the oxidation of tris-(p-tolyl) amine in acetonitrile at an illuminated platinum electrode. *Journal of the Chemical Society, Faraday Transactions*, 86(21):3603–3606, 1990.
- [136] Richard G Compton and Robert AW Dryfe. The photoelectrochemical reduction of p-bromo-nitrobenzene: an ecee, ece or disp process? mechanistic resolution via channel electrode voltammetry. *Journal of Electroanalytical Chemistry*, 375(1-2):247–255, 1994.
- [137] Sunita Kumbhat, Richard Webster, Frank Marken, John C Eklund, and Richard G Compton. Voltammetric monitoring of photochemical reactions: Photo-induced electron transfer to p-chloronitrobenzene. *Electroanalysis*, 8(6):515–518, 1996.
- [138] Iain E Henley and Adrian C Fisher. Computational electrochemistry: The simulation of voltammetry in microchannels with low conductivity solutions. *The Journal of Physical Chemistry B*, 107(27):6579–6585, 2003.
- [139] Andrew J Wain, Richard G Compton, Rudolph Le Roux, Sinead Matthews, and Adrian C Fisher. Microfluidic channel flow cell for simultaneous cryoelectrochemical electron spin resonance. *Analytical chemistry*, 79(5):1865–1873, 2007.
- [140] Kin Yip Tam, Rui Lin Wang, Chi Woo Lee, and Richard G Compton. Applications of the channel flow cell for uv-visible spectroelectrochemical studies: The kinetics of dimerization of the methyl viologen radical cation. *Electroanalysis*, 9(3):219–224, 1997.
- [141] D-T Chin and C-H Tsang. Mass transfer to an impinging jet electrode. *Journal of the Electrochemical Society*, 125(9):1461, 1978.
- [142] MB Glauert. The wall jet. *Journal of Fluid Mechanics*, 1(6):625–643, 1956.
- [143] V Bouet, C Gabrielli, G Maurin, and H Takenouti. Application of electrochemical impedance analysis to the characterization of mass transfer in a submerged impinging jet cell. *Journal of Electroanalytical Chemistry*, 340(1-2):325–331, 1992.

- [144] Stephen G Weber and William C Purdy. Electrochemical detection with a regenerative flow cell in liquid chromatography. *Analytical Chemistry*, 54(11):1757–1764, 1982.
- [145] J-P Bouchez and Richard J Goldstein. Impingement cooling from a circular jet in a cross flow. *International Journal of Heat and Mass Transfer*, 18(6):719–730, 1975.
- [146] T Strand. On the theory of normal ground impingement of axisymmetric jets in inviscid incompressible flow. In *1st Annual Meeting*, page 424, 1964.
- [147] NV Rees and RG Compton. Hydrodynamic microelectrode voltammetry. *Russian Journal of Electrochemistry*, 44(4):368–389, 2008.
- [148] Joseph Yamada and Hiroaki Matsuda. Limiting diffusion currents in hydrodynamic voltammetry: Iii. wall jet electrodes. *Journal of Electroanalytical Chemistry and Interfacial Electrochemistry*, 44(2):189–198, 1973.
- [149] Hadil M Elbardisy, Eduardo M Richter, Robert D Crapnell, Michael P Down, Peter G Gough, Tarek S Belal, Wael Talaat, Hoda G Daabees, and Craig E Banks. Versatile additively manufactured (3d printed) wall-jet flow cell for high performance liquid chromatography-amperometric analysis: application to the detection and quantification of new psychoactive substances (nbomes). *Analytical Methods*, 12(16):2152–2165, 2020.
- [150] Bernard Fleet and CoJ Little. Design and evaluation of electrochemical detectors for hplc. *Journal of Chromatographic Science*, 12(12):747–752, 1974.
- [151] James L Melville, Barry A Coles, Richard G Compton, Nafeesa Simjee, Julie V Macpherson, and Patrick R Unwin. Hydrodynamics and mass transport in wall tube and microjet electrodes. simulation and experiment for micrometer-scale electrodes. *The Journal of Physical Chemistry B*, 107(1):379–386, 2003.
- [152] W John Albery. The current distribution on a wall-jet electrode. *Journal of electroanalytical chemistry and interfacial electrochemistry*, 191(1):1–13, 1985.
- [153] F Homann. Zamm, 16, 153 (1936). *Forschg. Ing. Wes*, 7:1, 1936.
- [154] N Frossling. Verdunstung, warmeübertragung und geschwindigkeitsverteilung bei zweidimensionaler und rotationssymmetrischer laminarer grenzschichtströmung. *Lunds. Univ. Arsskr. NF Avd*, 2:35, 1940.
- [155] Hiroaki Matsuda and Joseph Yamada. Limiting diffusion currents in hydrodynamic voltammetry: I. fixed disk and ring electrodes in laminar uniform flow. *Journal of Electroanalytical Chemistry and Interfacial Electrochemistry*, 30(2):261–270, 1971.
- [156] Chu-Jen Chia, Francesc Giralt, and Olev Trass. Mass transfer in axisymmetric turbulent impinging jets. *Industrial & Engineering Chemistry Fundamentals*, 16(1):28–35, 1977.
- [157] Neil V Rees, Oleksiy V Klymenko, Barry A Coles, and Richard G Compton. Hydrodynamics and mass transport in wall-tube and microjet electrodes: an experimental evaluation of current theory. *The Journal of Physical Chemistry B*, 107(49):13649–13660, 2003.
- [158] James L Melville, Nafeesa Simjee, Patrick R Unwin, Barry A Coles, and Richard G Compton. Hydrodynamics and mass transport in wall tube and microjet electrodes: Effect of vortex formation and cell geometry on limiting currents. *The Journal of Physical Chemistry B*, 106(40):10424–10431, 2002.

- [159] GK Morris, SV Garimella, and JA Fitzgerald. Flow-field prediction in submerged and confined jet impingement using the reynolds stress model. 1999.
- [160] Julie V Macpherson, Scott Marcar, and Patrick R Unwin. Microjet electrode: a hydrodynamic ultramicroelectrode with high mass-transfer rates. *Analytical Chemistry*, 66(13):2175–2179, 1994.
- [161] Julie V Macpherson, Nafeesa Simjee, and Patrick R Unwin. Hydrodynamic ultramicroelectrodes: kinetic and analytical applications. *Electrochimica acta*, 47(1-2):29–45, 2001.
- [162] RG Compton, CR Greaves, and AM Waller. The wall-jet electrode and its application to the study of electrode reactions with coupled homogeneous kinetics: the disp1 reaction. *Journal of applied electrochemistry*, 20(4):586–589, 1990.
- [163] Hari Gunasingham, KP Ang, and CC Ngo. Stripping voltammetry of thin mercury films at the wall-jet electrode. *Analytical Chemistry*, 57(2):505–508, 1985.
- [164] H Gunasingham, KP Ang, CC Ngo, and PC Thiak. Differential pulse anodic stripping voltammetry at the wall-jet electrode. *Journal of electroanalytical chemistry and interfacial electrochemistry*, 198(1):27–35, 1986.
- [165] Joseph Wang, Howard D Dewald, and Benjamin Greene. Anodic stripping voltammetry of heavy metals with a flow injection system. *Analytica Chimica Acta*, 146:45–50, 1983.
- [166] James G Douglas. Characterization of an ion-selective electrode wall-jet detector for flow injection analysis. *Analytical Chemistry*, 61(8):922–924, 1989.
- [167] H Gunasingham, KP Ang, and CC Ngo. Medium effects in the stripping voltammetry of mercury. *Analyst*, 113(10):1533–1536, 1988.
- [168] Dennis G Swartzfager. Amperometric and differential pulse voltammetric detection in high performance liquid chromatography. *Analytical Chemistry*, 48(14):2189–2191, 1976.
- [169] Hari Gunasingham. Analytical applications of the wall-jet detector. *TrAC Trends in Analytical Chemistry*, 7(6):217–221, 1988.
- [170] Rachel D Martin and Patrick R Unwin. Measurement of fast kinetics with the microjet electrode: the ce mechanism. *Journal of Electroanalytical Chemistry*, 397(1-2):325–329, 1995.
- [171] Julie V Macpherson and Patrick R Unwin. Radial flow microring electrode: Development and characterization. *Analytical Chemistry*, 70(14):2914–2921, 1998.
- [172] Susan Cannan and Patrick R Unwin. Characterization and assessment of the microjet electrode as a detector for hplc. *Electroanalysis: An International Journal Devoted to Fundamental and Practical Aspects of Electroanalysis*, 16(9):712–718, 2004.
- [173] Dan S Kercher, Jeong-Bong Lee, Oliver Brand, Mark G Allen, and Ari Glezer. Microjet cooling devices for thermal management of electronics. *IEEE Transactions on Components and Packaging Technologies*, 26(2):359–366, 2003.
- [174] T Węgrzyn and J Piwnik. Low alloy steel welding with micro-jet cooling. *Archives of Metallurgy and Materials*, 57:540–543, 2012.

- [175] Eleni Bitziou, Nicola C Rudd, Martin A Edwards, and Patrick R Unwin. Visualization and modeling of the hydrodynamics of an impinging microjet. *Analytical chemistry*, 78(5):1435–1443, 2006.
- [176] Asmaa Hadj Ahmed, Jean-Vincent Daurelle, and Vincent Fourmond. Optimizing the mass transport of wall-tube electrodes for protein film electrochemistry. *Electrochimica Acta*, 403:139521, 2022.
- [177] S Patankar. Numerical heat transfer and fluid flow, ser. *Coputational Methods Mech. Therm. Sci*, pages 1–197, 1980.
- [178] Mark J Eddowes. Numerical methods for the solution of the rotating disc electrode system. *Journal of electroanalytical chemistry and interfacial electrochemistry*, 159(1):1–22, 1983.
- [179] Cesar A Real-Ramirez, Raul Miranda-Tello, Luis F Hoyos-Reyes, and Jesus I Gonzalez-Trejo. Hydrodynamic characterization of an electrochemical cell with rotating disc electrode: a three-dimensional biphasic model. *International Journal of Chemical Reactor Engineering*, 8(1), 2010.
- [180] Jacques Goupy. *Plans d'expériences*. Ed. Techniques Ingénieur, 2006.
- [181] Jiju Antony. *Design of experiments for engineers and scientists*. Elsevier, 2014.
- [182] R Myers, Douglas C Montgomery, and CM ANDERSON-COOK. Design and analysis of experiments, 2001.
- [183] Edward L Paul, Victor A Atiemo-Obeng, and Suzanne M Kresta. *Handbook of industrial mixing: science and practice*, volume 1. John Wiley & Sons, 2003.
- [184] Michael H Oddy, Juan G Santiago, and Jim C Mikkelsen. Electrokinetic instability micromixing. *Analytical chemistry*, 73(24):5822–5832, 2001.
- [185] Robin H Liu, Jianing Yang, Maciej Z Pindera, Mahesh Athavale, and Piotr Grodzinski. Bubble-induced acoustic micromixing. *Lab on a Chip*, 2(3):151–157, 2002.
- [186] Arshad Afzal and Kwang-Yong Kim. Convergent–divergent micromixer coupled with pulsatile flow. *Sensors and Actuators B: Chemical*, 211:198–205, 2015.
- [187] Steffen Hardt, Klaus Drese, Volker Hessel, and Friedhelm Schönfeld. Passive micro mixers for applications in the micro reactor and μ tas field. In *International Conference on Nanochannels, Microchannels, and Minichannels*, volume 41642, pages 45–55, 2004.
- [188] Arshad Afzal and Kwang-Yong Kim. Mixing performance of passive micromixer with sinusoidal channel walls. *Journal of chemical engineering of Japan*, 46(3):230–238, 2013.
- [189] Yung-Chiang Chung, Yuh-Lih Hsu, Chun-Ping Jen, Ming-Chang Lu, and Yu-Cheng Lin. Design of passive mixers utilizing microfluidic self-circulation in the mixing chamber. *Lab on a Chip*, 4(1):70–77, 2004.
- [190] HM Xia, SYM Wan, Chang Shu, and YT Chew. Chaotic micromixers using two-layer crossing channels to exhibit fast mixing at low reynolds numbers. *Lab on a Chip*, 5(7):748–755, 2005.
- [191] Arshad Afzal and Kwang-Yong Kim. *Analysis and Design Optimization of Micromixers*. Springer, 2021.

- [192] Chia-Yen Lee, Wen-Teng Wang, Chan-Chiung Liu, and Lung-Ming Fu. Passive mixers in microfluidic systems: A review. *Chemical Engineering Journal*, 288:146–160, 2016.
- [193] Terje Tofteberg, Maciej Skolimowski, Erik Andreassen, and Oliver Geschke. A novel passive micromixer: lamination in a planar channel system. *Microfluidics and Nanofluidics*, 8(2):209–215, 2010.
- [194] Wolfgang Buchegger, Christoph Wagner, Bernhard Lendl, Martin Kraft, and Michael J Vellekoop. A highly uniform lamination micromixer with wedge shaped inlet channels for time resolved infrared spectroscopy. *Microfluidics and Nanofluidics*, 10(4):889–897, 2011.
- [195] Nam-Trung Nguyen and Zhigang Wu. Micromixers—a review. 15(2):R1–R16, dec 2004.
- [196] Julio M Ottino and JM Ottino. *The kinematics of mixing: stretching, chaos, and transport*, volume 3. Cambridge university press, 1989.
- [197] Jang Min Park, Kyoung Duck Seo, and Tai Hun Kwon. A chaotic micromixer using obstruction-pairs. *Journal of Micromechanics and Microengineering*, 20(1):015023, 2009.
- [198] Li-Yu Tseng, An-Shik Yang, Chun-Ying Lee, and Chang-Yu Hsieh. Cfd-based optimization of a diamond-obstacles inserted micromixer with boundary protrusions. *Engineering Applications of Computational Fluid Mechanics*, 5(2):210–222, 2011.
- [199] Robert Goovaerts, Wim Smits, Gert Desmet, Joeri Denayer, and Wim De Malsche. Combined improved mixing and reduced energy dissipation by combining convective effects and lamination. *Chemical engineering journal*, 211:260–269, 2012.
- [200] Shih-Jeh Wu, Hsiang-Chen Hsu, and Wen-Jui Feng. Novel design and fabrication of a geometrical obstacle-embedded micromixer with notched wall. *Japanese Journal of Applied Physics*, 53(9):097201, 2014.
- [201] Yuqiang Fang, Yinghua Ye, Ruiqi Shen, Peng Zhu, Rui Guo, Yan Hu, and Lizhi Wu. Mixing enhancement by simple periodic geometric features in microchannels. *Chemical Engineering Journal*, 187:306–310, 2012.
- [202] Jian Li, Guodong Xia, and Yifan Li. Numerical and experimental analyses of planar asymmetric split-and-recombine micromixer with dislocation sub-channels. *Journal of Chemical Technology & Biotechnology*, 88(9):1757–1765, 2013.
- [203] Mubashshir Ahmad Ansari, Kwang-Yong Kim, Khalid Anwar, and Sun Min Kim. A novel passive micromixer based on unbalanced splits and collisions of fluid streams. *Journal of Micromechanics and Microengineering*, 20(5):055007, 2010.
- [204] Arshad Afzal and Kwang-Yong Kim. Passive split and recombination micromixer with convergent–divergent walls. *Chemical Engineering Journal*, 203:182–192, 2012.
- [205] Mohsen Khosravi Parsa, Faramarz Hormozi, and Davoud Jafari. Mixing enhancement in a passive micromixer with convergent–divergent sinusoidal microchannels and different ratio of amplitude to wave length. *Computers & Fluids*, 105:82–90, 2014.
- [206] Ying Lin, Xinhai Yu, Zhenyu Wang, Shan-Tung Tu, and Zhengdong Wang. Design and evaluation of an easily fabricated micromixer with three-dimensional periodic perturbation. *Chemical engineering journal*, 171(1):291–300, 2011.

- [207] Jun Yang, Li Qi, Yi Chen, and Huimin Ma. Design and fabrication of a three dimensional spiral micromixer. *Chinese Journal of Chemistry*, 31(2):209–214, 2013.
- [208] Mohammad Nimafar, Vladimir Viktorov, and Matteo Martinelli. Experimental comparative mixing performance of passive micromixers with h-shaped sub-channels. *Chemical engineering science*, 76:37–44, 2012.
- [209] RK Thakur, Ch Vial, KDP Nigam, EB Nauman, and G Djelveh. Static mixers in the process industries—a review. *Chemical engineering research and design*, 81(7):787–826, 2003.
- [210] Seyyed Mahdi Hosseini, Kiyanoosh Razzaghi, and Farhad Shahraki. Design and characterization of a low-pressure-drop static mixer. *AIChE Journal*, 65(3):1126–1133, 2019.
- [211] Akram Ghanem, Charbel Habchi, Thierry Lemenand, Dominique Della Valle, and Hassan Peerhossaini. Mixing performances of swirl flow and corrugated channel reactors. *Chemical Engineering Research and Design*, 92(11):2213–2222, 2014.
- [212] Akram Ghanem, Thierry Lemenand, Dominique Della Valle, and Hassan Peerhossaini. Static mixers: Mechanisms, applications, and characterization methods—a review. *Chemical engineering research and design*, 92(2):205–228, 2014.
- [213] Sulzer Chemtech. Mixing and reaction technology. *Sulzer brochure*, 23:06–40, 1997.
- [214] JM Zalc, ES Szalai, FJ Muzzio, and S Jaffer. Characterization of flow and mixing in an smx static mixer. *AIChE Journal*, 48(3):427–436, 2002.
- [215] ES Szalai and FJ Muzzio. Fundamental approach to the design and optimization of static mixers. *AIChE journal*, 49(11):2687–2699, 2003.
- [216] Shiping Liu, Andrew N Hrymak, and Philip E Wood. Design modifications to smx static mixer for improving mixing. *AIChE journal*, 52(1):150–157, 2006.
- [217] Philippe Carrière. On a three-dimensional implementation of the baker’s transformation. *Physics of fluids*, 19(11):118110, 2007.
- [218] Mathieu Creyssels, Simon Prigent, Yixian Zhou, Xin Jianjin, Christian Nicot, and Philippe Carrière. Laminar heat transfer in the “mllm” static mixer. *International Journal of Heat and Mass Transfer*, 81:774–783, 2015.
- [219] Mushtak Al-Atabi. Design and assessment of a novel static mixer. *The Canadian Journal of Chemical Engineering*, 89(3):550–554, 2011.
- [220] Vincent Fourmond. Qsoas: a versatile software for data analysis. *Analytical chemistry*, 88(10):5050–5052, 2016.

Appendix A

Material and methods

This chapter presents the material and methods that we have used throughout this thesis.

A.1 Electrochemical cell

The wall-tube electrochemical cell consists of two parts. The bottom part of the cell is composed of the three electrodes system (fig A.1). Two working electrodes were used to perform electrochemical experiments in this cell (see section A.2).

- One with a diameter of 0.1 mm: it was used in the validating experiments of mass transport formula (see section 3.6).
- The other one of 1 mm diameter: it was used in mixing experiments (see section 5.1.1), and also in shear stress experiments (see section 4.1).

The counter electrode is a platinum wire of 0.5 mm diameter, and the reference electrode is an AG/AgCl electrode. The reference compartment consists of a volume filled with a KCl saturated solution and contains a silver wire. The contact between the RE and the WE compartments was ensure by a frit.

Experiments outside the glovebox were carried out using PGSTAT101 potentiostat from Metrohm controlled by Nova software.

Enzymes experiments were done in a JACOMEX glovebox under N₂. We used a potentiostat from Metrohm and it was controlled by GPES software.

A.2 Preparation of electrodes

The two working electrodes mentioned above are homemade electrodes. They are composed of edge pyrolytic graphite embedded in a resin.

The resin was prepared by mixing 1 parts of the hardener HY991 and 2,5 parts of ARALDITE AY103-1 from Huntsman advanced Material (UK). It is necessary to mix for a long time, at least for half a minute, to obtain a homogeneous mixture.

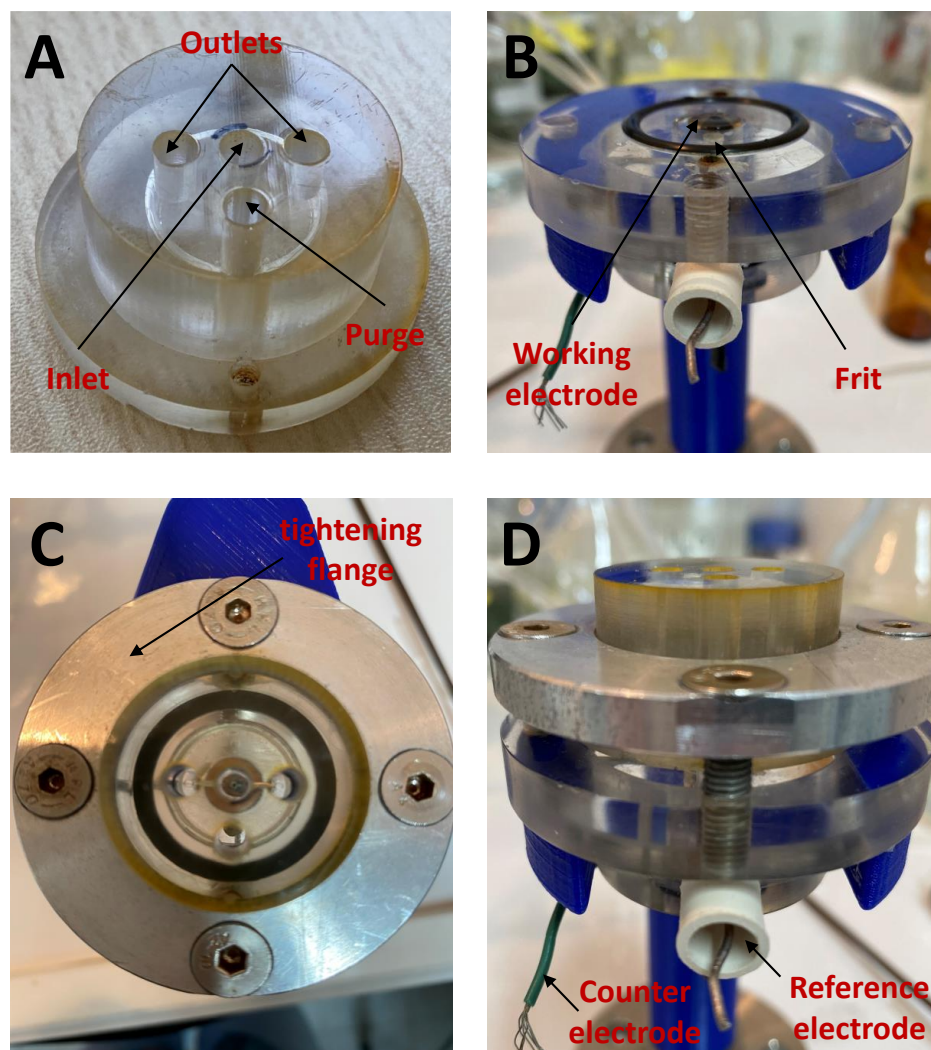


Fig. A.1 Photos of the wall-tube electrochemical cell. (A) is the top part of the cell, (B) is the bottom part of the cell design, (C) is a top view of the closed cell, and (D) is a side view of the closed cell.

- The graphite with 1 mm was reshaped in the workshop at the IUSTI laboratory in Marseille.
- The graphite with 0.1 mm diameter was reshaped in the laboratory “Lasers, Plasmas et Procédés Photoniques” in Marseille.

The graphite rods were put in a Teflon cast of 8 mm diameter then the latter was filled with the mixture of the resin and left in the oven at 60 °C overnight.

After taking out the electrodes from the cast, we polished them well, starting with sand paper getting down to the finest size (from 600 to 4000), then finishing by diamond paste of 3 μm then 1 μm and cleaning the electrode surface by alumina (1 μm).

A.3 Syringe pump



Fig. A.2 Photo of the syringe pumps used in the experiments.

For pumping the flow to the wall-tube electrochemical cell, we used syringe pumps “Fusion 4000” from Chemyx Inc [A.2](#). The volume of each syringe was 100 mL.

A.4 Preparation of solutions

For experiments with the enzymes, a mixed buffer have been used, in which the composition is shown in table [A.1](#). We have adjusted the pH using HCl and/or NaOH solutions.

Compound	Final Concentration mM	Molar mass (g/mol)
MES	5	195.24
CHES	5	207.29
HEPES	5	238.3
TAPS	5	243.28
Sodium Acetate	5	136.1
NaCl	100	58.44

Table A.1 Composition of the mixed buffer used in the PFE experiments

A.5 List of materials

The chemicals and materials used throughout this thesis are summarized in table [A.2](#).

Material	Supplier
Pyrolytic Graphite Edge rods	
Hardener HY 991	Araldite, UK.
Araldite AY 103-1	Araldite. UK
MQ Water	Millo QTM unit, Millipore Corp., U.S.A.
Potassium hexacyanoferrate (III) ($MW = 329.4$ g/mol)	Sigma-Aldrich. France
Sodium chloride ($MW = 58.44$ g/mol)	Sigma-Aldrich. France
Sodium nitrite ;($MW = 69$ g/mol)	Sigma-Aldrich. France
Ethanol (99.99%)	Fishier Scientific Ltd. France

Table A.2 List of all the materials used for work in this thesis.

Appendix B

Data analysis

All the data were analysed using our in-house, open source program QSoas [220] that was developed by my supervisor Vincent FOURMOND.

B.1 Analysis of the electrochemical experiments data

The scripts that were used to determine shear stress rates are presented in section 4.1.

Determining the limiting current and mass transport coefficient from CVs

```
# Loading the CVs:
l '${1}'
l '${2}'
# Subtracting the background:
S 1 0 /mode=indices
# Extracting the limiting current as function of the flow rate
and exporting it to the output file: strip-if x<-0.6||x>-0.5
output ilim=f(buffer).dat
eval flow: $stats.buffer ilim: $stats.y-average /output=true
# Loading the limiting current file:
l ilim=f(flow).dat
# Dividing the current by  $n F A$  to obtain the mass transport coefficient:
apply-formula y=abs(y)/(1*96485*8e-9) /flags=m-exp
# Plotting m-exp as a function of the flow rate:
@ style.txt (note that the file ‘‘style.txt’’ includes the scripts
of the figure mode).
plot-xy flagged:m-exp /symbol=circle
/symbol-scale=0.4 /symbol-color=green
# Exporting the plot as a pdf file:
print m-exp.pdf
```

B.2 Analysis of CFD data

Determining the hydrodynamic constant As shown in chapter 3, section 3.7, we extracted the files that include axial and radial velocities as a function of r and z in a small region around the center of the electrode inside the stagnation region (the zoomed area in red frame in red in fig S4).

We determined the constant “a” by fitting the data to both equations (B.1b) and (B.1b):

$$u = 2\alpha a^{3/2} \nu^{-1/2} r z \quad (\text{B.1a})$$

$$v = -2\alpha a^{3/2} \nu^{-1/2} z^2 \quad (\text{B.1b})$$

To fit to radial velocity equation (B.1b), for each file, we run the script:

```
l '${1}' /columns=3,1,4,2
sort
set-column-names z v r u
tweak-columns
/select=$c.z,$c.u,$c.r,$c.v
apply-formula x=x+0.15e-3
strip-if x>5e-6
apply-formula y=y/y2
fit-arb 2*alpha*a**(3/2)*nu**(-1/2)*x
eval a:$meta.a file:$stats.buffer /output=true
```

To fit to axial velocity equation (B.1b), for each file, we run the script:

```
l '${1}' /columns=3,1,4,2
sort
set-column-names z v r u
tweak-columns select=$c.z,$c.v,$c.r,$c.u
apply-formula x=x+0.20e-3
strip-if x>5e-6
fit-arb
-2*alpha*a**(3/2)*nu**(-1/2)*(x)**2
eval a:$meta.a file:$stats.buffer output=true
```

Average mass transport coefficient, shear stress and pressure drop From each simulations, We exported a file “Table Exp*.csv” (in which * = simulation number), that includes the mass flux, shear stress, pressure drop as a function of the radial distance from the center of the electrode: To determine the average values of each of the quantities mentioned above at different radius values in the range $r_0 \dots r_n$: we run for each file “Table Exp*.csv” this script:

```

output "${1}-Average.dat" /overwrite=true
run-for-each Average.cmds $r_0...r_n$:100 /range-type=log
/silent=true '/arg2=${1}'

```

in which, the file “Average.dat” includes the following script:

```

1 '${2}' /columns=1,2,6,9,10,3,7,8
sort
set-column-names area flux shear radius m avshear homog pressure
tweak-columns /select=$c.radius,$c.flux,$c.shear,$c.area,$c.m,
$c.avshear,$c.homog,$c.pressure
strip-if x>${1}||x==0
set-meta r ${1}
apply-formula
y4=y/997.561*y3/$stats.y3_sum
apply-formula y5=y2/x*y3/$stats.y3_sum
apply-formula y6=($stats.y_max-$stats.y_min)
/$stats.y4_sum
eval r:$meta.r m:$stats.y4_sum s:$stats.y5_sum nh:$stats.y6_average
p:$stats.y7_max w:$stats.rows file:$stats.buffer /output=true

```

To select the combinations (geometry/cell) in which the heterogeneity of the flux is smaller than 10%, we run for each file the script:

```

1 '${1}'
sort
strip-if y2>10
apply-formula y3=$stats.y2_max
strip-if y2<y3
output "rmax-homogeneity.cmds"
eval r:$stats.x_average nh:$stats.y2_max m:$stats.y_average
file:$stats.buffer /output=true

```

